Stony Brook University

The Structure and Dynamics of Barrier Jets along the Southeast Alaskan Coast

A Dissertation Presented

by

Joseph Benjamin Olson

to

The Graduate School

in Partial Fulfillment of the

Requirements

for the Degree of

Doctor of Philosophy

in

Marine and Atmospheric Science

Stony Brook University

December 2007

Stony Brook University

The Graduate School

Joseph Benjamin Olson

We, the dissertation committee for the above candidate for the

Doctor of Philosophy degree, hereby recommend

acceptance of this dissertation.

Dr. Brian A. Colle
Advisor
School of Marine and Atmospheric Sciences, Stony Brook University

Dr. Minghua Zhang
Chairperson, Professor, and Director of ITPA
School of Marine and Atmospheric Sciences, Stony Brook University

Dr. Edmund K. M. Chang
Associate Professor
School of Marine and Atmospheric Sciences, Stony Brook University

Dr. Dong-Ping Wang
Professor
School of Marine and Atmospheric Sciences, Stony Brook University

Dr. Scott Braun
Research Scientist
NASA Goddard Space Flight Center

This dissertation is accepted by the Graduate School

Lawrence Martin
Dean of the Graduate School

Abstract of the Dissertation

The Structure and Dynamics of Barrier Jets along

the Southeast Alaskan Coast

by

Joseph Benjamin Olson

Doctor of Philosophy

in

Marine and Atmospheric Science

Stony Brook University

2007

Coastal barrier jets along the complex orography of southeastern Alaska were investigated using high resolution observations and model simulations. Barrier jet events were sampled with the Wyoming King-Air research aircraft during the Southeastern Alaskan Regional Jet (SARJET) field experiment in 2004. These observations, combined with simulations of select cases by the Penn State-NCAR Mesoscale Model (MM5), were used to better understand barrier jet structure and dynamics. A suite of idealized simulations were used to put the case studies in perspective with a larger set of atmospheric conditions, while also evaluating previous theoretical and observational results.

Two SARJET case studies were investigated along the tall and steep Fairweather Mountains near Juneau, Alaska. The first case (24 September 2004) was a classical barrier jet forced primarily by onshore flow and upslope adiabatic cooling, with

maximum winds >30 m s^{-1} at the coast between 600-800 m ASL and an offshore extent of ~60 km. In contrast, the hybrid jet (12 October 2004) was influenced by an offshore-directed gap flow at the coast, which produced a warm anomaly over the coast associated with downslope flow and a wind maximum (~30 m s^{-1}) that was displaced 30-40 km offshore at 500 m ASL. A sensitivity experiment in which the coastal mountain gap was filled led to a ~40% reduction in the jet width, and the position of the jet maximum shifted ~40 km to the coast, but the overall jet intensity remained approximately the same.

The generality of these SARJET results was tested by generating a set of three-dimensional idealized MM5 simulations by varying wind speeds, wind directions, and static stabilities for the classical jet simulations, while incrementing the magnitude of the inland cold pool (instead of static stability) for hybrid jet simulations. The broad inland terrain was shown to impact the upstream winds by rotating them cyclonically to become more terrain-parallel within 500-1000 km of the coast. This reduced cross-barrier component acted to reduce the local Froude number of the impinging flow, thus enhancing the potential for flow blocking. Thus, the enhancement of the large-scale mountain anticyclone by the inland terrain acts to "precondition" the impinging flow for barrier jet development.

The largest simulated wind speed enhancements (~1.9-2.0) for the classic and hybrid jets occurred for low Froude numbers (*Fr)*, with a maximum at *Fr* ~0.3-0.4. Low ambient wind speeds (10 –15 m s^{-1}) and southerly (170-180^{o}) wind directions (~30-45^{o} from coast-parallel) were also ingredients for the largest wind speed enhancements. The widest barrier jets were found in simulations with ambient winds oriented nearly terrain-

parallel (~160^{o}) with strong static stability ($N > 0.01$ s^{-1}). Hybrid barrier jets were slightly wider than the classical, with the gap outflows acting to shift the position of the jet maximum further away from the coast. During periods of maximal gap outflow (hrs 6-18), the height of the jet maximums were typically lower than the classical simulations, since the hybrid jet maximum was located at the top of the shallow gap outflow. The jet height was most correlated with total wind speed, U_{total}, and negatively correlated with static stability, N, suggesting that the height of the jet maximum approximately scales as U_{total}/N, which is proportional to the vertical wavelength of a mountain wave.

Finally, a detailed assessment of the usefulness of the previous linear theory and scale analysis on barrier jets was performed. The high Fr relationship ($L = Nh_m/f$) performed better than the low Fr relationship ($L = U_n/f$) in determining the offshore extent of the barrier jet. The implementation of the dividing streamline concept of Sheppard's model for determining the proper blocking height (h_d) resulted in a modified form ($L = Nh_d/f$), which improved the predictive skill. For the determination of maximum wind speeds, the high Fr relationship ($\Delta V = Nh_m$) was found to be better correlated with the measured values than the low Fr relationship ($\Delta V = U_n$) throughout the full range of Fr. Two-dimensional linear theory performed poorly for $Fr < 0.5$. Modifications were made to these previous relationships to better account for the three dimensional winds, which helped to improve the estimated wind speed enhancements.

Table of Contents

List of Figures

Chapter 1 **Page**

Chapter 2

Chapter 3

Chapter 4

Chapter 5.

List of Tables

Chapter 2

Chapter 4

Chapter 5

Acknowledgements

I would like to thank my advisor, Dr. Brian A. Colle, for his guidance, teaching, and many fruitful discussions. I would like to thank Dr. Nicholas A. Bond (NOAA - Pacific Marine Environmental Laboratory) for his suggestions with the SARJET case study manuscript, the idealized barrier jet work, and the on-flight tutelage during the SARJET field study. I thank Dr. Nathaniel Winstead (Johns Hopkins University - Applied Physics Laboratory) for his review of the SARJET manuscript and for the SAR imagery. I thank Dr. Scott Braun (NASA – Goddard Space Flight Center) for serving as the external member on my dissertation committee and for a thorough review of my dissertation with many important suggestions for improvement. I would also like to thank my internal committee members, Dr. Minghua Zhang, Dr. Edmund Chang, and Dr. Dong-Ping Wang (School of Marine and Atmospheric Sciences, Stony Brook University) for their reviews of my dissertation, suggestions for improvement, and for teaching me the dynamics of the oceans and atmosphere.

I would like to thank my closest friends: Hen, Aleya, Kyoko, Steve, Mike Harris, Rob for enriching my life. And of course, I would like to express a deep thanks to my family: Mom, Dad, Jake, Sarah, Josh, Ben, and Lacey for an important collection of memories and transcendental connections I often take for granted.

Chapter I:

Introduction

1.1 Background

The Pacific Cordillera of western North America represents a series of mountain ranges stretching from Alaska to Mexico (Fig. 1.1). Some of the mountain ranges include the Rockies, Saint Elias Mountains, Cascade Ranges, and the Sierra-Nevadas. The Rocky Mountains form a broad plateau with a zonal width of ~1000 km in Canada to ~2000 km in the United States, with many prominent peaks above 14,000 ft (~4.3 km). The Pacific Coast Ranges can rise steeply from the ocean, reaching heights of 2000 m above sea-level (ASL) within 50 km from the coast in some areas. The coastal mountains of British Columbia and Alaska include a complex maze of fjords with hundreds of islands.

During the cool season, the synoptic-scale westerly flow interacts with the tall and steep coastal terrain. The onshore flow can become blocked and subsequently accelerated down the along-barrier pressure gradient to produce strong low-level winds, known as *barrier jets* (Schwerdtfeger 1974, 1975; Parish 1982). Barrier jets can interact with landfalling fronts to cause a rapid change in frontal strength within the coastal region, resulting in enhanced precipitation and coastal winds (Doyle 1997; Colle et. al. 2002; Yu and Smull 2001; among others). These events often create hazardous conditions for mariners and aviators, which can result in significant losses for the fishing and shipping industries (Macklin et al. 1990). Some of the previous work on barrier jets is summarized in the following sections.

1.2 Barrier jets

a. Theory and observations.

When stable flow encounters a topographic barrier, it undergoes forced ascent, which converts the kinetic energy of the flow into potential energy. The *Froude number*,

$$Fr = U_n/Nh_m, \qquad 1.1$$

can be interpreted as the ratio of the kinetic energy of the ambient flow to the amount of

energy required to surmount a barrier (Sheppard 1956)[1]; where U_n is the mean barrier-perpendicular velocity, h_m is the height of the barrier, and N is the Brunt-Väisälä frequency $N = [(g/\theta)\partial\theta/\partial z]^{1/2}$. For $Fr > 1$, the flow is said to be supercritical and has enough kinetic energy to pass over the barrier, but flows with $Fr < 1$, are subcritical and are at least partially blocked by the barrier. An alternative interpretation of the Froude number is the ratio of the background wind speed (U) to the maximum horizontal velocity of a linear mountain wave (Nh_m) (Smolarkeiwcz and Routnno 1989). This interpretation may be useful for portions of the phase space [Fr ~0(1)], where large-amplitude gravity waves are produced by the mountain-disturbed flow as it undergoes geostrophic adjustment (Smolarkiewicz and Rotunno 1990; Ólafsson and Bougeault 1996). These waves can produce pressure perturbations at the surface that enhance the blocking efficiency of the barrier (Smith 1980).

Many previous studies have used linear theory or two-dimensional simulations (Miles and Huppert 1969; Pierrehumbert and Wyman 1985; Smith 1989b; Lin and Wang 1996) to determine the onset of upstream stagnation and wave breaking for hydrostatic flow over a bell-shaped isolated mountain. Decelerated flows developed as the Fr dropped below 1.0-1.3 and stagnation on the windward slope occurred as Fr dropped below ~0.4. Gravity wave breaking was largest near Fr ~ 1, but weakened as the windward flow stagnated.

Three dimensional simulations (Smolarkiewicz and Rotunno 1990; Smith and Grønås 1993; Ólafsson and Bougeault 1996) modified these results to include the transition from flow over to flow around the obstacle at low Fr. Ólafsson and Bougeault (1996) explained that a low Fr (< 1) results in flow blocking and a dividing streamline that separates the blocked flow (below) from the flow over (above). The Froude number relevant to the flow above this partition must use a modified height $h = h_m - h_d$, where h_d is the height of the dividing streamline. They also extended these results for mountain ridges with aspect ratio 5 ($L_y > L_x$). They found that an elongated mountain ridge increased blocking and produced 30-60% greater wind speed maxima in the surface flow, since the increased residence time of the blocked flow allowed for a longer time period of acceleration down the large-scale pressure gradient. These results may be more applicable to the Pacific Cordillera, due to its significant meridional extent.

The flow blocking that occurs for low Froude number flows ($Fr < 1$) can produce barrier jets that exceed 30 m s^{-1}. They form when a positive pressure perturbation is created against a steep mountain barrier. This anomaly can either result from advection of cold air from a nearby source region, such as in cold air damming (Bell and Bosart 1988; Colle and Mass 1995), adiabatic cooling of ascending air over the barrier (Mass and Ferber 1990), diabatic cooling (Marwitz 1983), density anomaly aloft associated with a standing mountain wave (Smith 1980; Smolarkiewicz and Rotunno 1990), or a combination of these factors. This pressure perturbation decelerates the impinging flow, resulting in a reduced Coriolis force and a leftward (rightward) deflection in the northern (southern) hemisphere. The blocked flow is then accelerated down the large-scale pressure gradient, which results in an increase in the Coriolis force until an approximate geostrophic balance develops with the cross-barrier pressure gradient. Figure 1.2 shows

[1] The inverse of the Froude number, or non-dimension mountain height, $\hat{H}=Nh_m/U$, was used by Queney (1948), Pierrehumbert and Wyman (1985), and many others as a measure of the strength of the mountain-induced disturbance.

an example of a barrier jet sampled with research aircraft over the slope of a Sierra Nevada mountain, with strong winds (> 25 m s^{-1}) at 1000 m over the base of the mountain (taken from Parish 1982). Barrier jets have also been observed along the coasts of California-Oregon (Doyle 1997; Yu and Smull 2000), Antarctica (Schwerdtfeger 1975), Greenland (Moore and Renfrew 2005), Norway (Barstad and Grønås 2005) and Taiwan (Li and Chen 1998, Yeh and Chen 2003), and in the Rockies (Colle and Mass 1995), Appalachians (Richwein 1980; Bell and Bosart 1988), and along the Alps (Chen and Smith 1987).

b. Previous idealized studies of barrier jets.

Idealized simulations of barrier jets were performed by Pierrehumbert and Wyman (1995), Xu et al. (1990; 1996), and Braun et al. (1999a,b). Pierrehumbert and Wyman (1985) used inviscid two-dimensional simulations to show that the non-dimensionalized upstream extent of this decelerated flow was O(Fr^{-1}) for *Rossby number* $Ro > 1$ ($Ro = U_n/fL_m$; where L_m is the mountain half-width) and O($RoFr^{-1}$) for $Ro < 1$. Thus, the Coriolis force reduced blocking by accelerating the terrain-parallel flow toward the barrier and up the windward slope. This limited the upstream extent of the barrier jet to approximately a Rossby radius of deformation,

$$L_R = Nh_m/f. \qquad 1.2$$

Xu et al. (1990) alternately shows that the upstream width is also a function of the *Fr*.

The upstream extent may further be modified by barriers with synoptic-scale dimensions. The large-scale response associated with flow over synoptic-scale (> 1000 km) orography produces a "mountain anticyclone", which is symmetric about the barrier and decreases with height (Smith 1979a). Smith (1979b) showed that the upstream response is a combination of column stretching and compressibility. As a column of air approaches a barrier, it will undergo a vertical stretching due to the vertical displacement of the isentropes aloft (see Fig. 3 in Buzzi and Tibaldi 1977; Smith 1979a and b). This acts to create an upstream cyclonic turning of the impinging flow, which can reach ~1000 km upstream. The forced lifting results in parcel expansion and further induces a large-scale anti-cyclonic circulation over the barrier (Smith 1979b). This latter effect is primarily responsible for the far-field circulation, as it decays O(R^{-1}) while the stretching mechanism decays O(R^{-2}) (where R is the distance from the edge of the mountain; Smith 1979b).

In two-dimensional idealized simulations, Braun et al. (1999a) shows that the terrain geometry of a plateau acts to increase the magnitude of coastal jets. They show that the upstream deceleration is determined largely by the short-wave characteristics of the orography, while the barrier jet strength is determined approximately by the long-wave characteristics:

$$\frac{v}{U} \propto h_m\left[1 + \ln(L_2)\right], \qquad 1.3$$

where L_2 is the plateau width. The early development of the jet is related to the formation of a cold temperature anomaly over the windward slope, which occurs on a timescale of $t=L_1/U$ (where L_1 is the width of the windward slope). Subsequent jet enhancement is attributed to the building of the "mountain anticyclone", which generates an approximate geostrophic far-field circulation on timescales of $t=L_2/U$ (the time it takes for the ambient flow to traverse the plateau). They found barrier jet development to include a rapid

increase in the along-barrier flow to ~75% of maximum steady state strength during the first 12 hours, with a steady and slower increase through 90 hours as the large-scale flow adjusts over a ~2000 km plateau.

Idealized studies using real terrain have been performed over the orography of California (Cui et al. 1998), Norway (Barstad and Grønås 2005), Taiwan (Yeh and Chen 2003), and the Alps (Zängl 2005). They all noted the importance of wind direction influencing the structure and intensity of the terrain enhanced winds. Yeh and Chen (2003) showed that variations in the ambient wind speed and direction impacted the strength and position of the barrier jets in northwestern Taiwan, but they only investigated two wind directions (200 and 250^{o}) and two variations of wind speed. Cui et al. (1997) varied the ambient wind direction at 45 degree increments for wind speeds of 7 m s^{-1} over the central coast of California. For westerly and southwesterly background flows, there was strong along-coast variability in the jet strength, and wind speed maxima were located slightly downstream of the highest coastal terrain. They found that the strongest winds occurred for southwesterly cases (~45^{o} from terrain parallel), producing winds ~2.5 times the background wind speed.

Barstad and Grønås (2005) performed a similar idealized modeling study over the orography of Norway, where they incremented both wind speed (10, 15, 22.5 m s^{-1}) and wind direction (170, 200, 230, and 260 degrees). For southwesterly flows (~30-40 degrees from parallel to the largest terrain), the barrier jet was strongest; however, the variance in maximum wind speeds was smaller than expected. They attributed the similarities to the isotropy of the large-scale terrain. Although they did not provide strict measurements of the barrier jet width, they noted a slightly increased jet width as the ambient flow became more southerly (near-parallel to the largest terrain) and the maximum barrier jet winds became elevated.

c. Previous barrier jet fieldwork

Some of the earliest case studies of barrier jets were in Antarctica (Schwerdtfeger 1975) and along the Sierra Nevada Mountains (Parish 1982; Marwitz 1983, 1987). These barrier jets are produced mainly by the damming of stable airflow, where upslope flow produced adiabatic cooling. Barrier jets forced primarily by this mechanism are known as *classical barrier jets*.

Other types of barrier jets originate from cold-air damming (Bell and Bosart 1988), mountain gap flows (Mass and Albright 1985; Macklin et al. 1990; Overland and Bond 1995; among others), or cold surges along mountain ranges (Colle and Mass 1995). For example, Bell and Bosart (1988) showed that the along-barrier cold advections, as well as adiabatic and evaporative cooling, were responsible for the creation of a cold dome along the eastern edge of the Appalachian Mountains, with a northeasterly low-level wind maximum of 17 m s^{-1}. They performed a momentum budget analysis to show that the force balance in the along-mountain direction (after cold dome formation) was primarily an antitriptic balance, while a geostrophic balance existed in the cross-mountain direction.

Overland and Bond (1995), performed a scale analysis on two distinct coastal jets observed during the Coastal Observation and Simulation with Topography (COAST) field program. Their purpose was to determine which flow parameters controlled the

offshore extent of the barrier jet as well as the magnitude of the coastal wind speed enhancement. They found that for flows with $Fr < 1$, the offshore extent scaled as:

$$L_R = \frac{U}{f}, \qquad 1.4$$

and the alongshore wind speed enhancement scaled as:

$$\Delta V = U; \qquad 1.5$$

while for flows with $Fr > 1$, the offshore extent scaled as:

$$L_R = \frac{Nh_m}{f}, \qquad \text{(same as 1.2)}$$

and the alongshore wind speed enhancement scaled as:

$$\Delta V = Nh_m. \qquad 1.6$$

The low Froude number case they examined had some offshore-directed gap flow feeding the jet, while the other was a more classical jet with onshore flow at all levels. Although the scale analysis performed well for these cases, it is unclear how robustly it will apply to other cases and locations. A three-dimensional idealized study of flows over this region would aid in deducing the general applicability and usefulness of these results.

Loescher et al. (2006) completed a climatology of Alaskan coastal barrier jets using five years (1998–2003) of Synthetic Aperture Radar (SAR) and National Center for Environmental Prediction (NCEP) reanalysis. They noted both classic barrier jets and *hybrid barrier jets*, which had some gap outflows at the coast (Fig. 1.3). The strongest jets were located immediately adjacent to and downstream of the Fairweathers and Valdez-Cordova coastal mountains for a wide variety of flow conditions, with enhanced wind speeds typically 2-3 times larger than the ambient flow. The width of most jets extended 40-60 km from the coast, but some jet widths extended as much as ~250-km. Some hybrid jets were detached 10-15 km from the coast, while others had sharp wind speed boundaries (shock jets), which does not conform to the gradual offshore weakening of barrier jets observed in other studies (Parish 1982). The addition of the cold air source and associated gap outflows may enhance the development of the windward pressure ridge and therefore, influence the structure and intensity of the barrier jet.

1.3 Motivation

Although there have been many studies of barrier jets, more research is needed to understand the different structure and evolution of classical and hybrid barrier jets. Field data is needed to compile a unique data set of observations of coastal barrier jets. High resolution simulations of these observed events are needed to explore the three-dimensional structures and dynamics of various jet types. A diverse set of three-dimensional idealized simulations is needed in order to put the barrier jet features in perspective within a large atmospheric phase-space along the complex orography of the Alaskan coast. This can also help bridge the gap between observations of barrier jets and the existing theory, which is largely derived from two-dimensional studies or three-dimensional studies with simplified terrain. Additional idealized simulations are needed with baroclinic waves to determine how the coastal flows may impact the structure of the landfalling frontal systems.

Some questions this thesis will address are:

(1) What are the general structural and evolutionary differences between the idealized classical and hybrid jets?
(2) What are the controlling flow parameters that govern the evolution of the coastal barrier jets?
(3) How applicable is the scale analysis of Overland and Bond (1995) for a full phase-space of idealized classical and hybrid coastal jets?
(4) What is the impact of the broad inland terrain in contributing to the structure and intensity of the coastal jet?
(5) What is the impact of the time-dependent far-field adjustment on the upstream flow conditioning? How does this affect the applicability of the dimensional parameters used in the scale analysis?

Two case studies from the Southeastern Alaskan Region Jet (SARJET) field experiment (Winstead et al. 2006) have been performed to detail the three-dimensional structural differences between a classical and hybrid barrier jet. High-resolution simulations of both IOPS were compared in order to document the important structural differences resulting from the different ambient conditions.

A three-dimensional idealized initialization technique was developed for the Penn State/NCAR MM5 in order to provide an efficient tool generating a wide variety of initial conditions to explore a complete phase space of environments conducive to barrier jet development. This scheme was tested for three-dimensional idealized simulations of landfalling fronts in order to motivate future barrier jet work in a non-steady-state environment. The dominant mechanisms producing strong wind speed enhancements and wide barrier jets are uncovered for both types of jets. The importance of the inland terrain of the Pacific Cordillera is quantified in order to better understand the multi-scale processes associated with the barrier jets. Real and modified terrain are used to explore the influence of terrain geometry on the coastal jets and landfalling systems.

The following chapter discusses the idealized initialization technique used to create initial conditions for the MM5. Chapter 3 presents the results from two case studies of classical and hybrid barrier jets sampled during SARJET. Momentum budgets, trajectory analyses, and sensitivity tests were performed to help elucidate the mechanisms responsible for the evolution of both jet types. Chapter 4 presents the idealized barrier jet component of this thesis, which expands on the results from the case studies by exploring a practical phase space of ambient conditions suitable for the generation of coastal barrier jets. Important variables influencing the wind speed enhancement, offshore extent, and height of the barrier jets were determined. Chapter 5 presents an assessment of the scale analysis of Overland and Bond (1995) and the linear theory of Braun et al (1999) on determining the structure and intensity of the coastal jets. Modifications are proposed, which extend the results of this previous work. Chapter 6 discusses the major findings and conclusions.

Figures

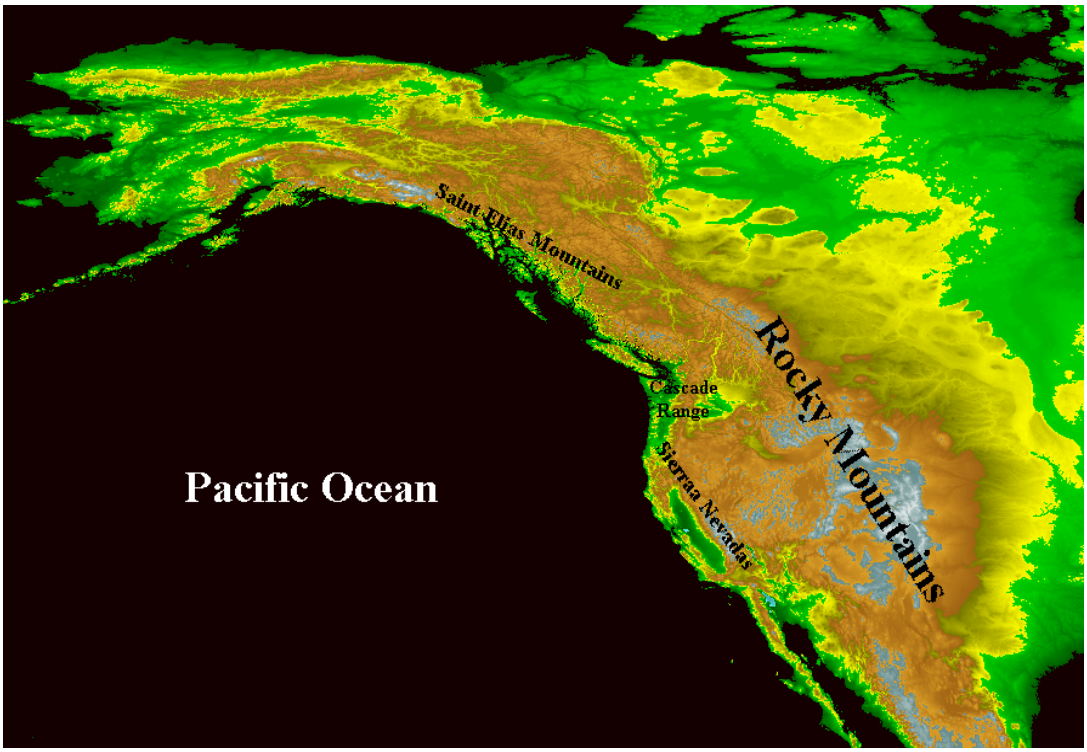

Figure 1.1 The Pacific Cordillera of western North America showing terrain height (color).

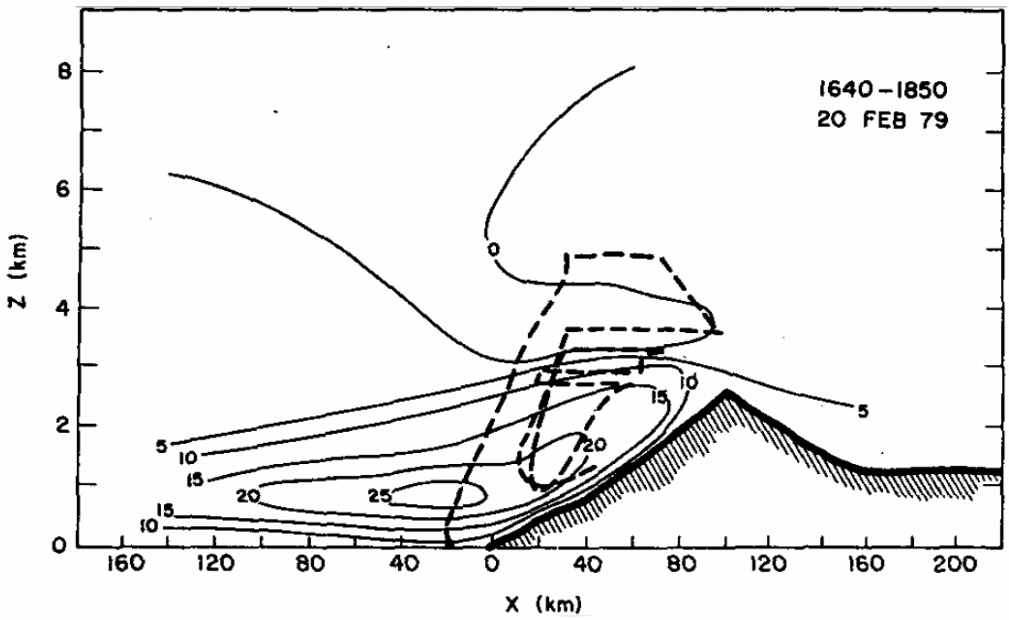

Figure 1.2 Mountain-parallel wind speed (m s^{-1}) derived from rawinsondes and Wyoming King-Air aircraft over the Sierra Nevadas during 20 February 1979. Flight track is shown by dashed line (from Parish 1982).

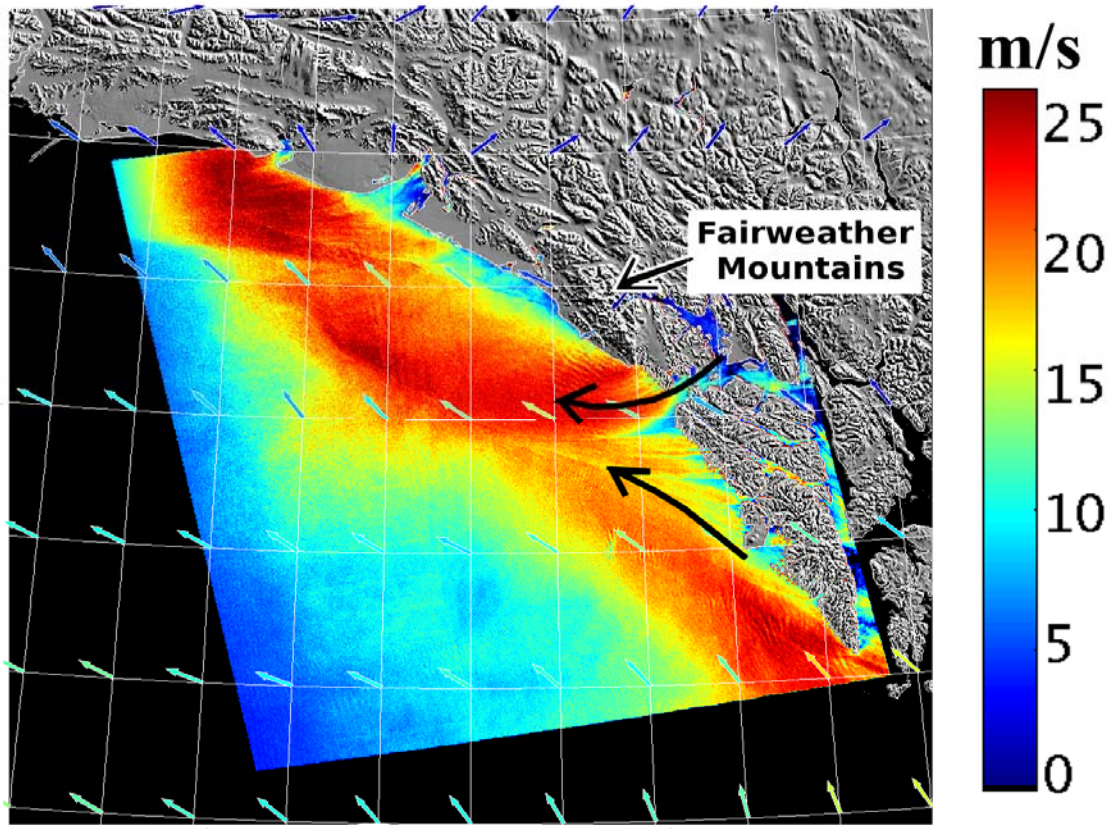

Figure 1.3 SAR wind speed (color; m s^{-1}) and vectors (from NOGAPS) of a hybrid barrier jet off the coast of Alaska as depicted by SAR imagery.

Chapter II:

An Approach to Create Three-Dimensional Idealized Initial Conditions for the MM5

2.1 Overview

Mesoscale models have been utilized in idealized configurations to explore specific atmospheric processes, while minimizing some of the complexities associated with case study simulations. To complement the case study portion of this thesis, an idealized tool was needed to create a three-dimensional idealized initial condition of a cyclone and attendant fronts in order to investigate how they interact with steep coastal topography. This tool enhances our ability to generate a wide variety of basic states and rotate the ambient fields in order to examine the impact wind direction. Many case studies have quantified terrain-frontal interactions by removing terrain within a model simulation (Wang et al. 2005, Colle et al. 2002, among others); however, defining the portion of atmosphere below ground is often arbitrary and can be inconsistent with the real atmosphere above. An idealized initialization removes this problem, since the initialized atmosphere is consistent down to sea level.

Many previous methods of initializing idealized baroclinic waves used a small-amplitude disturbance of normal-mode form (Simmons and Hoskins 1976 and 1978; Hoskins and West 1979; Heckley and Hoskins 1982; Davies et al. 1991; Thorncroft et al. 1993), which produced zonally periodic perturbations embedded within a prescribed basic state. This approach has been employed for cyclone-mountain interaction studies using idealized terrain (Speranza et al. 1985; Malguzzi et al. 1987; Davis and Stoelinga 1999). This method allows for minimal control of the initialized structure of the cyclone/fronts; therefore, it is best suited for synoptic-scale studies of cyclone-mountain interaction.

Since observed cyclones are often preceded by upper-level precursor disturbances (Petterssen and Smebye 1971), another series of studies developed isolated finite-amplitude initial perturbations in order to study non-modal evolution of extratropical cyclones (Montgomery and Farrell 1992; Schar and Wernli 1993; among others). This

approach has been used for cyclone-terrain interaction studies (Davis et al. 1997; Li et al. 1996; Orlanski and Gross 1994; Gross 1994; and Tibaldi et al. 1980), in which small amplitude perturbations were spun up 72-96 hours prior to their interaction with the terrain. This method allows for an isolated cyclone rather than the periodic wave train of a normal mode; thus, one can focus on how a single cyclone or front interacts with a barrier. A non-modal framework was adopted for our idealized frontal work; however, a technique to initialize a more mature baroclinic wave was needed in order to obtain more control of the cyclone/frontal structures early in the forecast. This allows quantification of how these structures are modified as they interact with terrain.

There have been some attempts to create initial conditions for a more realistic baroclinic wave using a non-modal approach. One technique has been to define the temperature and pressure structures explicitly (Fritsch et al. 1980; Nuss and Anthes 1987; Chuang and Sousounis 2000), and assumes a balance condition (eg., geostrophy or non-linear balance) to derive the winds. This approach has been used to investigate physical processes and sensitivities associated with rapid cyclogenesis (Nuss and Anthes 1987), lake-aggregate impacts on cyclones (Chuang and Sousounis 2003), extra-tropical convective mesovortices (Chen and Frank 1993). However, their methods have limitations. For example, the Fritsch et al. (1980) method produces realistic upper-level wind and temperature structures, but unfortunately the temperature wave at low-levels still requires 2-3 days to develop well-defined surface fronts. Nuss and Anthes (1987) introduced separate terms for the large- and small-scale pressure and temperature gradients in order to add more flexibility to Fritsch et al. (1980). However, their cyclones had the maximum temperature and pressure amplitude at low levels, with much weaker perturbations aloft. More recently, Chuang and Sousounis (2000) developed an approach that allows for the baroclinic wave to be specified in terms of vertical phase lag, wavelength, phase speed, and a reference sounding. The baroclinic cyclone is initialized using sinusoidal waves with maximum perturbations at mid-levels; however, their analytical functions produce no regions of enhanced baroclinicity and deformation; therefore, only weak frontogenesis occurs by hour 48 of their simulations (see their Fig. 5c).

Previous techniques initialized a strong but highly simplified analytical front in order to avoid the need to spin-up a mature front. For example, Schumann (1987) created a well-defined north-south oriented cold front within a three-dimensional model to investigate how an idealized mountain can modify the specified frontal structures. Because a mature analytical front was specified, no spin-up was necessary; however, this approach did not include the realism of a full baroclinic wave. Our goal was to define a realistic front within the context of a three-dimensional baroclinic wave; therefore, the Fritsch et al. (1980) and Nuss and Anthes (1987) methods were improved to increase the low-level frontal deformations and add more control of the low-level temperature and pressure waves, while maintaining a robust wave aloft. Finally, this tool has been interfaced with the Pennsylvania State University/National Center for Atmospheric Research Mesoscale Model Version 5 (MM5 version 3.7; Grell et al. 1994) and the Weather Research and Forecasting (WRF) Model (Skamarock et al. 2005).

The following section presents the procedure and some insight into the key parameters. Section 2.3 shows some examples of different initializations and section 2.4 provides a summary.

2.2 Idealized Initialization Technique

As in Fritsch et al. (1980), the cyclone is first initialized on height surfaces every 0.5 km in the vertical. Below is a detailed description of the procedure.

a. Step 1: Formulation of 4-km pressure level

As in Fritsch et al. (1980), the pressure field is specified as a combination of a reference pressure (P_o), a pressure function governing the meridional structure of the basic state (P_y), and a zonally oriented wave perturbation (P_x):

$$P(x, y, 4km) = P_0 + P_y + P_x \,. \tag{2.1}$$

The 4-km level was chosen as opposed to 6-km in Fritsch et al. (1980) and Nuss and Anthes (1987), since it was found that the 4-km level helped initialize the surface cyclone better, while still preserving control of the upper-level structures. Two hyperbolic tangents define the meridional basic state at 4-km:

$$P_y(x,y) = -A_{y1}\tanh\left[\frac{y-y_c}{p_1 - \frac{p_1}{8}D_x(x)}\right] - A_{y2}\tanh\left[\frac{y-y_c}{p_2}\right] + p_y \quad , \tag{2.2}$$

which is similar to Nuss and Anthes (1987). The coefficients A_{y1} and A_{y2} determine the magnitude of the total north-south pressure difference, while parameters p_1 and p_2 determine the concentration of the basic state pressure gradient at the center of the domain (y_c). The first term in eq. (2.2) produces an enhanced meridional pressure gradient for the basic state jet, while the second term initializes the background pressure gradient. For horizontally homogeneous barotropic basic states, $P_y(x,y)$ must be specified as a plane surface of the form:

$$P_y(x,y) = \frac{\partial p}{\partial y}(y - y_c)\,, \tag{2.3}$$

where $\partial p/\partial$y can be determined by the geostrophic relationship for a desired background velocity. With this configuration, the basic state temperature (below) should be set to zero.

Unlike previous studies, the function $(p_1/8)D_x(x)$ was added to create a jet-streak at the base of the mid-level trough and confine it zonally using a damping function, $D_x(x)$,

$$D_x(x) = \frac{1}{2}\left[\tanh\left(\frac{x-(x_c - \frac{L_x}{2})}{\frac{L_x}{8}}\right) + \tanh\left(\frac{(x_c + \frac{L_x}{2}) - x}{\frac{L_x}{8}}\right)\right], \tag{2.4}$$

where x_c is the zonal center of the baroclinic wave and L_x and L_y are the zonal and meridional wavelengths, respectively. This allows for a single wave packet perturbation (Fig. 2.1a) rather than a wave train. Our modified approach also includes an extra term to eq. (2.2),

$$p_y(y) = \sum_{y=y_c}^{\pm\frac{L_y}{2}} -U_y\left[\frac{y-y_c}{2000}\right]\rho f dy\,, \tag{2.5}$$

which produces a linearly varying background horizontal shear. The parameter, U_y, governs the magnitude of the change of the zonal wind per 2000 km; positive values result in cyclonic shear environments and LC2-type cyclones (strong warm fronts) (Thorncroft et al. 1993 and Wernli et al. 1998), while negative values yield anti-cyclonic shear environments and LC3-type storms (elongated strong cold fronts).

The wave perturbation in the zonal direction is specified by:

$$P_x(x,y) = A_x C_p(x,y) \sin\left[\frac{2\pi(x - X_c(y))}{L_x}\right] D_x(x) D_y(y), \tag{2.6}$$

using an amplitude factor of $A_x \sim 5$ mb and

$$C_p(x,y) = d_1 - d_2 \sin\left(\frac{2\pi(x - X_c(y))}{L_x} + \pi\right), \tag{2.7}$$

which makes the trough slightly larger in magnitude than the ridge for values of d_1=0.9 and d_2=0.1. The function,

$$X_c(y) = x_c + \Delta x\left[\sin\left(\frac{\pi y}{L_y}\right) - 1\right], \tag{2.8}$$

specifies the longitudinal distortion of the zonal wave (relative to x_c) by the jet stream, which causes a portion of the cyclone in the center of the domain to be extended further (by Δx kilometers) than at the north and south boundaries of the domain.

The function

$$D_y(y) = \sin\left(\frac{\pi y}{L_y}\right)^d \tag{2.9}$$

is from Fritsch et al. (1980), which damps the zonal wave perturbation towards the north and south boundaries of the domain with the exponent d controlling the meridional confinement of the zonal wave, which is set to 3 in our examples below.

b. Step 2: Formulation of the three-dimensional temperature and moisture

As in Fritsch et al. (1980), the three-dimensional temperature field is specified as a combination of the reference surface temperature (T_o), meridional structure of the basic state (T_y), zonal wave perturbation (T_x), and vertical lapse rate (Γ):

$$T(x,y,z) = T_0 + T_y + T_x + \Gamma(y)\Delta z \ , \tag{2.10}$$

where $T_0 \sim 281$ K, and the basic state is similar to Nuss (1986) and Nuss and Anthes (1987):

$$T_y(x,y) = -B_{y1}\tanh\left[\frac{y - y_c}{p_{b1} - \frac{p_{b1}}{8} D_x(x)}\right] - B_{y2}\tanh\left[\frac{y - y_c}{p_{b2}}\right]. \tag{2.11}$$

The parameters B_{y1} and B_{y2} control the magnitude of the north-south temperature difference. Parameters p_{b1} and p_{b2} determine the concentration of the basic state temperature gradient, while $-(p_{b1}/8)D_x(x)$ enhances the temperature gradient in the wave perturbation region. For barotropic initial conditions, B_{y1} and B_{y2} are set to zero.

The temperature wave in the zonal direction is similar to Nuss and Anthes (1987):

$$T_x(x,y,z) = B_x C_T(x,y,z)\sin\left[\frac{2\pi\left(x - X_c(y) + def\ (x)\right)}{L_x} + \Phi(z)\right] D_x(x) D_y(y) D_z(z), \quad (2.12)$$

where the amplitude factor B_x ~ 5 K and

$$C_T(x,y,z) = d_1 + d_2 \sin\left(\frac{2\pi\left(x - X_c(y)\right)}{L_x} + \pi + \Phi(z)\right) \quad (2.13)$$

introduces an east-west amplitude asymmetry between the thermal troughs and ridges. A phase function Φ(z),

$$\Phi(z) = -\Phi_z\left[\frac{(4km - z)}{10km}\right] + \Phi_{lag} \quad (2.14)$$

controls the tilt of the temperature wave. For a developing wave, a small tilting of $\Phi_z = \pi/10$ was used with a phase lag (Φ_{lag}) of 0.35π.

A modification of Nuss and Anthes (1987) is the replacement of their frontal enhancement function (their Eq. 2.14) with a deformation function,

$$def\ (x,y,z) = \frac{1}{4}[x - X_c(y)]\exp\left[\frac{(x - X_c(y))}{700}\right]\exp\left[-\left(\frac{z}{3}\right)^2\right], \quad (2.15)$$

which is added to the zonal temperature perturbation (eq. 2.12). This function contracts the wave perturbation horizontally by decreasing the wavelength of the temperature wave at low levels where surface convergence is prevalent.

The damping of the temperature wave in the vertical (D_z) has varied in previous studies to allow a maximum wave amplitude at about 8 km in Fritsch et al. (1980) and a maximum at the surface in Nuss and Anthes (1987). A $D_z(z) = 1$ was utilized in our examples below in order to initialize a developed wave throughout the depth of the troposphere.

Tropospheric and stratospheric lapse rates are defined by equations 2.16a and 2.16b, respectively,

$$\Gamma_T(y) = \gamma_T - .3 \cdot \tanh\left[\frac{y - y_c}{p_{b2}}\right], \quad (2.16a)$$

$$\Gamma_S(y) = \gamma_S - .05 \cdot \tanh\left[\frac{y - y_c}{p_{b2}}\right], \quad (2.16b)$$

where the lapse rate at the center of the domain is dependent on whether the troposphere, γ_T = 6.5 K km^{-1}, or the stratosphere, γ_S = 0.5 K km^{-1}, is initialized. In this framework, the tropopause represents a transition in the lapse rates, similar to the standard definition of the World Meteorological Organization (WMO 1957).

Similar to Fritsch et al. (1980), the height of the tropopause is specified by:

$$Z_{TROP}(x,y) = Z_0 - Z_{DIFF}\tanh\left[\frac{y - y_c}{p_{b2}}\right] - \frac{1}{2}[T(0, y_c, Z_0) - T(x,y,Z_0)] D_x(x) D_y(y). \quad (2.17)$$

With a reference height of Z_0=8.5 km, the tropopause varies in the north-south direction by $Z_{DIFF,}$ which is a function of the lapse rates and the total temperature change across the domain, $\Delta T_{total} = 2(B_{y1} + B_{y2})$:

$$Z_{DIFF} = \frac{\Delta T_{total}}{2(\gamma_T + \gamma_S)} \tag{2.18}$$

For the parameters listed in Table 1, the tropopause will change vertically by 2.5, 3.3, and 4.5 km between $y_c \pm 2000$ km for the weak, moderate, and strong baroclinicity examples. Figure 2.1b shows a north-south cross section (AA') of the basic state winds, potential temperature, and potential vorticity for the "strong baroclinicity" example (BS3; control run). The last term on the right hand side of (2.17) lowers (raises) the tropopause over the thermal trough (ridge) relative to the reference height, Z_0.[2] $D_y(y)$ and $D_x(x)$ are damping functions with the same form as (2.4) and (2.9), respectively.

The inclusion of topography requires an extra step to initialize the surface temperature. The surface temperature field can easily be derived by subtracting $\Delta T = T(x,y,0) - \Gamma_T(y) \cdot z_{ter}$, where $\Gamma_T(y)$ is the tropospheric lapse rate (2.16a) and z_{ter} is the height of the terrain.

The moisture can be initialized with a horizontally homogeneous relative humidity profile. One simple specification is a constant relative humidity of about 95% below 1500 m (~850 mb) and a linear decrease with height above (Moore and Montgomery 2005). A more complex moisture distribution, which relates to the three-dimensional temperature structure, can be found in Tan et al. (2004). This relative humidity is then converted to a mixing ratio needed for a virtual temperature calculation. With the 3-dimensional virtual temperature and the 2-dimensional pressure wave at 4 km specified, the hydrostatic equation is used to integrate from the 4-km pressure level to obtain the full 3-dimensional pressure field.

c. Step 3: Wind calculation

Nuss and Anthes (1987) used nonlinear balance to initialize the winds (Haltiner and Williams 1980). However, we found the gradient wind approximation to be sufficient for a balanced solution, since the MM5 and WRF preprocessing programs further remove the integrated mean divergence (Grell et al. 1995). Since the gradient wind calculation requires the estimation of a radius of curvature, a first estimation of the curvature of the winds is obtained by the geostrophic approximation. The gradient wind field can then be calculated using eq. 3.15 of Holton (2004).

d. Step 4: Interfacing with mesoscale models

Finally, we transform the three-dimensional fields from height to pressure coordinates in order to ingest into the MM5 or WRF preprocessing programs. For example, for the MM5 examples shown below, the initial conditions are formatted as REGRID (MM5v3) output files. The MM5 program INTERP then performs the interpolation from pressure to sigma coordinates. The advantages of this approach are that INTERP: (1) performs the vertical interpolation from constant pressure surfaces to the model sigma levels, (2) initializes the pressure perturbations (p') and vertical motion

2. Since the tropopause height is a function of the tropospheric temperature field, the full three-dimensional temperature must first be calculated using the tropospheric lapse rate. Then the tropopause height can be determined by eq. 2.17. Finally, the temperatures for grid points above the tropopause are recalculated with the proper stratospheric lapse rate.

(w), (3) removes mass-integrated divergence, and (4) creates boundary files. The lateral boundary conditions are held fixed provided the domain is specified large enough to contain the full baroclinic wave packet. The data from this domain can be run through the MM5 program NESTDOWN to initialize any inner nests.

2.3 Examples

In order to highlight the utility of this initialization approach, MM5 simulations were performed with incremental changes made to important parameters (Table 2.1), such as the basic state baroclinicity ($A_{y1\text{-}2}$ and $B_{y1\text{-}2}$), the amplitude of the initial wave perturbation (A_x and B_x), and the background barotropic shear (U_y). A domain with grid spacing of 54 km was used, with 250 and 120 grid points in the zonal and meridional directions, respectively, as well as 32 vertical sigma levels. The domain size is determined by the duration of model integration, such that the region of interest is far from the fixed lateral boundary conditions. No radiation or moisture was included, but the Blackadar planetary boundary layer scheme was used to parameterize surface friction and turbulence (Zhang and Anthes 1982). In order to illustrate the basic cyclone evolution, no terrain was used except in section 2.3d, and all land areas were set to "coniferous forest". High resolution examples using a barotropic basic state without an embedded cyclone are shown in section 2.3e and were used for the study of idealized barrier jets (chapter 4).

a. Baroclinic basic state

Four simulations illustrate cyclone evolution in varying baroclinic basic states for parameters A_{y1}, A_{y2}, B_{y1}, and B_{y2} in Table 1. The four initializations yield basic state jets at 300 mb ranging from 21 m s^{-1} to 45 m s^{-1}. The procedure for the "strong" cyclone setup (BS3; Table 2.1) generates a realistic solitary wave centered about 1200 km to the west of the U.S. West Coast (Fig. 2.1a), with a closed surface cyclone, a westward tilt with height of the trough axis, and a jet centered at 300 mb (Fig. 2.1b).

Figure 2.2 shows the surface evolution difference between the weak (BS1) and strong (BS3) baroclinic states for hours 0, 30, and 60. Both cyclones were initialized with the same central pressure (Fig. 2.2a-b), but the BS3 cyclone deepened to 984 mb by hour 30, while the BS1 cyclone reached 994 mb. Both cyclones produced well-defined surface fronts (3.5-5 K $[100\ km]^{-1}$) and a more amplified trough-ridge couplet at 500 mb by hour 30 (Fig. 2.2c-d). By hour 60 (Fig. 2.2e-f), both cyclones were occluded and vertically stacked up to 500 mb, with the BS3 cyclone 9 mb deeper and a few hundred kilometers farther east than BS1. The BS3 run also produces a well-defined baroclinic wave packet downstream (east) of the primary cyclone. Figure 2.3a shows a time-series of sea-level pressure minimum for the cyclones in all four baroclinic simulations (Table 2.1). The "very strong" case (BS4) produced rapid cyclone deepening of 21 mb within 24 h at 42 °N, thus qualifying it as an explosive cyclone at this latitude (Sanders and Gyakum 1980).

b. Initial perturbation

A second set of simulations illustrates the capability of initializing cyclones at various amplitudes. Parameters A_x and B_x control the magnitude of the zonal wave

perturbations for the pressure and temperature, respectively (Table 2.1). Two simulations with weaker (IP1) and stronger (IP3) perturbations were varied around the "strong" baroclinic run (BS3) in Fig. 2.2a, which is hereafter referred to as the control run (CTL).

The IP1 and IP3 runs were initialized at 1004 and 997 mb, respectively (Fig. 2.4a-b). IP3 experienced a slightly larger growth rate in the first 30 hours and became 19 mb deeper than IP1 by hour 30 (Figs. 2.4c,d). However, IP3 was occluded by hour 30 and no longer deepened after hour 40 (Fig. 2.4d), while the IP1 run deepened through hour 66 (Fig. 2.3b). The fronts in IP3 intensified more rapidly than the other IP runs, but all runs eventually reached maximum around 6.5˚C $[100\ \text{km}]^{-1}$.

c. Barotropic shear

The impact of horizontal shear is illustrated by varying U_y in Table 2.1, which was varied to include either cyclonic shear (LC2) or anti-cyclonic shear (LC3) as compared to the control run (BS3). The contrasting shear values were taken from Figs. 2a,e of Wernli et al. (1998), which induce barotropic shears of $\pm 10\ \text{m s}^{-1}$ $[2000\ \text{km}]^{-1}$. Figures 2.5a,b show the basic state winds, potential temperature, and PV along section AA'.

Both simulations were initialized with approximately the same surface cyclone central pressure of 1001 mb, but they were embedded within different basic states (Fig. 2.6a-b). The LC2 simulation had the smallest growth rate (~10 mb 24 hrs^{-1}) and reached maximum strength by hour 36 (Fig. 2.3c). The cyclonic shear rotated the vortex, such that the occluded front became oriented more northwest to southeast as compared to the control run (cf. Figs. 2.6c, 2.2d). The LC3 cyclone deepened throughout the 72 h simulation (Fig. 2.3c), but much of this deepening is from the cyclone moving northward into a region of lower pressure in the basic state. The anti-cyclonic shear delays the time of occlusion and keeps the cold front oriented more southwest-northeast through hour 30 (Fig. 2.6d). Both horizontal shear runs evolve similar to Wernli et al. (1998).

d. Terrain

To show the utility this approach over terrain, Fig. 2.7 shows a 54-km simulation initialized the same as the control run (Fig. 2.2b), but model terrain is utilized (TER run). The cyclone initially develops similarly to the control run early in the simulation (Fig. 2.7a); however, the difference in cyclone central pressure between the terrain and no terrain runs increases after the TER cyclone is within a few hundred kilometers of the the coast by hour 30 (Fig. 2.7b). The TER cyclone makes landfall over Vancouver Island at hour 42 and then experiences cyclolysis, or at least a reduction in growth rate, over the steep coastal terrain by hour 60 (Fig. 2.7c), which is consistent with previous idealized studies (i.e. Davis and Stoelinga 1999; Tibaldi et al. 1980). In contrast, the cyclone in the control simulation deepens through hour 48 (cf. Fig. 2.3a), and the cold front is located approximately 500 km further to the east by hour 60 (Figs. 2f). Furthermore, a cyclone develops in the lee of the Rockies, which has a central sea-level pressure of 990 mb and a well-developed cold front over the Ohio Valley.

e. Zonal barotropic basic states at higher resolution.

Section 2.2 noted that horizontally homogeneous barotropic flow could be initialized for an examination of barrier jets without a baroclinic wave. This

configuration will be utilized for the idealized barrier jet simulations of chapter 4. An additional feature useful for quantifying the impact of wind direction on the barrier jet structures was added to the above technique, such that the initialized structure could be rotated 360° by the following transformation:

$$x' = x_c + (j * dy - y_c)\sin\left(\frac{\alpha\pi}{180}\right) + (i * dx - x_c)\cos\left(\frac{\alpha\pi}{180}\right) \qquad (2.19a)$$

and

$$y' = y_c + (j * dy - y_c)\cos\left(\frac{\alpha\pi}{180}\right) + (x_c - i * dx)\sin\left(\frac{\alpha\pi}{180}\right), \qquad (2.19b)$$

where α is the angle of rotation relative to zonal and the three-dimensional fields are rotated around the point (x_c, y_c).

An example of a barotropic initial condition is shown in Fig. 2.8a and 2.9a. The atmosphere was initialized with 15 m s^{-1} winds from the south (α = 90°) and was nested down to 6-km resolution as described in section 2.2d. Figure 2.8 shows the wind speed and wind vectors at 500 m ASL within a nest centered over the coast of southeastern Alaska (a configuration detailed in chapter 4). The mesoscale flow undergoes rapid geostrophic adjustment during the first 12 hours (Fig. 2.8a-c) as the barrier jet develops, reaching wind speeds of ~25 m s^{-1}. A cross-section through the barrier jet (XX' in Fig. 2.8d) shows the initialized vertical structure over the coastal region (Fig. 2.9a) and the subsequent evolution. This simulation demonstrates the stability of this technique for impulsive start-up simulations over tall and steep terrain and the development of a realistic barrier jet.

2.4 Summary

A technique for initializing realistic idealized cyclones within a 24-36 h period is described. The approach is similar to that of Fritsch et al. (1980) and Nuss and Anthes (1987), but it is modified to prescribe a full 3-dimensional cyclone with strong surface fronts and a more realistic jet and tropopause structure. The baroclinic wave initialization system can produce a variety of basic states and synoptic disturbances, ranging from weak cyclones to explosively developing cases. Simulations for a wide range of initial conditions are shown to illustrate cyclone realism. The examples also provide some insight on how to adjust selected parameters in order to modify cyclone development.

This initialization scheme is used to explore the mesoscale terrain-forced coastal flows (chapter 4) and associated interaction of frontal systems along the U. S. West Coast (future work).

Tables

	Basic State Baroclinicity				***Initial Perturbation***		***Barotropic Shear***	
Parameter and Description	***BS1 weak***	***BS2 moderate***	***BS3 strong (control)***	***BS4 very strong***	***IP1 small***	***IP3 large***	***LC2***	***LC3***
P_0 mean pressure at 4 km (mb)	607	607	607	607	607	607	607	607
A_{y1} small scale pressure gradient amplitude factor (mb)	**6**	**7**	**9**	**11**	9	9	9	9
A_{y2} large scale pressure gradient amplitude factor (mb)	**8**	**10**	**13**	**16**	13	13	13	13
p_1 small scale pressure gradient packing factor (km)	1200	1200	1200	1200	1200	1200	1200	1200
P_2 large scale pressure gradient packing factor (km)	1800	1800	1800	1800	1800	1800	1800	1800
A_x zonal pressure perturbation (mb)	5	5	5	5	**3**	**7**	5	5
U_y horizontal shear (m s^{-1} per 2000 km)	0	0	0	0	0	0	**10**	**-10**
T_0 mean temperature at ground level (K)	281	281	281	281	281	281	281	281
B_{y1} small scale temperature gradient amplitude factor (K)	**4**	**5**	**7**	**9**	7	7	7	7
B_{y2} small scale temperature gradient amplitude factor (K)	**5**	**7**	**9**	**11**	9	9	9	9
p_{b1} small scale temperature gradient packing factor (km)	1200	1200	1200	1200	1200	1200	1200	1200
p_{b2} small scale temperature gradient packing factor (km)	1800	1800	1800	1800	1800	1800	1800	1800
B_x zonal temperature perturbation (K)	5	5	5	5	**3**	**7**	5	5
Z_0 mean height of Tropopause (km)	8	8	8	8	8	8	8	8
Basic State Jet (m s^{-1})	21	28	36	44	36	36	35	37
Minimum Sea-level Pressure (mb)	985	981	975	970	970	980	989	959

Table 2.1 Parameters used to define various cyclones and basic states. The bold numbers represent those parameters adjusted for the text discussion.

Figures

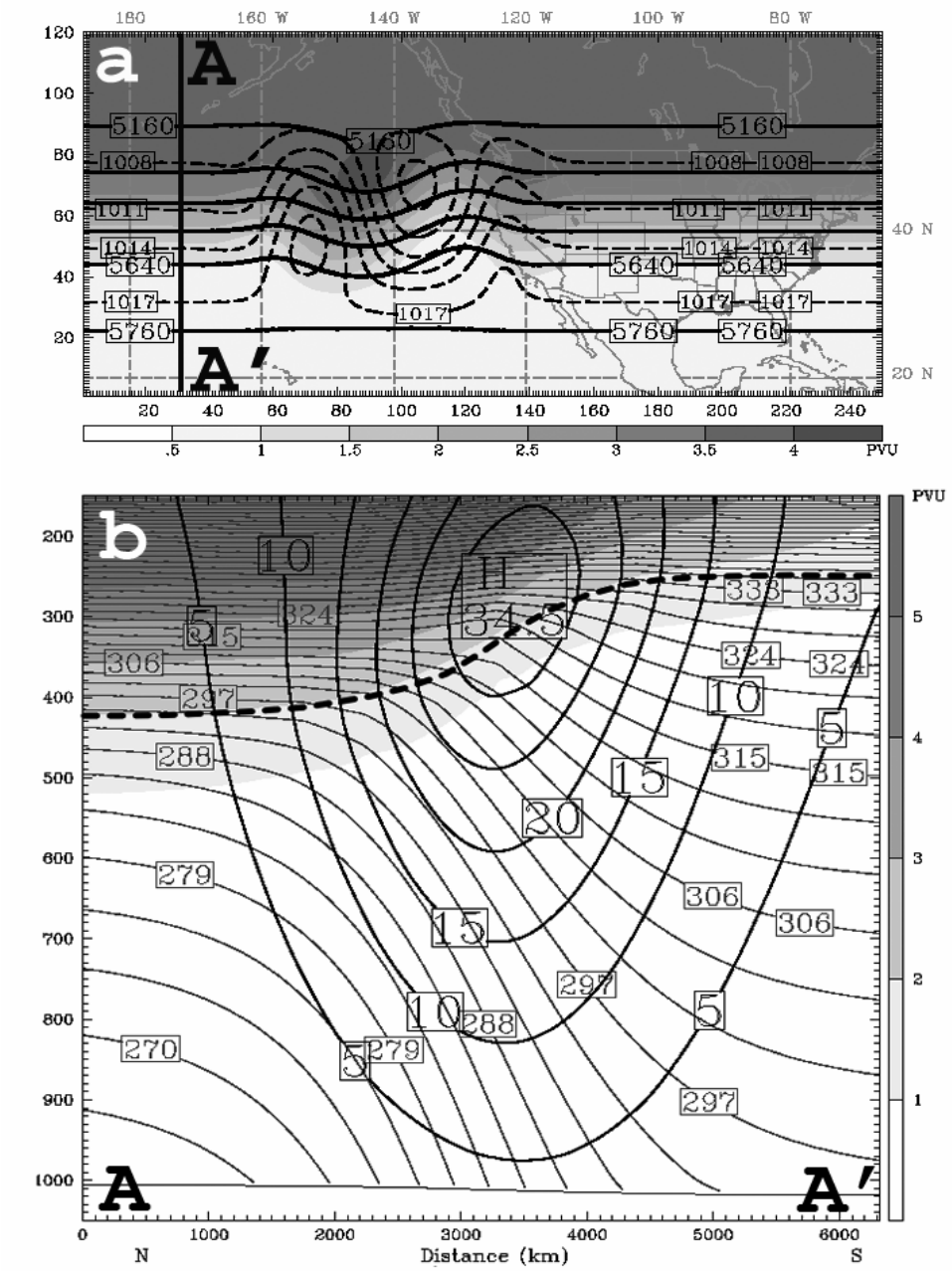

Figure 2.1 (a) Potential vorticity (PV) at 300 mb (shaded in PVU), 500 mb geopotential height (black contours every 120 m), and sea-level pressure (dashed every 3 mb) for the control (BS3 in Table 1) run. (b) Vertical cross-section AA' of the baroclinic basic state showing zonal wind speed (black contours every 5 m s^{-1}), potential temperature (gray lines every 3 K), and PV (shaded in PVU) for the BS3. The tropopause is shown by the bold dashed line. The location of AA' is shown in (a).

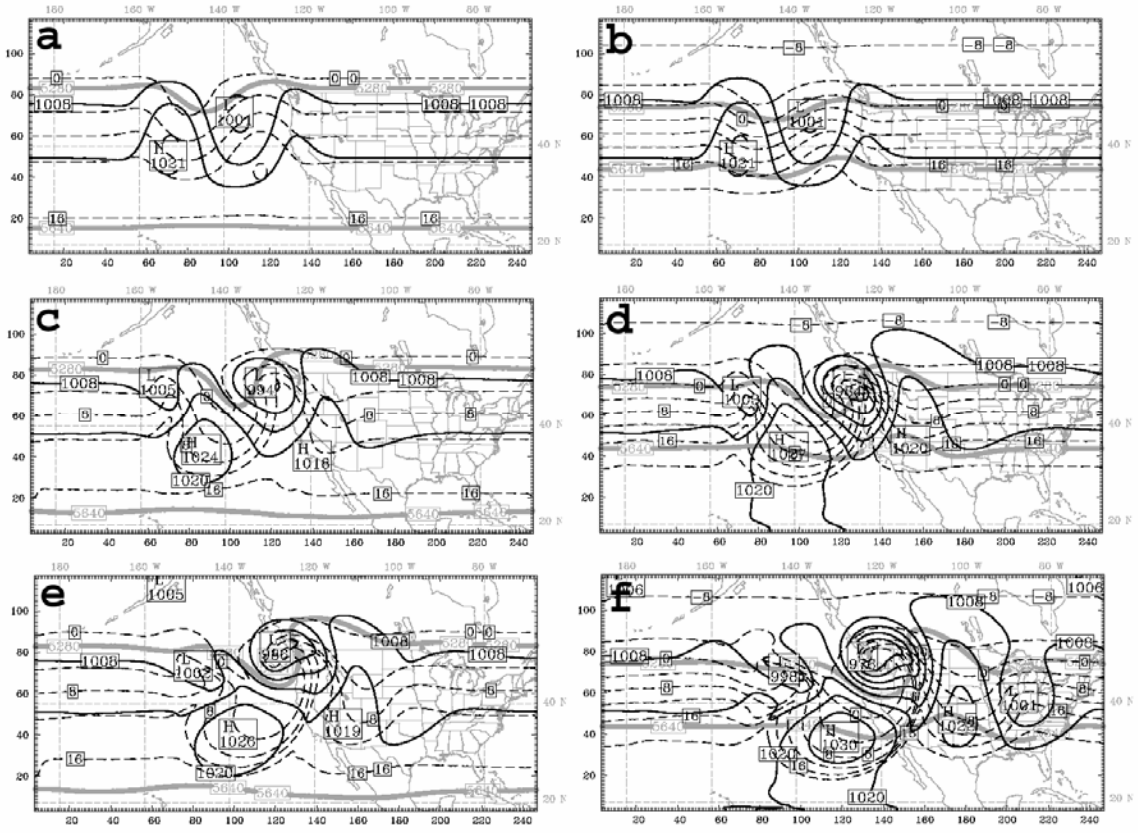

Figure 2.2 Sea-level pressure (black lines every 6 mb), temperature (dashed gray every 4 ^{o}C), and 500 mb geopotential height (thick gray every 380 m) for (a) BS1 at hour 0, (b) BS3 hour 0, (c) BS1 hour 30, (d) BS3 hour 30, (e) BS1 hour 60, and (f) BS3 hour 60.

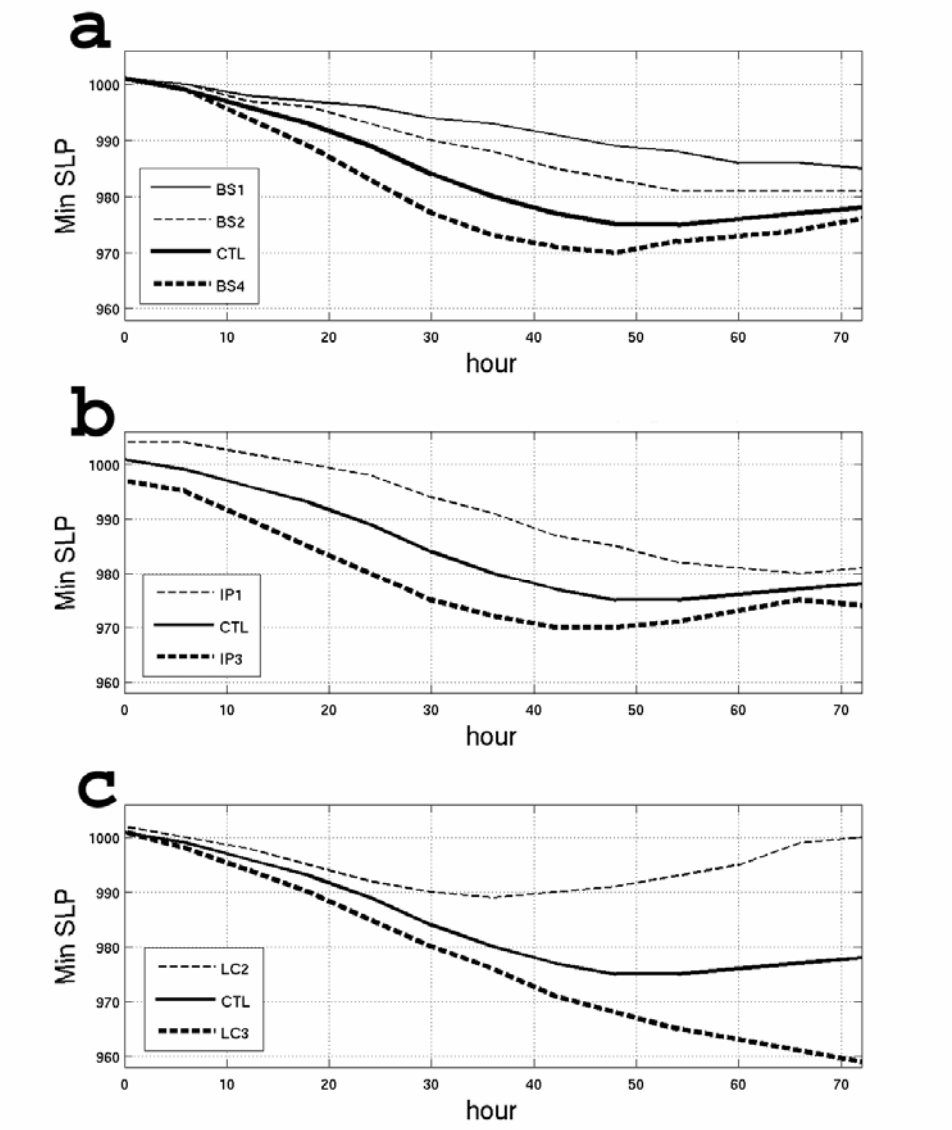

Figure 2.3 Time series of the central sea-level pressure for the (a) baroclinicity (BS), (b) initial perturbation (IP), and (c) barotropic shear (LC) cyclone experiments. See Table 1 for the parameter definitions.

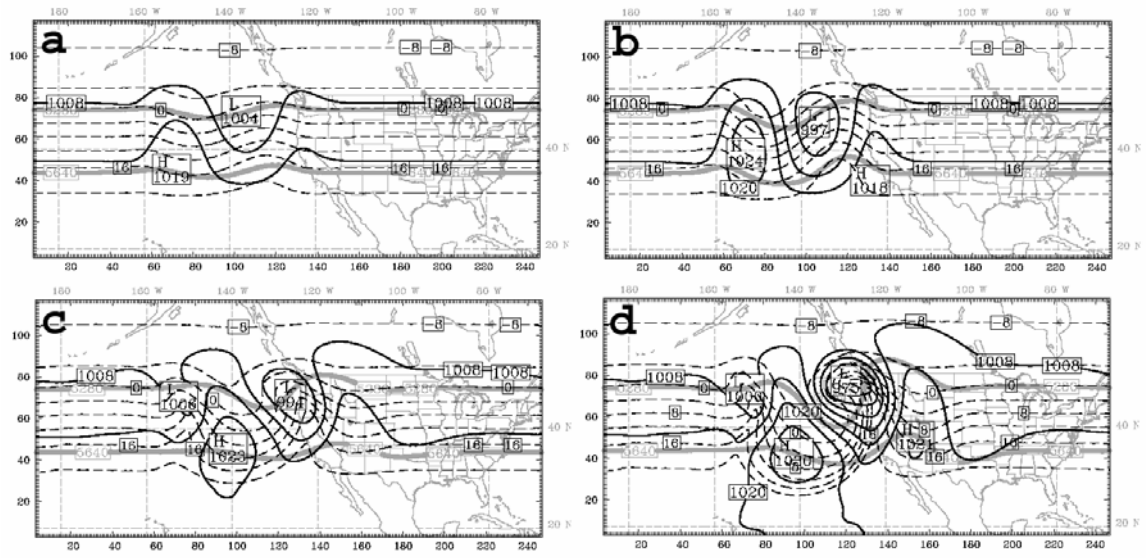

Figure 2.4 Sea-level pressure (black lines every 6 mb), temperature (dashed every 4 ^{o}C), and 500 mb geopotential height (thick gray every 380 m) of the (a) weak (IP1) and (b) strong (IP3) initial perturbation simulation at hour 0 and hour 30 for the (c) IP1 nd (d) IP3.

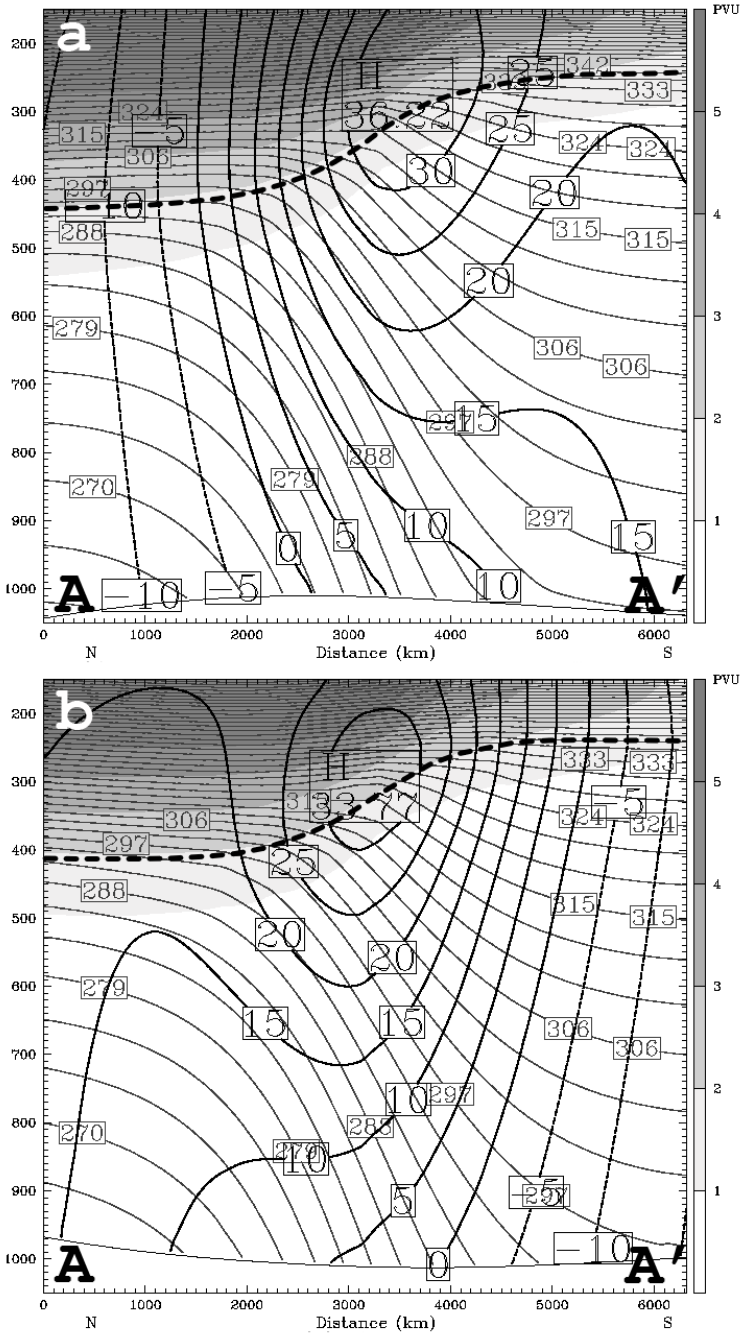

Figure 2.5 Cross-section AA' of the basic states showing zonal wind speed (black lines every 5 m s^{-1}), potential temperature (gray lines every 2 K), and potential vorticity (shaded in PVU) for the (a) LC2 and (b) LC3 barotropic shear simulations.

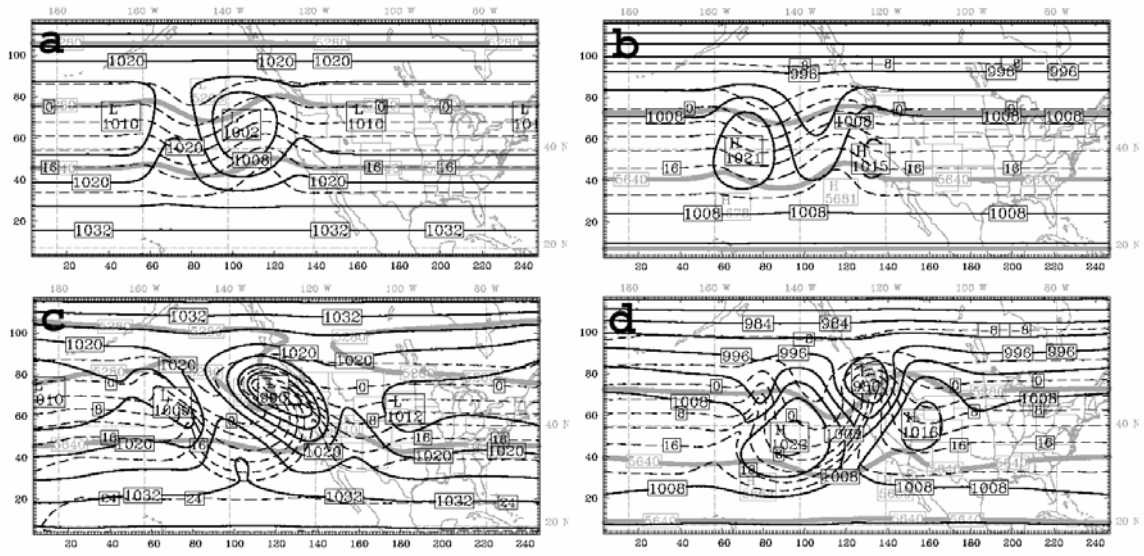

Figure 2.6 Sea-level pressure (black lines every 6 mb), temperature (dashed every 4 ^{o}C), and 500 mb geopotential height (thick gray every 380 m) at hour 0 for the (a) cyclonic shear (LC2) and (b) anti-cyclonic shear (LC3) simulations and hour 30 for (c) LC2 (d) LC3.

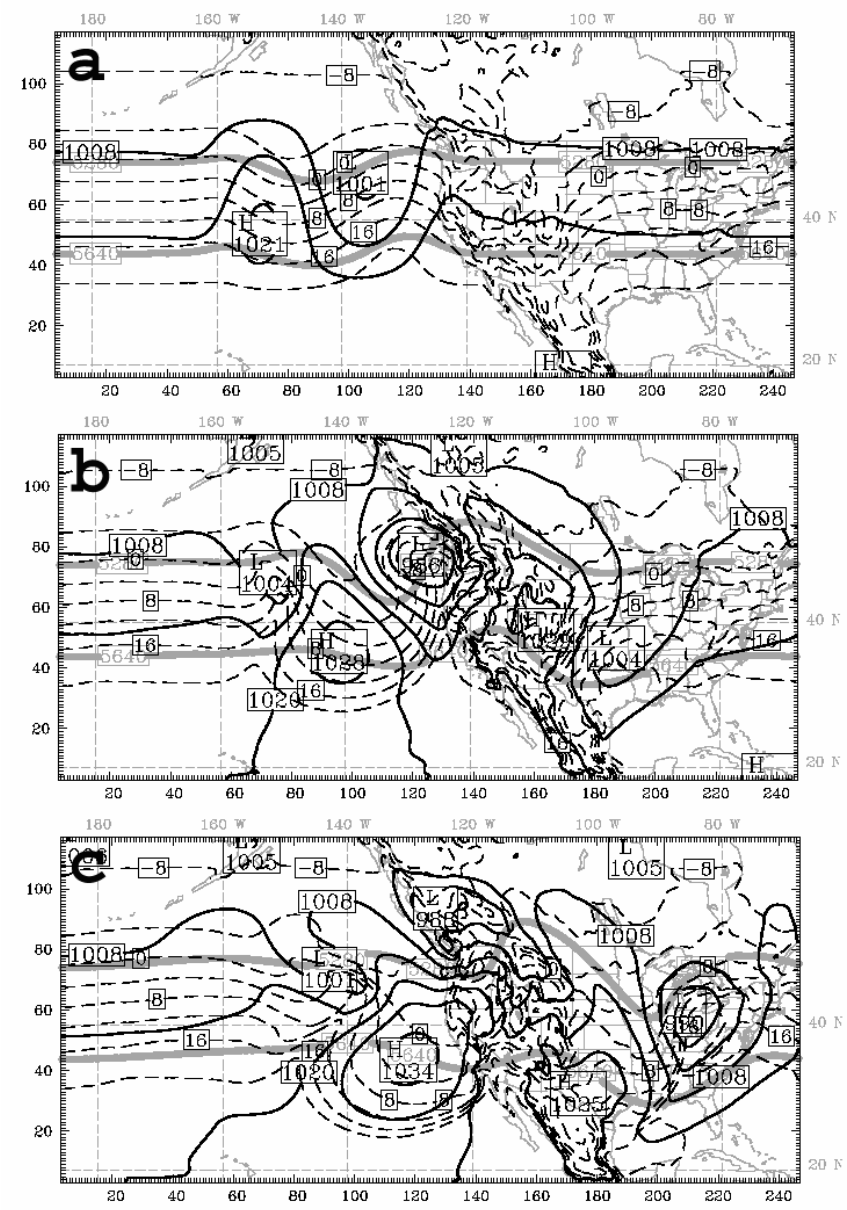

Figure 2.7 Sea-level pressure (black lines every 6 mb), temperature (dashed every 4 ^{o}C), and 500 mb geopotential height (thick gray every 380 m) at (a) hour 0, (b) hour 30, and (c) hour 60 of the terrain (TER) simulation.

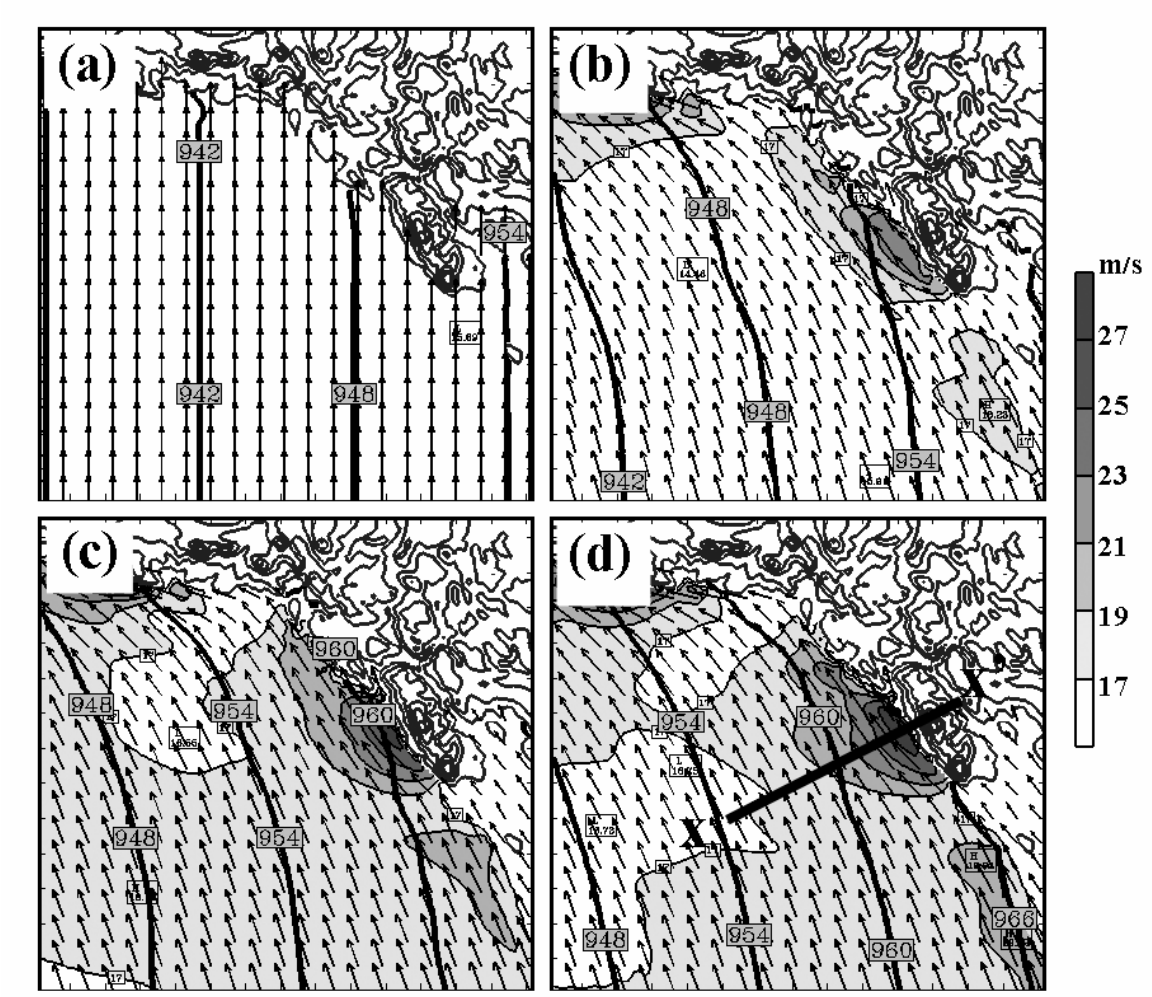

Figure 2.8 500 m pressure (black lines every 6 mb), wind speed (gray shade every 2 m s^{-1}), and wind vectors (black) at (a) hour 0, (b) hour 6, (c) hour 12, and (d) hour 18 of a barotropic simulation initialized at 15 m s^{-1} from 180^{o} over the southeastern coast of Alaska.

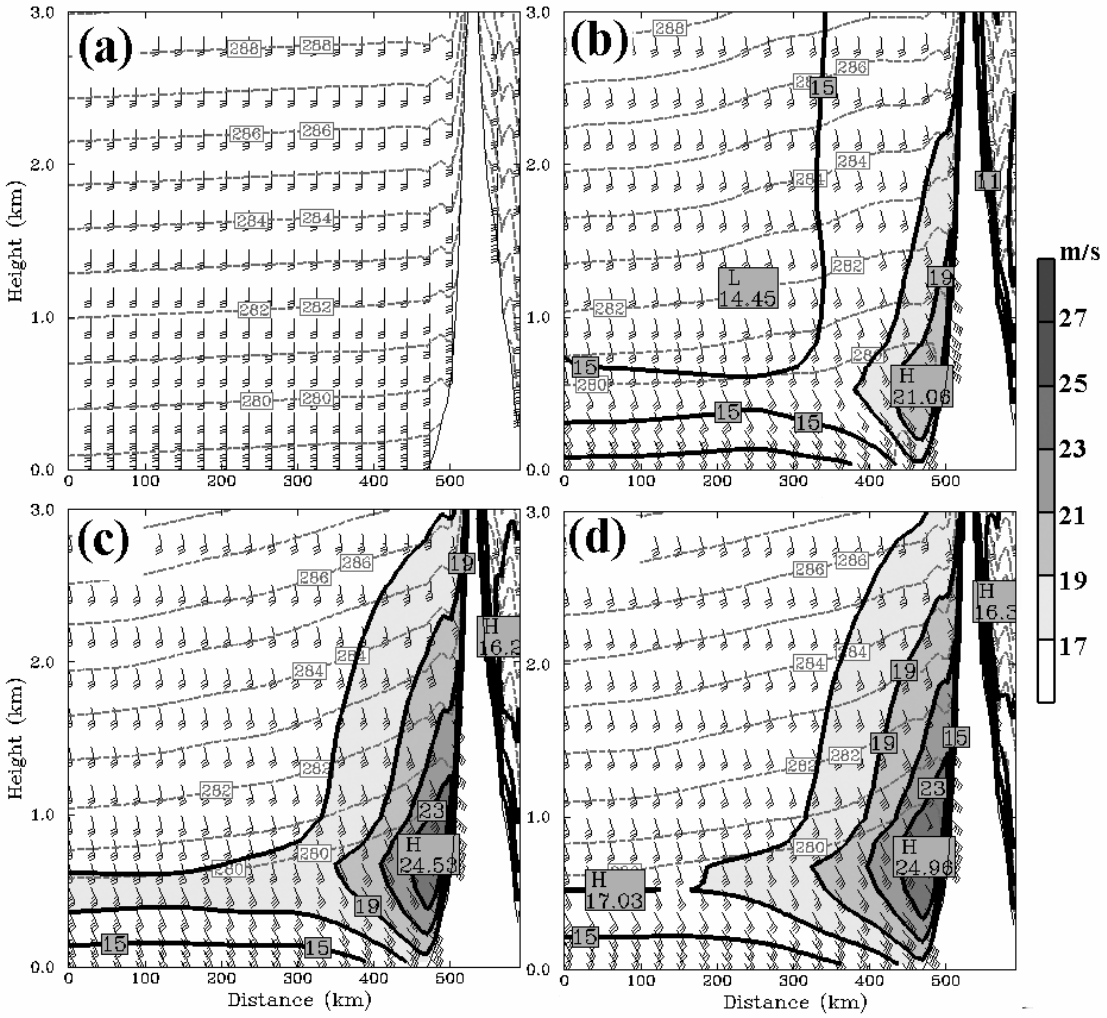

Figure 2.9 Cross-section of wind speed (gray shade every 2 m s^{-1}) and wind barbs (black) along XX' (Fig. 2.8d) at (a) hour 0, (b) hour 6, (c) hour 12, and (d) hour 18 for the same barotropic simulation as Fig. 2.8.

Chapter III:

A Comparison of Two Coastal Barrier Jet Events along the Southeast Alaskan Coast during the SARJET Field Experiment

3.1 Introduction

The Southeastern Alaskan Regional Jets experiment (SARJET) investigated the structure and physical processes of barrier jets along the southeastern coast of Alaska from 24 September to 21 October 2004. SARJET focused on a steep coastal Fairweather Mountains near Juneau, Alaska, which have peaks over 3000 m ASL within ~25 km of the coast (Fig. 3.1). The terrain in the SARJET region is highly complex with numerous coastal gaps, such as Cross Sound gap, which is a sea-level gap ~50 km wide located immediately to the southeast of the Fairweathers. Cross Sound is a common location for gap outflows as quantified using Synthetic Aperture Radar (SAR) observations (Loescher et al. 2006). This chapter compares in-situ aircraft data and high-resolution simulations from the first intensive observation period (IOP1), which featured a nearly terrain-parallel barrier jet (classical jet), with another coastal jet event (IOP7) that was influenced by offshore-directed gap flows at the coast (hybrid jet). The goal of this work is to provide a more detailed three-dimensional analysis of both events in order to increase our understanding of the structural and dynamical differences between "classical" and "hybrid" barrier jets. This study addresses the following questions:

* How do mesoscale structures (e.g., jet morphologies and thermodynamic distributions) and ambient conditions differ between the classic and hybrid jet cases?
* What is the impact of gap outflow from Cross Sound and coastal downslope flows during hybrid barrier jet situations?
* How do the momentum balances and associated airflows differ between a classic and hybrid barrier jet?

The following section describes the field observations and the setup of the mesoscale model simulations. Sections 3.3 and 3.4 present the observations and model

simulations for IOP1 and IOP7, respectively. Section 3.5 compares a trajectory analysis for both IOPs and section 3.6 presents a momentum budget analysis. Section 3.7 describes a sensitivity test to quantify the influence of the gap outflow on the hybrid jet. Our results are summarized in section 3.8.

3.2 Data and Methods

Flight-level measurements for SARJET were obtained from the University of Wyoming's King Air research aircraft. These measurements consisted of in situ observations from south of Cross Sound (pt. A in Fig. 3.1) to near Yakutat (pt. D), and from four southwest-northeast flight legs at various altitudes from the coast (pt. C) to 75 – 120 km offshore (E or E'). This flight pattern was completed twice for each IOP, and will be referred to as flight 1 and flight 2, respectively. The aircraft data was augmented by some additional data, such as buoy 46083 and the sounding site at Yakutat (PAYA) (Fig. 3.1).

The Penn-State-NCAR Mesoscale Model (MM5; Grell et al. 1994) was used to further elucidate the differences between the two SARJET cases. Three computational domains were used (Fig. 3.3a), with grid spacings of 36-, 12-, and 4-km. A 1.33-km nest was also utilized; however, the simulated structures were not significantly different from the 4-km nest, so the 1.33-km results are not highlighted in this paper. Each model domain was run simultaneously using one-way nesting, so that the impact of different model resolutions can be quantified. Thirty-two model sigma levels were applied, with 15 levels below 700-hPa in order to resolve the boundary layer processes. A 10- and 1-minute land-use and topography data set was utilized in the 36- and 12-km domains, respectively, while the 4-km domain used a 30" topography dataset.

Many different model configurations were tested to obtain the best simulation. A majority of variance in the model solutions occurred when applying various planetary boundary layer (PBL) schemes. The control model configuration for IOP1 applied the Blackadar planetary boundary layer (Zhang and Anthes 1982) scheme, while the 1.5-level closure (TKE-based) Mellor-Yamada scheme (Mellor and Yamada 1974) was applied for IOP7. The TKE-based scheme was not utilized in IOP1, since the wind variations were not well simulated along the Fairweathers, while the Blackadar PBL scheme was more realistic. For both IOPs, the Grell cumulus parameterization (Grell 1993) was used on the 36- and 12-km domains, while the precipitation was explicitly resolved in the 4-km domain using the simple ice microphysical scheme (Dudhia 1989). Klemp and Durran's (1983) upper-radiative boundary condition was used in order to prevent gravity waves from being reflected off the model top.

The initial and boundary conditions were provided by National Centers for Environmental Prediction (NCEP) Global Forecast System (GFS) analyses at 1-deg resolution every 6 hours. Four-dimensional data assimilation (FDDA), as described in Stauffer and Seaman (1994), was applied to the 36-km domain in which moisture, temperature, and winds fields were nudged during the first 12-hours.

3.3 IOP1: Classical barrier jet (26 September 2004)

a. Synoptic evolution

The large-scale flow during 26 September 2004 was similar to the "classic" jet composite (Colle et al. 2006), with a high amplitude 500-mb ridge over western North America and a broad trough over western Alaska at 1200 UTC 26 September (Fig. 3.2a). A surface cyclone was over the northern Gulf of Alaska at 1800 UTC 26 September (Fig. 3.2b), which was well forecast by the 36-km MM5 (Fig. 3.3a), with model sea-level pressure errors typically < 1 mb. Both the observations and model indicate a weak trough extending southward along 140 ^{o}W, while the surface winds a few hundred kilometers east of this trough over the SARJET region were south-southeasterly at ~20 m s^{-1}.

By 2100 UTC 26 September 2004 (Fig. 3.3b), the surface trough located 150 km southwest of the Fairweathers separated the enhanced (20-25 m s^{-1}) southeasterly winds near the coast and the 10-15 m s^{-1} south-southwesterlies behind (west) of the trough. At 12-km grid spacing there was weak flow blocking and deflection of the winds along the coast. The following mesoscale analysis further validates the model simulation at 4-km grid spacing.

b. Aircraft observations and model simulations

In situ observations taken as the aircraft ascended and descended to different altitudes between 150 to 1000 m ASL ~90 km west of the coast (point E in Fig. 3.1) were combined to illustrate the ambient low-level conditions during flight 1 (Fig. 3.4; black lines). Since the relative humidity in this layer was nearly saturated (~88-98%), both a moist Brunt-Väisälä frequency (N_m) (Durran and Klemp 1982) and dry N were calculated. Figure 3.4b shows an average $N_{\rm m}$ of ~0.001 s^{-1}, while the dry N was ~0.009 s^{-1} (not shown). At point E there was a slight decrease in equivalent potential temperature with height (Fig. 3.4a), with the model having a slight cool bias (1-2 K). The mean wind speed in this layer was ~27 m s^{-1}, with the model having a 2-3 m s^{-1} wind speed overprediction at 700-850 m ASL (Fig. 3.4c).

The flow and stability were also calculated for an upstream volume in the model (boxed U region on Fig. 3.1) between 0 and 2500 m in order to better represent the average ambient flow conditions approaching the Fairweathers. The average terrain-normal component was ~12 m s^{-1}, with a dry and moist N of 0.01 s^{-1} and 0.003 s^{-1}, respectively[3]. This yields a dry and moist Fr of 0.48 and 1.6, respectively. Early in the IOP, there were only scattered areas of precipitation over the windward slope (not shown), so the actual Froude number was likely between the dry and moist values (Fr ~1). The nondimensional mountain slope, given by the square root of the Burger number, [Nh_m/fL_m], (Cushman-Roisin 1994), is 8.0 and 2.4 for a dry and moist N (where h_m ~2500 m, f ~1.25×10^{-4} s^{-1}, and L_m ~25 km), respectively, with both numbers suggesting the potential for flow blocking (Smith 1979; Pierrehumbert and Wyman 1985).

During flight 1 (1445–1815 UTC), the observed near-coast wind speed enhancement at 150 m ASL was ~5 m s^{-1} relative to the winds ~60 km southwest of the Fairweathers (Fig. 3.5a). The 4-km MM5 wind enhancement at 1700 UTC 26 September 2004 was somewhat weaker than observed, with ~25 m s^{-1} southeasterlies adjacent to the

[3] Both a moist and dry N were calculated at this time since the relative humidity was 85-95% upstream of the barrier (not shown).

Fairweathers decreasing to ~22 m s^{-1} about 80 km offshore (Fig. 3.5b). Meanwhile, at 1000 m (Fig. 3.5c,d), the observed and simulated winds were ~30 m s^{-1} and oriented nearly parallel to the coastal terrain. The observations at both levels show a slight cool anomaly (~1 ^{o}C) near the coast.

During flight 2 (2100 – 2350 UTC) at point E, it was saturated between 150 and 1000 m (not shown). Both the model and observations (Fig. 3.4b; thin gray lines) had an N_m of ~0.006 s^{-1}, which is much greater than flight 1. Meanwhile, there was a slight decrease in the onshore wind component to ~10 m s^{-1} between flight 1 and 2 (Figs. 3.4c,d). For the region ~200 km upstream of the Fairweathers (around point U in Fig. 3.1), the average flow component towards the barrier varied from 12 m s^{-1} below 1000 m to 18 m s^{-1} above 1800 m, while N_m increased from 0.006 s^{-1} below 1000 m to 0.01 s^{-1} above 1800 m. As a result, the moist *Fr* varied from a partially blocked regime of ~0.8 below 1000 m ASL to an unblocked regime (*Fr* ~2.5) above 1800 m ASL.

The observed and simulated winds at 150 m during flight 2 had a barrier jet maximum (to 25 m s^{-1}) adjacent to and slightly downstream (northwest) of the highest peak of the Fairweathers (Figs. 3.6a,b). The 150-m winds veered to southerly ~150 km upstream (south) of the coast; however, some of this windshift may have been associated with the approaching surface trough at 2100 UTC 26 September 2004 (Fig. 3.3b). At the 1000-m ASL (Fig. 3.6c), the winds veered 40^{o} from southeasterly to southerly with the offshore trough, with the model indicating a weak thermal ridge at this location. There was a weak wind speed enhancement from ~27 m s^{-1} at point E to ~30 m s^{-1} about 20 km upstream (west) of the coast, which was well simulated by the model. During the next 3 hours, the barrier jet width at 1000 m narrowed as the surface trough approached the coast (not shown).

The sounding at point C during flight 2 (Fig. 3.4; thick gray lines) represents the vertical profile through the barrier jet near the coast[4]. Although the model had a 1-3 K cool bias at all levels (Fig. 3.4a), the moist static stability was similar to that observed below 1500 m ASL, with the exception of the spike observed in the 800-900 m layer (Fig. 3.4b). The peak winds of 34 m s^{-1} occurred at 800-1000 m ASL (Fig. 3.4c). The 5-10 m s^{-1} wind speed enhancement of the along-shore flow is consistent with the scale analysis of Overland and Bond (1995). They found for $Fr < 1$ (neglecting friction) that the alongshore wind enhancement was comparable to the onshore component of the incident flow. Their work will be further assessed in chapter 5. Above 1000 m ASL, the *Fr* was > 1; therefore, the alongshore wind enhancement scales as $N_m h_m$, which is ~7.5 m s^{-1} (N_m ~ 0.005 s^{-1} and h_m ~ 1500 m), and this enhancement decreases linearly to zero at ridge top (2500 m ASL).

A cross-section of terrain-parallel winds and potential temperatures was constructed using the west to east (E to C) flight legs at 150, 300, 500, and 1000 m (Fig. 3.7). For flight 1 (Figs. 3.7a,b), the terrain-parallel winds were ~30 m s^{-1} near the coast between 500- and 1000-m ASL in both the aircraft and 4-km MM5. The terrain-parallel wind speed in the model decreased to ~25 m s^{-1} at 1500 m ASL about 20 km upstream of the barrier, with relatively little terrain flow enhancements extending offshore above this level. This reduced blocking at ~1500 m likely results from an increase in the effective moist Froude number above mid-mountain level (*Fr* ~3, where *h* ~1000 m, U_n ~15 m s^{-1}, and N_m ~0.005 s^{-1}), since this flow only has to surmount the remaining 1000 m of the

[4] The profile at point C was not available during flight 1.

Fairweathers. Both model and observations have a slight tilt of the isentropes upward towards the coast above 500 m. There is a weak cold dome at the surface early in the event (Fig. 3.7a), which was somewhat weaker than observed in the model.

During flight 2 (2100 to 2350 UTC), the observed and simulated winds (valid for 2100 UTC) were directed more onshore as the weak surface trough approached (Fig. 3.7c,d). The terrain-parallel wind speed component in the 500-1000 m layer increased from ~20 m s^{-1} offshore (point E) to over 30 m s^{-1} at the coast. Meanwhile, the offshore flow above 2000 m ASL was considerably less blocked, with terrain-parallel winds speeds < 20 m s^{-1} at the coast in the model.

In order to illustrate the small-scale variability within the jet during flight 2, Fig. 3.8 shows the observed time-series for the C to E flight legs at 1000-, 300-, and 500-m ASL as well as the 15-minute model data linearly interpolated in time and space along these flight legs. Southwestward along leg C to E at 1000 m for 2150-2207 UTC (Fig. 3.8a), the model accurately simulated the gradual increase in temperature of ~1 ^{o}C (Fig. 3.8a), the small decrease in wind speed of about 2-3 m s^{-1} (Fig. 3.8b), and the ~20 degree wind shift to more southerly (Fig. 3.8c); however, the model was slightly more southerly than observed towards point E. At 300-m (2208-2219 UTC), there was a reduction in wind speed of 2-3 m s^{-1}, and the observed horizontal wind speeds were more variable than at 1000 m, suggesting significant vertical transport of momentum associated with the +2 to -1 m s^{-1} vertical motions (Fig. 3.8d). Although the model wind speeds were less variable, it did capture the area of enhanced winds to 32 m s^{-1} at the eastern end of the second leg at 300 m and the third leg at 500 m (near point C at 2220 UTC). The rain water content (Fig. 3.8e), as measured by the aircraft 2D-P probe, had a maximum of ~1 g m^{-3} near the shore (pt. C at 2220 UTC). The simulated rain maximum occurred over twice the horizontal distance as observed, but it remained near this location for much of the second flight (not shown). The model indicated that there was enhanced convergence at 500-1000 m ASL at point C (Fig. 3.7), which enhanced the upward motion between 500 and 1500 m and the precipitation rates upstream of the barrier. This precipitation enhancement upstream of the barrier associated with flow blocking is similar to the "blocking front" events documented by Colle et al. (2005) along the Wasatch Mountains and Neiman et al. (2006) along the California coast. At 500-m (2220-2239 UTC), both model and observations had a slight increase in temperature offshore, a decrease in wind speed, and a transition to a more southerly flow towards pt. E.

3.4 IOP7: Hybrid barrier jet (12 October 2004)

a. Synoptic setting

At 1200 UTC 12 October 2004, a broad trough was located over the Aleutian Islands and a high-amplitude ridge centered over the Pacific Coast (Fig. 3.9a). The clouds over the Gulf of Alaska were associated with developing baroclinic waves beneath the jet stream. At the start of the aircraft mission at 1800 UTC 12 October 2004 (Fig. 3.9b), there was a surface cyclone (982 mb) near the southern tip of the Alaskan Peninsula, while a secondary low (~998 mb) over the central Gulf of Alaska was moving eastward towards the SARJET study area. The MM5 accurately simulated the position and depth of these features to within 1 mb (Fig. 3.10a). IOP7 had 4-8 ^{o}C colder inland surface temperatures than IOP1 (cf. Fig. 3.3a). A 1028 mb surface high over western Canada

during IOP7 resulted in an off-shore pressure gradient, which forced cold continental air through the coastal mountain gaps.

By 0000 UTC 13 October 2004 (Fig. 3.10b), the secondary low pressure was within 500 km of the coast and had intensified to 995 mb. The circulation associated with this feature advected ~10 ^{o}C warmer surface air into the SARJET study area during the last 6 hours. The surface trough at the leading edge of the warm air was about 2 hours slow in the model, as revealed by the aircraft time series and buoy 46083 (not shown). Therefore, in order to directly compare the model with the flight-level data, the model analysis was shifted back 2 hours for flight 2, such that 0100 – 0200 UTC was used in the model rather than 2300 – 0000 UTC.

b. Aircraft observations and model simulations.

As compared to the King-Air profile from 300 to 1000 m ASL for a location ~130 km offshore at 1848 UTC (point E' in Fig. 3.1) (Fig. 3.11; thin black lines), the model was 1-2 ^{o}C too cool (Fig. 3.11a). The average relative humidity in this layer was ~90% (not shown), with the model producing a similar moist static stability as observed (0.008-0.015 s^{-1}). The average observed wind speed in this layer was east-southeasterly at ~20 m s^{-1} (Figs. 3.11c,d). The model winds were 1-2 m s^{-1} stronger than observed below 500-m ASL and had a small (~10^{o}) easterly wind direction error. Flow blocking parameters, such as the Froude number, were not calculated since the low-level flow had an offshore component during flight 1.

During flight 1 (1700 to 1930 UTC), east-southeasterly flow existed throughout the study region at 150-m ASL (Fig. 3.12a). The winds were more easterly to the north and south of the Fairweathers, where continental flow accelerated offshore through the coastal gaps. In particular, gap outflow of ~20 m s^{-1} at the exit of the Cross Sound turned anticyclonically and merged with the southeasterly flow 40-80 km offshore. The temperatures were 2-3 ^{o}C cooler within this gap outflow than 200 km offshore. In contrast, there was a pocket of warm air (+3-6 ^{o}C) adjacent to the Fairweathers at 150 m, which resulted in a cross-shore temperature gradient near the coast that was opposite of IOP1 (cf. Fig. 3.6). The 4-km MM5 at 1900 UTC 12 Oct 2004 (Fig. 3.12b) illustrates more completely the anticyclonic turning of the cold gap outflow, which surrounds the area of warm air centered near the Fairweathers. A region of enhanced winds (>20 m s^{-1}) was located between the cold gap outflow and the coastal warm anomaly.

At 500 m ASL (Figs. 12c,d), the observed and simulated flow was more coast-parallel than at 150-m ASL, with 15-20 m s^{-1} winds along flight leg C-E'. There was a slight wind enhancement and deflection of the ambient flow as it encountered the region of the gap outflow. The observed temperatures were >11 ^{o}C at the coast, and decreased to <9 ^{o}C about 20 km offshore. The model reproduced this temperature gradient, but it was ~1 ^{o}C too cool.

At 1000 m ASL (Fig. 3.12e), the observed southeasterly winds of 15-17 m s^{-1} were 2-3 m s^{-1} stronger 80 km offshore at point E' than near the coast. The model wind speeds also increased slightly offshore in the region downstream of the tallest peaks, but were fairly uniform upstream (Fig. 3.12f). The temperatures were also more uniform at this level than below, thus indicating that the gap outflow and warm anomaly near the coast were fairly shallow.

During flight 2 (2300 UTC 12 October to 0230 UTC 13 October), the temperature profile for 300-1000 m ASL at point E' was 10-12 ^{o}C warmer than flight 1 as a result of warm advection from the offshore cyclone (Fig. 3.11a), while the winds had weakened to 18 m s^{-1} (Fig. 3.11c) and veered ~60 degrees to more southerly (Fig. 3.11d). A similar low-level temperature increase was obtained upstream (south) of the Fairweathers for the region around point U (Fig. 3.1), where the average moist Froude number below 2000 m was ~0.75 (U_n ~15 m s^{-1}, N_m ~0.01 s^{-1}, and h ~2500 m), so flow blocking is expected.

A vertical profile at point C (Fig. 3.11; heavy gray lines) through the barrier jet core at 0140 UTC 13 October 2004 indicates that the model equivalent potential temperature profile was within 1 K of the observed below 1500m ASL (Fig. 3.11a), but was slightly too cool at ~500 m ASL. The temperatures at point E' between 500-1000 m ASL were ~4-5 K warmer than point C. The stabilities below 500 m ASL were weaker in the warm anomaly region near the coast than offshore at E. The model accurately simulated the jet profile above 400 m ASL, with winds reaching ~27 m s^{-1} and veering from east-southeasterly near the surface to southerly above 1000 m ASL.

The weak surface trough noted earlier at 1800 UTC (cf. Fig. 3.10) entered the region and began interacting with the gap outflow at 0100 UTC 13 Oct 2004. The observed and simulated winds at 150-m ASL became southeasterly and exceeded 25 m s^{-1} 20-60 km offshore of the coast (Figs. 3.13a,b). The low-level temperatures near the coast were >11 ^{o}C, coincident with a 5-10 m s^{-1} decrease in wind speed. Meanwhile, the flow was more south-southeasterly at 15 m s^{-1} offshore at point E'. The near surface temperature gradient was largest in the outer region of the offshore flight leg given the flow confluence between the advancing warm air offshore with the surface trough and the offshore-directed gap outflow. The model suggests that the temperature gradient of ~2 ^{o}C [100 km]$^{-1}$ in the offshore portion of the 4-km MM5 (Fig. 3.12b) increased to ~10 ^{o}C [100 km]$^{-1}$ (Fig. 3.13b) as the trough interacted with the gap outflow. A similar pattern of low-level frontogenesis has been documented for cold gap outflow from the Strait of Juan de Fuca interacting with a landfalling warm front (Doyle and Bond 2001).

At 500 m ASL (Figs. 3.13c,d), the flow exceeded 25 m s^{-1} 20-80 km offshore, while the winds were ~13 m s^{-1} offshore near point E'. The coldest temperatures associated with the gap outflow were ~20 km closer to the Fairweathers than at 150-m ASL, while a narrow (< 20 km) warm anomaly (+2 ^{o}C) persisted against the western portion of the barrier. The model had a similar jet structure between C-E', and it also indicates that the jet became wider and slightly stronger ~50 km farther downstream.

At 1000 m ASL (Figs. 3.13e,f), south-southwesterly flow at 17 m s^{-1} accelerated to 20 m s^{-1} and became southerly at the coast, with the simulated winds (Fig. 3.13f) 2-5 m s^{-1} too strong. In contrast to the warm anomaly near the coast at 500 m, there was weak cooling towards the coast at 1000-m in the observations, while the model temperatures were more uniform. The deflection of the onshore flow to more terrain-parallel and the cold anomaly near the coast is reminiscent of the more "classical" barrier jet observed in IOP1.

Figure 3.14 shows cross-section C-E' of the observed and simulated winds and potential temperatures for both flights. The flight 1 coastal winds (Figs. 3.14a,b) were 15-20 m s^{-1} and directed mainly offshore between 500 and 2000 m. The center of the gap outflow is identified by the shallow cold dome below 500 m centered ~80-90 km

offshore. There was a strong vertical potential temperature gradient capping the shallow gap outflow at 500 m, thus the stratification (N_m ~0.012 s^{-1}) was at least twice as large as IOP1 (cf. Fig. 3.7). Meanwhile, below 1 km ASL and at the coast, the isentropes tilted downward towards the coast associated with the low-level warm anomaly.

During flight 2 (Figs. 3.14c,d), there was a well-defined barrier-parallel jet, with speeds to 30 m s^{-1} within 50 km of the coast at 300-500 m ASL. The barrier jet was much weaker above 1-km ASL and the winds were more south-southwesterly. Between 1000-2000 m, the ambient flow became more southerly (terrain parallel) only within 10-20 km of the coast. The flow blocking above 1000 m was weaker given the Froude number for the box at U of ~1.3 (U_n ~20 m s^{-1}, N_m ~0.01 s^{-1}, and terrain height above 1000 m of ~1500 m).

Time series for the C to E' flight legs show that the warmest temperatures (~12 ^{o}C) were located at the coast at 150-m ASL (Fig. 3.15a). The model and observed winds decreased rapidly to 15 m s^{-1} while becoming southerly approaching point E' (Fig. 3.15b,c). Over the eastern portion of the 500-m flight leg (near 0030 UTC), there were large wind speed variations (21-28 m s^{-1}) and vertical velocities exceeding ±1 m s^{-1}. The peaks of these oscillations were separated every ~5 km, which is suggestive of wave-like perturbations at the top of the stable layer capping the gap outflow. The upward (downward) motions at 500 m were associated with a 2-3 m s^{-1} wind speed increase (decrease), as higher (lower) momentum was transported from below (above) this level. In contrast to IOP 1, there were higher concentrations of rain water observed for the offshore portion of the flight leg (Fig. 3.15e), while less was observed near the coast at pt. C. At the 500-m level (Fig. 3.15), there was an increase in wind speed, temperature, and a decrease in relative humidity towards the coast, but the simulated wind shift was slightly less pronounced.

3.5 Trajectory analysis

In order illustrate the origin of the coastal winds and temperature structures for both IOPs, backwards trajectories were calculated along cross-section C-E. A trajectory time step of 5 minutes was used with the spatial and temporal interpolation of 15-minute model data. The times of release were 2100 UTC 26 September and 0100 UTC 13 October for IOP1 and IOP7, respectively.

Figure 3.16 shows the trajectories released during the second flight of each IOP at the 150- and 500-m ASL. The relatively uniform south-southeasterly winds during IOP1 are evident in all the near-coast trajectories (3-6 in Fig. 3.16a and 9-12 in Fig. 3.16b), with all trajectories originating offshore at 150- and 500-m. The parcels released at the coast (#6 and #12) show a slight deflection to a more east-southeasterly component near the Fairweathers. The greater onshore component for trajectories 1-2 and 7-8 is a result of the weak trough offshore immediately west of the strongest winds (cf. Fig. 3.6).

The IOP7 trajectories (#3 and 4) released in or near the jet maximum within 100 km of the coast originate inland (Fig. 3.16c). Trajectories 5 and 6 follow the coastline, ascend the gap outflow to 1900 m, then descend adjacent to the Fairweathers to create the warm anomaly noted in Figs. 3.12-3.14. Trajectory 6 experienced a potential temperature increase of ~6 K as it ascended over the gap outflow and the southern portion of the Fairweathers from 600 to 2000 m (not shown). There was light to moderate precipitation

in this region, so latent heating was likely occurring. Subsequently, trajectory 6 descended from 2000 m to 150 m; however, the potential temperature decreased ~3 K given evaporative cooling and mixing. Therefore, the net diabatic heating of trajectory 6 was ~3 K, which was likely important in enhancing the warm anomaly at the coast. The trajectories released at the 500-m level (Fig. 3.16d) resemble the IOP1 trajectories at this level (cf. Fig. 3.16b), with offshore origins and confluent flow 100-150 km from the coast. Trajectories 11 and 12 ascend the gap outflow to 700-1300 m and then descend to 500 m at the base of the Fairweathers.

3.6 Momentum budget analysis

A momentum budgets were calculated for both IOPs in order to diagnose the mechanisms for the wind variations near the coast. The following momentum equation was separated into its components:

$$\frac{dV}{dt} = -\frac{1}{\rho}\nabla p + f\hat{k} \times V - F\,, \qquad (1)$$

where d/dt is the total derivative with respect to time and V is the horizontal velocity vector. The first two terms on the right-hand side represent the pressure-gradient and Coriolis acceleration, respectively. The last term, "F", is the tendency output from the PBL schemes, which include friction and turbulent mixing. Using this equation, the zonal and meridional momentum balances were output at all grid points within the 4-km MM5 nest every 5 minutes and averaged for a specified period.

Figure 3.17 shows the momentum terms plotted at 150, 500 and 1000 m ASL for a representative 30-minute period of flight 2 for both IOPs. For IOP1 (2045-2115 UTC), the ambient flow (south of pt. E in Fig. 3.17a) is nearly geostrophic at 150 and 500 m ASL (Figs. 3.17c,e). As the parcels approach to ~50 km of the Fairweathers, they are accelerated to the left by an offshore-directed pressure-gradient. Subsequently, they accelerate down the pressure-gradient parallel to the Fairweather Mountains, where at 150-m ASL, an approximate antitriptic balance exists in the along-barrier direction near point C between the pressure gradient force and friction (Fig. 3.17a). After the flow passes the Fairweathers (just offshore of pt D in Fig. 3.17a), an approximate geostrophic balance is obtained in the cross-barrier direction at 500 and 1000 m ASL (Figs. 3.17c,e). The total accelerations are largest near the Fairweathers at 500 m ASL (Fig. 3.17c). The friction/mixing term is small everywhere except at 150 m, while both the pressure gradient force and the net acceleration terms do not vary much with height within the coastal region.

In contrast, for IOP7, the flow accelerates out of the Cross Sound gap down the pressure gradient and turns to the right in part by the Coriolis force (Fig. 3.17b). If the Coriolis force was the only force, then the flow along the axis of the pressure ridge (dashed line) of the gap outflow would follow an inertial circle, with inertial radius $R_{ic}=U/f$ (Holton 2004). With a gap outflow wind speed of 20 m s^{-1} and $f = 1.25\text{x}10^{-1}$ s^{-1}, R_{ic} ~160 km; however, the radius for this trajectory is only ~100 km. This suggests an additional force is accelerating the flow to the north. The friction/mixing term has a relatively large component in the gap outflow region to the right of the flow, due to the mixing of southeasterly momentum into the gap outflow from above. The moist Richardson number, $R_i = N^2[du/dz]^{-2}$, was ~0.25, where ΔU = 20 m s^{-1} between 150 and

750 m ASL and N_m~0.005 s^{-1}, thus suggesting the potential for mixing. Unfortunately, there were no observations collected around this location, but the aircraft time series between CE suggested areas of significant vertical momentum transport within the gap outflow (cf. Fig. 3.15). The ambient flow at all levels entering the domain from the south is decelerated ~80 km upstream of the coast as it impinges on the gap outflow (Figs. 3.17b,d, and f). The deceleration is caused by the positive pressure perturbation associated with the gap outflow, thus acting to oppose the impinging flow, which causes the impact of terrain to extend farther upstream than for IOP1. Above the gap outflow (Fig. 3.17d,f), the momentum balances adjacent to the Fairweathers resembles more those of IOP1, with the impinging parcels being slightly deflected northward by the terrain-induced pressure gradient. Downstream of the Fairweathers (near pt. D), the flow at 500 and 1000 m ASL nears geostrophic balance in the cross-barrier direction, similar to IOP1.

3.7 Impact of gap outflow

One objective of this study is to determine how the gap outflow influenced the structure and intensity of the barrier jet during IOP7. We examined this by filling Cross Sound gap (hereafter referred to as NOGAP) in the 12 and 4 km domains. The added NOGAP terrain connects the south side of the Fairweathers to Chichagof Island (Fig. 3.1) and slopes linearly from 2000 m to 500 m over a 100 km distance (Fig. 3.18b). The effectiveness of the artificial ridge in blocking the flow across Cross Sound is shown in a cross-section (Y-Y' in Fig. 3.18a) through Cross Sound. The gap outflow was reduced from ~15 m s^{-1} in the control run (CTL) (Fig. 3.18c) to < 5 m s^{-1} in the NOGAP run (Fig. 3.18d), while the flow became more southerly (upslope) over the windward slope of the added barrier. However, the isentropes still have an upward tilting towards the coast associated with a ~2 ^{o}C cold anomaly, which suggests that at least a portion of this cooling was from adiabatic ascent of the southerly flow over the barrier. However, the warm anomaly adjacent to the Fairweathers is maintained, since the NOGAP run still produced a downslope flow (not shown).

At 0000 UTC 13 Oct 2004 (Fig. 3.19), the wind speeds exceed 25 m s^{-1} for both the NOGAP and control (CTL) simulations; however, the region of enhanced winds is about 40 km wider (west-east) and about 30 km longer (north-south) for the CTL than NOGAP. The cross-sections taken through points X-X' (Figs. 19a,b) illustrates that this change in width of the coastal jet is reduced from ~100 km in CTL (Fig. 3.19a) to ~60 km in NOGAP (Fig. 3.19b). Removing the Cross Sound gap also changes the position of the jet maximum, from slightly offshore in CTL to one centered closer to the coast in NOGAP, which is similar to IOP1.

A trajectory analysis was completed for the NOGAP experiment (Fig. 3.20) to diagnose how the NOGAP flow changed the airflow of the hybrid jet. Trajectories 5 and 6 at 150 m ASL (Fig. 3.20a) still originate along the coast, but trajectories 3 and 4 no longer exit from Cross Sound as in the control run (cf. Fig. 3.16c). Trajectory #4 originates inland for the NOGAP run as it is deflected around the filled gap, which suggests that a portion of the cold anomaly found in section YY' of Fig. 3.18d is a result of upstream leakage of cold continental air. Trajectory #3 originates offshore in NOGAP and experiences a slight deflection as it approaches the coastal region. At 500 m ASL (Fig. 3.20b), the trajectories have a more "classical" barrier jet signature, similar to IOP1.

Overall, these results suggest that the gap outflow through Cross Sound had a large impact on the barrier jet structures during IOP7.

3.8 Summary and Conclusions

Aircraft in-situ measurements were collected during the Southeastern Alaskan Regional Jets experiment (SARJET) to investigate the structure and physical processes of coastal barrier jets along the Fairweather Mountains near Juneau, Alaska. Much of the success of SARJET can be attributed to the detailed observations collected in a variety of conditions favoring strong low-level winds in the coastal zone. This chapter presented in situ aircraft data and high resolution simulations to compare a "classical" barrier jet (IOP1) with a "hybrid" jet (IOP7) that had gap flow influences at low-levels.

During IOP1 there was south-southeasterly flow preceding a landfalling trough, which became blocked by the coastal terrain and accelerated down the pressure gradient to produce a 5-10 m s^{-1} wind enhancement (maximum wind speeds ~30 m s^{-1}) in the alongshore direction near the Fairweathers. These features were similar to other "classical" barrier jet structures studied by Parrish (1982), Doyle (1997), and Yeh and Chen (2003), in which the windward pressure ridging and associated cold anomalies were produced from low-level upslope flow. In contrast, IOP7 featured greater surface pressure and colder low-level temperatures to the east (inland) of the study area than IOP1, which resulted in offshore-directed coastal gap flows below ~500 m. This event was similar to a barrier jet event near California's Petaluma Gap by Neiman et al. (2006). In their conceptual model, the gap outflows turn to the north, forming a hybrid jet similar to IOP7.

MM5 simulations were performed to further investigate the airflow through the jet structures and the dynamics governing their morphology. The simulations presented for both events were shown to adequately reproduce the low-level pressure perturbations and orographic flow response. The IOP7 simulation had a small timing bias associated with the approach of a pressure trough and warmer air; however, the model was still able to accurately simulate the sampled hybrid jet structure.

Momentum budget analysis revealed the dynamical differences between the two IOPs. The hybrid jet was accelerated with a greater anticyclonic curvature than an inertial circle as it exited Cross Sound. Farther downstream (to the north), the momentum balance along the coast was more characteristic of a classical jet, with approximate geostrophy in the cross-barrier direction. The flow ~150 km upstream of the SARJET region in IOP1 was nearly geostrophic, while the upstream flow in IOP7 was undergoing a deceleration as it interacted with the gap outflow.

Model trajectories illustrated that IOP1 only had onshore flow origins, while the coastal winds in IOP7 had both gap and offshore origins. Low-level trajectories in IOP7 originated offshore and were deflected westward by the gap outflow rather than the coastal terrain. To test the impact of the gap flow on the hybrid jet, a simulation was performed with the Cross Sound gap filled (NOGAP). This produced a coastal jet with a similar maximum wind speed to the control run, but the filled gap reduced the offshore width of the coastal jet by about 40% and shifted the maximum winds more towards the coast, which is similar to the classical jet in IOP1.

Figure 3.21 presents a conceptual model summarizing the three-dimensional structures of the southeast Alaskan hybrid jet using IOP7 results. For these events, the gap outflow rotates anticyclonically out of the coastal gap and merges with the ambient coastal jet adjacent to the steep coastal terrain. Unlike the classical jets (IOP1), there is a warm anomaly near the coast resulting from the downslope flow off the southern end of the Fairweathers (Fig. 3.21). A cold anomaly exists farther offshore associated with the gap outflow. Above the shallow gap flow at mid-mountain level, the flow is more representative of a classical barrier jet, with southerly flow deflecting and accelerating more parallel to the Fairweathers and there is a weak cold anomaly against the barrier. Farther downstream, the hybrid barrier jet structure becomes more similar to a terrain-parallel classical jet.

The coastal jets of the southeastern Alaskan Coast are often influenced by the gap outflows through the numerous sea-level mountain gaps in this region. This study will help forecasters recognize the different mechanisms between hybrid and classic barrier jets. The following chapter will further quantify the changes of the gap outflow and hybrid jet structures using a series of idealized simulations with varying ambient flow and stability conditions, as well as the depth of the inland cold anomaly.

Figures

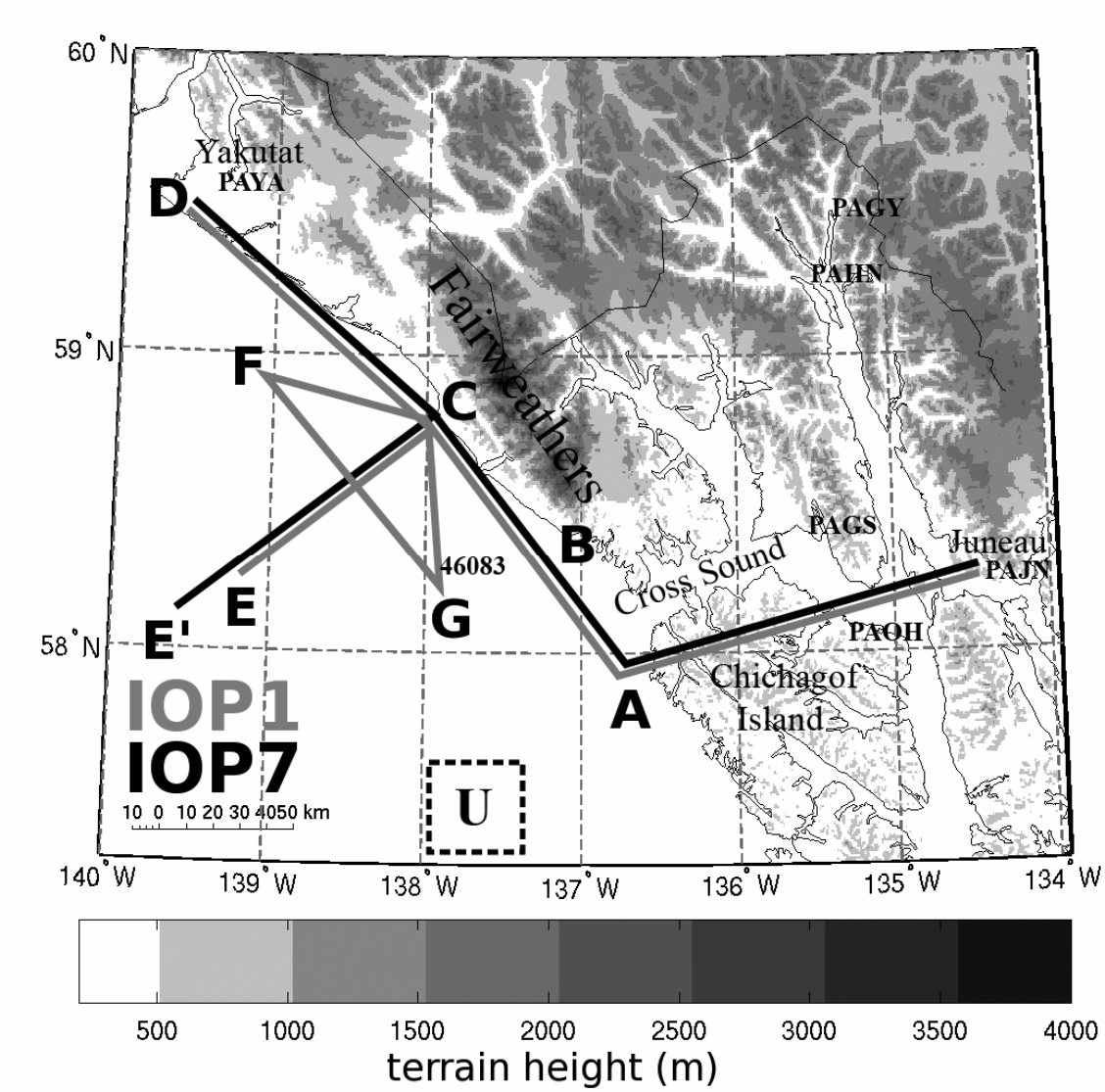

Figure 3.1 SARJET study region showing the flight tracks (IOP 1 gray and IOP 7 black) and terrain (gray shaded). The dashed box around U is used to estimate model-averaged flow parameters upstream of the Fairweather Mountains.

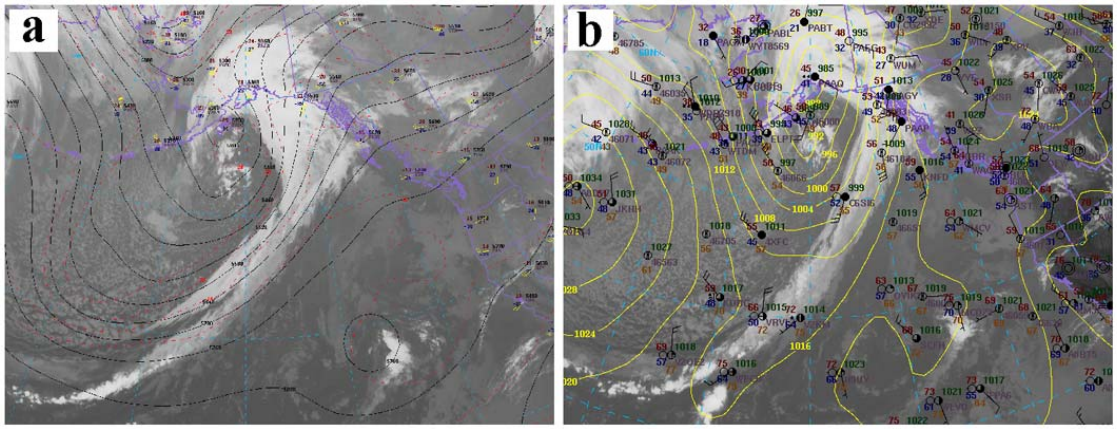

Figure 3.2 IR satellite image at (a) 1200 UTC 26 September 2004 with GFS 500 mb geopotential height (black every 60 meters) and observations from upper-air stations and (b) 1800 UTC 26 September 2004 with GFS sea level pressure analysis (yellow every 4 mb) and surface observations.

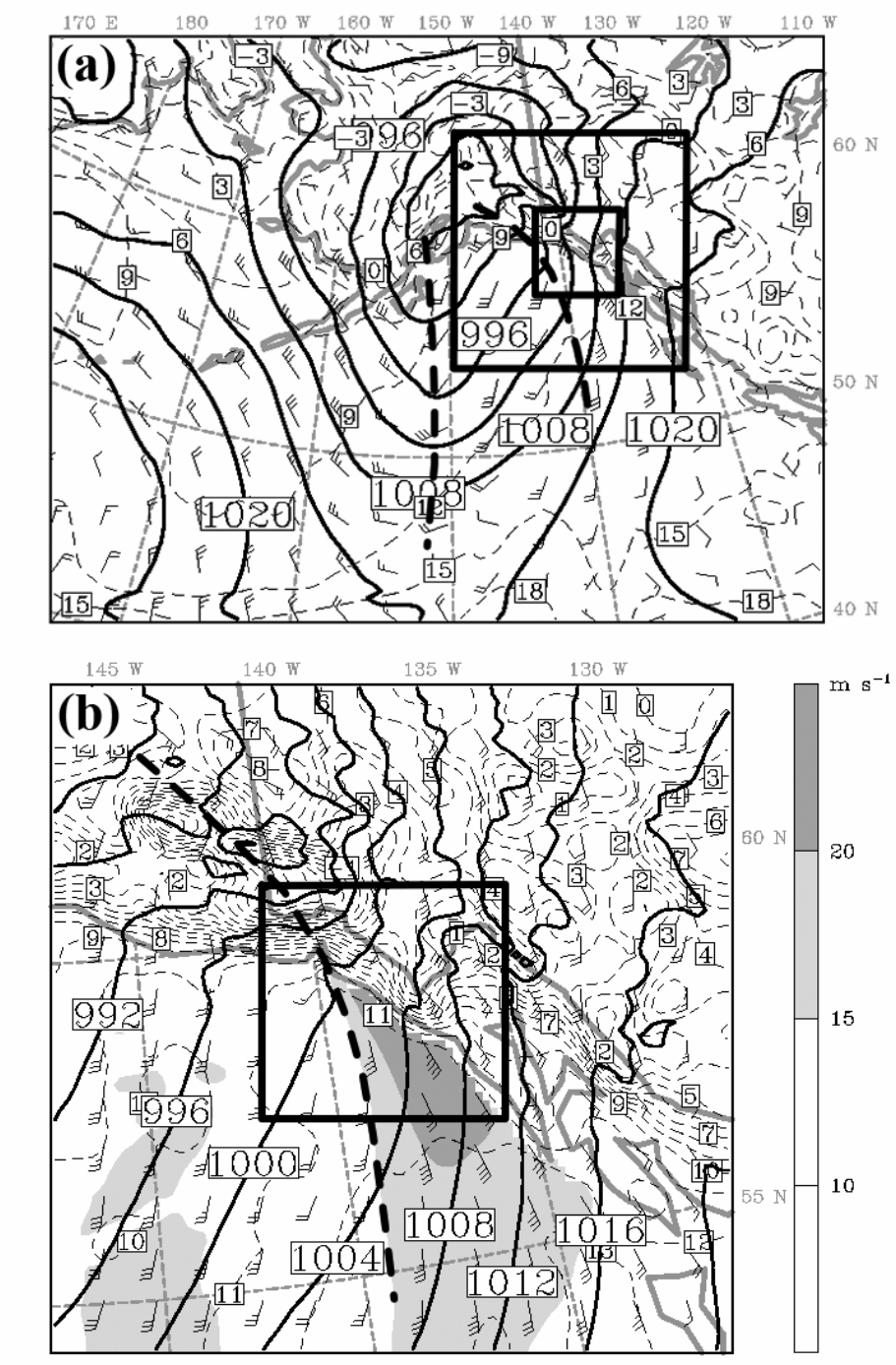

Figure 3.3 (a) 36-km MM5 showing sea-level pressure (black every 6 mb), surface temperature (thin dashed lines every 3 ^{o}C), and surface winds barbs (full barb = 5 m s^{-1}) at 1800 UTC 26 September 2004 (b) 12-km MM5 showing sea-level pressure (black every 4 mb), temperature (thin dashed lines every 2 ^{o}C), wind speed (gray shaded every 5 m s^{-1}), and winds barbs (full barb = 5 m s^{-1}) at 2100 UTC 26 September 2004. Bold dashed lines denote the position of the surface troughs.

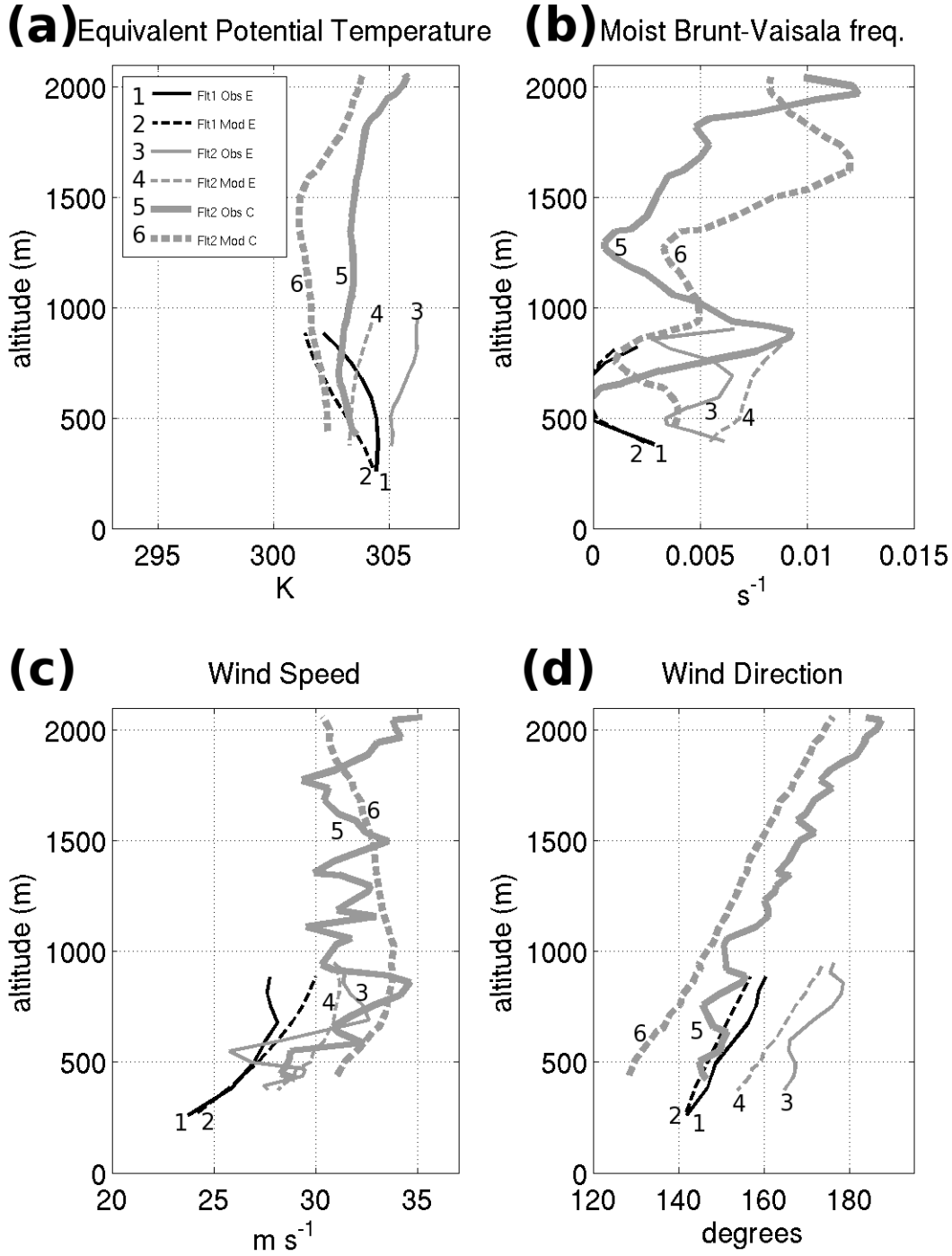

Figure 3.4 Aircraft vertical profile at point E showing (a) equivalent potential temperature (K), (b) moist Brunt-Väisälä frequency (s^{-1}), (c) wind speed (m s^{-1}), and (d) wind direction (degrees) for both flights during IOP 1. The black lines represent flight 1 and the gray lines represent flight 2. Solid and dashed lines represent the observed and model, respectively, while the thin lines represent point E and bold represent point C.

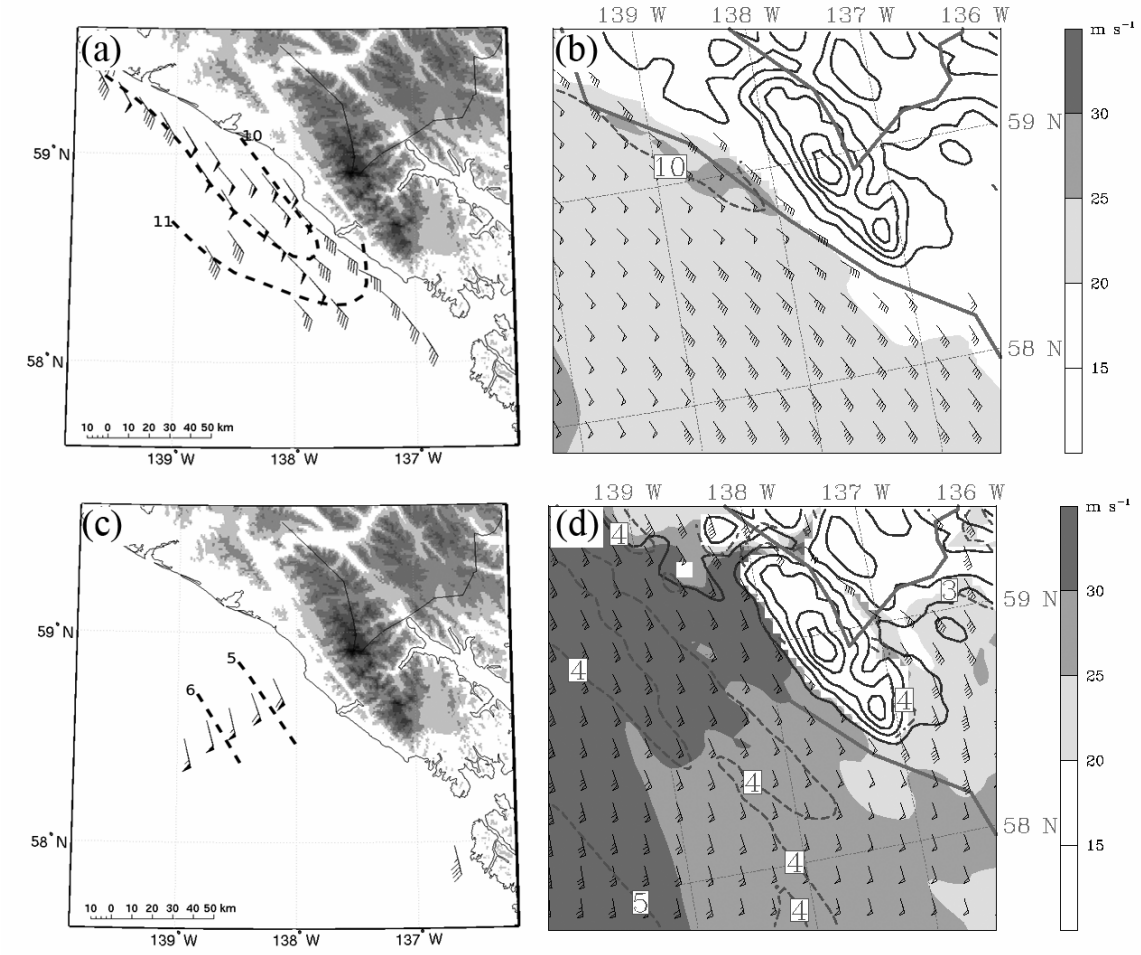

Figure 3.5 Winds (full barb = 5 m s^{-1}) and temperatures (dashed every 1 ^{o}C) at 150 m ASL for the (a) observations during flight 1 of IOP1 and (b) 4-km MM5 at 1700 UTC 26 September 2004. The model winds are also shaded (in m s^{-1}) and terrain is contoured every 500 m. (c) and (d) same as (a) and (b) except at 1000 m.

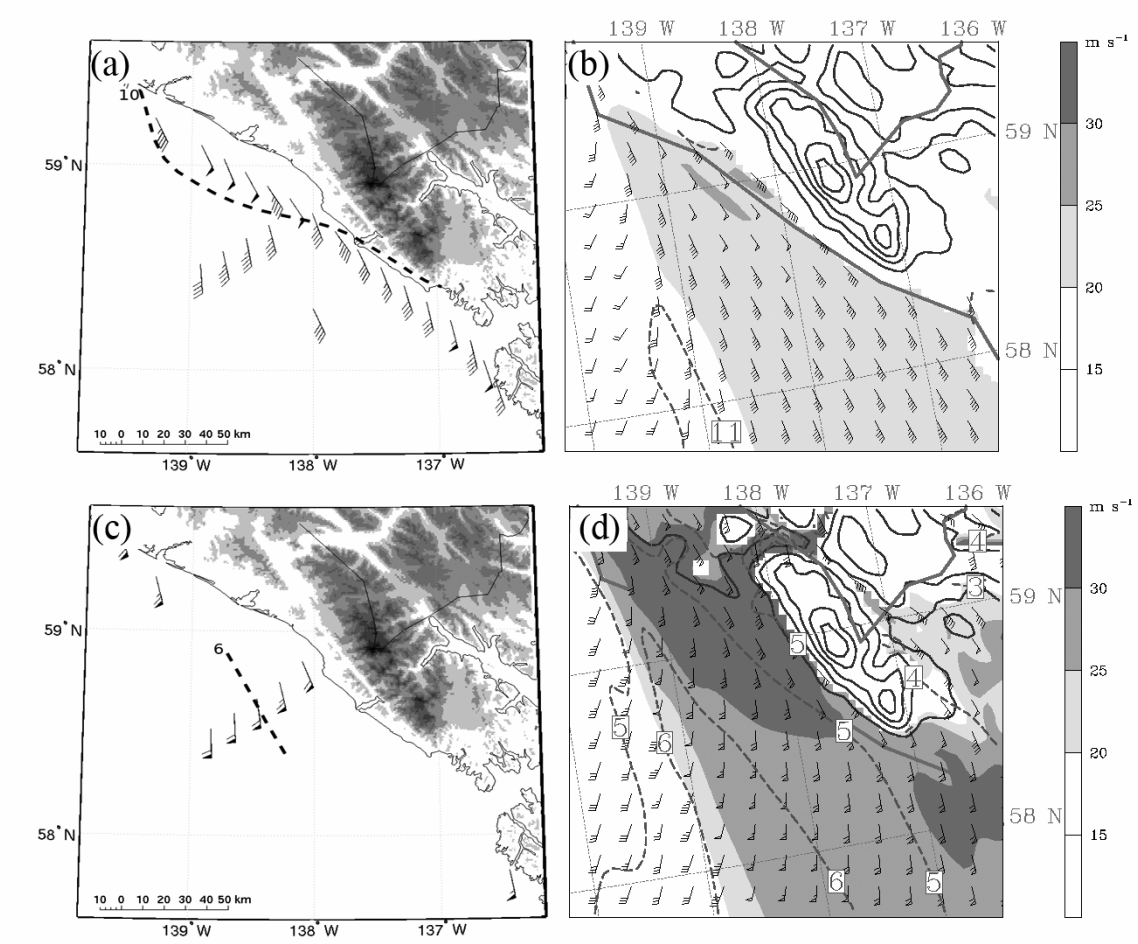

Figure 3.6 Winds (full barb = 5 m s^{-1}) and temperatures (dashed every 1 ^{o}C) at 150 m ASL for the (a) observations during flight 2 of IOP1 and (b) 4-km MM5 at 2100 UTC 26 September 2004. The model winds are also shaded (in m s^{-1}) and terrain is contoured every 500 m. (c) and (d) same as (a) and (b) except at 1000 m.

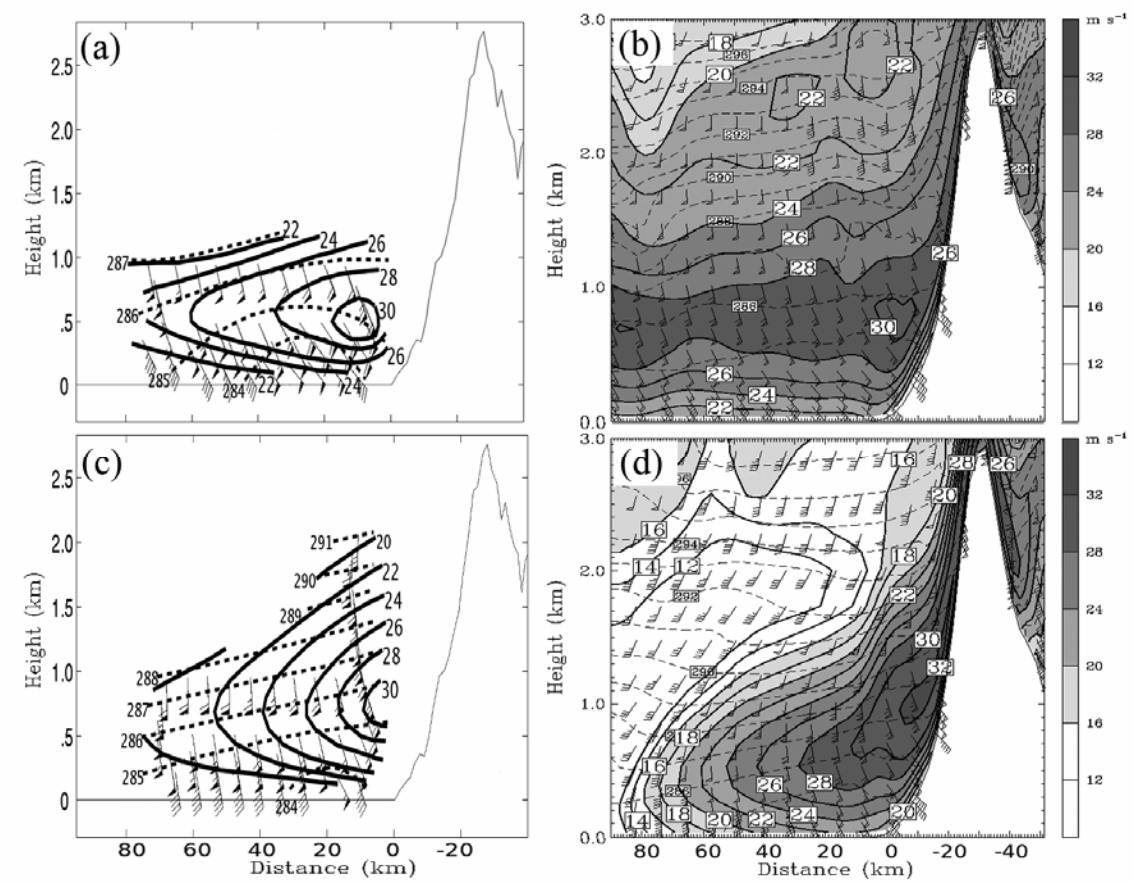

Figure 3.7 Cross-section between C-E showing winds (full barb = 5 m s^{-1}), terrain-parallel wind component (solid every 2 m s^{-1}), and potential temperatures (dashed every 1 K) between C-E for the (a) observations during flight1 of IOP1, (b) 4-km MM5 at 1700 UTC 26 September 2004. (c) Same as (a) except for flight 2. (d) Same as (b) except at 2100 UTC 26 September 2004. The model terrain-parallel winds are also shaded (every 4 m s^{-1}).

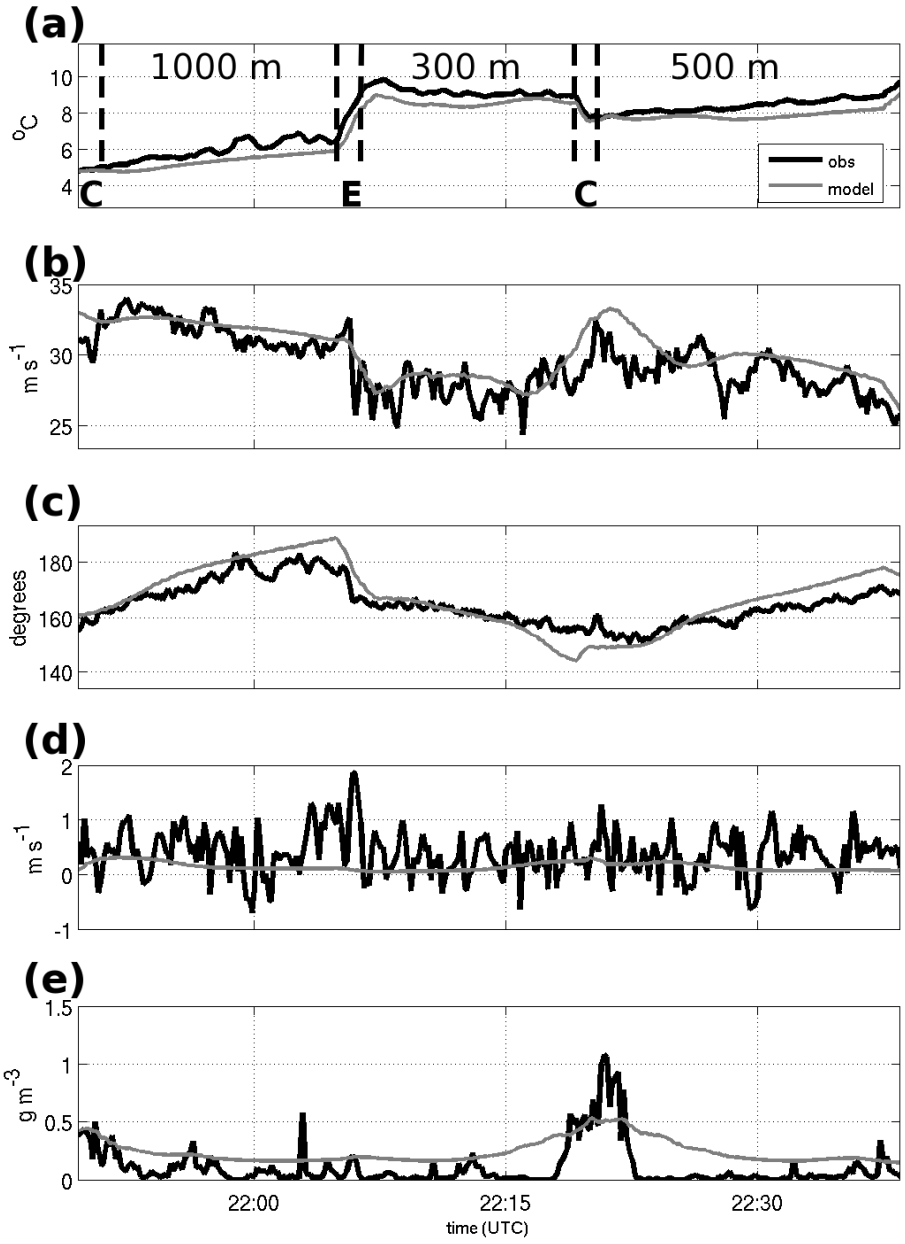

Figure 3.8 Aircraft (black) and 4-km MM5 (gray) time series for three levels (1000, 500, and 300 m) between points E and C of IOP 1 during 2150-2240 UTC 26 September 2004. Data is plotted at 10 s intervals showing (a) temperature (^{o}C), (b) wind speed (m s^{-1}), (c) wind direction (degrees), (d) vertical velocity (m s^{-1}), and (e) rain water content (g m^{-3}). The dashed lines indicate the periods of aircraft ascent/descent at points E and C.

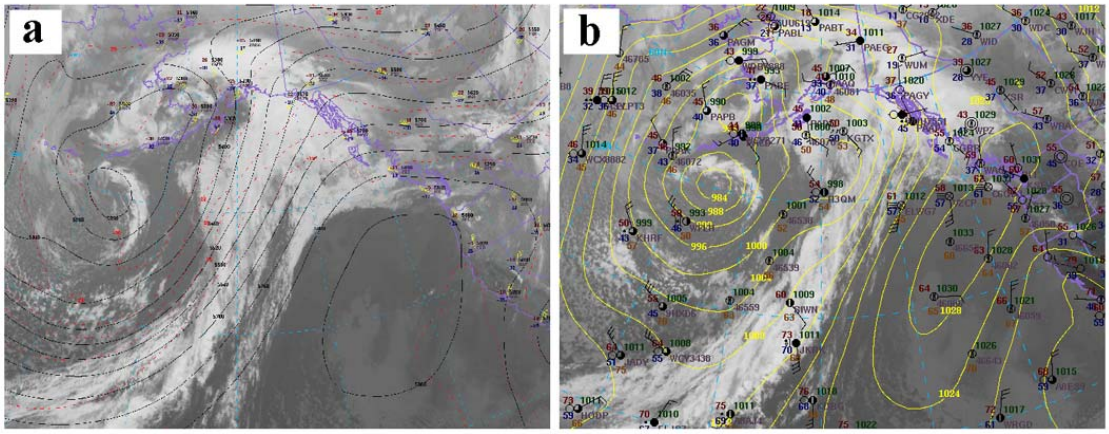

Figure 3.9 IR satellite image at (a) 1200 UTC 12 Oct 2004 with GFS 500 mb geopotential height (black every 60 meters) and observations from upper-air stations and (b) 1800 UTC 12 Oct 2004 with GFS sea level pressure analysis (yellow every 4 mb) and surface observations.

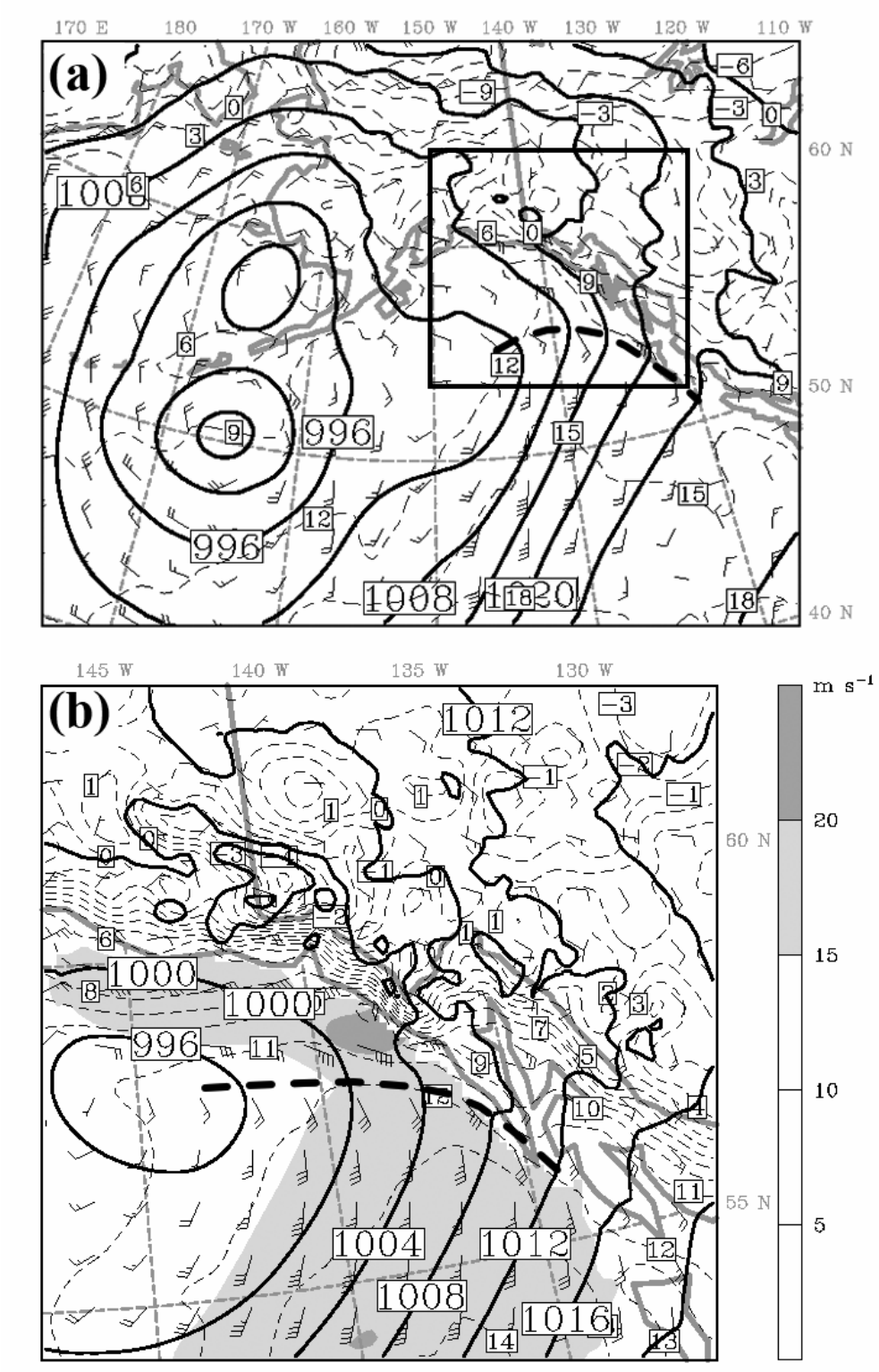

Figure 3.10 (a) Same as Fig. 3.2a except for IOP7 at 1800 UTC 12 October 2004. (b) Same as Fig. 3.2b except for 0000 UTC 13 October.

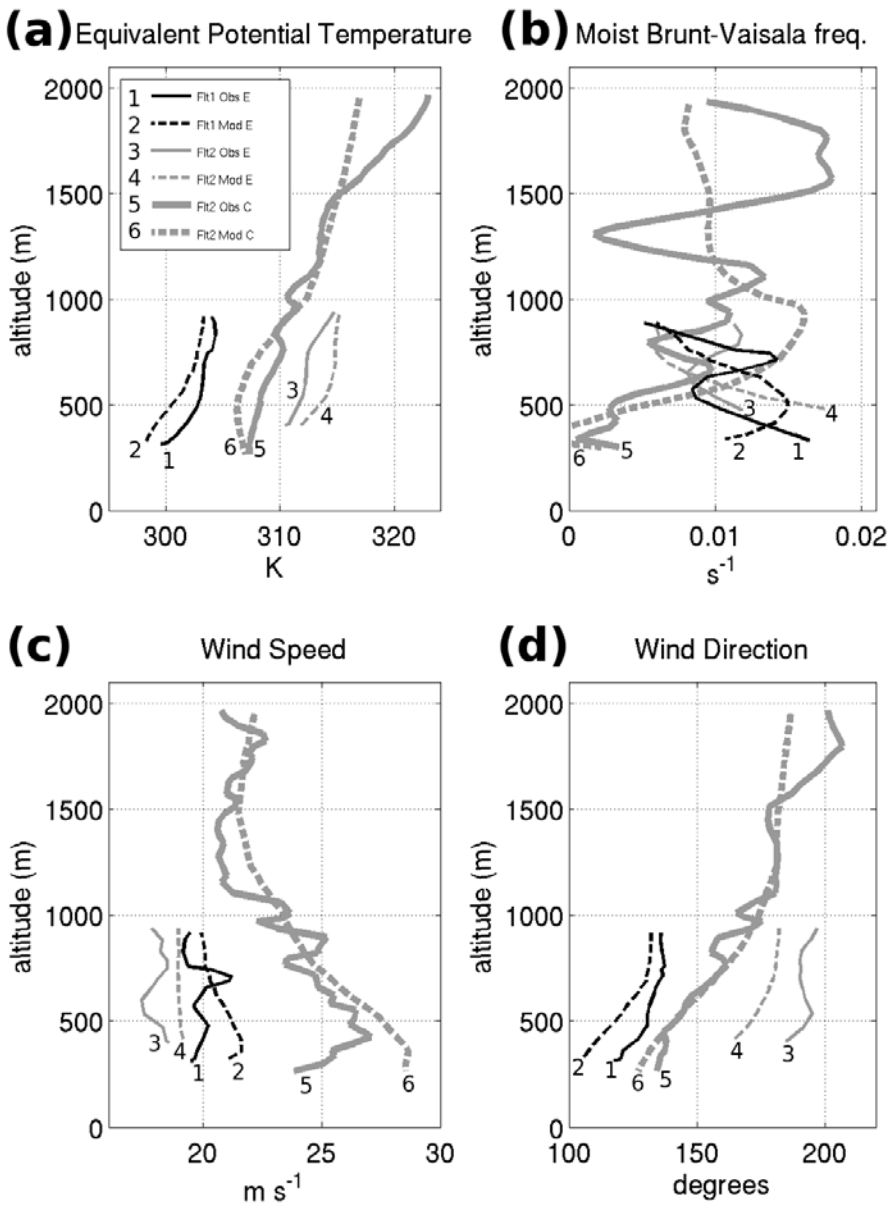

Figure 3.11 Aircraft vertical profile at point E' showing (a) equivalent potential temperature (K), (b) moist Brunt-Väisälä frequency (s^{-1}), (c) wind speed (m s^{-1}), and (d) wind direction (degrees) at for both flights during IOP7. Black lines represent flight 1 and gray lines represent flight 2, while solid and dashed lines represent observed and model, respectively. The thin lines represent point E' and bold represent point C.

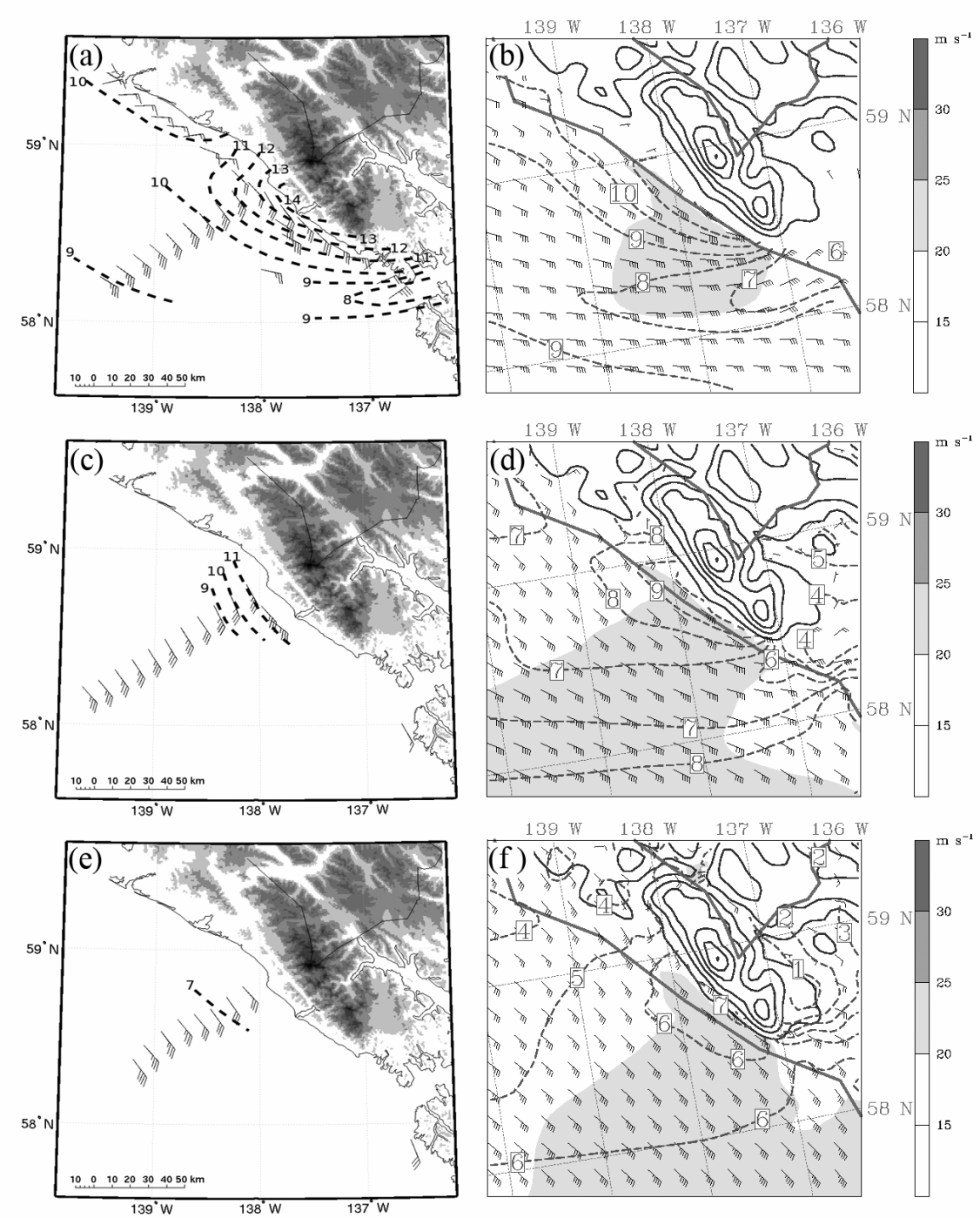

Figure 3.12. Winds (full barb = 5 m s-1) and temperatures (dashed every 1 ^{o}C) at 150 m ASL for the (a) observations during flight 1 of IOP7 and (b) 4-km MM5 at 1900 UTC 13 October 2004. The model winds are shaded (every 5 m s^{-1}) and terrain is contoured. (c) and (d) same as (a) and (b) except at 500 m. (e) and (f) same as (a) and (b) except at 1000 m

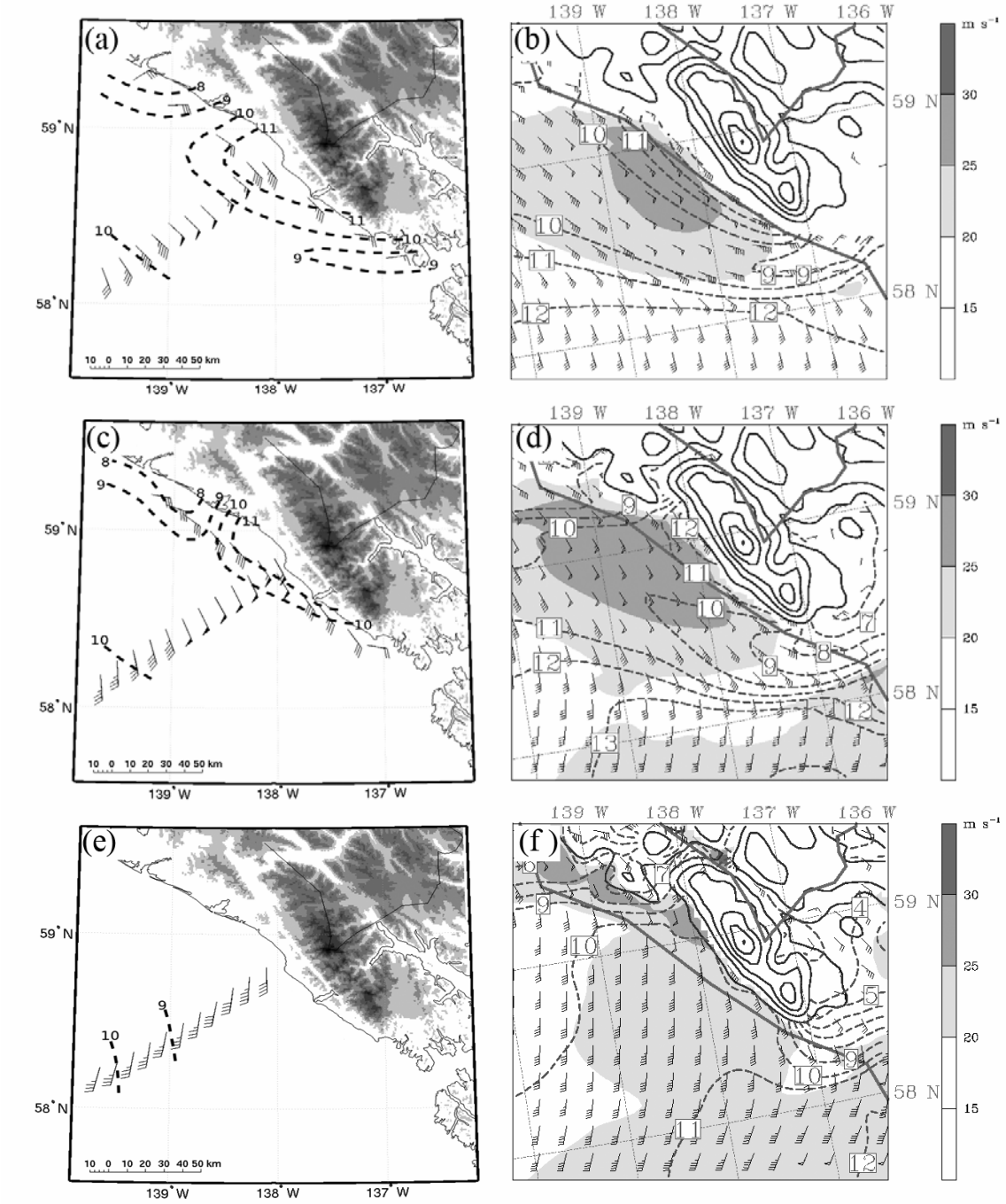

Figure 3.13 4-km MM5 winds (full barb = 5 m s^{-1}) and temperatures (dashed every 1 ^{o}C) at 150 m ASL for the (a) observations during flight 2 of IOP7 and (b) 4-km MM5 at 0100 UTC 13 October 2004. The model winds also shaded (in m s^{-1}) and terrain is contoured. (c) and (d) same as (a) and (b) except at 500 m. (e) and (f) same as (a) and (b) except at 1000 m.

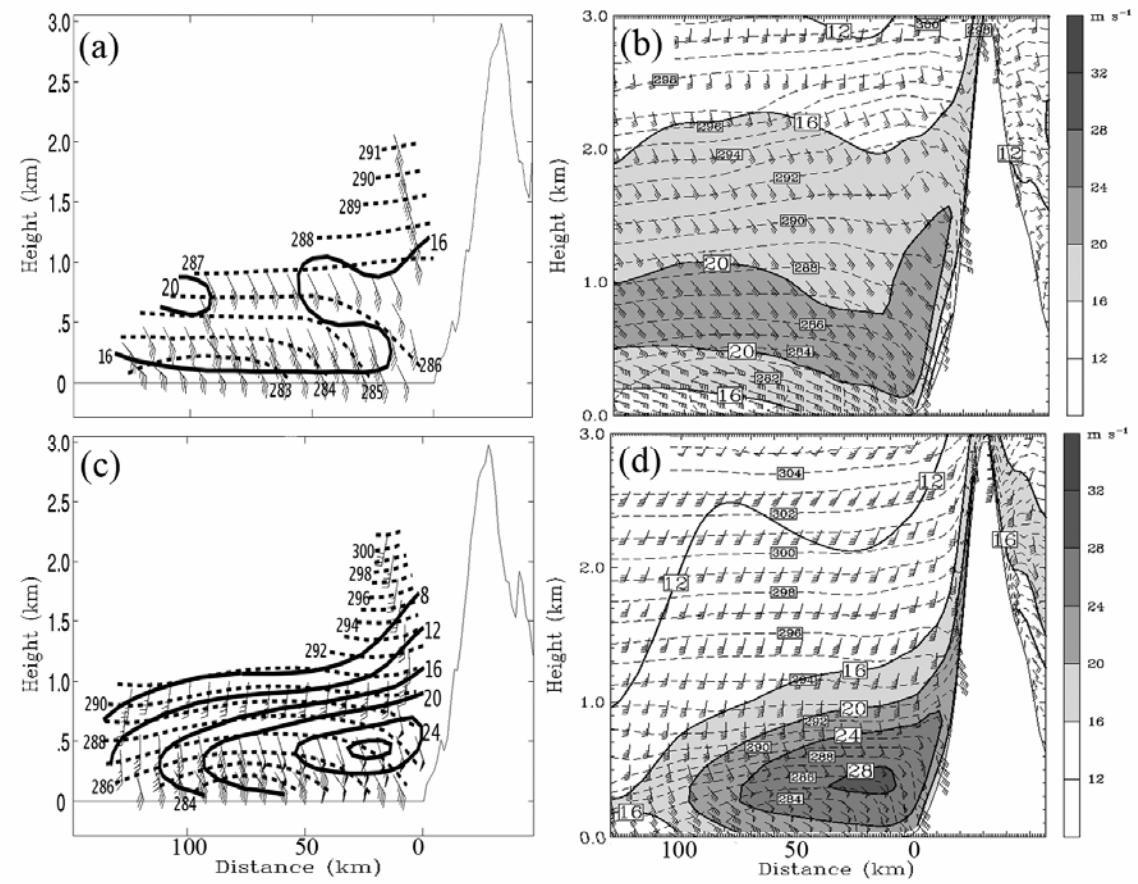

Figure 3.14 Vertical cross-section between C-E' showing winds (full barb = 5 m s^{-1}), terrain-parallel wind speeds (solid every 4 m s^{-1}), and potential temperatures (dashed every 1 K) for the (a) observations during flight 1 of IOP7, (b) 4-km MM5 at 1900 UTC 12 October 2004, (c) observations during flight 2, and (d) 4-km MM5 at 0100 UTC 13 October 2004. The model winds are shaded (every 4 m s^{-1}) and the terrain is shown.

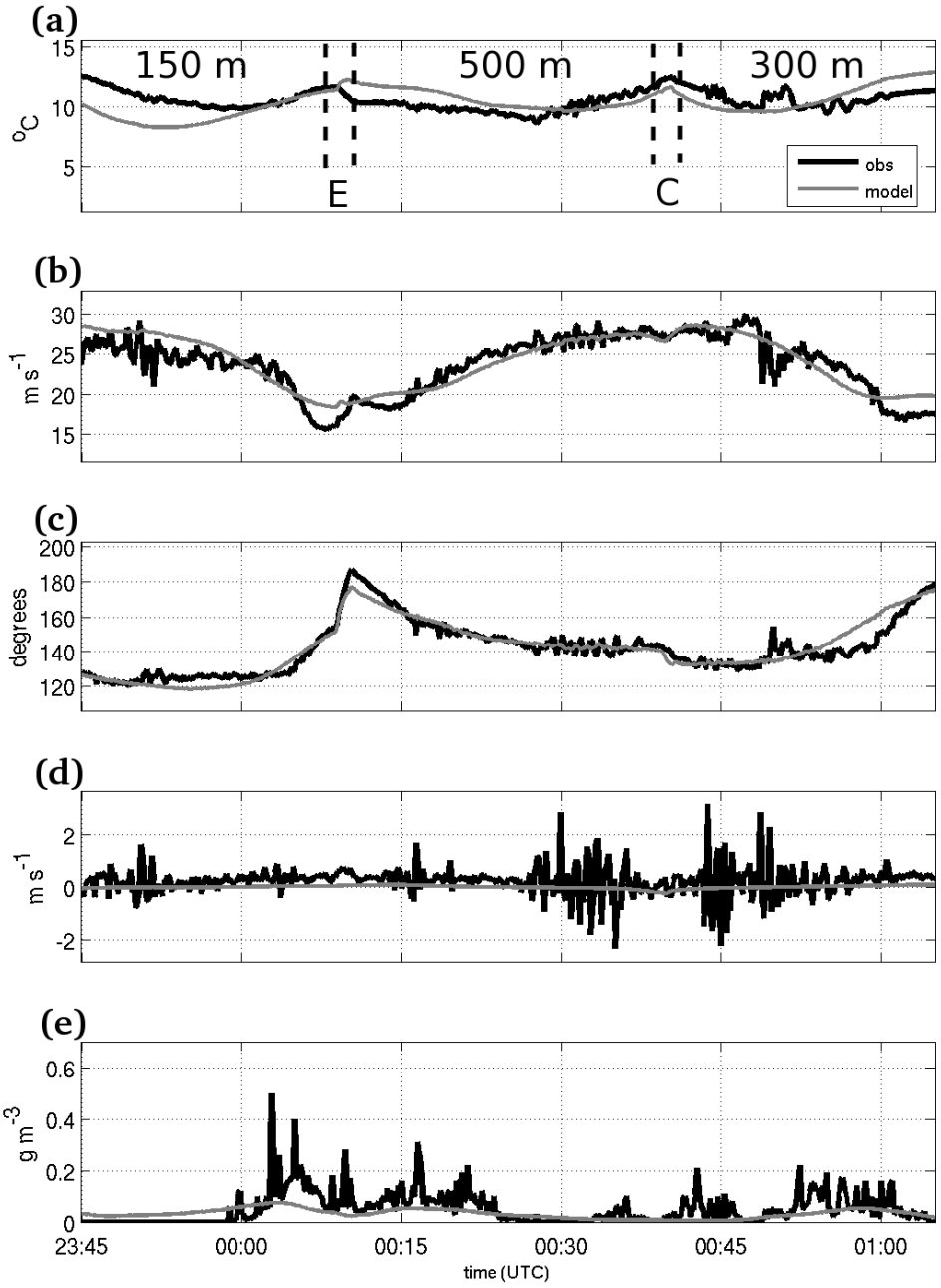

Figure 3.15 Same as Fig. 3.7, except for IOP 7 between C and E' during 2345-0110 UTC 12-13 October 2004.

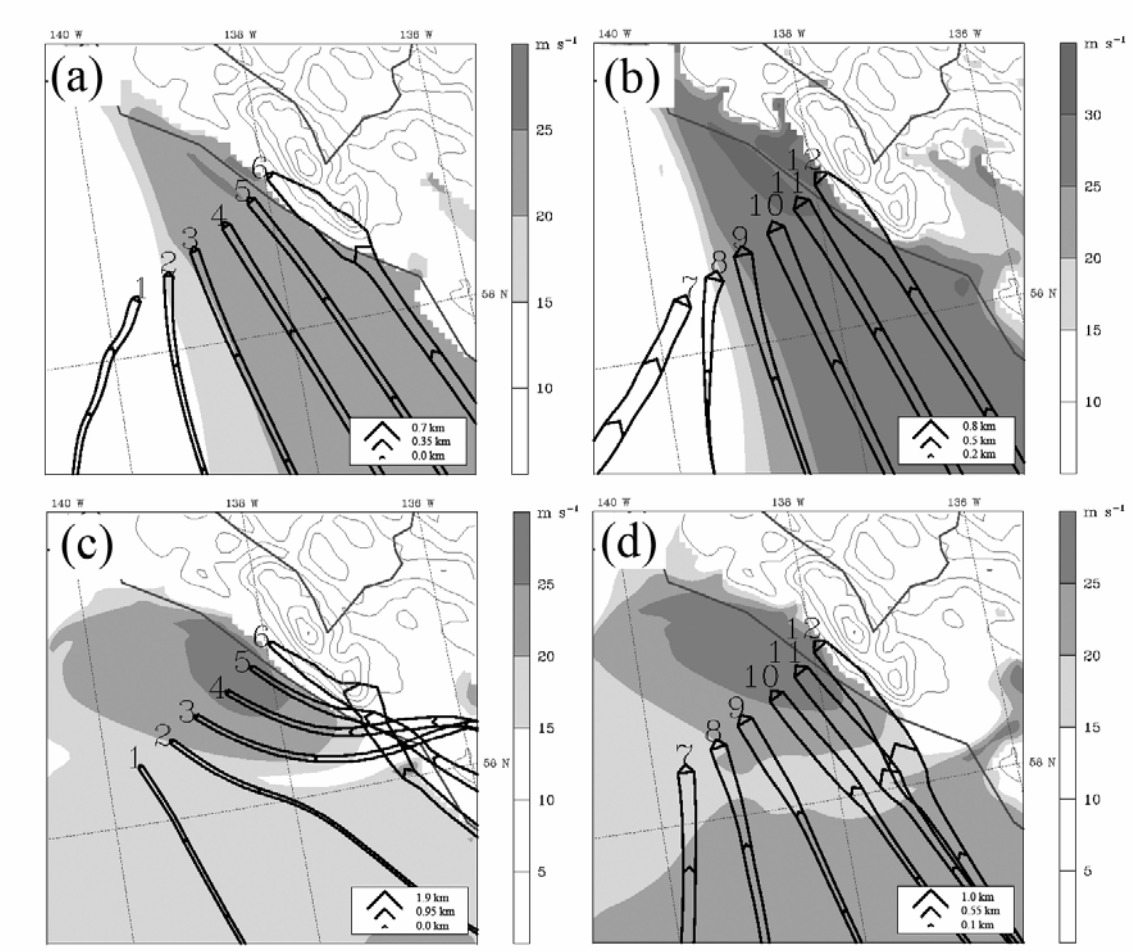

Figure 3.16 Backwards trajectories for IOP1 released at 2100 UTC September 2004 at (a) 150 m ASL and (b) 500 m ASL and for IOP7 released at 0100 UTC 13 October 2004 at (c) 150 m ASL and (d) 500 m ASL. The height of the trajectory is proportional to the size of the width of the trajectory (spaced at hourly intervals), and wind speed is gray shaded (every 5 m s^{-1}).

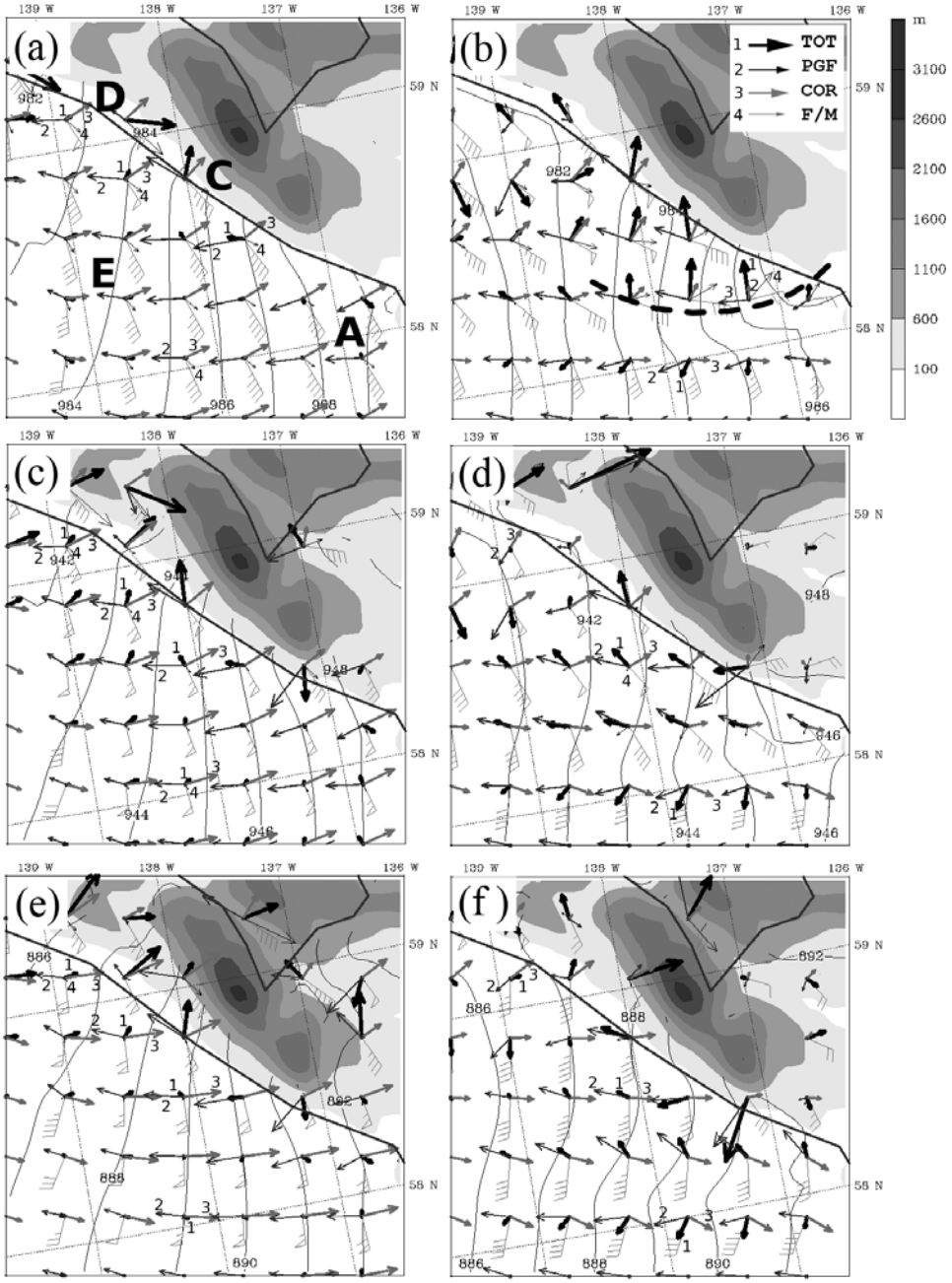

Figure 3.17 Momentum budget vectors for (a) IOP1 and (b) IOP7 at 150 m AGL, (c) IOP1 and (d) IOP7 at 500 m AGL, (e) IOP1 and (f) IOP7 at 1000 m AGL. Total acceleration (thick black), Coriolis (gray), pressure gradient (dark gray), and friction/mixing (thin black). The terms are numbered and labeled in a few areas. The dashed line in (b) represents the trajectory of the gap outflow.

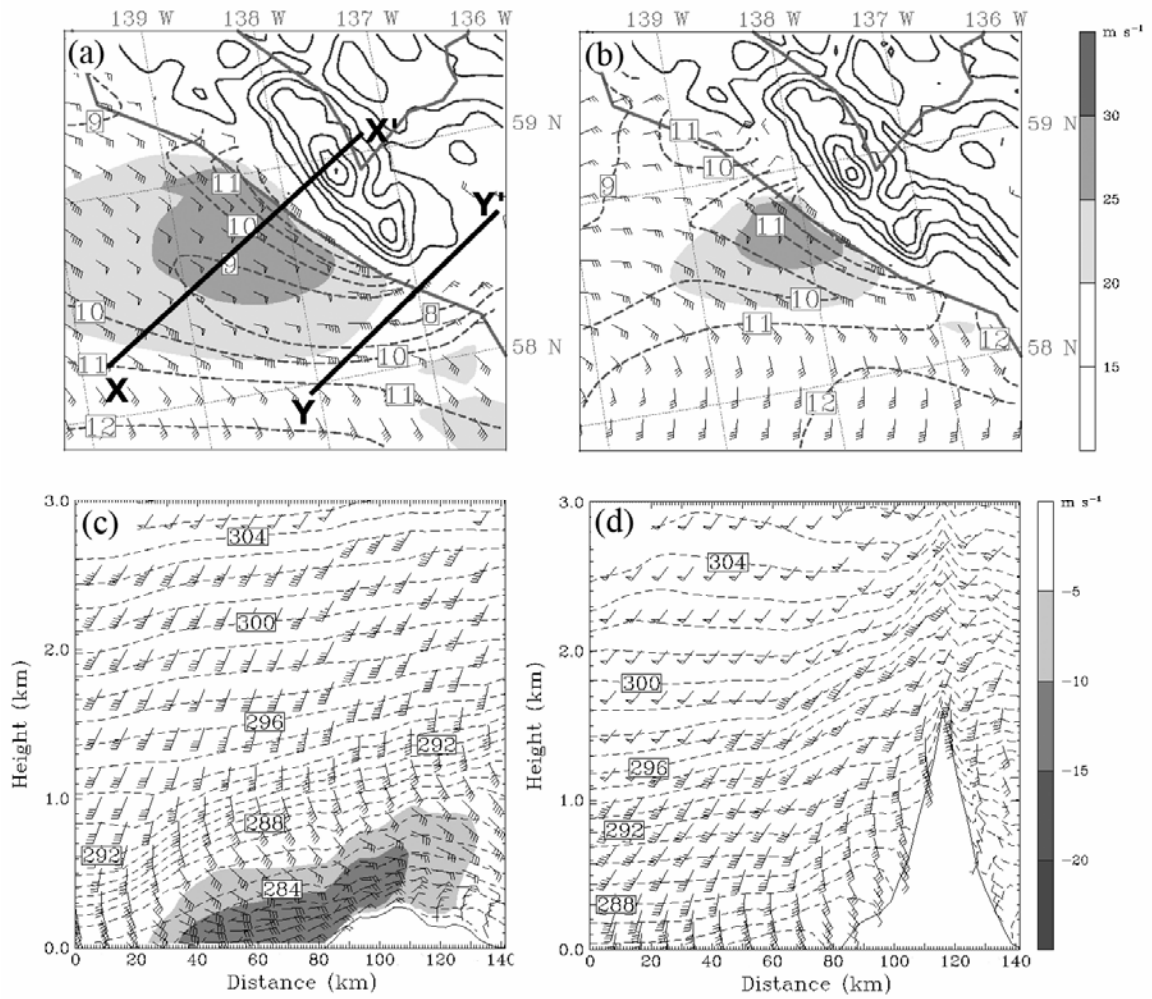

Figure 3.18 Comparison of control (a) CTL) and (b) NOGAP simulations showing the winds (full barb = 5 m s^{-1}) and temperatures (every 1 ^{o}C) at 150 m ASL. Cross-section YY' through Cross Sound of the coast-parallel wind speeds (shaded and barbs every 5 m s^{-1}) and potential temperature (every 1 K) for the (c) CTL and (d) NOGAP valid at 0000 UTC 13 October 2004. The location of Y-Y' is shown in (a).

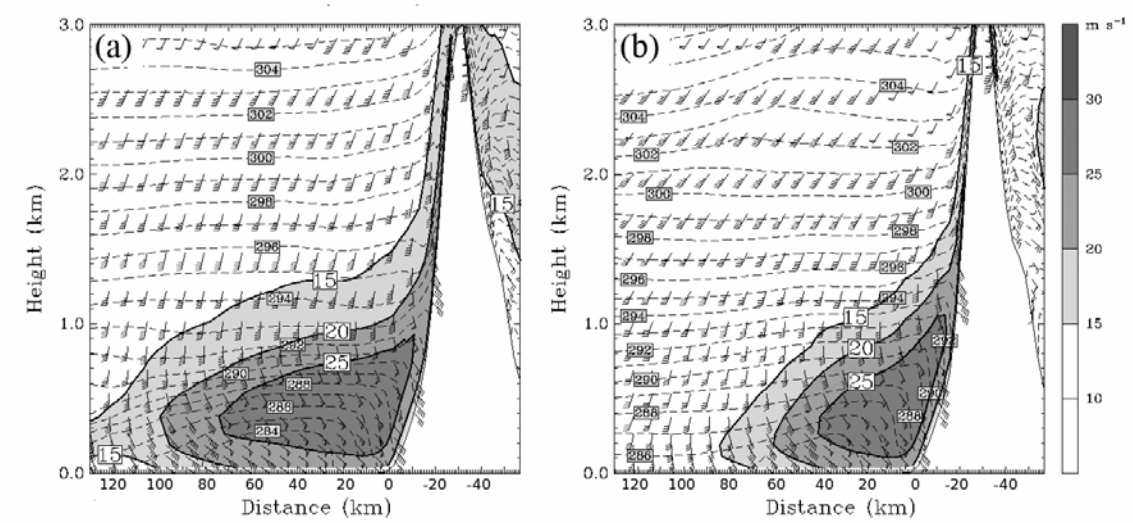

Figure 3.19 Cross section XX' showing the (a) CTL and (a) NOGAP simulations of terrain-parallel wind speeds (gray shaded every 5 m s^{-1}) and potential temperature (dashed every 1 K) at 0000 UTC 13 October 2004. The location of XX' is shown in Fig. 3.16a.

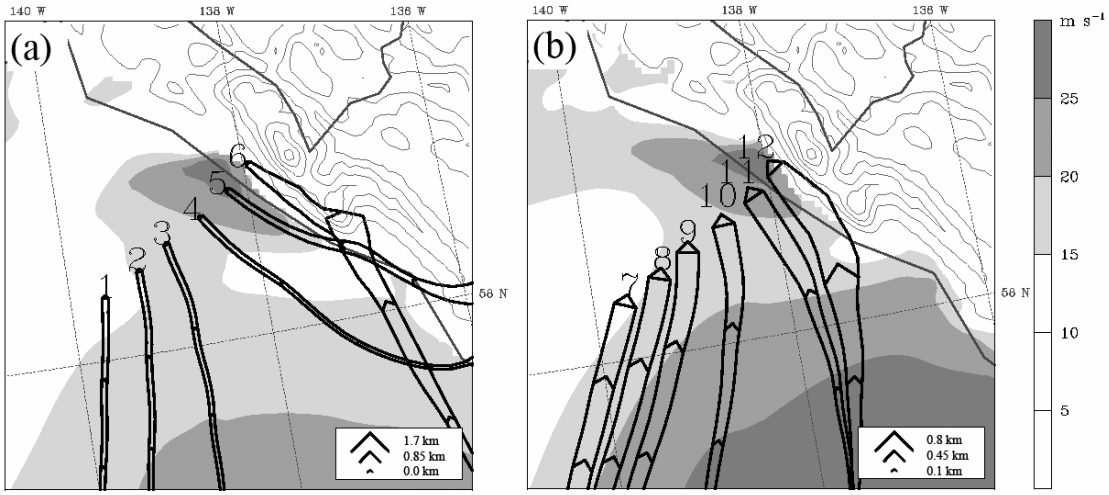

Figure 3.20 Backwards trajectories for the NOGAP experiment released at 0100 UTC October 2004 at (a) 150 m ASL and (b) 500 m ASL. The height of the trajectory is proportional to the width of the trajectories (spaced at hourly intervals). Wind speed is gray shaded (every 5 m s^{-1}).

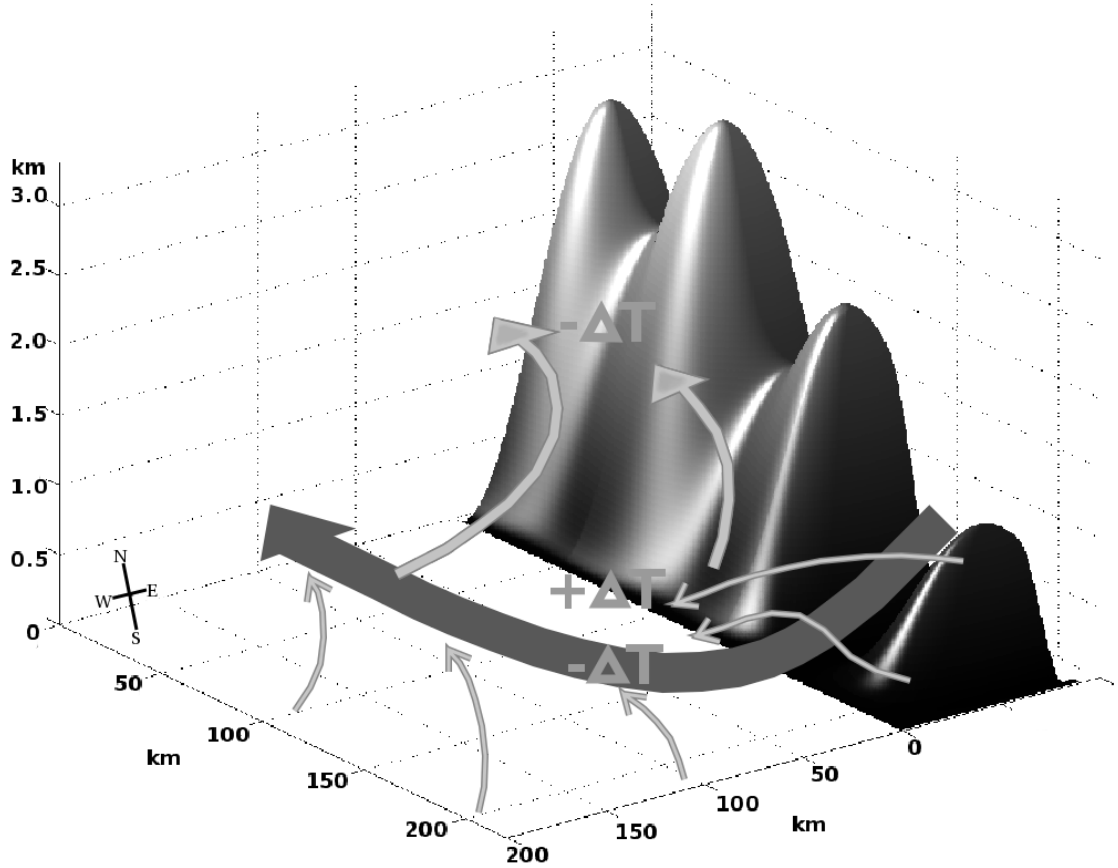

Figure 3.21 Conceptual model of the hybrid barrier jet near the Fairweather Mountains of southeastern Alaska. Thick dark gray arrow represents the gap outflow, medium thick arrows represent the 1000-1500 m flow, and the thin gray arrows represent the low-level flows. Temperature anomalies are denoted by "±ΔT".

Chapter IV:

Three-Dimensional Idealized Barrier Jet Simulations

4.1 Overview

The previous chapter detailed the structure and dynamics of classical and hybrid jets sampled during the Southern Alaskan Regional JETs Experiment (SARJET; Winstead et al. 2006). The generality of these results was extended with a suite of three-dimensional idealized simulations of barrier jets that span a large phase space of ambient conditions. Previous idealized studies of flow interaction with realistic coastal terrain have been performed over the orography of California (Cui et al. 1998), Norway (Barstad and Grønås 2005), Taiwan (Yeh and Chen 2003), and the Alps (Zängl 2005). Given the unique orographic setting of southern Alaska, with its inland plateau, steep coastal terrain, and many prominent coastal gaps, it needs to be determined how barrier jets evolve for different ambient conditions over this region. Using the idealized initial condition technique presented in chapter 2, a suite of three-dimensional simulations were performed to investigate the spectrum of "classical" and "hybrid" jets observed in the barrier jet climatology of Loescher et al. (2006) and the case studies in chapter 3. This study also aims to understand the impact of the broad inland topography of Alaska on the flow impinging towards the coast. Some questions that this study attempts to answer are:

* How does the structure of the barrier jets along the southeastern Alaskan Coast depend on the ambient wind speed, wind direction, stability, and terrain variability?
* How does the gap outflow impact the structure (width, height, and strength) of the coastal jets?
* What is the contribution to the structure of the coastal jet from the broad inland plateau versus the steep coastal terrain?

The next section discusses the model configuration and methods to measure the barrier jet properties. Section 4.3 compares selected idealized simulations to the case study simulations of chapter 3 in order to validate the idealized modeling approach. Section 4.4 addresses the large-scale response generated by the inland plateau. Sections

4.5 and 4.6 present the results for the classical and hybrid barrier jet simulations, respectively. Section 4.7 discusses the major findings and concludes.

4.2 Methodology

A set of three-dimensional idealized dry barotropic simulations on an f-plane (58 ^{o}N) was constructed over the Gulf of Alaska using the Penn State/NCAR MM5 version 3.7 (Grell et al. 1995). The three computational domains had horizontal grid spacings of 54-, 18-, and 6-km (Fig. 4.1) and were run using a one-way nest communication. The 54-km domain was large enough (>10,000 km wide), such that the fixed lateral boundary conditions would not impact the inner nest barrier jet solutions. The model domains were modified for idealized simulations by setting the map factors to unity and by removing the curvature terms (Holton 2004) from the momentum equations (Zängl 2003). Thirty-two vertical terrain-following sigma levels were used, with 14 levels below 700-hPa and a model top at 100 hPa. A 10- and 5-minute land-use and topography data set was utilized in the 54- and 18-km domains, respectively, while the 6-km domain used a 2-minute terrain dataset.

The model configuration included the Blackadar planetary boundary layer (PBL; Zhang and Anthes 1982) scheme to parameterize the frictional and turbulent processes. All land-surface values were configured as either water or coniferous forest. The surface fluxes of heat and moisture were turned off. All runs were dry, with no convective or microphysical parameterizations and no radiative processes. Horizontal diffusion was calculated on height surfaces (Zängl 2002) to help preserve vertical potential temperature gradients in mountainous regions. Klemp and Durran's (1983) upper-radiative boundary condition was used in order to prevent gravity waves from being reflected off the model top.

The initial and boundary conditions for the 54-km domain were created with the MM5 initialization approach described in chapter 2. Although the scheme was originally designed for initializing a baroclinic wave, it can also specify barotropic basic states without a wave perturbation (chapter 2, section 3). All simulations were initialized with straight barotropic flow, a constant stratification in the troposphere, and a tropopause initialized at 8.5 km above sea level (ASL).

An inland cold pool was initialized for select runs over the land grid points within a 1000 km radius of 59^{o} N, 138^{o} W, and the cold pool linearly decreased to zero at a 2000 km radius (Fig. 4.1). The cold pool had magnitudes of -5, -10, and -15^{o}C below 1 km and decreased linearly to zero at 2 km (Fig. 4.2), which encompasses the ~-8^{o}C cold anomaly found in the hybrid jet composite events at Whitehorse, Yukon Territory (Colle et al. 2006). Table 4.1 lists the simulations used for this study. The ambient wind speeds were incremented every 5 m s^{-1} from 10 to 25 m s^{-1} and the wind direction every 20 degrees from 160^{o} to 220^{o}, which corresponds to ~25^{o} to 85^{o} from coast-parallel. The static stability was incremented every 0.005 s^{-1} from N = 0.005 to 0.015 s^{-1}. All simulations were started impulsively with the ambient flow and run out 48 hours. Since the flow features during the early simulation period may be dependent on the startup procedure (Smolarkiewicz and Rotunno 1989a), only hours 12-48 were used in the analysis.

Characteristic barrier jet properties, such as width, height, and wind speed enhancement were measured for each simulation adjacent to the Fairweather Mountains (Fig. 4.3), which is the same study area for chapter 3. These properties were measured within the cross-sectional volume A-A' (dashed area in Fig. 4.3), which extends 100 km along the coast and ~400 km offshore, and includes the lowest 14 sigma levels (~2.7 km ASL). The barrier-parallel wind speed was first averaged along NW-SE sections within A-A' to obtain mean cross-barrier profiles of the jets. Barrier jet characteristics were then determined from this averaged A-A' cross-section.

The *offshore extent* of the barrier jet is defined as the horizontal distance over which the maximum barrier-parallel wind speed decreases by a factor of e^{-1} on either side of the jet maximum normal to the coast (Fig. 4.3)[5]. When the inner edge of the jet is located over the slope of the barrier, the base of the windward slope is taken as the position of the inner edge of the jet. If both the jet maximum and the inner edge are located over the slope, then the offshore extent is taken as the distance between the base of the windward slope and the offshore *e*-folding distance. The *barrier jet height* is the height of the maximum terrain-parallel wind speed in cross-section A-A'. In order to compare results with previous theoretical studies of barrier jets (Pierrehumbert and Wyman 1985; Braun et al. 1999a,b), the *wind speed enhancement* is determined by dividing the maximum barrier-parallel wind speed perturbation in A-A', which is defined as $v' - V_0$ (where v' is the maximum barrier-parallel wind speed and V_o is the initialized barrier-parallel wind speed), by the initialized barrier-normal wind speed U_n.

Previous case studies of Alaskan barrier jets related jet properties (enhancement, offshore extent, and height) to upstream conditions a few hundred kilometers upstream of the barrier (Loescher et al. 2006; Olson et al. 2007). Therefore, the simulated jets in our study are sometimes plotted as a function of the immediate upstream conditions within the box U (Fig. 4.3). This upstream box was positioned according to the ambient wind direction, such that a forward trajectory released from box U at 500 m ASL would approach the southwestern slopes of Mt. Fairweather. Since field studies can often only sample the local region, this will help relate the idealized results in the paper to the observations.

4.3 Comparison with SARJET case studies

In order to show the capability of the idealized simulations in predicting realistic coastal flows, two examples are presented that have similar ambient conditions as the two SARJET case studies presented in chapter 3. Hour 12 of the idealized runs were used for comparison, since this was the approximate time period for which these jets developed with the ambient conditions in chapter 3. Note that this with will miss the full large-scale contribution of the plateau to the barrier jet strength (Braun et al. 1999a).

a. IOP1: Classical barrier jet.

IOP1 (2000 UTC 26 September 2004) had south-southeasterly winds of ~25 m s^{-1} at 500 m ASL along the Fairweathers that preceded a weak surface trough located ~150 km offshore (Fig. 4.4a). This event was subsaturated at this time (RH ~90%), with dry *N*

[5] The barrier-parallel component was used as opposed to the total wind speed to keep consistent with the barrier-parallel jet definition used in Loescher et al. (2006).

of ~0.01 s^{-1} in the lowest 2.5 km ASL. An idealized simulation consisting of ambient wind speeds of 25 m s^{-1} initialized with southerly (180°) flow and N = 0.01 s^{-1} was chosen to compare with this IOP. A south wind was chosen instead of south-southeast, since the large-scale flow adjustment to the inland terrain and Ekman layer spin-up resulted in a turning the offshore flow at point U to more south-southeasterly by hour 12 (Fig. 4.4b). The 500-m wind speeds in both simulations show an increase from 25-27 m s^{-1} (upstream of the barrier) to ~30-33 m s^{-1} (along the western slope of the Fairweathers) with a ~15° cyclonic deflection of the low-level winds (Figs. 4a,b). The strong winds further offshore in the IOP were associated with the approaching surface trough, which cannot be duplicated in the idealized approach.

A vertical cross-section taken along A-A' (Fig. 4.4c,d) shows the terrain-parallel wind speeds and potential temperatures through the barrier jet. The jet is ~1 m s^{-1} stronger in the idealized case and it is ~20-50 km wider than the IOP jet, since the approaching trough shortened the offshore extent of the IOP1 jet (cf. Fig. 3.7b,d). The development of the well-mixed boundary layer in the idealized simulation results in a deeper boundary layer than observed in IOP1, thus resulting in ~100 m higher placement of the jet maximum. Overall, the wind speed enhancement, jet height, and width were realistically duplicated despite the lack of full physics.

b. IOP7: Hybrid barrier jet.

IOP7 (2200 UTC 12 October 2004) featured an approaching weak trough towards the seaward edge of a gap outflow (southwest of the Fairweathers), with south-southeasterly flow of ~15 m s^{-1} farther offshore to the southwest (Fig. 4.5a). The average relative humidity below 1000 m ASL was ~90%, with a dry static stability of ~0.008-0.015 s^{-1}, and there was a ~15 °C difference at the surface across the coastal mountains (Fig. 3.8a). An idealized simulation for comparison consisted of ambient wind speeds of 15 m s^{-1} initialized with south-easterly flow at 160°, N = 0.01 s^{-1}, and an inland cold pool with a magnitude of –15 °C up to 1000 m ASL (Fig. 4.5b). The maximum winds at 500m ASL in both simulations are ~28 m s^{-1} southwest of the Fairweathers, approximately 50 km offshore (Figs. 4.5a,b). A vertical cross-section taken along A-A' (located in Fig. 4.3) shows that the jet maxima are located ~500 m ASL and decay rapidly above 1000 m ASL, with the coldest temperatures located ~50 km offshore (Figs. 4.5c,c).

4.4 Large-scale flow response

The impact of the broad inland terrain on the low-level flow approaching the Alaskan coast was investigated, since Braun et al. (1999) showed using two-dimensional idealized simulations that a plateau-like barrier can produce a far upstream flow response. In order to understand the broad terrain impact, we first examine the spatial and temporal development within the outer 54-km grid. Figure 4.6 shows the sea-level pressure perturbation at hour 24 for simulations initialized using a background wind speed of 10 m s^{-1}, N = 0.01 s^{-1}, and wind directions of 220° (Fig. 4.6a) and 160° (Fig. 4.6b). A sea-level pressure perturbation of 15-23 mb developed along the windward edge of the Alaskan-Canadian coastal region for the 220° simulation, while a 10-14 mb perturbation occurred for the 160° simulation. This difference results from the greater cross-barrier flow and upslope (adiabatic) cooling in the 220° simulation than the 160° run. However,

simulations with the same U_n (defined at the Fairweathers), but different wind speeds and directions, may still produce a different large-scale response since U_n will be different almost everywhere else along the concave-shaped coast of Alaska. This was verified by comparing a 160° run with 25 m s^{-1} winds (same U_n of 10 m s^{-1} at the Fairweathers as the 220° run), which resulted in similar maximum pressure perturbations of ~20 mb over south-central Alaska, but large differences southeast of the Fairweathers (Fig. 4.7). Hence, the two-dimensional theory of barrier jets for plateau-like barrier of Braun et al. (1999) cannot be expected to completely capture the variations associated with changes in wind direction over irregularly shaped broad barriers.

The wind speed perturbations extend throughout the depth of the troposphere (~8km) (Fig. 4.8a), while the surface pressure perturbations decay by e^{-1} upstream of the coast over a Rossby radius, $L_R=NH/f$ ~700 km., where H ~ 8 km ASL is the approximate e-folding vertical depth of the upstream wind (and pressure) perturbation. The wind speed perturbation also extends much higher in the troposphere for the 220° simulation (Fig. 4.8a) compared to the 160° simulation (Fig. 4.8b). The impinging flow is decelerated and deflected cyclonically by this offshore pressure perturbation in the 220° simulation, which produces a terrain-parallel component of ~4 m s^{-1} ~1000 km upstream of the coast. The maximum positive sea-level pressure perturbation in the 160° simulation is positioned ~600 km downstream (northwest) of the Fairweathers, such that the perturbation circulation is easterly over the Gulf of Alaska (Fig. 4.6b). Since this large-scale perturbation has a component that superimposes onto the south-southeasterly ambient (initialized) flow, there is a 2-4 m s^{-1} terrain-parallel wind speed enhancement extending ~500 km offshore from the Fairweathers (Fig. 4.8b). The perturbation winds in the 220° simulation are approximately orthogonal to the initialized flow, thus only the flow perturbation induced by the terrain contributes to the barrier-parallel wind speeds at the coast.

The same simulations were performed with no inland terrain (NIT) specified >500 km east of the Pacific Coast, in order to quantify the upstream influence without the full inland plateau. The sea-level pressure perturbation for the 220° NIT run was nearly half as large as the 220° control run (Fig. 4.6c) near the Fairweathers, but it only decreased by ~30% for the 160° NIT run (Fig. 4.6d). The smaller change in 160° simulations was from the weaker change in the cross-barrier flow component (to be shown later) and resulting windward terrain perturbation. The wind speed perturbations decay faster upstream of the coast in the 220° NIT run (Fig. 4.8c) as compared to the full terrain 220° run (Fig. 4.8a), with the 2 m s^{-1} contour reaching nearly 3000 km upstream in the control, while only ~500 km in the NIT run. Overall, the inland terrain of the Pacific Cordillera can cyclonically rotate the winds cyclonically well upstream, thus adding to the barrier jet momentum approaching the coast.

Backwards trajectories released from the coast at hour 24 for the 220° wind direction with and without the inland terrain more clearly illustrates the impact of the inland terrain on the upstream flow (Fig. 4.9). Both simulations develop strong blocking at 500 m ASL in the vicinity of the coast (Fig. 4.9a,b), which agrees with the linear theory (Pierrehumbert 1984; Braun et al. 1999a), which shows that the mountain height and slope are responsible for the immediate upstream blocking. However, the flow ~1000 km upstream of the barrier became more southerly in the control (full terrain) run (Fig. 4.9a), and any additional accelerations near the coast had a component in the same

direction as the impinging flow, thus resulting in wind speeds exceeding 20 m s^{-1}. In contrast, the trajectories in the NIT run were more orthogonal to the coast and there was less total wind speed enhancement (Fig. 4.9b). Strong blocking was also present at 1000 m ASL in both runs (Fig. 4.9c,d), but once again, the large-scale flow response from the inland terrain in the control run accelerated the flow in a more coast-parallel direction than the NIT run. At 2000 m ASL (Fig. 4.9e,f), very little blocking is evident in the NIT run (Fig. 4.9f) as compared to the control run (Fig. 4.9e) suggesting that the stronger mountain anticyclone increases both the horizontal and vertical extent of the blocking. However, the near-coast blocking appears to be similar between the control and NIT.

The impact of the large-scale pressure perturbation on the upstream flow is shown in the evolution of the wind direction within the upstream box U (bottom of Fig. 4.3) averaged over the lowest 2 km, where a rapid ~12-20^o cyclonic change over the first six hours followed by a slower ~5-10^o rotation over the final 36 hours of the simulations, in agreement with Braun et al. (1999a) (Fig. 4.10). Some of the rapid cyclonic change is attributable to the development of Ekman layer, which alters the relevant U_n used for calculating *Fr* when quantifying the potential for flow blocking. The greatest wind direction changes (24-36^o) over the 48 h period occurred with the largest static stability (N = 0.015 s^{-1}; black lines) and the most terrain-normal flow (220^o). Upslope (adiabatic) cooling in more stable conditions result in larger temperature (and pressure) perturbations over the mountains. The acceleration induced by the stronger large-scale mountain anticyclone for this simulation was oriented more orthogonal to the initialized wind vector (Fig. 4.6a), resulting in a larger influence on the upstream wind direction. Thus, some of the total *v'* generated along the coast may be attributable to the large-scale adjustment, which is dependent on the ambient wind direction.

The influence of wind direction on the barrier-parallel wind speed enhancement (*v'*) is shown as a function of barrier-normal velocity U_n (Fig. 4.11). Panel (a) shows the total *v'*, in which the largest wind enhancements are associated with the most barrier-normal wind direction (220^o). For the same U_n ~10 m s^{-1}, there is a ~8 m s^{-1} difference in the overall wind enhancements for different wind directions. In an attempt to quantify the contribution of the large-scale mountain anticyclone to this total enhancement, the *v'* measured at a point 500 km offshore (point X in Fig. 4.3) is plotted in figure 4.11b. As expected, the 220^o simulations produce the largest enhancements well outside the coastal region. Since the *v'* measured 500 km offshore can safely be associated with the mountain anticyclone, the difference between the total *v'* and the *v'* measured at point X can be interpreted as the additional coastal acceleration. Figure 4.11c shows an approximately same enhancement within the coastal zone for all wind directions for a given U_n, except when the flow becomes oriented parallel to the coast. Note that the NIT runs with initialized wind speeds of 10 m s^{-1} at various wind direction are also included for comparison (see * symbols in Fig. 4.11). The *v'* generated for all NIT runs are similar in magnitude (7-9 m s^{-1}), which further suggests that the influence of the wind direction impacts the total *v'* through changes in the large-scale flow perturbation associated with the inland terrain.

The structure of *v'* for flows initialized with the same U_n = 10 m s^{-1} is shown in Fig. 4.12. The influence of wind direction on *v'* is large between the run with initialized wind speeds of 10 m s^{-1} at 220^o (Fig. 4.12a) and that with wind speeds of 25 m s^{-1} at 160^o (Fig. 4.12b). The *v'* = 4 m s^{-1} contours extend >300 km offshore for both runs, but the

maximum *v'* is roughly halved for the 160° simulation. For wind direction for 160°, the development of a mountain anticyclone combined with frictional turning results in flow oriented parallel to the barrier (U_n ~0) (Fig. 4.13d), whereas the other wind directions maintain a nonzero U_n with larger pressure perturbations. Thus, the upslope adiabatic forcing is diminished in the 160° run, resulting in a limiting growth of the mountain anticyclone and a weaker terrain-parallel flow enhancement. However, the coastal barrier jet in the 160° run is just as strong as the 220° run, but this is because the jet in the 160° run receives most of its momentum from the ambient southeasterly flow.

The strong influence of the broad inland terrain is illustrated for simulations with the same initialized wind speeds of 10 m s^{-1} at 220° (same U_n), but with the full terrain (Fig. 4.12a) and the NIT run (Fig. 4.12c). The much weaker enhancement (~ 6-7 m s^{-1}) for the NIT run suggests that the broad mountains of the Pacific Cordillera are capable of producing much stronger barrier jets than thinner ranges, such as the Andes, which is consistent with the results of Braun et al. 1999a.

Clearly, the above analysis indicates that the "ambient flow" at box U (cf. Fig. 4.10), which is typically measured a few hundred kilometers offshore of the coast in many previous studies along the West Coast (Overland and Bond 1995; Braun et al. 1997; Colle et al. 2002; chapter 3; among others) does not really represent the flow unperturbed by terrain, but rather this flow is strongly impacted by the larger-scale broad mountain response, which acts to turn the flow more coast parallel much farther offshore than the standard definition of a Rossby radius ($L_R = Nh_m/f$). A larger offshore-directed pressure gradient force associated with a larger mountain anticyclone helps to extend the upstream blocking while the superimposed large-scale circulation enhances the barrier-parallel flow. The next sections look at this coastal response in more detail.

4.5 Classical barrier jet simulations

The classical barrier jet simulations listed in Table 4.1 (columns 1-3) include Froude numbers of 0.15 to 1.95. The barrier jet structures evolved throughout the 48-h simulation are illustrated in a hovmöller diagram constructed along A-A' (Fig. 4.3), showing the terrain-parallel wind speed and barrier jet height for a representative simulation initialized with southerly flow of 15 m s^{-1} (U_n ~ 10 m s^{-1}) with a static stability of N = 0.01 s^{-1} (Fig. 4.14). As shown by Braun et al. (1999), there is a period of rapid adjustment during the first 12 hours as the terrain-parallel wind speed increases to ~22 m s^{-1}, followed by a slower speed increase and continued jet widening through hour 48. Since the growth of the barrier jet strength and height modulations after hour 24 are relatively small, hours 24-48 are used to diagnose the jet properties as a function of ambient conditions.

a. Wind speed enhancement.

Figure 4.14 shows the terrain-parallel wind speed enhancement as a function of N and U_n (Fig. 4.15a), wind speed (Fig. 4.15b), and wind direction (Fig. 4.15c)[6]. As before,

[6] U_n is the mean barrier-normal component between the surface and 2.5 km ASL measured ~2000 km offshore in the 54-km domain in order to avoid the influence of the mountain anticyclone, but capture the changes due to the Ekman layer spin-up. In contrast, the "ambient" wind speeds and direction were measured in upstream box U.

the wind enhancement is defined as the change in the barrier-parallel component relative to the initialized barrier–normal wind speeds, which allows a direct comparison with other idealized studies (Pierrehumbert and Wyman 1985; Braun et al. 1999). The largest wind speed enhancements (~1.9) were associated with Fr ~0.3-0.4 (Fig. 4.15a). The barrier-normal velocity component, U_n, and total wind speed, U_{total}, were negatively correlated (-0.54 to -0.66) with the simulated wind speed enhancement, while N had a positive correlation of 0.75 (Table 4.2). This suggests that wind speed enhancement scales as $\sim Nh_m/U_{total}$, which is similar to the non-dimensional mountain height (Smith 1979), but total wind speed is used instead of U_n. The correlation between the simulated wind speed enhancement and Nh_m/U_{total} is 0.76 with an R-squared value of 0.58.

Figures 4.15b,c show that the largest barrier-parallel wind speed enhancements (normalized with respect to U_n; v'/U_n) are associated with weak wind speeds (< 15 m s^{-1}) and wind direction (at upstream box U) from ~170°, respectively[7]. This result occurs because lower momentum flow can more easily become blocked, deflected, and subsequently accelerated in a terrain-parallel direction for quasi two-dimensional terrain. The optimal wind direction for wind speed enhancement is ~170°, because the wind speed enhancement is approximately a sum of the mountain anticyclone and the coastal flow that is accelerated down the along-barrier pressure gradient. The flows oriented more normal to the coast (at 200-230°) have the largest terrain-parallel accelerations, but also have the largest U_n. On the other hand, flows oriented more parallel to the coast (130-160°) have a small U_n, but receive little or no acceleration down the large-scale pressure gradient and less contribution by the weaker mountain anticyclones. Intermediate wind directions (160-200°) can result in barrier jets produced by a superposition of blocked flow accelerating down the along-barrier pressure gradient as well as the mountain anticyclone, with moderate barrier-normal velocities (U_n ~ 5-15 m s^{-1}).

The impact of wind direction versus ambient wind speed on the coastal wind speed enhancement was examined further for simulations that had the same terrain-normal wind speed component (U_n ~10 m s^{-1}) and stability (N = 0.01 s^{-1}), but different initialized wind directions (10 m s^{-1} at 220° versus 15 m s^{-1} at 180°) (Fig. 4.16). The maximum total wind speeds enhancements for the 220° simulation versus the 180° simulation was ~6 and ~12 m s^{-1}, which was associated with a similar total wind speed enhancements (V_{max}/V_0; where V_{max} is the total horizontal wind speed and V_0 is the initialized total wind speed) of ~1.6 and ~1.7, respectively (Fig. 4.16a,b). However, the enhancement of the barrier-parallel winds for both runs (Fig. 4.16c,d) has a similar maximum (~12 m s^{-1}), although the offshore extent of the enhanced winds was larger for the 180° run. The large-scale mountain anticyclone in the 180° simulation remains strong enough to enhance the barrier-parallel, such that the far offshore (>300 km) portion of the 6-km nest experiences a wind speed enhancement of 2-3 m s^{-1} near 500 m ASL. This resulted in an increase in the width of the region of enhanced winds for the 180° simulation (Fig. 4.16d) compared to the 220° simulation (Fig. 4.16c). Thus, if the most barrier-parallel oriented wind directions are omitted, simulations with the same U_n and N result in a similar wind speed enhancement. This suggests a much smaller impact on the

[7] If figures 4.15b and c are plotted against the initialized wind speeds and wind directions (not shown), the maximum wind speed enhancements are still found for weak initialized wind speeds, but the optimal wind direction becomes ~190°, as the same overall pattern shifts ~20°.

total barrier-parallel wind speed enhancements by changes in the large-scale perturbation associated with wind directional changes when the initialized wind directions are $\leq 45^{o}$ from barrier-normal.

b. Barrier jet width.

Figure 4.17 shows the total offshore extent as a function of Brunt-Väisälä frequency and U_n (measured > 2000 km upstream) (Fig. 4.17a) and wind direction (Fig. 4.17b). Both U_n and wind direction were negatively correlated with the offshore extent of the jet (-0.56 to -0.75) throughout the complete set of classical simulations (Table 4.2). This negative correlation of U_n with offshore extent implies that an increase in U_n will lead to a decrease in jet width. This finding is in contrast to previous studies (i.e. Overland and Bond 1995), which found that jet width was proportional to the cross barrier wind speed ($L = U_n/f$) for $Fr < 1$. This result will be discussed further in the following chapter. The effect of the larger onshore wind speed component is to decrease blocking, since more kinetic energy allows the flow to surmount the barrier, resulting in less jet development.

The relationship of jet width and wind direction (Fig. 4.17b) is very similar to that with U_n (Fig. 4.17a), suggesting that wind direction (as opposed to wind speed) is the primary factor in determining the relationship between U_n and the total jet width. The physical reasoning can be deduced from Figure 4.17, which shows examples of the barrier jet along section A-A' at hour 24 for four different wind directions using an initialized wind speed of 15 m s^{-1} and $N \sim 0.01$ s^{-1}. The jet width increases dramatically from ~50 km to ~250 km and the jet maximum moves offshore as the winds become more coast-parallel. As the wind is rotated from 220^{o} to 180^{o}, the "ambient winds", which are really a combination of the initialized basic state flow and the large-scale response, projects more onto the jet and increases the offshore extent of the enhanced winds. Also, the flow becomes more efficiently blocked, since the Fr decreases from ~0.6 to ~0.4 as the wind direction shifts from 220^{o} to 180^{o}; thus, there is more blocked flow that is accelerated down the large-scale pressure gradient. The jet remains wide as the wind direction is further rotated to 160^{o}, but the contribution of the acceleration down the along-barrier pressure gradient is weaker, resulting in a weaker jet core within a broad area of accelerated flow.

Stability has a moderate positive correlation with the total offshore extent of the jet (0.53 to 0.56) (Table 4.2) throughout the full set of simulations. This is not surprising, since increased stability increases blocking and favors jet development; however, the correlation is only modest because the total offshore extent stopped increasing for $N >$ 0.009 s^{-1} and small U_n (Fig. 4.17a) and/or more terrain-parallel wind directions (Fig. 4.17b). This was due to the weakening of the jet core (as noted in the above discussion of Fig. 4.16), which resulted in a smaller offshore *e*-folding distance of the jet as defined in section 4.2.

c. Barrier jet height.

The height of the barrier jets slowly increased during the first 24 hours of the simulation, but became steady over the remainder of the simulations (e.g. Fig. 4.14b). The jet height had a negligible correlation with the U_n measured > 2000 km upstream (0.03 to 0.11), but had significant correlations with the total wind speed (0.74 to 0.75)

and stability (-0.32 to -0.34) (Table 4.2), suggesting that the jet height scaled as U_{total}/N. This relationship is shown in Fig. 4.19a, in which low jet heights (< 400 m ASL) occur for low wind speeds and high stabilities. Since flow blocking and deflection is favored in the boundary layer (Chen and Smith 1987), and friction acts to dampen the surface winds, barrier jets are typically found at or near the top of the boundary layer (Braun et al. 1999b; Peng et al. 2001). This appears to be the case for the SARJET IOP1 classical jet case (cf. Fig. 3.7), which had the maximum winds in the vertical at or near the top of the well-mixed layer.

The depth of the boundary layer is driven in part by turbulent mixing, which will be greater as the wind speed increases and/or stability decreases. The influence of wind speed on the height of the jet is shown in simulations initialized with the same static stability (N = 0.01 s^{-1}) and wind direction of 180^o, but with incremented wind speeds of 10 m s^{-1}, 15 m s^{-1}, 20 m s^{-1}, and 25 m s^{-1} (Fig. 4.20). The jet maximum is shallowest (~ 500 m ASL) for the 10 m s^{-1} simulation and located at the coast (Fig. 4.20a), but becomes elevated and shifts over the slope of the barrier when the wind speed is increased to 15 m s^{-1} and 20 m s^{-1} (Figs. 4.20b,c). Further increasing the speeds to 25 m s^{-1} lifts the jet maximum to ~1200 m ASL (Fig. 4.20d).

The moderate correlations between jet height and wind direction (-0.44 to -0.52) suggest that rotating the impinging winds cyclonically to become more coast parallel results in a deeper jet. This is likely due to less blocking (stronger winds) for the more terrain-parallel directions, which allows for more mixing and a higher PBL height. This effect has been noted in other idealized studies (i.e. Barstad and Grønås 2005).

6. Hybrid barrier jet simulations

The hybrid barrier jet simulations were initialized with a constant static stability (N = 0.01 s^{-1}) and a 1000 m deep cold pool over the interior varying in magnitude from ΔT = -5 to -15^o C. (columns 1, 2, and 4 of Table 4.1). The simulations were initialized at upstream box U with Froude numbers of 0.2 - 1.0, but the Fr range increased to 0.2 - 3.0 after the well-mixed boundary layer developed. The stability for these simulations was measured in the 250-750 m ASL layer directly southwest of the Fairweathers, which encompasses the transition layer over the top of the gap outflow (Lackmann and Overland 1989; Overland and Bond 1995).

As for the classical barrier jet (c.f. Fig. 4.14), the hybrid jet with a ΔT=-15^{o}C underwent rapid development, increasing from ~12 to ~22 m s^{-1} by hour 12 (Fig. 4.21a); however, the position of the hybrid jet maximum is located ~50 km farther offshore than the classic jet at early stages. During the first 18 hours, the height of the jet maximum remain at ~450 m ASL (Fig. 4.21b), while the classical jet experienced a gradual increase in height from 300 to 450 m ASL (c.f. Fig. 4.14b). Meanwhile, the seaward edge of the hybrid jet was elevated (~600 m ASL) as ambient winds were lifted over the gap outflow. After hour 18, the hybrid jet began to move closer to the coast as the cold air over the interior became more shallow (< 500 m ASL; not shown), resulting in weaker gap outflow. Subsequently, the hybrid jet height rose to 700-800 m ASL as the gap outflow weakened (Fig. 4.21b). The last 24 hours of the simulation has a similar wind speed and jet width as the classical jet. Since the influence of the gap outflow on the hybrid jet is weak after hour 24, we will use hours 12-24 for the analysis below.

a. Wind speed enhancement.

Figure 4.22 shows the relationship between wind speed enhancement and U_n measure > 2000 km upstream (Fig. 4.22a), wind speed (Fig. 4.22b), and wind direction (Fig. 4.22c) for the 48 hybrid jet simulations. The greatest wind speed enhancement, as for the classical jets, were associated with weak (< 15 m s^{-1}) ambient flows (Fig. 4.22b), but the maxima shifted to a lower *Fr* (< 0.2) (Fig. 4.22a) and barrier-parallel wind directions near ~140^o (Fig. 4.22c). The onshore flow component, U_n, and the wind speed were both strongly negatively correlated with wind speed enhancement (-0.76 to -0.88), suggesting that low momentum flow (typically low *Fr*) favors enhancement (Table 4.3). The overall correlation between wind direction and wind speed enhancement was weak (-0.36 to -0.48), suggesting that a more terrain-normal flow favors a decrease in wind speed enhancement for hybrid jets. The cold pool strength had little influence on jet wind speed enhancement throughout most of the simulations, with correlations of < |0.18| (Table 4.3). This result is consistent with those for the SARJET IOP7 in chapter 3, in which a simulation with a filled coastal gap produced a jet of similar intensity as a simulation with the gap outflow.

The relative contributions of wind speed and wind direction for the hybrid jets were explored by examining the wind speeds at 500 m ASL (Fig. 4.23). The variations in the wind speeds > 300 km offshore result from the large-scale mountain anticyclone (section 4.4). The largest wind speed enhancement (~2.4) is found for relatively weak background flow (10-15 m s^{-1}) and coast-parallel wind directions (140-150^o) (upper left corner of Fig. 4.23). These conditions with the largest offshore-directed pressure gradient (top row of Fig. 4.23) generated the largest gap outflows, extending the total area of enhanced winds.

The cross-sections of terrain-parallel wind speed through A-A' also shows the influence of wind direction on hybrid jet structure (Fig. 4.24). Enhanced wind speeds of > 4 m s^{-1} extend more than 200 km offshore for wind directions ≤ 180^o, while the enhancement region is reduced by ~200 km when the flow is directed more onshore. For barrier-normal flows and winds ≥ 20 m s^{-1}, there is little gap outflow, and the jets appear more classical (cf. Fig. 4.20c,d).

b. Hybrid jet width.

The offshore extent of the hybrid jet was negatively correlated with the U_n measured > 2000 km upstream (-0.76 to -0.77) and wind direction measured in the upstream box U (-0.78 to -0.82) (Table 4.3). The phase lines of constant jet width are oriented nearly vertically for increasing U_n and wind direction versus static stability (Fig. 4.25a,b), which suggests that U_n and wind direction are important factors in determining the jet width. This is evident in Fig. 4.24 (top row) where simulations initialized with a wind direction of 160^o have wide jets, with jet maximums located offshore. The simulations with a larger U_n ≥ 10 m s^{-1} (bottom rows) have the hybrid jet maximum located closer to the coast because a strong U_n favors a downstream advection of mountain-induced perturbation and the downward mixing of onshore momentum into the gap outflow that further accelerates the jet toward the coast (chapter 3). The gap outflow in the hybrid jet simulations enhanced the total offshore extent for the most coast-parallel wind directions (140-160^o), since the large-scale pressure gradient can more effectively

accelerate the cold air through the coastal mountain gaps (Figs. 4.23 and 4.24). Therefore, wind direction is the most important factor in governing the occurrence of the gap outflows, which in turn have a profound impact on the total offshore extent.

The strength of the inland cold pool was a secondary factor in determining the barrier jet width, with an overall correlation with offshore extent of only 0.11-0.15 (Table 4.3). However, since gap outflows were more prevalent for conditions with coast-parallel flows, a significant correlation of 0.44 was computed for $Fr < 1$ during hrs 12-24. The effects of cold pool strength versus wind direction can be seen in Figs. 4.26 and 4.27, where the offshore extent is primarily a function of wind direction for all cases with flows oriented at angles $\geq 180^{o}$ (bottom three rows). For flows oriented at 160^{o}, the inland cold pool initiates gap outflow, which approximately doubles the width of the jet for a cold pool approaching -15^{o}C. In contrast, a pressure gradient orientated more coast parallel cannot accelerate the cold pool through the coastal gaps. This is consistent with the results of Zängl (2005), in which Alpine cold pool drainage was found to be highly sensitive to the ambient wind direction. The ambient wind speed was found to have a negligible influence on the hybrid barrier jet width, with overall correlations of < -0.35 (Table 4.3).

c. Hybrid jet height.

The range of hybrid jet heights (250 - 950 m ASL) were comparable to the heights measured in the classical barrier jet simulations (cf. Figs 4.19 and 4.28), since many simulations with the inland cold pool exhibited only weak gap outflows. Strong correlations existed between jet height and wind speed (0.81) and moderate negative correlations with wind direction (-.44 to -0.54). The combined effect of wind direction and wind speed can be seen in Fig. 4.24, where simulations with the largest wind speeds and most barrier-parallel wind directions have the highest barrier jets (upper right corner). These same conditions also dictated jet heights in the classical jet simulations; therefore, the cold pool did not strong strongly influence the height of the jet. This is consistent with the findings of the SARJET IOP7 study in chapter 3, where their sensitivity test with the filled gap produced a jet maximum at a similar height to the control simulation. However, in simulations with flows oriented in a more barrier-parallel direction, during periods of maximal gap outflow (hrs 6-18), the hybrid jet height was typically located at the top of the gap outflow (~ 450 m ASL) (Fig. 4.21b).

4.7 Discussion and conclusion

Three-dimensional idealized simulations with the MM5 were completed down to 6-km grid spacing over the southeastern Alaskan coast. The model was initialized with varying wind speeds, wind directions, and static stabilities for a set of classical barrier jet simulations, while an inland cold pool was initialized for the hybrid jet simulations. The diverse set of simulations produced a vast mixture of classical and hybrid barrier jets, with large variations of width, height, and intensity, which compare reasonably to previous observational studies (Schwerdtfeger 1975; Parish 1982; Marwitz 1982; Loescher et al. 2006; among others).

Loescher et al. (2006) showed that there was an approximate equal number of hybrid versus classical jets along the southeast Alaskan coast and that their maximum

wind speeds were comparable, while the hybrid jets have slightly larger jet widths. A jet width distribution from their climatology is shown in figure 4.29, in which median widths of ~50 km and ~60 km were calculated for the classical and hybrid jets, respectively. They found a tail in the distribution to ~250 km, but did not explain the causes of these variations. The simulations presented herein also show comparable maximum wind speeds and slightly wider jets for the hybrid runs. Our results suggest that the long (~250 km) tail in the distribution of jet widths in Loescher et al. (2006) (Fig. 4.29) may be explained by events with ambient winds oriented nearly terrain-parallel (~160^o) and strong static stability ($N > 0.01$ s^{-1}). For example, the 30 April 2000 event in their dataset had a width of 267 km and involved a southeasterly (~160^o) flow with wind speeds of 8 m s^{-1}.

As in Loescher et al. (2006), the jet width distribution of our simulations also show a slightly wider hybrid jet as compared to the classical jets (Fig. 4.30); however the median of the measured hybrid and classical jet widths were ~105 km and ~95 km, respectively, as compared to 50-60 km in Loescher et al. (2006). This difference may be due to a variety of reasons, such as: (1) dry simulations, which can not include the reduction in stability due to moisture processes[8]; (2) our focus on the barrier jets produced by the tall and steep Fairweather Mountains; (3) the straight idealized flows, which allow the flow response to approach steady state, whereas transient frontal systems are likely the dominant forcing in reality; or (4) the difference in the definition of a jet width, which they defined as the distance between the base of the windward slope of the mountain and the offshore edge of the barrier jet, defined as the point where flow reaches 1.25 times that of the ambient synoptic flow. Our definitions are equivalent when the ratio of the enhancement to the total ambient wind speed ($\Delta V/U_{total}$) = 0.25e = 0.68, but their definition could underestimate (overestimate) the jet width when $\Delta V/U_{total} <$ (>) 0.68. Since the widest jets occurred for wind directions of ~160^o, when there was only weak coastal acceleration down the large-scale pressure gradient, $\Delta V/U_{total}$ was typically < 0.68. Therefore, their definition may have underestimated the jet widths for the widest jets.

Although it was not shown, it should be noted that the particular definition of the jet width, using total wind speed as opposed to barrier-parallel winds, did not have a large effect on the results. The correlations between the jet width and the independent variables did not change more than ± 0.15 between the two different definitions; thus, all independent variables influenced the jet width approximately the same using either definition. However, there are two noteworthy effects that will alter the results: (1) the definition using the barrier-parallel component results in a non-zero offshore extent, since the mountains act to deflect the impinging flow even when $Fr > 1$. The definition using the total wind speed can result in zero widths for $Fr > 1$, since the total wind speed enhancements are typically very small (< 1.1) in this Fr range. Thus, the particular definition only affects the measured widths for large Fr, but has little or no effect on diagnosing the important parameters influencing the jet structure. (2) For wind speed enhancement defined as v'/U_n, the enhancements are larger for the hybrid jets that the classical jets, since conditions with terrain-parallel flow ($U_n < 5$ m s^{-1}) can result in strong gap outflows. This also acts to shift the maxima to lower Fr (<0.2) for cold pool

[8] If the simulations with measured static stabilities of $N \geq 0.012$ are excluded in Fig. 4.26, the median widths become 65 km and 69 km for the classical and hybrid jets, respectively.

simulations whereas the maxima was Fr ~0.3-0.4 for classical jets. If wind speed enhancement is defined with respect to the total wind speeds (i..e. Loescher et al. 2006), the maximum enhancements become similar for hybrid and classical jets.

The impact of the broad inland plateau was shown to rotate the upstream winds cyclonically to become more terrain-parallel 500-1000 km upstream of the coast. Simulations with the broad inland terrain removed resulted in less blocking and a weaker coastal barrier jet. The flow impinging on a wide barrier produces a time-dependent flow response, in which the mountain anticyclone begins to develop (hrs 0-12), but does not yet impact the flow well upstream of the coast. In this stage, the higher U_n creates a large pressure perturbation over the windward slopes and undergoes geostrophic adjustment within L_R of the barrier, resulting in a rapidly developing coastal barrier jet. After the large-scale circulation has developed (> 12 h), the far upstream flow is rotated cyclonically and develops a barrier-parallel component. Thus, a portion of the total geostrophic adjustment to the broad mountain already occurs by the time the flow is within L_R of the barrier, which develops a barrier-parallel component well upstream of the coastal region. Therefore, the large-scale mountain anticyclone acts to "precondition" the impinging flow for barrier jet development and the superimposed circulation of the mountain anticyclone on the accelerated coastal flow also acts to expand the region of enhanced barrier-parallel wind speeds. This reinforces the results obtained by the two-dimensional simulations of Braun et al. (1999a), which showed that barrier jets are stronger for flow over a plateau-like barrier, but our results expand on their results by showing that simulations with the same barrier-normal velocity, but different ambient wind direction, can slightly alter the barrier jet structures through changes in the large-scale response, which superimposing a terrain-parallel circulation onto the jet.

When the low-level ambient flow was nearly coast-parallel with an inland cold pool, offshore-directed gap outflows were initiated. This enhanced the offshore extent of the hybrid jets during periods of strong gap outflows, but had little effect after the inland cold pool was drained. The gap outflows also acted to shift the position of the jet maximum further away from the coast. In contrast, flows oriented more perpendicular to the coast (having a pressure gradient oriented more coast-parallel) prevent acceleration of the cold pool through the coastal gaps. Thus, the hybrid barrier jet structures forced by southwesterly flows resembled the classical barrier simulations, which had no inland cold pool initialized.

Our largest simulated wind speed enhancements for classical jets (~1.9) occurred for low Fr, consistent with other studies (Ólafsson and Bougeault 1996; Braun et al. 1999 Petersen et al. 2003), but we found a maximum at Fr ~0.3-0.4. The ambient flows with $Fr < 0.3$ are typically oriented more barrier-parallel, so the coastal flow is less accelerated by the ambient pressure gradient. Low ambient wind speeds (10–15 m s^{-1}) and southerly (170-180^o) wind directions (~30-45^o from coast-parallel) were also ingredients for the largest wind speed enhancements.

Our simulated wind speed enhancements were weaker than that measured in others studies (Cui et al 1998; Loescher et al. 2006). The stronger simulated wind speed enhancements (~2.5) off the California coast by Cui et al. (1998) occurred for weaker ambient winds (7.5 m s^{-1}). Also, the broader barrier width associated with the Rockies may have lead to greater enhancements. The stronger observed wind speed enhancements (2-3 times the ambient flow) observed in the SAR imagery along the Alaskan coast by

Loescher et al. (2006) were also measured during events for relatively weak ambient wind speeds (<12 m s^{-1}). Other possible factors for this difference could be due to higher static stabilities or different terrain geometry.

During periods of maximal gap outflow (hrs 6-18), the height of the jet maximums were typically lower than their counterparts in the classical simulations, since the jet maximums were located at the top of the shallow gap outflow. After the inland cold pool drained, hybrid jet heights were comparable to the classical jet heights. The jet height was positively correlated with total wind speed, U_{total}, and negatively correlated with static stability, N, suggesting that the height of the jet maximum approximately scales as U_{total}/N. The total wind speed, U_{total}, governed the strength of the turbulent mixing in the PBL by increasing the wind shear, but this mixing was countered by increases in static stability. The turbulent mixing created an enhancement of the stability at the top of the PBL; thus regulating the height of the barrier jets. A larger U_n also produces a deeper flow perturbation, thus impacting the depth of the barrier jet.

This numerical study advances our understanding of the nature of barrier jets produced by the interaction of impinging flow towards the complex three-dimensional orography of coastal Alaska. The results complement that found in the case study analysis (chapter 3) and the SAR climatology of Loescher et al (2006). Additional insight may be gained by an examination of moisture and cloud microphysics as well as the inclusion of idealized baroclinic waves.

Tables

Wind speed ($m\ s^{-1}$)	Wind direction (degrees)	Static Stability (s^{-1})	cold pool ($-\Delta^{o}C$)
10	160	0.015, 0.01, 0.005	-5, -10, -15
10	180	0.015 ,0.01, 0.005	-5, -10, -15
10	200	0.015, 0.01, 0.005	-5, -10, -15
10	220	0.015, 0.01, 0.005	-5, -10, -15
15	160	0.015, 0.0125, 0.01, 0.0075, 0.005	-5, -10, -15
15	180	0.015, 0.0125, 0.01, 0.0075, 0.005	-5, -10, -15
15	200	0.015, 0.0125, 0.01, 0.0075, 0.005	-5, -10, -15
15	220	0.015, 0.0125, 0.01, 0.0075, 0.005	-5, -10, -15
20	160	0.015, 0.01, 0.005	-5, -10, -15
20	180	0.015, 0.01, 0.005	-5, -10, -15
20	200	0.015, 0.01, 0.005	-5, -10, -15
20	220	0.015, 0.01, 0.005	-5, -10, -15
25	160	0.015, 0.01, 0.005	-5, -10, -15
25	180	0.015, 0.01, 0.005	-5, -10, -15
25	200	0.015, 0.01, 0.005	-5, -10, -15
25	220	0.015, 0.01, 0.005	-5, -10, -15

Table 4.1. The complete set of idealized simulations used in this study. The first two columns show the combinations of wind speeds and wind direction used. The third column shows the variations of static stability for each combination of wind speed and direction. The fourth column lists the inland cold pools initialized for each set of wind speed and wind direction, but used a fixed stability of $N=0.01\ s^{-1}$. A total of 104 simulations (56 classical jet and 48 hybrid jet simulations) were performed to sample a comprehensive portion of the phase space.

Classical jet characteristic	**Atmospheric parameter**	**Total correlation** (h 12-24, h 24-48)	**Fr < 1** (h 12-24, h 24-48)	**Fr > 1** (h 12-24, h 24-48)
Wind speed enhancement	Barrier-normal flow	**-0.62, -0.54**	**-0.46, -0.38**	-0.42, -0.33
	Wind speed	**-0.59, -0.66**	**-0.52, -0.61**	-0.47, -0.52
	Wind direction	**-0.39,** -0.26	-0.24, -0.08	-0.21, -0.14
	Stability	**0.75, 0.75**	**0.59, 0.58**	**0.56**, 0.51
Offshore extent	Barrier-normal flow	**-0.56, -0.58**	**-0.54, -0.55**	-0.26, -0.10
	Wind speed	0.01, -0.11	0.14, 0.06	**0.58**, 0.47
	Wind direction	**-0.73, -0.75**	**-0.77, -0.81**	-0.14, -0.39
	Stability	**0.53, 0.56**	**0.33, 0.37**	0.45, 0.15
Jet max height	Barrier-normal flow	0.03, 0.11	0.14, 0.22	-0.44, -0.41
	Wind speed	**0.74, 0.75**	**0.82, 0.87**	0.48, 0.36
	Wind direction	**-0.52, -0.44**	**-0.49, -0.36**	**-0.86, -0.84**
	Stability	**-0.32, -0.34**	**-0.34, -0.31**	-0.31, -0.30

Table 4.2. Correlations of atmospheric parameters with barrier jet characteristics for the 56 classical barrier jet simulations. There were 43 simulations with $Fr < 1$ and 13 with $Fr > 1$. The bold values represent correlations with p-values < 0.05, testing the hypothesis of no correlation against the alternative that there is a non-zero correlation.

Hybrid jet characteristic	**Atmospheric parameter**	**Total correlation** (h 12-24, h 24-48)	**Fr < 1** (h 12-24, h 24-48)	**Fr > 1** (h 12-24, h 24-48)
Wind speed enhancement	Barrier-normal flow	**-0.86, -0.81**	**-0.81, -0.85**	**-0.86, -0.61**
	Wind speed	**-0.76, -0.88**	**-0.50, -0.72**	**-0.55, -0.56**
	Wind direction	**-0.48, -0.36**	**-0.47, -0.49**	**-0.72, -0.46**
	Cold pool strength	0.08, -0.03	0.11, 0.05	-0.20, -0.34
Offshore extent	Barrier-normal flow	**-0.77, -0.76**	**-0.88, -0.87**	**-0.66, -0.75**
	Wind speed	-0.15, -0.35	-0.12, -0.05	0.35, -0.11
	Wind direction	**-0.78, -0.82**	**-0.89, -0.91**	**-0.71, -0.76**
	Cold pool strength	0.15, 0.11	**0.44**, 0.28	-0.18, -0.09
Jet height	Barrier-normal flow	0.03, 0.16	-0.15, 0.11	-0.18, -0.11
	Wind speed	**0.81, 0.81**	**0.97, 0.92**	**0.65, 0.48**
	Wind direction	**-0.54, -0.44**	**-0.61, -0.45**	**-0.75, -0.85**
	Cold pool strength	0.02, 0.00	0.15, 0.12	0.08, 0.02

Table 4.3. Correlations of atmospheric parameters with barrier jet characteristics for the 48 hybrid barrier jet simulations. There were 28 simulations with $Fr < 1$ and 20 with $Fr > 1$. The bold values represent correlations with p-values < 0.05, testing the hypothesis of no correlation against the alternative that there is a non-zero correlation.

Figures

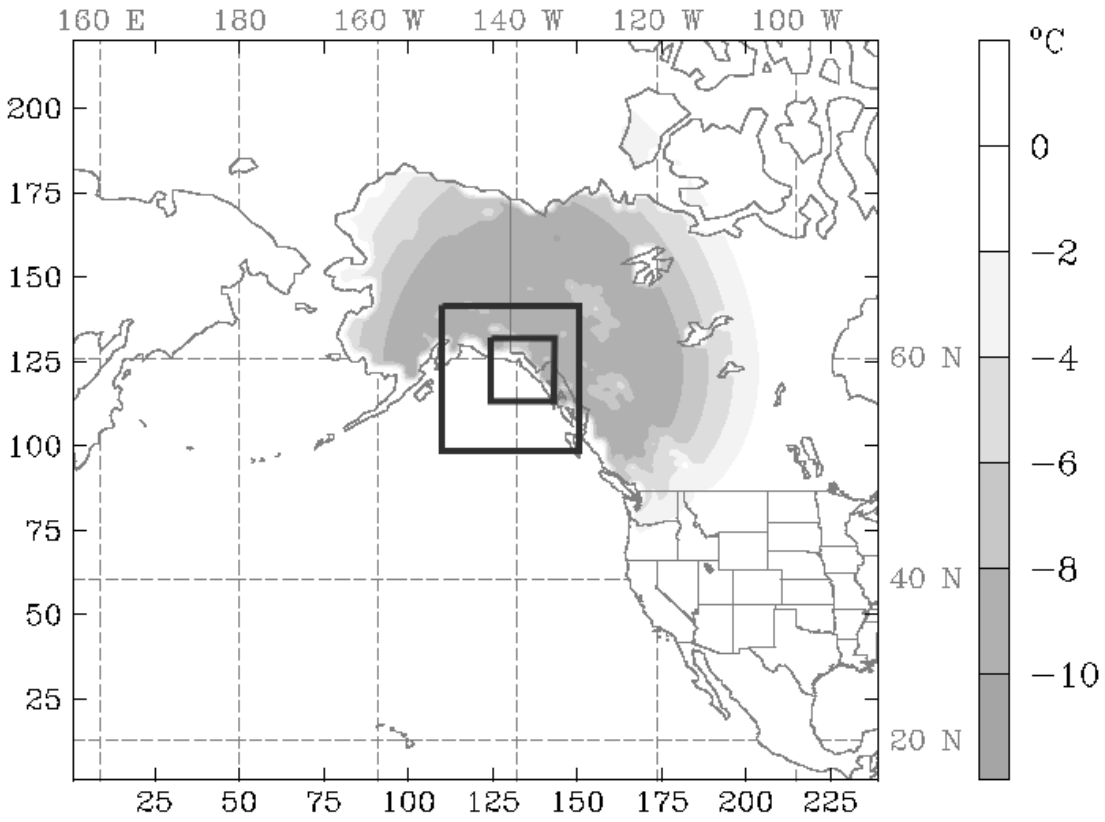

Figure 4.1 The 54-km domain with 18-, and 6-km nests. The 500-m level temperature perturbation field is shown for an initialized cold pool run (gray shade, every 2°C) with maximum perturbation of ΔT = -10 °C within 1000 km radius of (138°W, 59°N) decreasing linearly to zero by 2000 km radius.

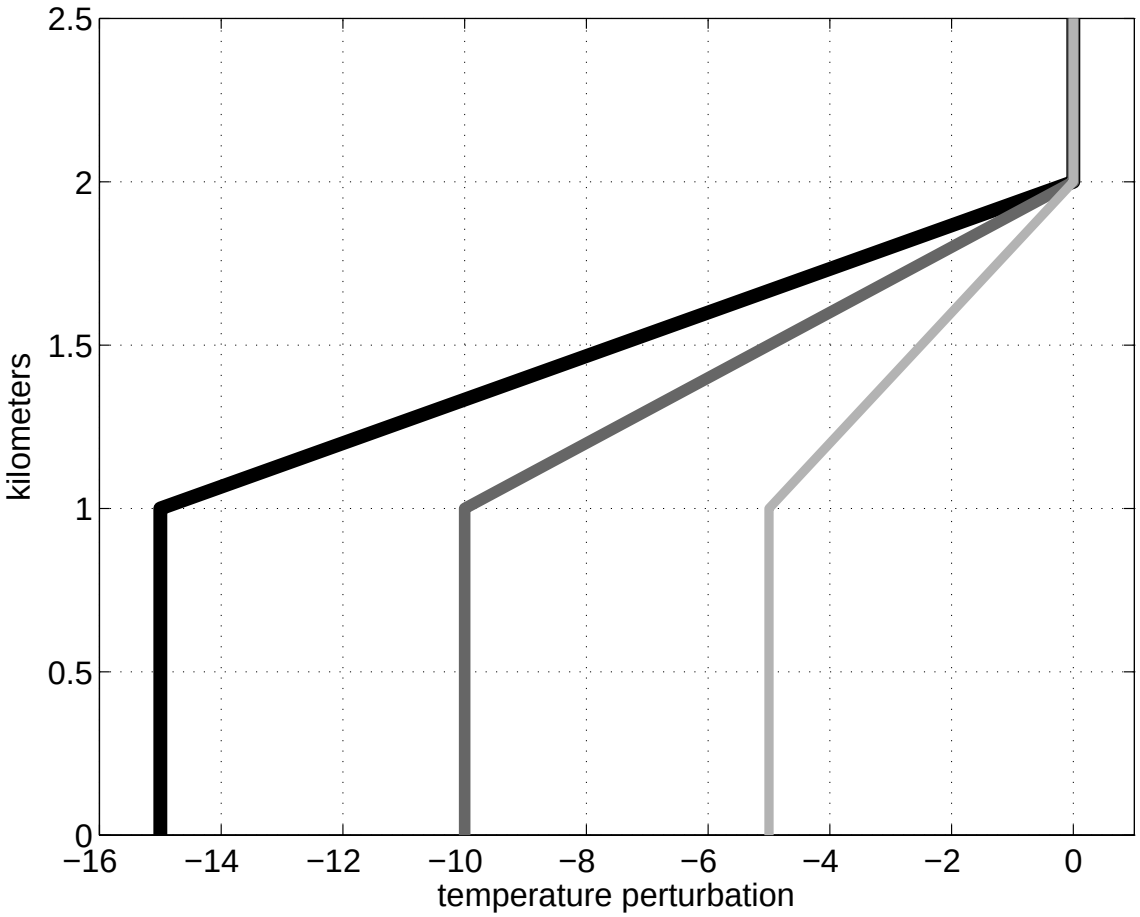

Figure 4.2. Vertical temperature perturbations added over the gray region of Fig. 1 for the specification of inland cold pools.

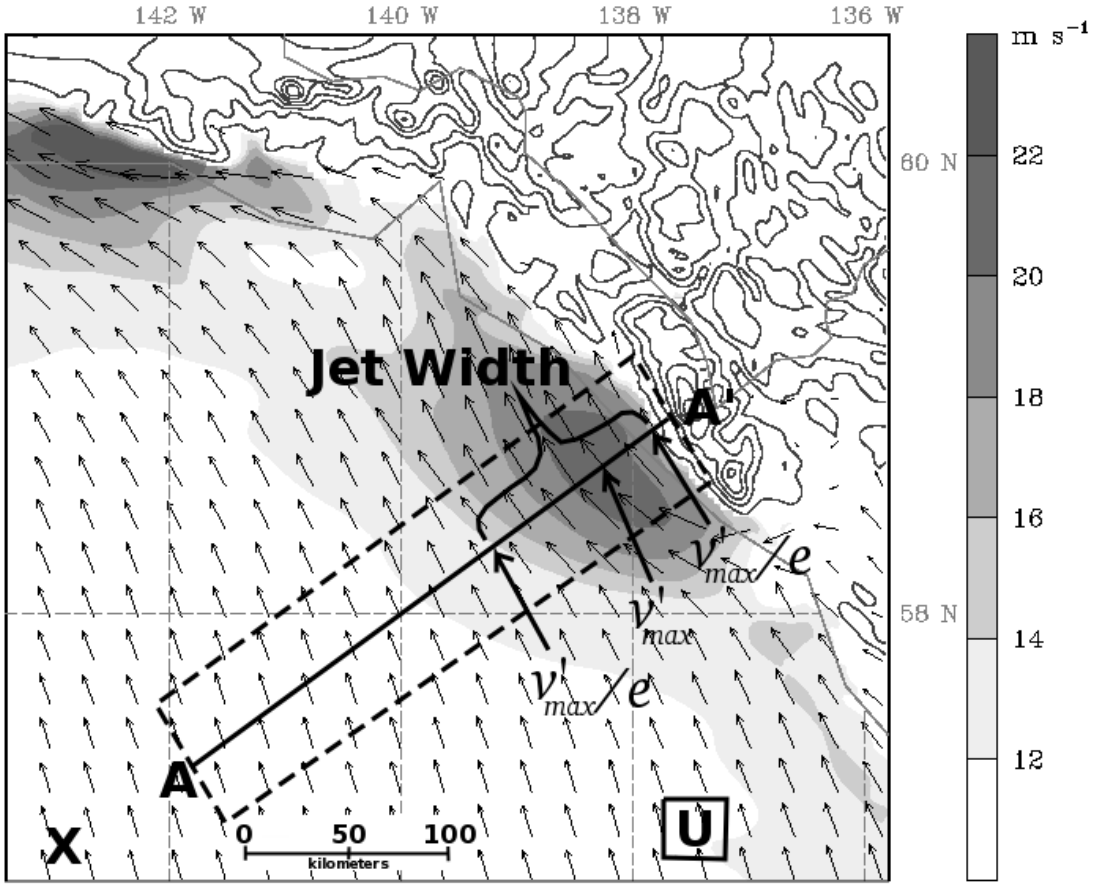

Figure 4.3. The 6-km nest with cross-sectional volume between A-A', encompassing the dashed area between the surface and ~2.7 km ASL. This region was used to measure barrier jet properties, such as the jet width, separation width, height, and wind speed enhancement. The area in the box U, located upstream of the jet region, was where the ambient flow conditions were measured. This box was moved longitudinally, depending on the ambient wind direction. Point X was used to measure large-scale impacts ~500 km offshore.

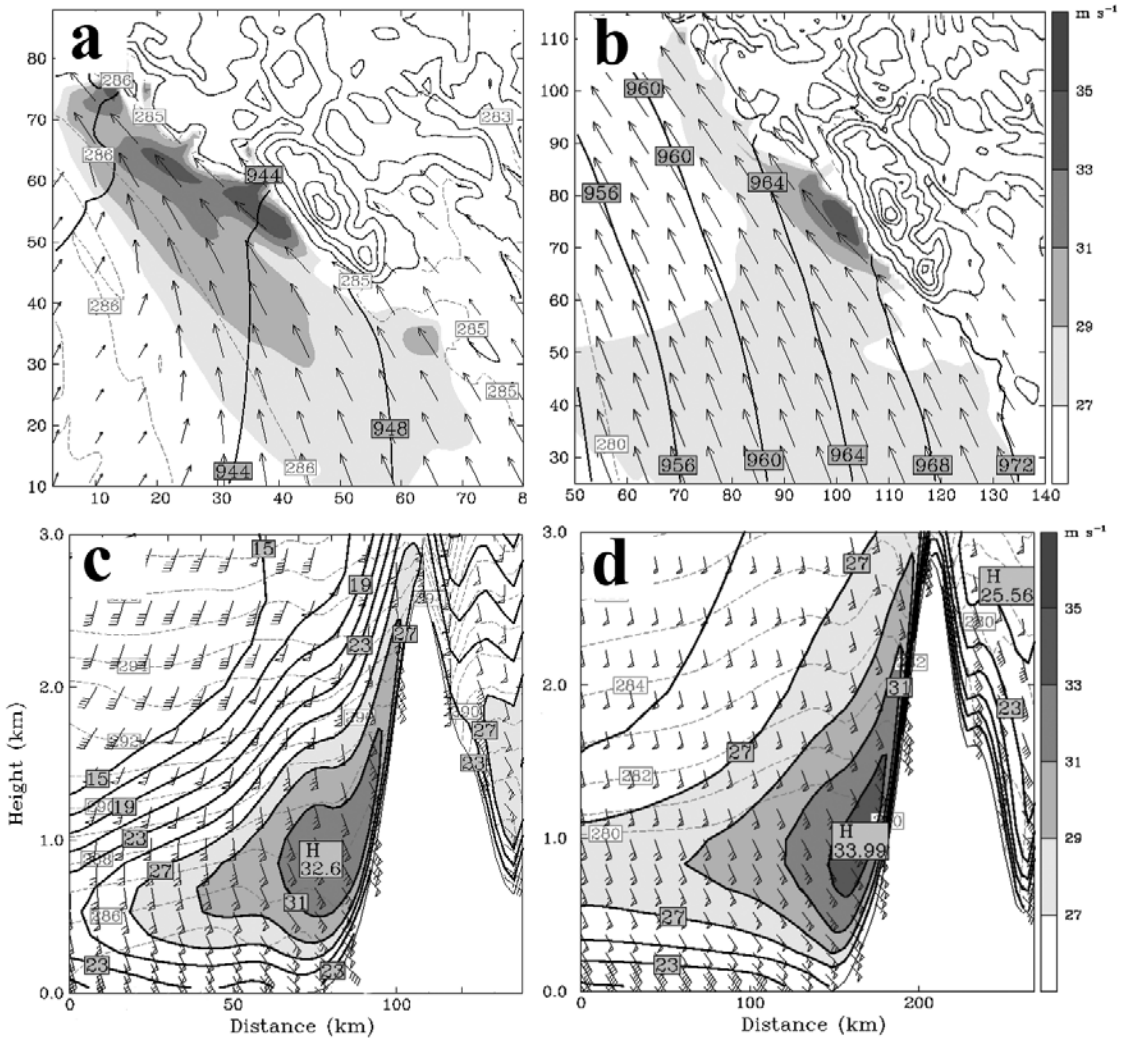

Figure 4.4. Wind speed (gray shade every 2 m s^{-1}), pressure (black every 4 mb), potential temperature (dashed gray every 1 K) and wind vectors at 500 m ASL for (a) SARJET IOP1 and (b) idealized analog. Panels (c) and (d) shows the terrain-parallel wind speed (gray shade every 2 m s^{-1}), wind barbs (1 flag = 25 m s^{-1} and full barb = 5 m s^{-1}) and potential temperature (dashed gray every 1 K) along the cross-section A-A' (Fig. 3). The idealized simulation was initialized with 25 m s^{-1} winds at 180°, and N = 0.01 s^{-1}.

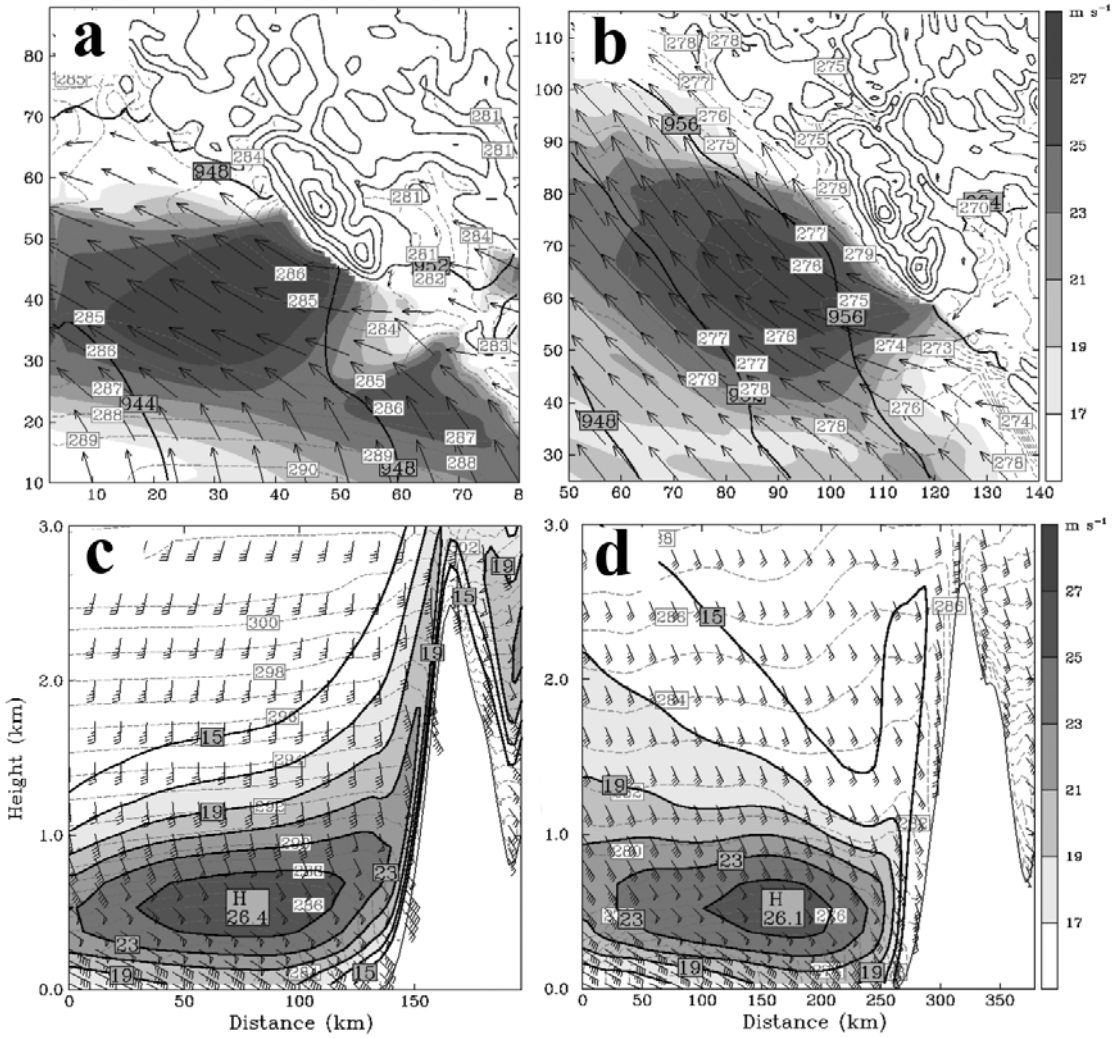

Figure 4.5. Wind speed (gray shade every 2 m s^{-1}), pressure (black every 4 mb), potential temperature (dashed gray every 1 k) and wind vectors at 500 m ASL for (a) SARJET IOP7 and (b) idealized analog. Panels (c) and (d) shows the terrain-parallel wind speed (gray shade every 2 m s^{-1}), wind barbs (1 flag = 25 m s^{-1} and full barb = 5 m s^{-1}) and potential temperature (dashed gray every 1 K) along the cross-section A-A' (Fig. 3). The idealized simulation was initialized with 15 m s^{-1} winds at 160^{o}, with N = 0.01 s^{-1} and a cold pool depth of 15^{o} Celsius.

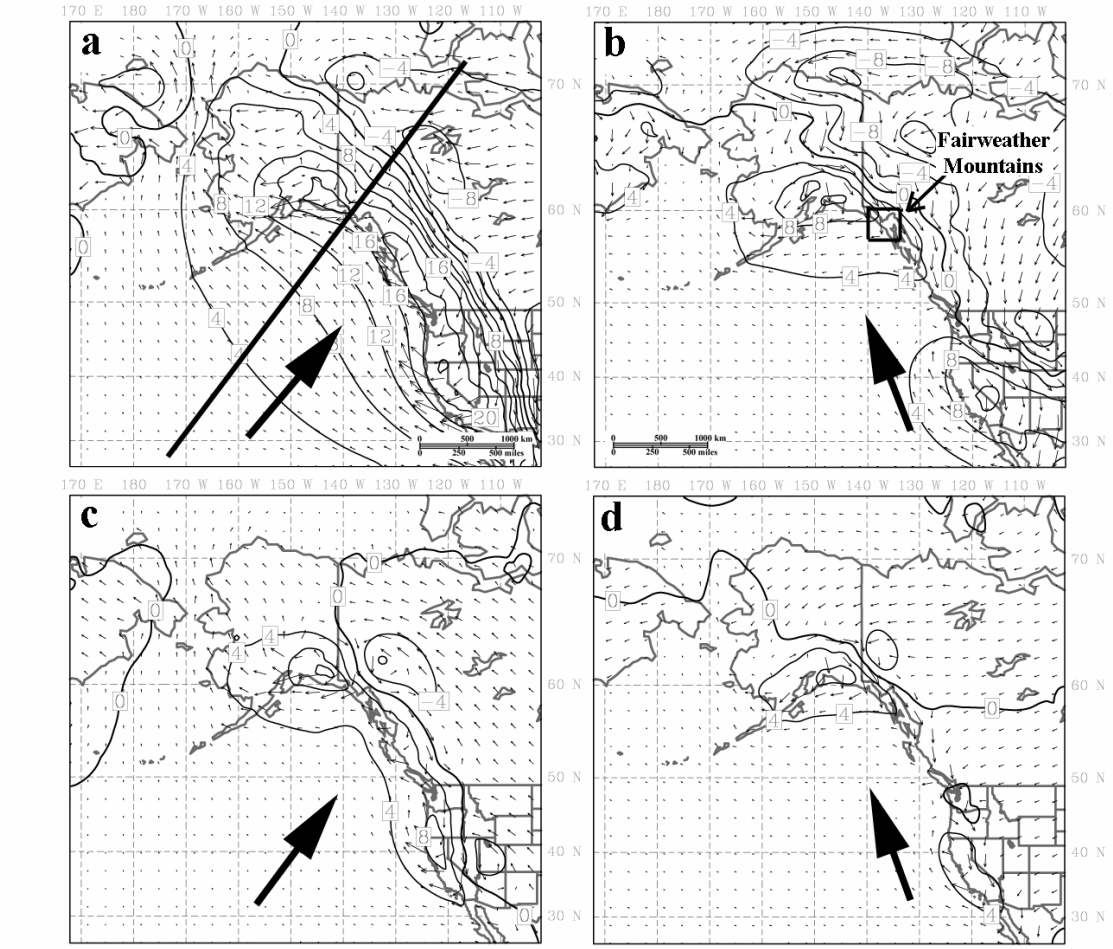

Figure 4.6. Perturbation sea-level pressure (black every 4 mb) and 500-m wind vectors at hour 24 for simulations initialized with 10 m s^{-1} and N=0.01 s^{-1} with wind directions of (a) 220^0 and (b) 160^0, (c) 220^o NIT, and (d) 160^o NIT. The dark arrows show the initialized wind direction.

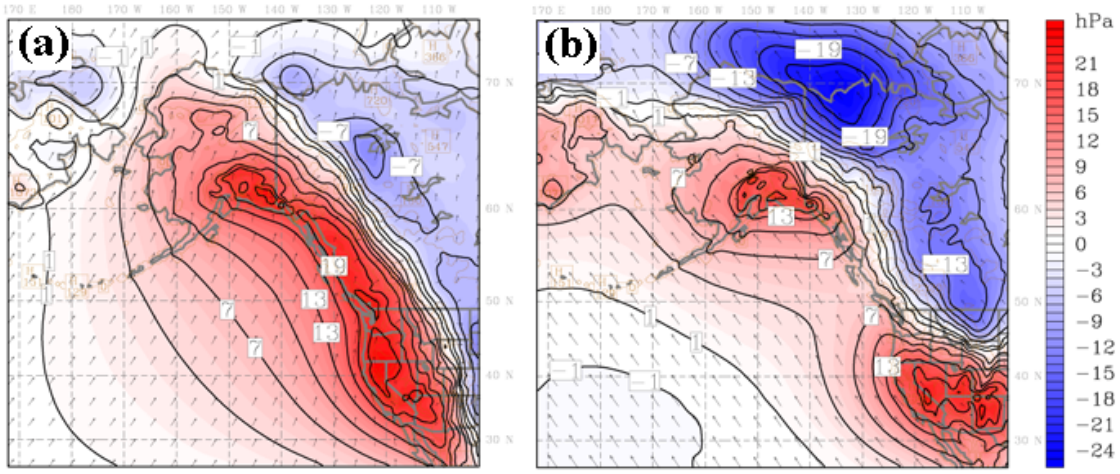

Figure 4.7 A comparison of the large-scale pressure perturbation (colored and contoured every 3 mb) for two simulations at hour 24 with the same U_n at the Fairweathers, but different initialized wind speeds and directions of (a) 10 m s^{-1} at 220° and (b) 25 m s^{-1} at 160°. The black vectors represent the 500 m winds.

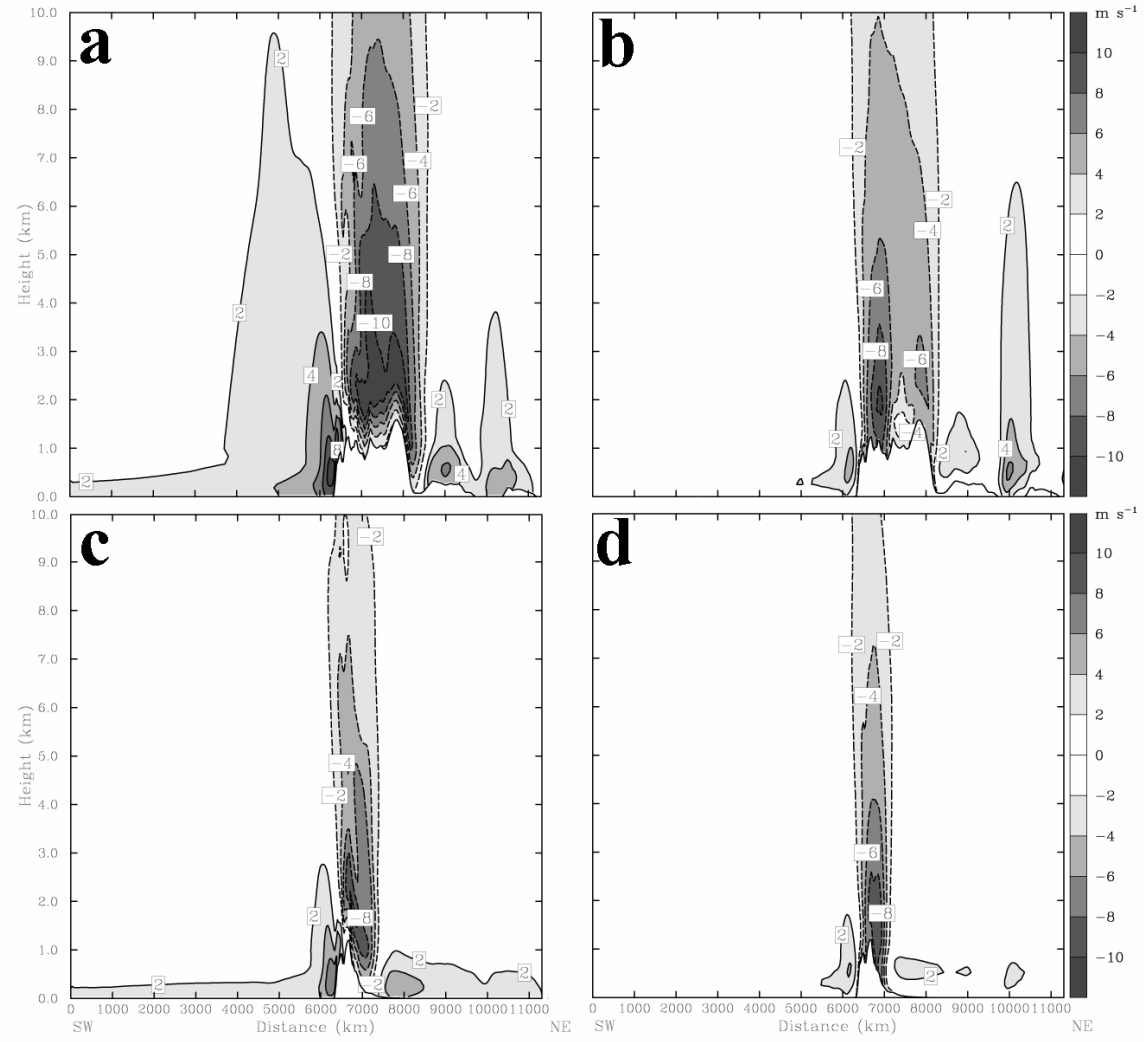

Figure 4.8 Cross-sections of perturbation wind speed (gray shade) along the cross-section in (4.6a) for the (a) 220^{o} and (b) 160^{o}, (c) 220^{o} NIT, and (d) 160^{o} NIT simulations.

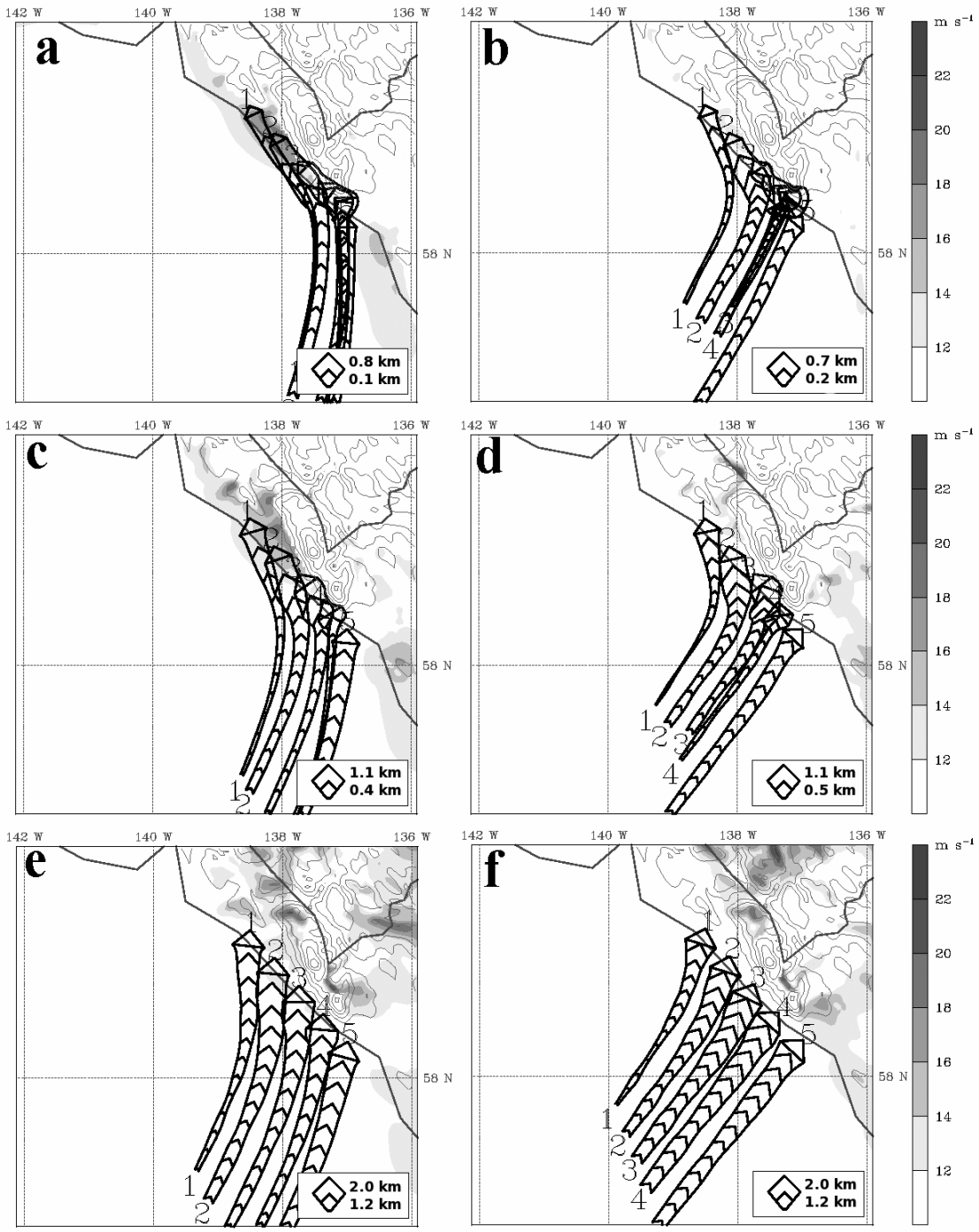

Figure 4.9 Backwards trajectories released over the coast at hour 24 for simulations with the full topography (left column) and no inland terrain (NIT; right column). The vertical levels of release are 500 m ASL (a-b), 1000 m ASL (c-d), and 2000 m ASL (e-f). Both simulations were initialized with wind speeds of 10 m s^{-1}, 220 degrees and N=0.01 s^{-1}. The width of the arrow indicates the height above mean sea level. The total wind speed is shaded (every 2 m s^{-1}).

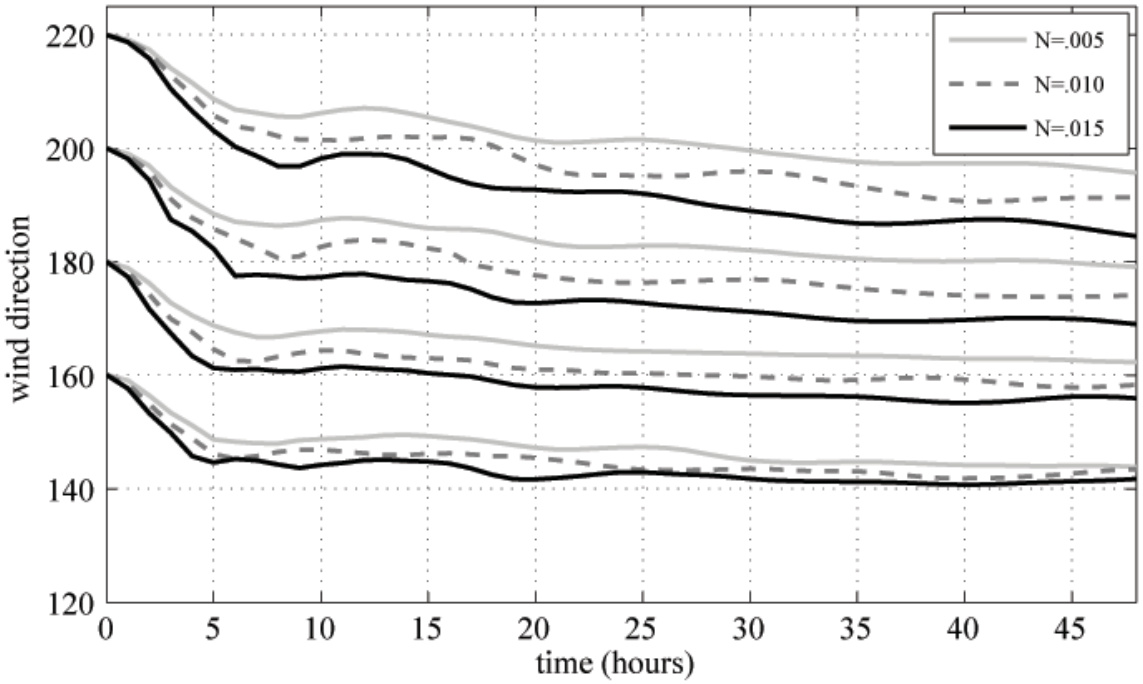

Figure 4.10 Time series of the mean upstream wind direction (in upstream box in Fig. 3). All simulations shown were initialized with wind speeds of 15 m s^{-1}, but at various wind directions of 220, 200, 180, and 160 degrees and static stabilities of N=0.005 s^{-1} (light gray), N=0.01 s^{-1} (medium gray dashed), and N=0.015 s^{-1} (black).

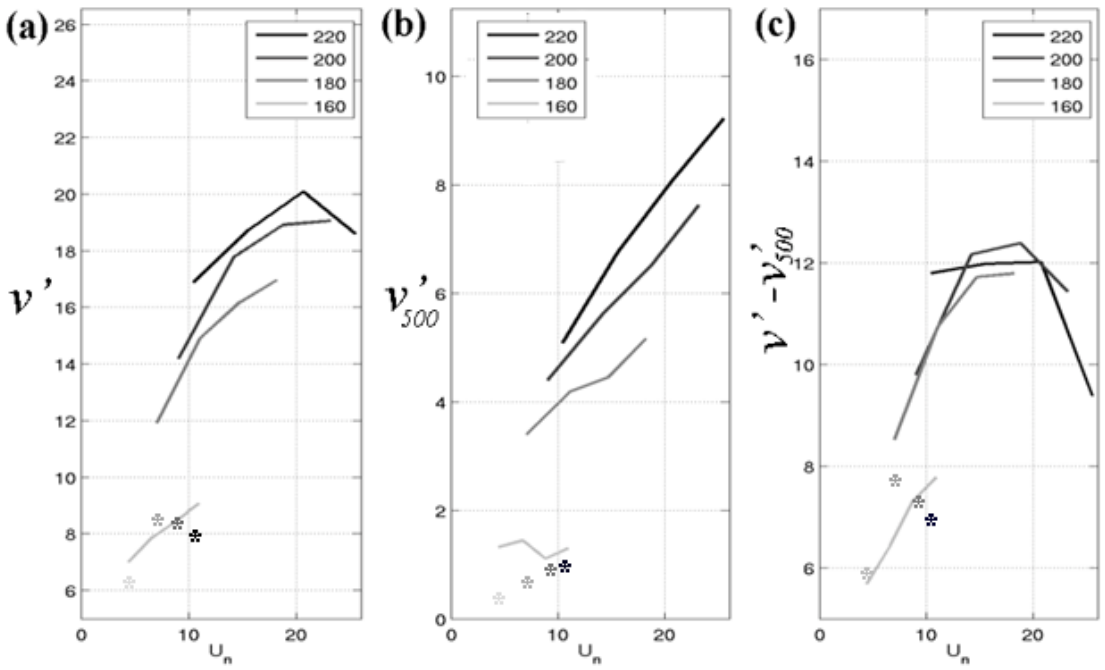

Figure 4.11 (a) Maximum barrier-parallel velocity, *v'*, as a function of U_n for different initialized wind directions (gray shaded lines) (b) *v'* associated with the mountain anticyclone (measured at upstream point X in Fig. 3), and (c) the difference between (a)-(b), which shows the *v'* generated within the coastal zone (< 500 km offshore). The NIT runs are plotted as '*' and gray shaded the same as the full terrain runs.

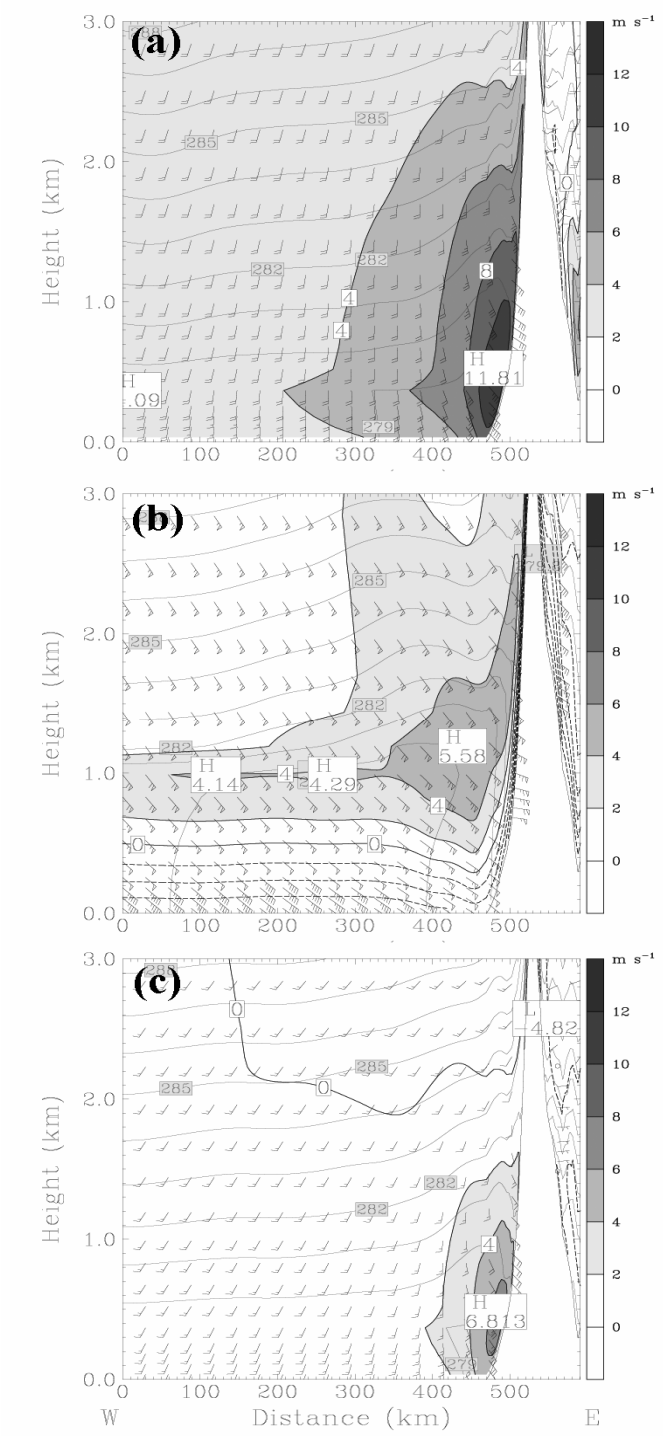

Figure 4.12 The impact of wind direction and broad inland terrain for three simulations with the same initialized U_n =10 m s^{-1}: (a) wind speeds of 10 m s^{-1} at 220^o with the full terrain, (b) wind speeds of 25 m s^{-1} at 160^o with the full terrain, and (c) wind speeds of 10 m s^{-1} at 220^o with NIT. Plotted is the perturbation barrier-parallel velocities (m s^{-1}; gray shade), potential temperature (K, gray contours), and wind barbs.

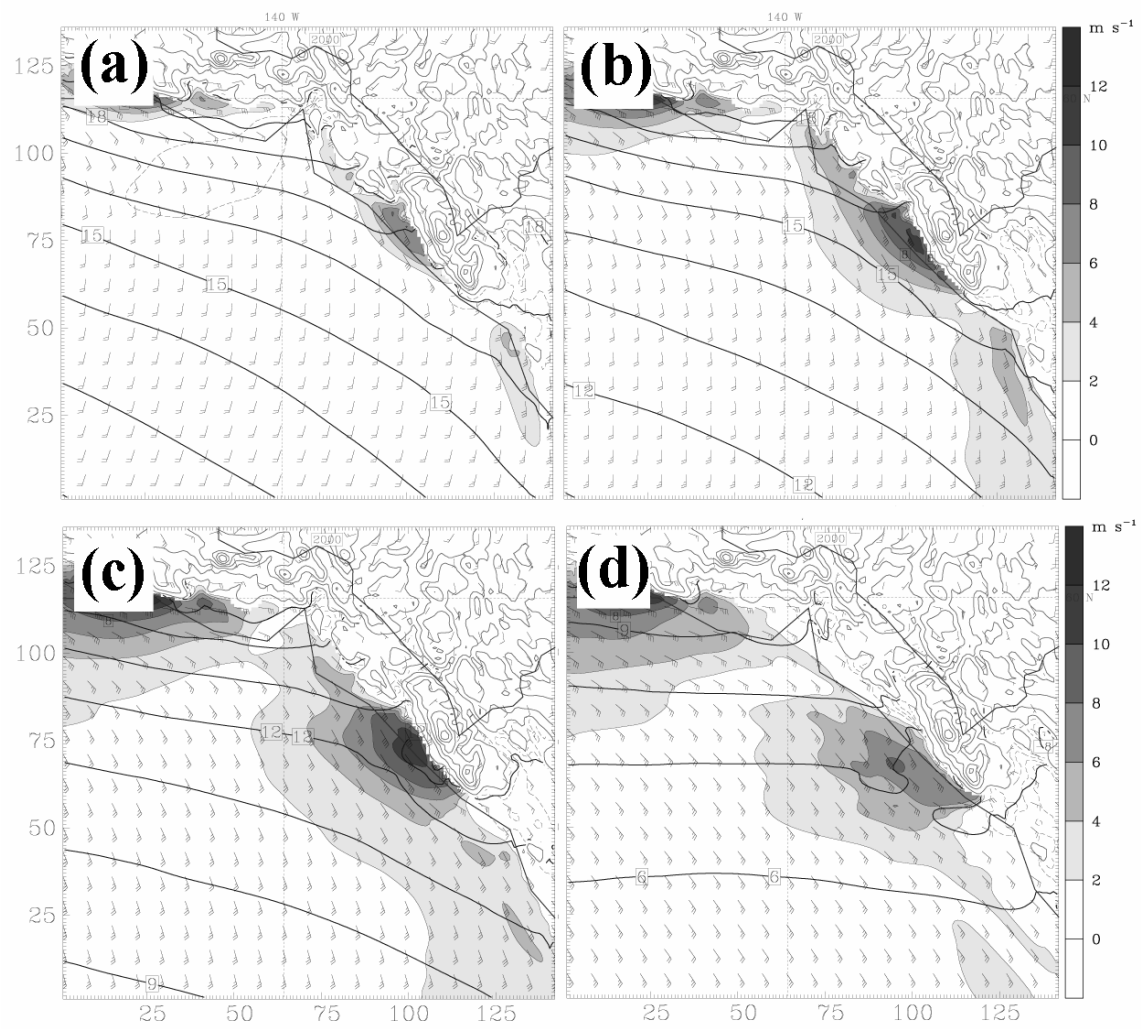

Figure 4.13 Total horizontal wind speed enhancement (gray shade ever 2 m s^{-1}) at 500 m ASL, wind barbs (full barb = 10 kts), and pressure perturbation (black every 1 mb) for simulations with initialized wind speed of 10 m s^{-1}, N = 0.01 s^{-1}, and wind directions of (a) 220°, (b) 200°, (c) 180°, and (d) 160°.

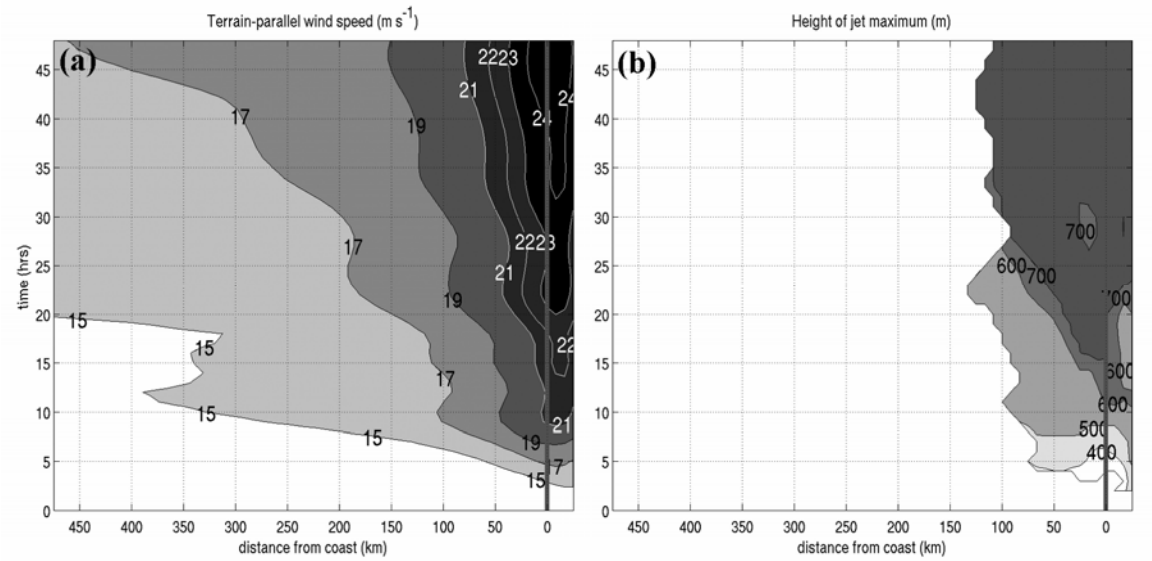

Figure 4.14 Hovmöller diagram of (a) terrain-parallel wind speed (m s^{-1}) and (b) jet width (m) for the classical barrier jet simulation initialized with U=15 m s^{-1}, N=0.01 s^{-1}, and wind direction of 180^{o}.

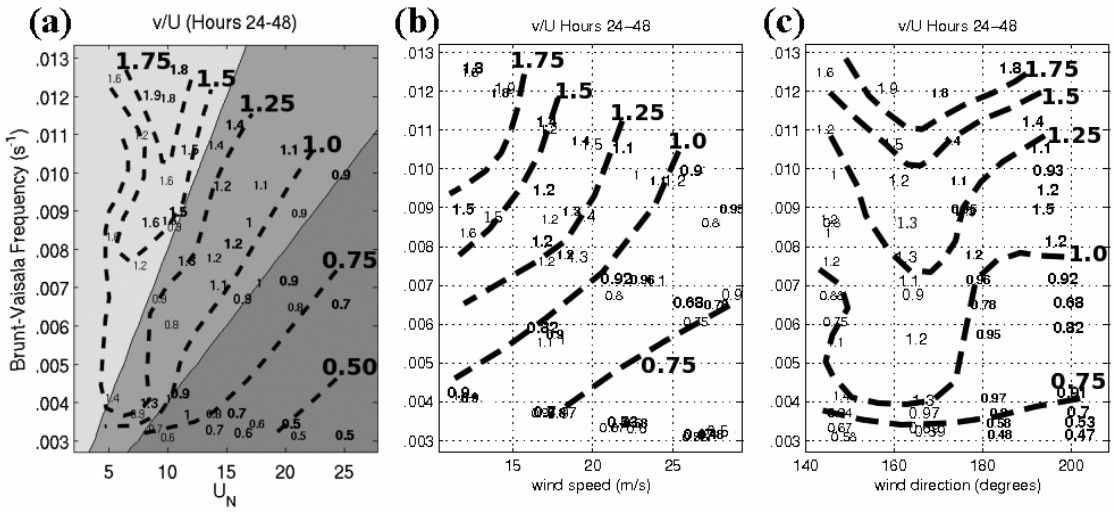

Figure 4.15 Phase space diagrams showing wind speed enhancement (numbers and dashed) as a function of N and (a) U_N, (b) wind speed (m s^{-1}) and (c) wind direction (degrees). The gray shade in (a) represent Froude number regimes: $0 < Fr < 0.5$ (light gray), $0.5 < Fr < 1.0$ (medium gray), and $1.0 < Fr$ (dark gray). The different font sizes and thickness represent: 220^o (large bold), 200^o (small bold), 180^o (large thin), and 160^o (small thin). All measurements represent averages of hours 24-48.

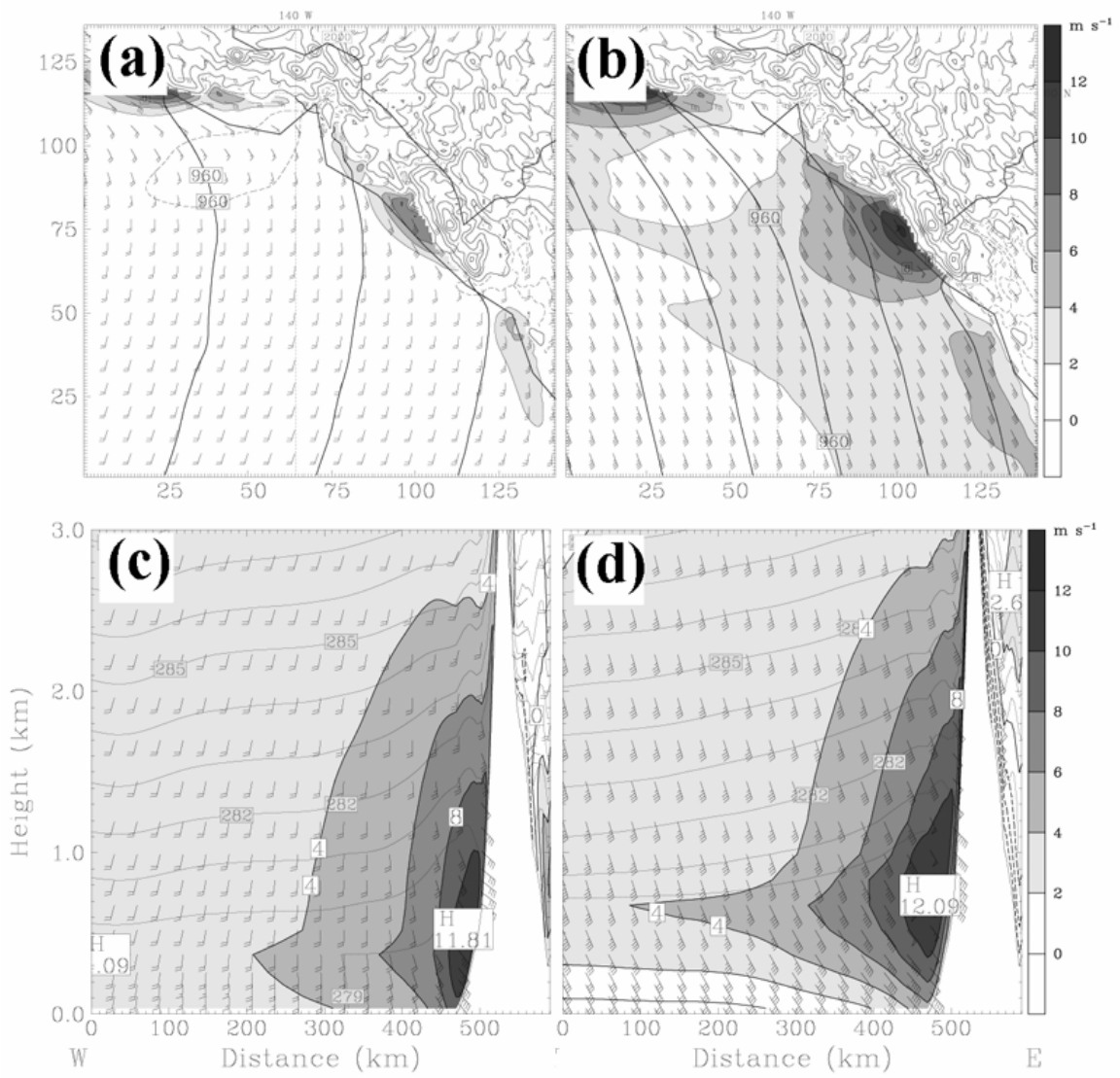

Figure 4.16 Wind speed enhancement comparison of two simulations with the same terrain-normal wind component. The 500-m total wind speed enhancement (gray shade and contoured every 2 m s^{-1}), pressure (dark gray every 4 mb) is shown for (a) 10 m s^{-1} winds at 220^{o} and (b) 15 m s^{-1} winds at 180^{o}. The terrain-parallel wind speed enhancement (gray shade and contoured every 2 m s^{-1}) and potential temperature (dashed gray every 1 K) through cross-section A-A' for (c) 10 m s^{-1} winds at 220^{o} and (d) 15 m s^{-1} winds at 180^{o}.

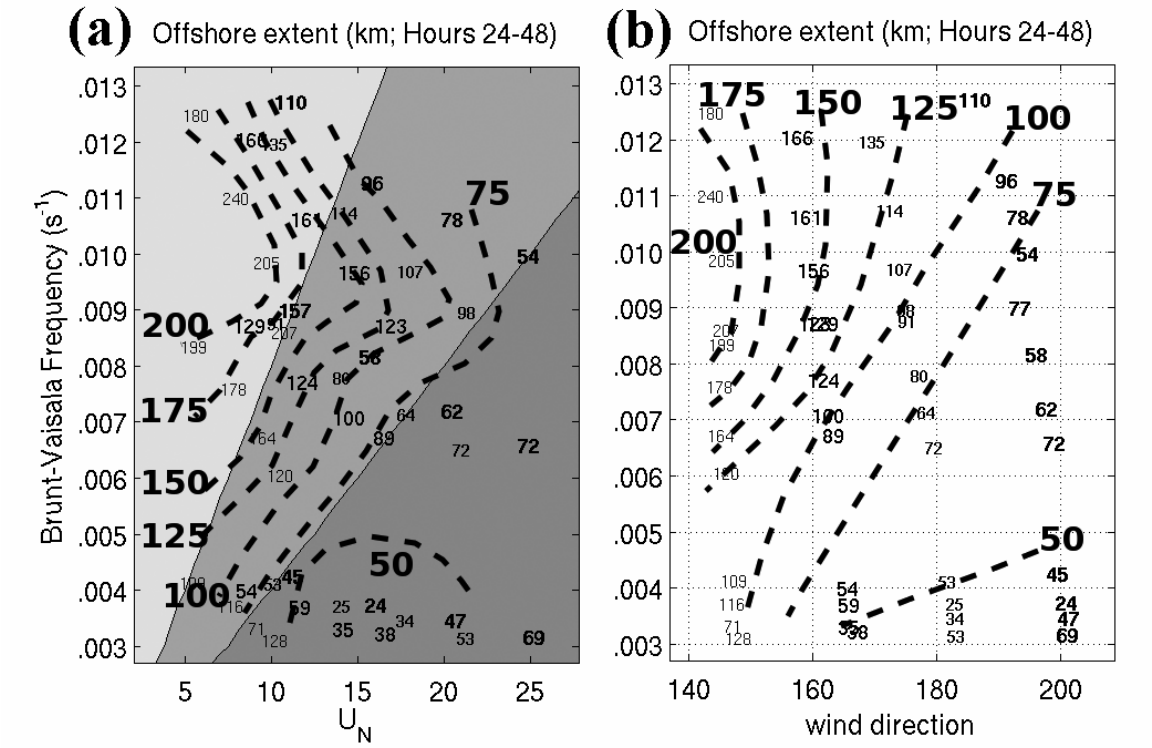

Figure 4.17 Phase space diagrams of the total offshore extent (numbers in km and dashed every 25 km) as a function of N and (a) U_n and (b) wind direction. The gray shade in (a) represent Froude number regimes: $0 < Fr < 0.5$ (light gray), $0.5 < Fr < 1.0$ (medium gray), and $1.0 < Fr$ (dark gray). The variations in the size and thickness of the numbers are relative to the initialized wind direction (see Fig. 4.15).

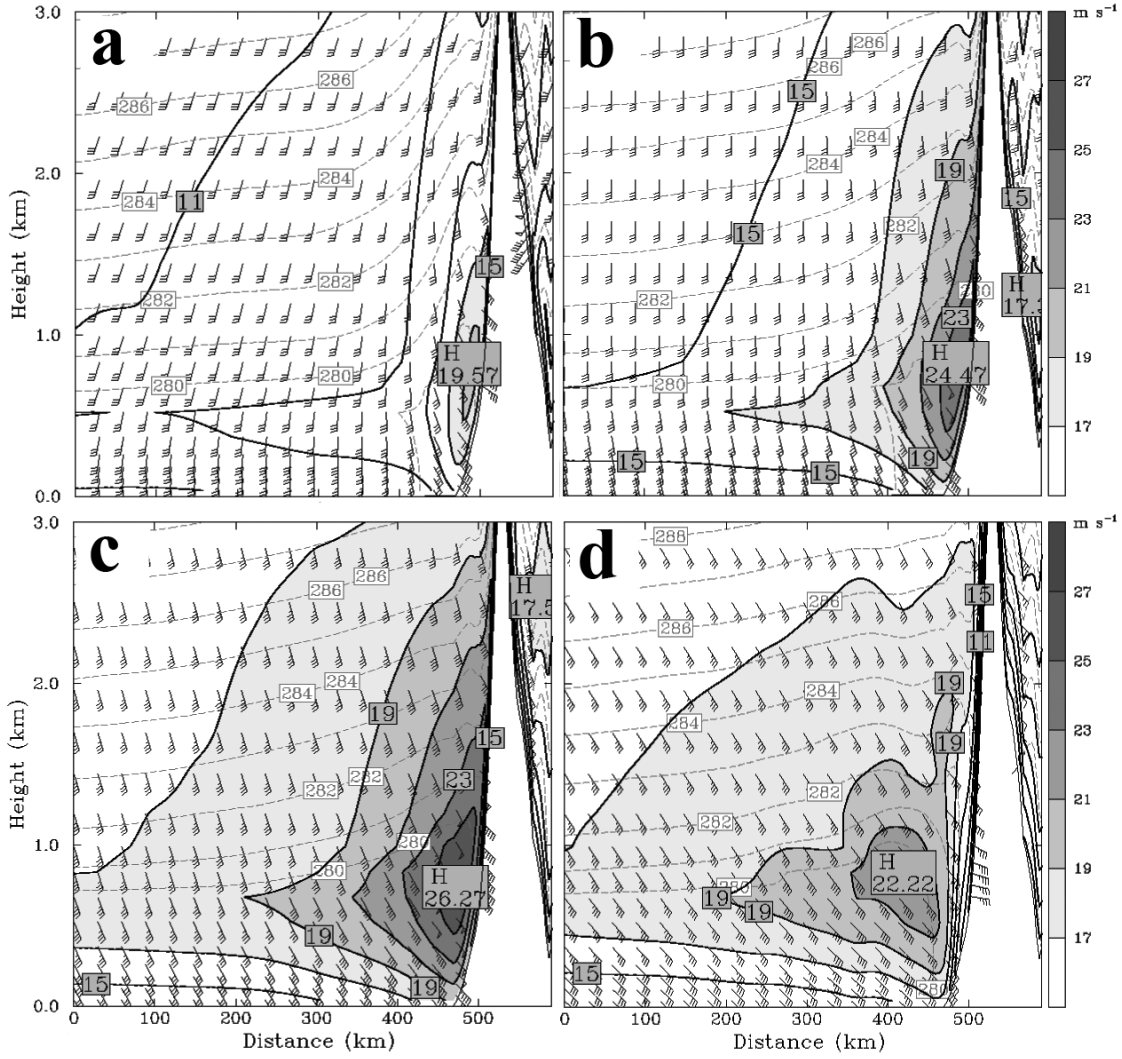

Figure 4.18 Cross-sections of along-barrier wind speed (gray shade ever 2 m s^{-1}), wind barbs (full barb = 10 kts), and potential temperature (dashed gray every 1 K) for simulations with initialized wind speed of 15 m s^{-1}, N = 0.01 s^{-1}, and wind directions of (a) 220°, (b) 200°, (c) 180°, and (d) 160°.

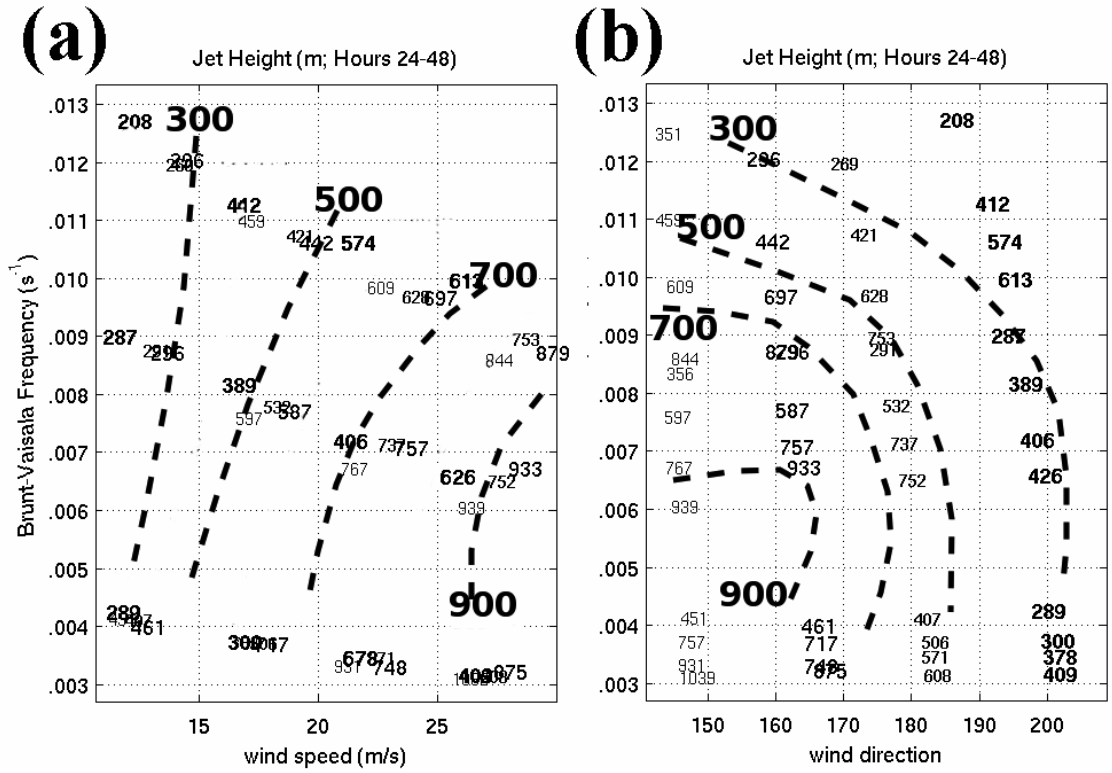

Figure 4.19 Barrier jet height as a function of Brunt-Väisälä frequency and (a) wind speed (m s^{-1}) and (b) wind direction (degrees). The variations in the size and thickness of the numbers are relative to the initialized wind direction (see Fig. 4.15).

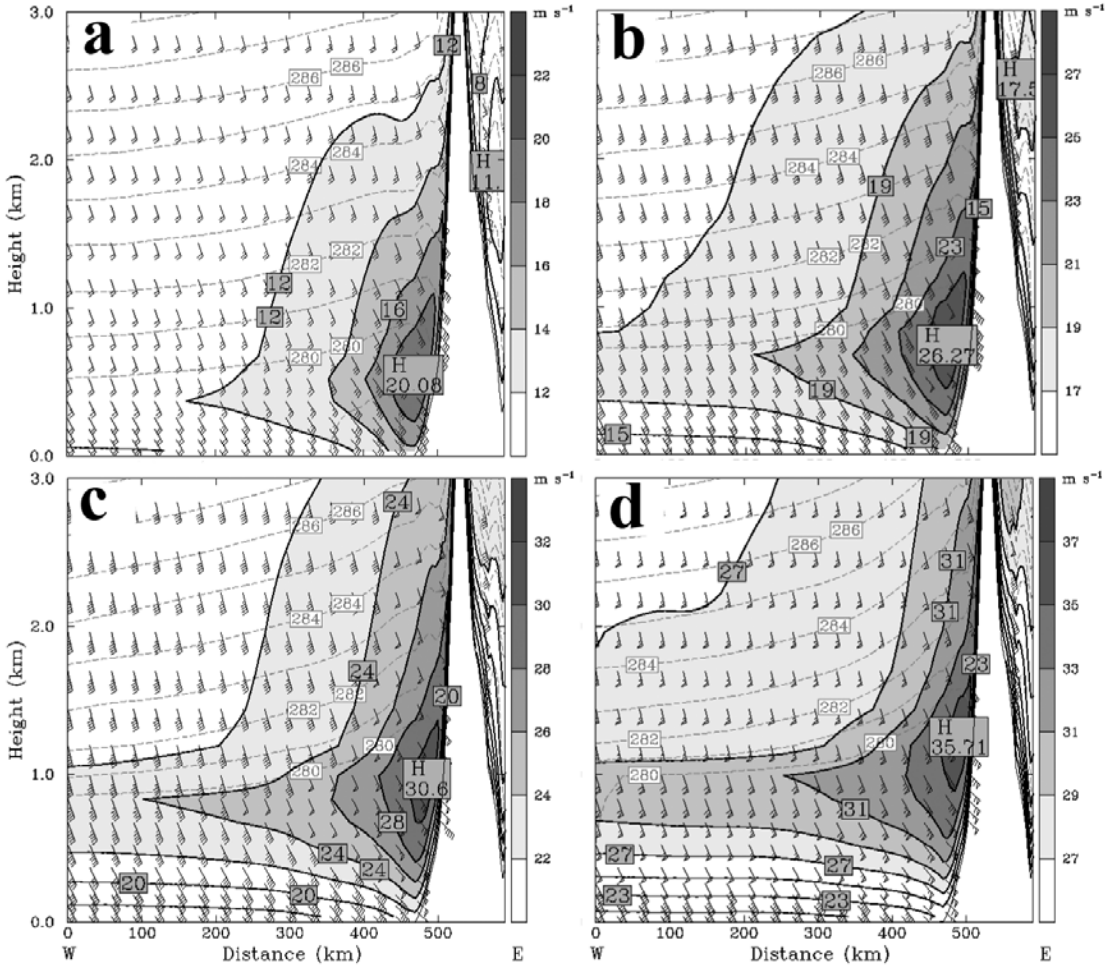

Figure 4.20 Cross-sections of terrain-parallel wind speed (gray shade every 2 m s^{-1}), wind barbs (full barb = 10 kts), and potential temperature (dashed gray every 1 K) for simulations with an initialized wind direction of 180^{o} and static stability of N=0.01 s^{-1} and wind speeds of (a) 10 m s^{-1}, (b) 15 m s^{-1}, (c) 20 m s^{-1}, and (d) 25 m s^{-1}.

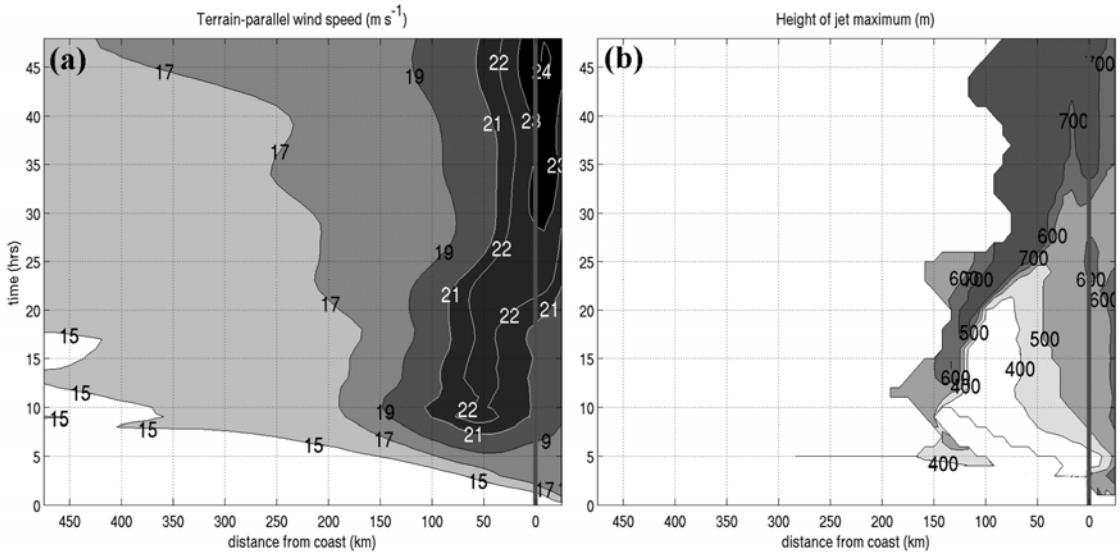

Figure 4.21 Hovmöller diagrams of (a) terrain parallel wind speed (shaded every 2 m s^{-1}) and (b) jet height (m) initialized with U=15 m s^{-1}, N=0.01 s^{-1}, wind direction of 180°, and an inland cold pool of ΔT=-15°C.

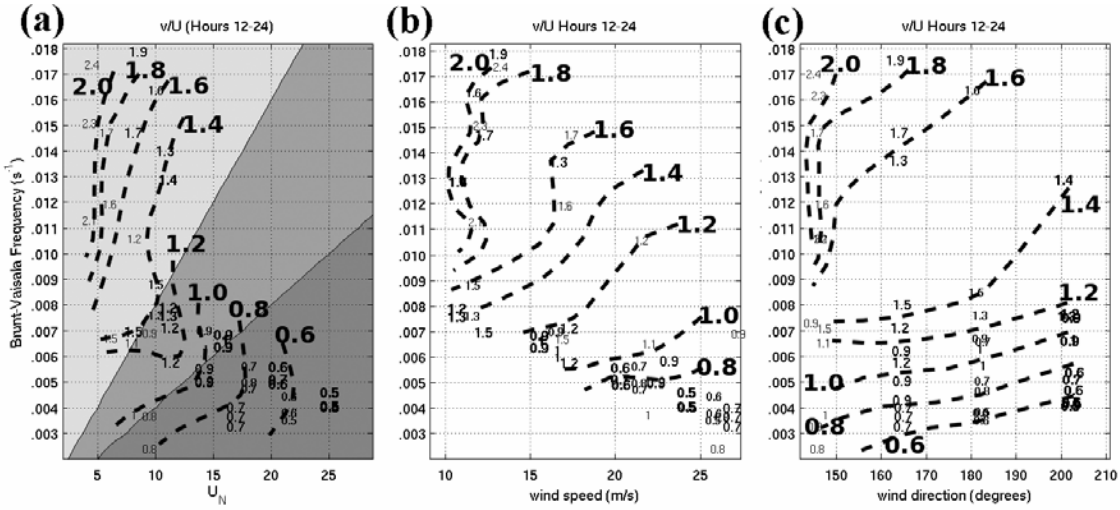

Figure 4.22 Wind speed enhancement as a function of Brunt-Väisälä frequency (s^{-1}) and (a) U_N, (b) wind speed (m s^{-1}), and (c) wind direction (degrees). The variations in the size and thickness of the numbers are relative to the initialized wind direction (see Fig. 4.15) and the gray shade in (a) denotes different *Fr* regimes (see Fig. 4.15).

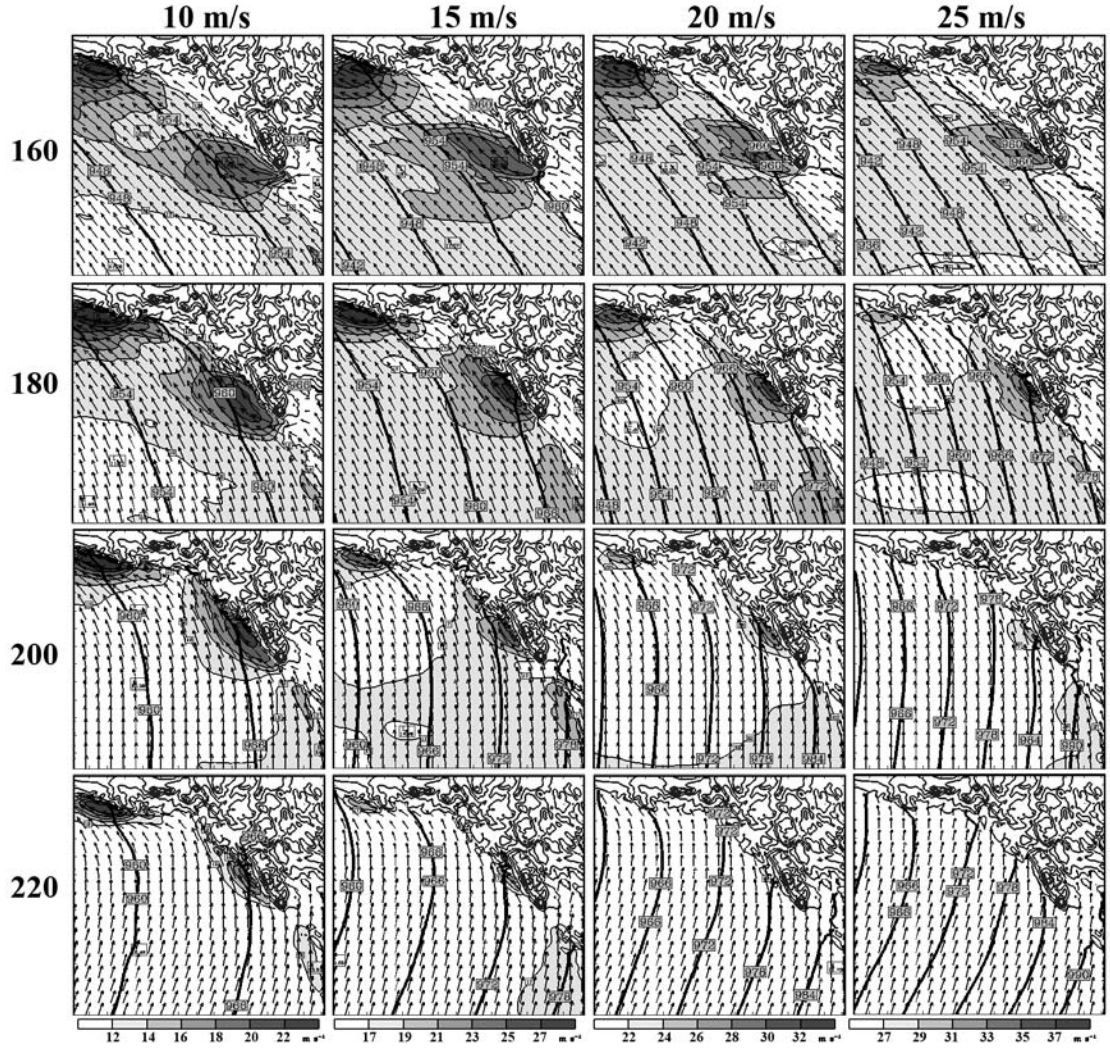

Figure 4.23 Wind speeds (gray shade every 2 m s^{-1}) and pressure (black every 4 mb) at 500 m ASL for simulations initialized with cold pool ΔT=-10 Celsius as a function of wind speed (columns) and wind direction (rows).

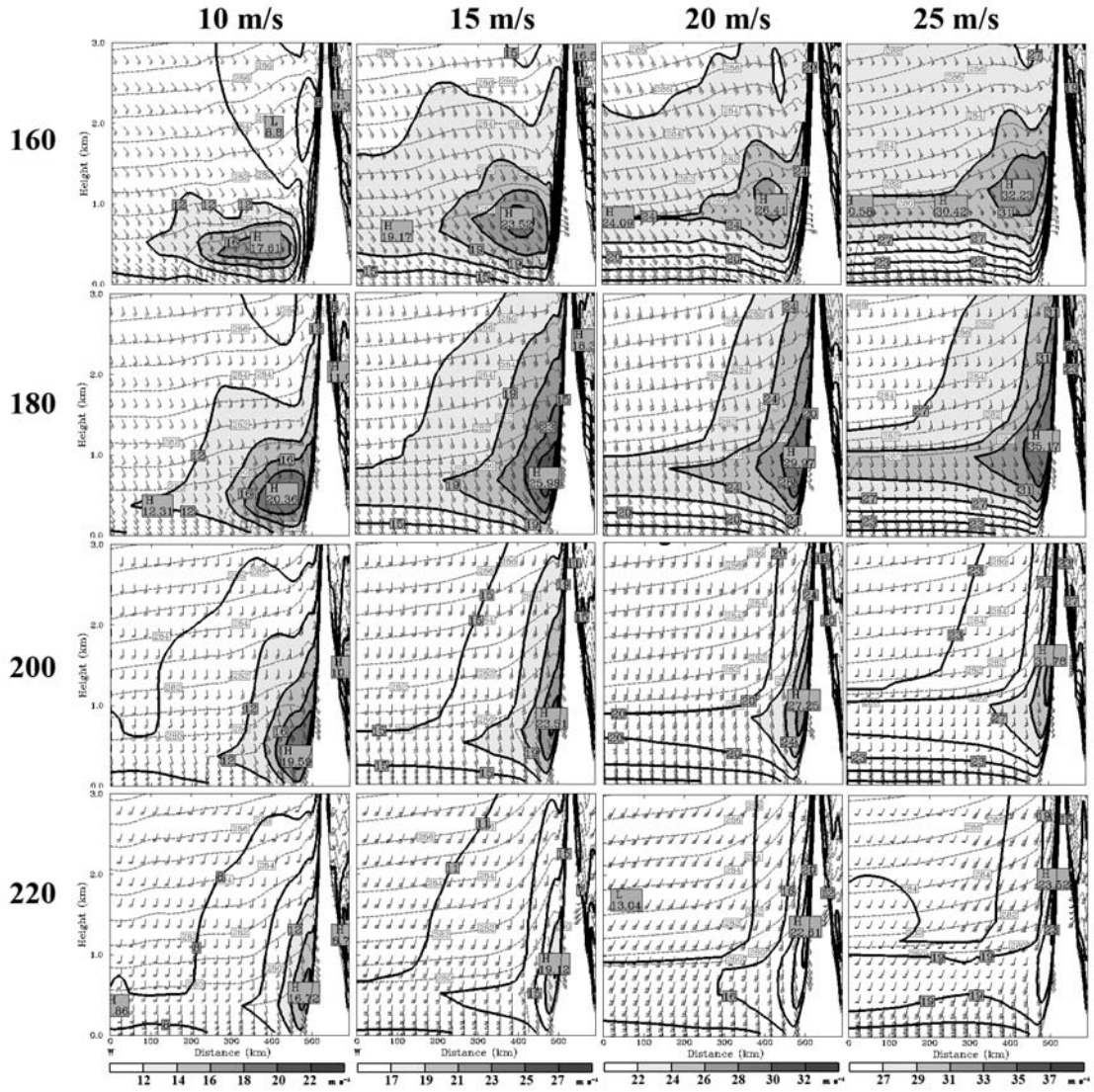

Figure 4.24 Cross-sections of wind speed (gray shade every 2 m s^{-1}), wind barbs (full barb = 10 kts), and potential temperature (dashed gray every 1 K) taken across A-A' for simulations initialized with cold pool ΔT=-10 Celsius as a function of wind speed (columns) and wind direction (rows).

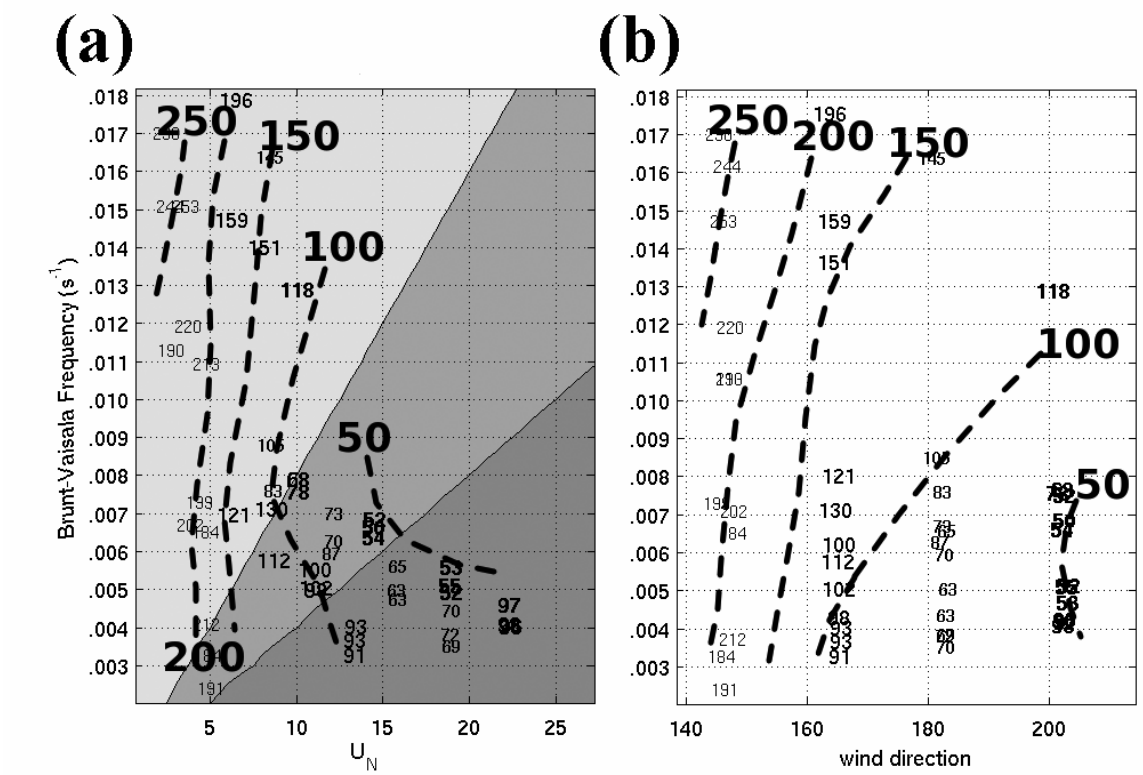

Figure 4.25 Total offshore extent (numbers and dashed every 25 km) as a function of N and (a) U_n and (b) wind direction. The variations in the size and thickness of the numbers are relative to the initialized wind direction (see Fig. 4.15).

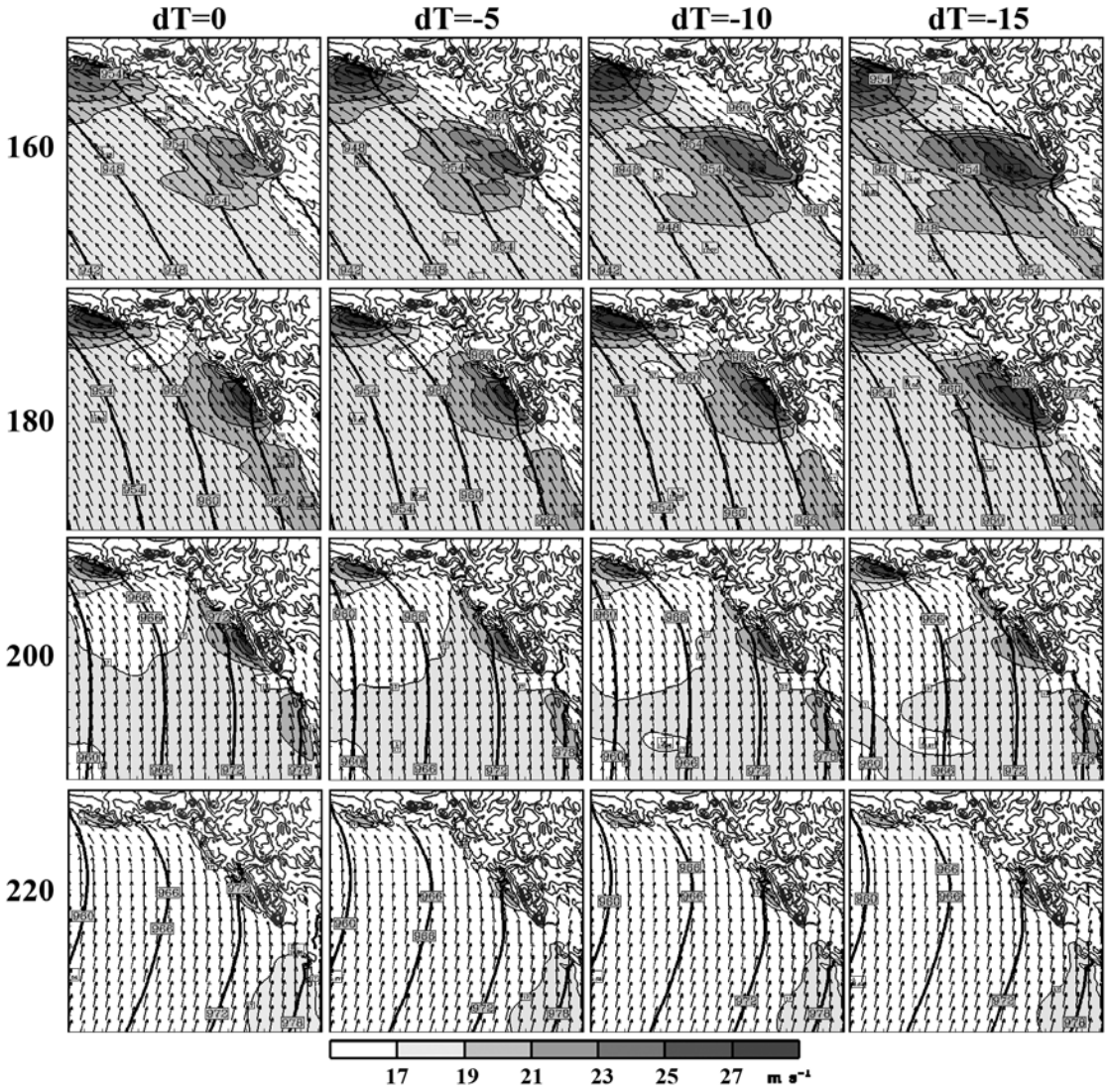

Figure 4.26 Wind speed (gray shade every 2 m s^{-1}) and pressure (black every 4 mb) at 500 m ASL for simulations initialized with a constant wind speed of 15 m s^{-1} and N = 0.01 s^{-1} as a function of cold pool strength (^{o}C; columns) and wind direction (degrees; rows).

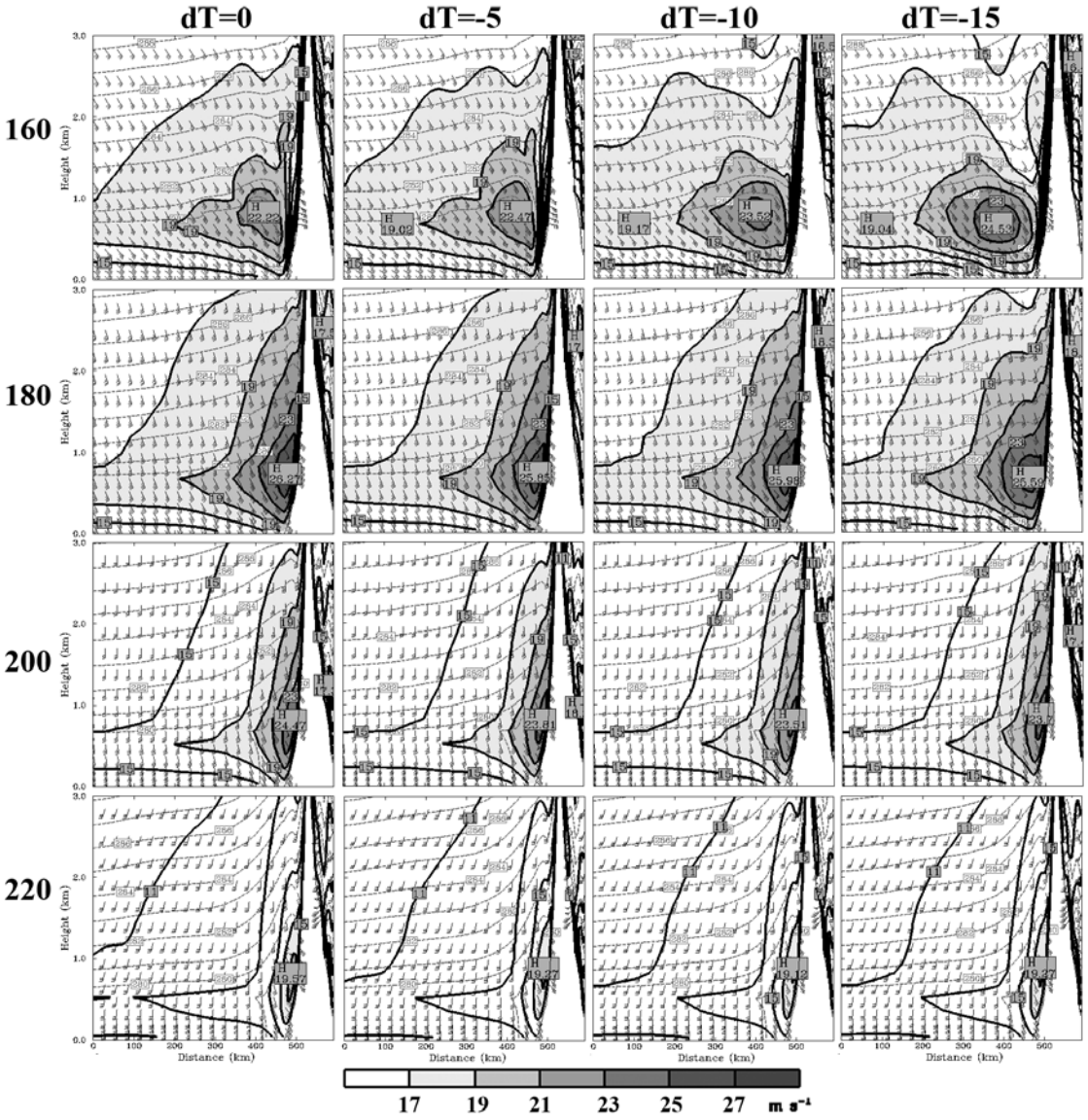

Figure 4.27 Cross-sections of wind speed (gray shade every 2 m s^{-1}) and potential temperature (dashed gray every 1 K) taken across A-A' for simulations initialized with a constant wind speed of 15 m s^{-1} and N = 0.01 s^{-1} as a function of cold pool strength (^{o}C; columns) and wind direction (degrees; rows).

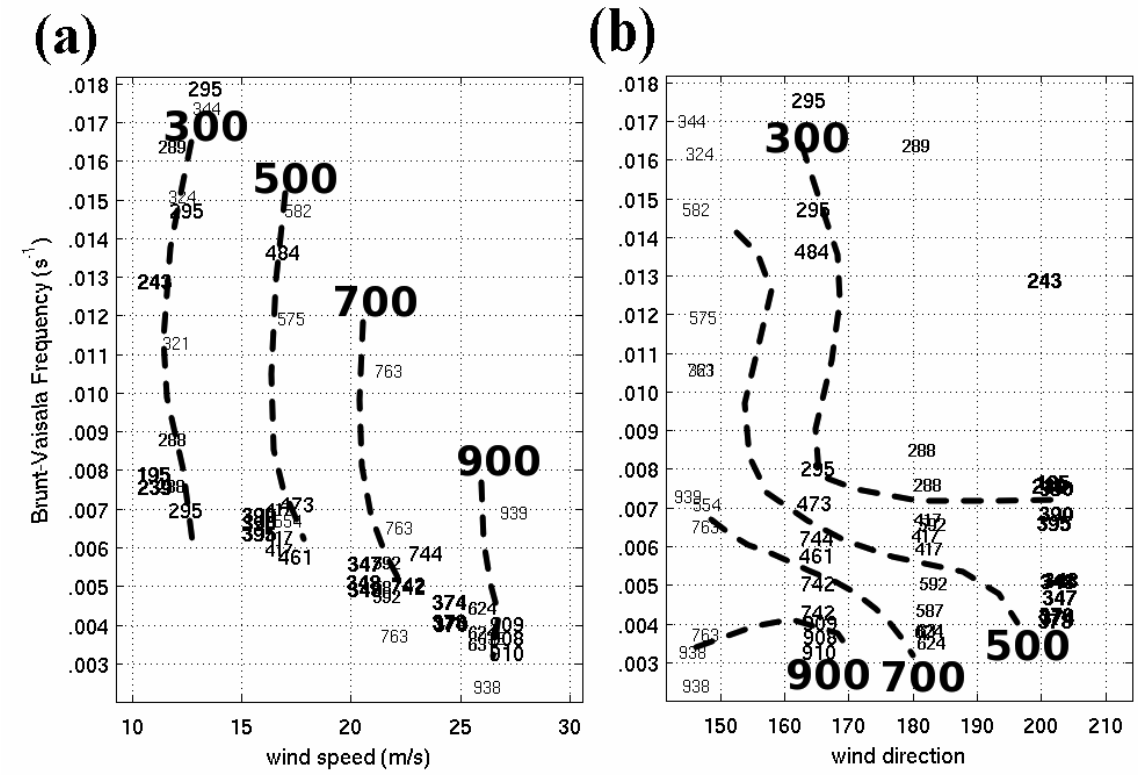

Figure 4.28 Hybrid barrier jet height (m) as a function of Brunt-Väisälä frequency (s^{-1}) and (a) wind speed (m s^{-1}) and (b) wind direction (degrees). The variations in the size and thickness of the numbers are relative to the initialized wind direction (see Fig. 4.15).

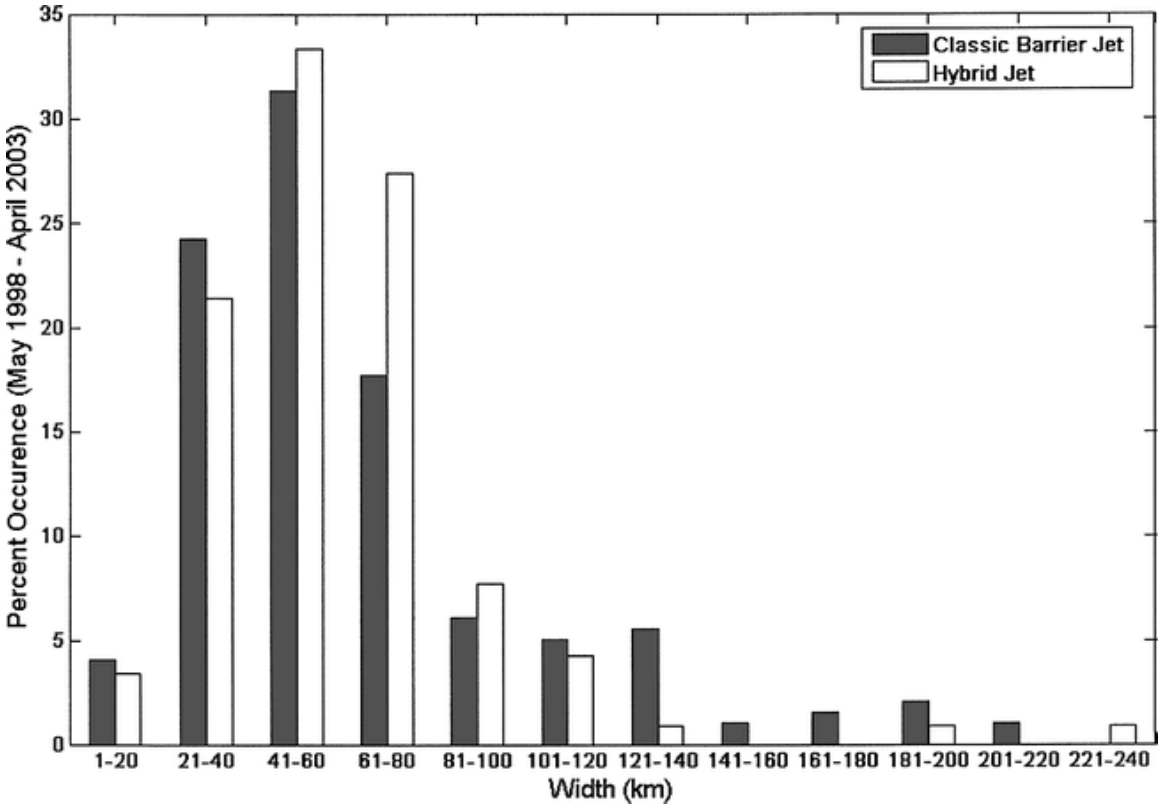

Figure 4.29 Jet width distribution for the classical and hybrid barrier jets in the Loescher et al. (2006) climatology. The horizontal axis is the SAR-derived width in 20-km bins. The histogram includes both classical (gray) and hybrid barrier jets (white). From Loescher et al. (2006; their Fig. 14).

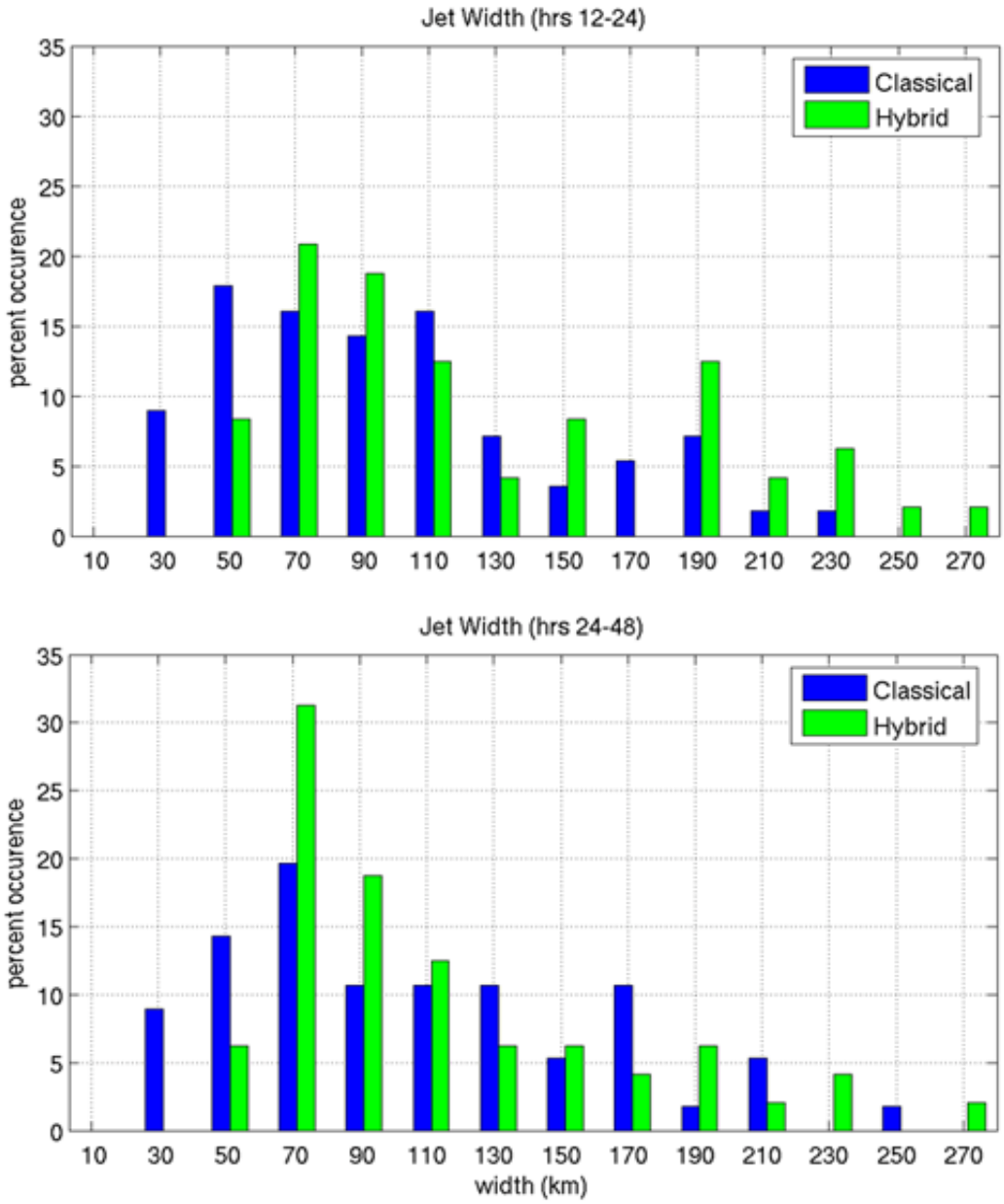

Figure 4.30 Jet width distribution for the simulated classic and hybrid jets. The horizontal axis is the measures width in 20-km bins (± 10 km from the labeled distance). The histogram includes both classical (blue) and hybrid (green) barrier jets.

Chapter V:

Evaluation and modification of scale analysis and linear theory of coastal barrier jets over southeast Alaska

5.1 Overview

The prediction of coastal barrier jet wind speeds and their offshore extent is important for the safety of small vessels and aircraft near the coast. The NOAA/NCEP Ocean Prediction Center issues special marine warnings if wind gusts exceed 34 knots (~17 m s^{-1}) (Chelton et al. 2006), which are frequently exceeded during barrier jet events along the Alaskan coast (Loescher et al. 2006). Improvement in forecasting of barrier jets can help one anticipate the risk level and the extent of the region where rough seas and low-level turbulence exists.

To improve our understanding of the properties of coastal barrier jets, the idealized barrier jet simulations in chapter 4 were used to investigate the applicability of the scale analysis of terrain-forced flows presented in Overland and Bond (1995) (hereafter OB95) and the linear theory of flow over a plateau (Braun et al. 1999a, hereafter BR99). Admittedly, neither scale analysis nor linear theory can be expected to capture all the properties of coastal jets, due to the jets highly transient nature and considerable spatial and temporal wind and stability inhomogeneities; however, some of the fundamental assumptions and interpretations need further examination. Modifications are proposed to more accurately quantify the offshore extent of the coastal barrier jets of Alaska.

5.2 Offshore extent of the coastal jets

a. The scale analysis of Overland and Bond (1995)

OB95 used the Rossby radius of deformation, $L_R = Nh/f$, for determining the offshore extent of the coastal barrier jets, with the appropriate h is dependent upon the flow regime, which has also been used by several other investigators (Chen and Smith 1987; Doyle 1997; Cox et al. 2005; among many others). For $Fr < 1$, the flow is more blocked and OB95 noted that the height of the wind perturbation along the terrain (barrier jet) is given as the gravity height, $h = U/N$, since the blocked flow often does not extend up to the height of the mountain (h_m). Inserting the gravity height into (eq. 1.2) yields a

Rossby radius of $L_R = U_n/f$ (eq. 1.4). For $Fr > 1$, h_m is a more appropriate height scale, resulting in the Rossby radius, $L_R = Nh_m/f$ (eq 1.2).

The work of OB95 has never been tested against a large enough sample of cases to meaningfully assess the overall accuracy in determining the offshore extent of barrier jets. Using the idealized classical jet simulations in chapter 4 (Table 4.1), the two Rossby radius expressions above were compared to the simulated jet widths. For all *Fr* numbers, the estimates from the high *Fr* relationship ($L_R = Nh_m/f$) agreed more with the simulated jet widths than the low *Fr* relationship ($L_R = U_n/f$) (Table 5.1). The *e*-folding jet widths from the low *Fr* relationship are negatively correlated (-0.56 to -0.76) with the simulated offshore extents for both classical and hybrid jets types as well as for low $Fr < 1$ events (-0.51 to -0.87). In contrast, the high *Fr* relationship results in a positive correlation (0.49 to 0.59) with all simulated jets as well as for the $Fr < 1$ cases (0.33 to 0.56).

The negative correlation between the measured offshore extent and the estimates from the low *Fr* relationship suggests that L is proportional to U_n^{-1}. Therefore, the U_n/f relationship cannot explain variations of jet width for the low *Fr* regime as suggested by BR99, since an increase in U_n would imply a wider jet, which is in contrast to the narrowing of the simulated jets with an increase in U_n (cf. Fig. 4.13 and 4.21). Physically, an increase in U_n results in a higher *Fr*, which favors less blocking and a narrower jet[9].

The two Rossby radius relationships of OB95 were verified quantitatively for classical and hybrid jets by computing mean errors (ME) using the simulated offshore extent as the true value (Table 5.1). The results show that despite the negative correlation noted above, the MEs using the low *Fr* relationship for all simulations (1 to -15 km error) are slightly less than the high *Fr* relationship (4 to 64 km). However, the small ME for the low Fr relationship (U_n/f) is largely from the cancellation of negative (positive) errors found in low (high) *Fr* regimes. For $Fr < 1$, the low *Fr* relationship significantly underestimates the jet widths (-21 to -65 km) for both classical and hybrid jets, but has a positive bias (> 52 km) when $Fr > 1$. The high *Fr* relationship generally has positive ME (4 to 64 km) for both jet types. The mean absolute errors (MAEs) for all classical jets were 72 and 59 km for U_n/f and Nh_m/f, respectively and 87 and 59 km for the hybrid jets, respectively. For Fr < 1, the MAEs for U_n/f and Nh_m/f, were 66 and 60 km, respectively, for the classical jets, and 93 and 76 km, respectively, for the hybrid jets.

Overall, the high *Fr* relationship ($L = Nh_m/f$) seems more appropriate than the low Fr relationship ($L = U_n/f$) proposed by OB95, since it is positively correlated with the measured jet widths and it has lower MAEs for $Fr < 1$. An examination of the energetics of flow blocking in the next section will reveal that the gravity height (in the low *Fr* relationship) is not an appropriate scale height for quantifying the offshore extent of the coastal barrier jets. This will lead to an alternate approach.

b. Sheppard's airflow model of orographic lifting.

Sheppard (1956) postulated that the amount of kinetic energy in a stably stratified flow impinging on a barrier determines whether the flow will travel over a mountain or become blocked by the barrier. In other words, the potential energy gained by lifting a parcel at height h_1 to higher elevation h_2 exactly balances the kinetic energy lost. The

[9] This assumes near steady state. If the *Fr* is low and there is a sudden increase in U_n, there should be a momentary mass accumulation along the barrier, leading to a wider jet; however, this imbalance will undergo adjustment and the steady state argument should apply.

lowest streamline height, h_d, for which the incoming flow will have enough kinetic energy to pass over the mountain, can be determined from Bernoulli's theorem, with variations in pressure and internal energy neglected (Batchelor 1967):

$$B = KE + PE \tag{5.1}$$

The potential energy required to lift a parcel of unit mass to h_m is essentially the convective inhibition (CIN), calculated from h_d to h_m,

$$PE = CIN = -\frac{g}{\bar{\theta}} \int_{h_d}^{h_m} [\theta_p(z) - \theta_a(z)] dz \tag{5.2}$$

where θ is potential temperature, g is gravity, z is height, θ_p and θ_a are the potential temperatures of the parcel and ambient air, respectively. Assuming dry adiabatic ascent, $\theta_p(z)=\theta_a(0)$, and constant stratification, $\theta_a(z) = \theta_a(0) + z\, d\theta/dz$, the potential energy becomes:

$$\begin{aligned} PE &= -\frac{g}{\bar{\theta}} \int_{h_d}^{h_m} \left[\theta_p(z) - \theta_a(0) - z \frac{d\theta_a}{dz} \right] dz \\ &= N^2 \int_{h_d}^{h_m} (z) dz \end{aligned} \tag{5.3}$$

where $N^2 = g/\theta_o(\partial\theta/\partial z)$ is the Brunt–Väisälä frequency squared. This allows us to write the KE and PE balance as:

$$\frac{1}{2} U^2(h_d) = N^2 \left(\frac{h_m^2 - h_d^2}{2} \right) \tag{5.4}$$

where h_d is the height of the streamline which divides the air that travels over the mountain top (above) from the blocked flow (below) (Fig. 5.1). For the idealized barotropic simulations of chapter 4, constant $U(z)$ and $N(z)$ simplify (5.4) to:

$$h_d = h_m(1 - Fr) \tag{5.5}$$

or

$$h_d = h_m - U/N, \tag{5.6}$$

which is known as Sheppard's formula (Sheppard 1956). Thus, the air that reaches the mountaintop has been lifted by $h_m - h_d = U/N$. From this perspective, the gravity height, $h = U/N$, used by Overland and Bond (1995) should not be interpreted as the height of the blocked flow, but rather the depth of the upstream unblocked flow extending below crest level. This may explain the negative correlation between OB95's low Fr relationship ($L_R = U_n/f$) and the measured barrier jet widths in the idealized simulations since, an increased gravity wave height implies less blocking and a narrower jet. Sheppard's formula also implies that the relevant scale height for the blocked flow is the dividing streamline height h_d.

c. Application of the dividing streamline to determine the offshore extent of barrier jets.

Sheppard's dividing streamline approach has been utilized in atmospheric trace studies (Rowe 1980; Strimaitis et al. 1983) and orographic cloud production (Kleissl et al. 2007), but has not been formally applied towards the determination of barrier jet width. Hunt and Snyder (1980) performed towing-tank experiments, which broadly confirmed Sheppard's model for small hills and ridges; however, evaluations by numerical modeling (Arritt et al. 1987), isentropic analyses (Trombetti and Tampierri 1987), and upstream plume releases (Sprangler 1987) have shown departures from this

theory. For example, the isentropic analysis of Trombetti and Tampierri (1987) detected an upstream influence for $Fr > 1.5$ over a mesoscale mountain chain with a mean height of ~1500 m ASL, whereas Sheppard's model suggests all flow will surmount the barrier when $Fr > 1$. Arritt et al. (1987) showed that Sheppard's model underestimated h_d for Fr ~ 0.5-1.0 by ~20%, while it slightly overestimated h_d for $Fr < 0.5$.

Some of the departure of Sheppard's model from the observed or simulated values is related to its inherent assumptions. Sheppard (1956) assumed an inviscid flow and that the pressure fluctuations surrounding the mountain were zero; therefore, the portion of the kinetic energy lost during forced ascent over the mountain is completely converted to potential energy when the fluid parcel reaches the summit. This is not accurate since pressure perturbations by the mountain (e.g. gravity waves) can create accelerated flows on the same order of magnitude as the ambient flows (Smith 1982, 1989) and frictional effects increase the upstream flow deceleration (Braun et al. 1999b). The rotation of the earth was also neglected; however, Smith (1980) suggested that the Coriolis force may be neglected for isolated mountains with horizontal dimensions < 50 km, such that flows of ~10 m s^{-1} typically have Rossby numbers (U/fL) > 1. The Fairweather mountains of Alaska have a small half-width of $L_m < 50$ km, but the alongshore dimensions exceed 100 km and the inland plateau (L_{plat} ~ 500-1000 km) effects were shown to be important in determining the structure of the jets (Chapter 4). In order to successfully apply Sheppard's model to the barrier jet width problem, a modified version of (eq. 5.5) is needed that can account for some of the biases produced by the above simplifications. Thus, we suggest the formula for h_d should take the form:

$$h_d = h_m(1 - \alpha Fr + \beta), \tag{5.7}$$

where α will reduce the dependence on Fr in order to correct for the biases noted by Arrit et al. (above; 1987). The constant β allows for a minimum height of the dividing streamline, such that flows with $Fr \geq 1$ may still result in some partial blocking. As in Trombetti and Tampierri (1987), the values for α and β can be determined by least-squares regression of the measured offshore extent, L_{jet}, against the ambient Fr, which are related through (eq. 5.7) and the Rossby radius of deformation (eq. 1.2):

$$L_{jet} \approx L_{Rd} = \frac{Nh_d}{f} = \frac{Nh_m}{f}(1 - \alpha Fr + \beta). \tag{5.8}$$

Using data from the Alpine field experiment (ALPEX; Kuettner 1986) on easterly flow over the Dinaric Alps (~1500 m mean height), Trombetti and Tampierri (1987) found values for α ranging between 0.5-0.75 and values for β of 0.3-0.6, with variations occurring due to three-dimensional changes of the impinging flow. The values of α and β may also be dependent on the mountain shape and the type of barrier jet, since the gap outflows increase the offshore extent of the hybrid barrier jets (chapter 4). By regressing the simulated barrier jet widths of chapter 4 with the measured ambient Froude numbers characterizing the flow ~1000 km upstream of the coast, α and β were found to be 0.51 and 0.02, respectively, for the classical jets (hours 24-48) and 0.37 and 0.09, respectively, for the hybrid jets (hours 12-24). These sets of coefficients had R-squared values of 0.58 and 0.49 for the classical and hybrid jets, respectively. The values for α and β are different from than found by Trombetti and Tampierri (1987); however, they tuned α and β for a different barrier and for a different application. Since it may be difficult to know when to apply α and β for a classical or a hybrid jet in an operational setting for the Fairweather Mountain region, a combined set of classical and hybrid jet simulations were

also used to compute an α and β of 0.43 and 0.05, respectively. A reasonable approximation to the estimated α and β is 0.5 and 0, respectively. This approximation adds a factor (1-*Fr*/2) onto the standard Rossby radius,

$$L_{jet} \approx \frac{Nh_m}{f}\left(1-\frac{Fr}{2}\right), \tag{5.9}$$

which can correct for the hypervariant dependence on *Fr* found by Trombetti and Tampierri (1987) and should adequately extend the use of Sheppard's model to flows with $Fr < 2$.

The offshore extent of the barrier jet predicted by (eq. 1.4), (eq. 1.2), and (eq. 5.9) were plotted against the simulated values for the classical (Fig. 5.2a-c) and hybrid (Fig. 5.2d-f) barrier jets. The negative correlation between (eq. 1.4) and the measured offshore extent is evident in Figs. 5.2a and 5.2d, since the measured quantities decrease as U_n/f increases. The high *Fr* relationship (Nh_m/f) (eq. 1.2) and the modified relationship (Nh_d/f) (eq. 5.9) result in considerable variability in jet width (Figs. 5.2b-c and 5.2e-f), but using h_d reduces the overestimated widths for $Fr > 0.5$ (Figs. 5.3a and b); thus, this approach reduces the errors for weak-moderate jets by 10-50% for the classical jets, but reduces the jet widths too much (by 50-100%) for $Fr > 1$. The overall correlations between (eq. 5.9) and the measured widths is slightly higher (0.63 − 0.70) than the unmodified L_R (eq. 1.2) (0.49 − 0.56) (Table 5.1). The overall ME for L_{Rd} has a slightly lower bias (-38 to 14 km) than that for L_R (4 − 64 km), and the MAE was 38 − 55 km for L_{rd} (eq. 5.9), while the unmodified relationship had MAE of 61-75 km. These results suggest that the modified dividing streamline height relationship (eq. 5.9) is a more appropriate scale height for determining the offshore extent of coastal barrier jets than the mountain height (h_m) or the gravity height ($h = U_n/N$). When applied to the SARJET cases using the observed data in chapter 3, (eq. 5.9) accurately estimates the offshore extent of the classical and hybrid jets, yielding 75 and 126 km, respectively.

5.3 Wind speed enhancement of the coastal barrier jets.

a. The scale analysis of Overland and Bond (1995)

The scale analysis of OB95 uses the semi-geostrophic approximation and the thermal wind relation to yield the following relationship for the along-barrier wind speed enhancement:

$$\Delta V \approx \frac{gh\Delta\theta}{fL\theta_0} = \frac{N^2h^2}{fL} \tag{5.10}$$

(their eq. 3) where the appropriate *h* and *L* was dependent upon the *Fr* number flow regime. For $Fr < 1$, the gravity wave height, $h = U/N$, and $L=U/f$ yields $\Delta V = U_n$ (eq. 1.5), while for $Fr > 1$, $h = h_m$ and $L = Nh_m/f$ results in $\Delta V = Nh_m$ (eq. 1.6)[10]. Braun et al. (1999a) noted that the low *Fr* relationship (eq. 1.5) yields a value of $\Delta V/U_n = U_n/U_n = 1$, suggesting that the gravity height is a poor scale height for this application as well.

The two ΔV relationships of OB95 (eqs. 1.5 and 1.6) were correlated with our simulated wind speed enhancement in the along-barrier direction in chapter 4 (Table 5.2).

[10] To make OB95s relationships of wind speed enhancement comparable to our definition, equations (1.5) and (1.6) were reformulated as $\Delta V/U_n$, where U_n is the time varying barrier-normal velocity component > 1000 km upstream.

For the full set of simulations, there is a strong positive correlation (0.81 to 0.94) between the flow perturbations predicted by the high *Fr* relationship ($\Delta V = Nh_m$) and the model simulated wind speed enhancements. Meanwhile, the OB95 low *Fr* relationship ($\Delta V = U_n$) has no correlation with the simulated wind enhancements, since the estimated wind speed enhancements become equal to one after normalizing with respect to U_n.

Since the maximum wind speed enhancement is found for $Fr \sim 0.3-0.4$ (U_n ~3-6 m s^{-1}) for the classical jets (Fig. 4.11), the *Fr* number range to be investigated was changed to examine the wind speed enhancement. A $Fr = 0.5$ was used to partition the set of simulations in order to provide more meaningful correlations between the relationships and the simulated values. The large *Fr* relationship (eq. 1.6) is weakly correlated (0.37 to 0.57) with the simulated classical jet wind speed enhancements, but has larger correlations (0.70−0.89) for the hybrid jets for $Fr < 0.5$, while maintaining high correlations (0.79−0.95) for $Fr > 0.5$. This indicates that $\Delta V = Nh_m$ (eq. 1.6) is a more valid relationship.

The wind speed enhancement relationships (eq. 1.5) and (eq. 1.6) were further assessed by computing the ME (Table 5.2). Despite the constant wind speed enhancement estimates of unity given by the low *Fr* relationship, the overall MEs were smaller (0 to -9%) than for the high *Fr* relationship (68 to 80%). The high *Fr* relationship (eq. 1.6) consistently overestimated the wind speed enhancements for both jet types. The mean absolute errors show limited skill for both relationship, with errors of ~30% and ~56% for the low and high *Fr* relationship, respectively.

b. The linear theory of Braun et al. (1999)

The two-dimensional simulations of BR99 with broad topography also found large differences from the scale analysis results of OB95. They measured wind speed enhancements of 2-4, while noting the limitations of the low *Fr* relationship of OB95 ($\Delta V = U_n$). They suggested that the inability of the OB95 scale analysis to account for strong jets resulted primarily from the use of the gravity wave height for a height scale rather than the semi-geostrophic approximation of the coastal winds. BR99 utilized linear theory to show that the along-barrier wind speed enhancement v/U was proportional to the mountain height and width,

$$v/U \approx \frac{Fr^{-1}}{\pi}\left[1 + \ln\left(\overline{L}_2\right)\right], \tag{5.11}$$

which is an approximate form of their Eq. 20:

$$v/U = \frac{Fr^{-1}}{\pi}\left[1 + \frac{3}{4}\overline{L}_1 - \frac{\overline{L}_1}{2}\ln\left(\overline{L}_1\right)\right]_{NF} + \frac{Fr^{-1}}{\pi}\left[\ln\left|\overline{L}_2 - \overline{L}_1\right|\right]_{FF}. \tag{5.12}$$

The first term (near-field term) represents the contribution by the shortwave characteristics of the terrain and the second term (far-field term) represents the contribution by the broad plateau. The parameters $\overline{L}_2 = \mathrm{Ro}_2^{-1} = fL_{plat}/U_n$ and $\overline{L}_1 = \mathrm{Ro}_1^{-1} = fL_M/U_n$ and L_{plat} and L_M are the widths of the plateau and mountain slope half-width, respectively. For use along the coastal orography of Alaska, we let $L_{plat} = 500$ km and $L_M = 50$ km. Equations (5.11 and 5.12) suggest that the wind speed enhancement scales as Fr^{-1} and it is dependent on the width of the barrier.

Although linear theory is formally invalid for $Fr < 1$, Smolarkiewicz and Rotunno (1990) showed a good overall agreement with their numerical results down to the point of

near stagnation of the impinging flow ($Fr \sim 0.5$). If a lower limit of $Fr \sim 0.4$ is imposed on (eq. 5.11), in order to avoid the singularity at $Fr = 0$ and remain approximately within the bounds of linear theory, estimates from (eq. 5.11) can be compared over the same approximate range of N and U_n as the set of idealized simulations of chapter 4 (Fig. 5.4). Figure 5.4 shows that the calculated wind speed enhancements compare well with our measured wind speed enhancements (cf. Fig 4.11a and 4.18a). The magnitude of the wind speed enhancement agrees well with that measured in chapter 4.

The correlations between BR99's (eqs. 5.11 and 5.12) and the coastal wind speed enhancement in the simulations in chapter 4 are high for the both classical and hybrid jets (0.80−0.97) with the approximate form (eq. 5.12) generally slightly higher correlated the full equation (eq. 5.12) (Table 5.2). For classical jets with $Fr < 0.5$, both forms have relatively poor correlations (0.02 to 0.35), but much larger correlations (0.65−0.78) for hybrid jets when $Fr > 0.5$. The MEs for the linear theory of BR99 are much lower than the high Fr relationship of OB95 (Table 5.2), but overestimate jet widths when $Fr > 0.5$ and underestimate jet widths when $Fr > 0.5$. The MAEs for eqs. (eq. 5.11) and (eq. 5.12) were also lower (47 and 51% error, respectively) than OB95's high Fr relationship (eq. 1.6) (84%).

In order to illustrate how the estimated values of barrier-parallel wind speed enhancement (v'/U_n) compare to the simulated values, the wind speed enhancement predicted by OB95's low Fr relationship (eq. 1.5), high Fr relationship (eq. 1.6), and BR99's (eq. 5.11) and (eq. 5.12) were plotted against the simulated values for the classical (Figs. 5.5a-d) and hybrid (Figs. 5.5e-h) barrier jets. The high Fr relationship of OB95 (eq. 1.5) and the relationships of BR99 (eqs. 5.11 and 5.12) all generally overestimate the wind speed enhancement for $Fr < 0.5$ and underestimate the enhancement for $Fr > 0.5$ for both types of jets (Figs. 5.6 a, b). The simplicity and fair overall performance of OB95's high Fr relationship justifies its use in future barrier jet work; however, the approximate form of BR99's wind speed enhancement (eq. 5.11) provides the best overall skill and should perform best for regions with broad orography.

5.4 Discussion

In order to quantify the properties of coastal barrier jets, the previous work of OB95 and BR99 was compared against a set of three-dimensional idealized barrier jet simulations spanning a wide range of Froude numbers. A modification of the Rossby radius of deformation was proposed to more accurately describe the offshore extent of the coastal barrier jets.

For determining the offshore extent of the coastal barrier jets, it was found that the high Fr relationship of OB95 ($L = Nh_m/f$) performed better than the low Fr relationship ($L = U_n/f$) throughout the entire set of idealized simulations. The main reason for the poor performance of the low Fr relationship was shown to be the use of the gravity wave height, given by $h = U/N$, in agreement with BR99. The implementation of the dividing streamline concept of Sheppard's model for determining the proper scale height resulted in a modified form, $L = Nh_d/f = Nh_m/f(1\text{-}Fr/2)$, which was shown to improve the correlations with the simulated offshore extent of the jet. The modified form also helped to reduce the errors of the estimated offshore extents, especially for $0.5 < Fr$

< 1.5, since OB95's high *Fr* relationship often overestimated the offshore extent by ~50 km for both classical and hybrid barrier jets.

For the determination of maximum wind speeds, the high *Fr* relationship ($\Delta V = Nh_m$) of OB95 was found to better correlate with the measured values than the low *Fr* relationship ($\Delta V = U_n$) for the full range of *Fr*. However, the high *Fr* relationship overestimated the maximum wind speed enhancements for $Fr < 0.5$ by ~50-100%. The two-dimensional linear theory of BR99, which relates the wind speed enhancement to the non-dimensional mountain height and the inland plateau width, was well correlated with both classical jets (0.77−0.85) and hybrid jets (0.94−0.97) (Table 5.2). All relationships tested seem to struggle more with classical jets when $Fr < 0.5$, with correlations typically less than 0.50, but had much higher correlations (> 0.73) for $Fr > 0.5$. The poorer performance for low *Fr* regime was likely due to the inability of linear theory (and scale analysis) to address the nonlinear nature of strongly blocked flows.

The limited success of applying any particular relationship to the determination of coastal barrier jet properties can result from the considerable spatial and temporal inhomogeneities in the wind and stability inherent in observed data; however, a thorough evaluation of these relationships, by use of idealized simulations, helped to shed light on their usefulness throughout a wide range of *Fr* flows. Although the proposed modified Rossby radius relationship (eq. 5.9) was formulated to fit the idealized simulations, it also accurately estimated the offshore extent of the SARJET IOPs (chapter 3) and may help quantify the structure of barrier jets in future case studies.

Tables

Barrier Jet Width	Jet type	Variable	All simulations (h 12-24, h 24-48)	Fr < 1 (h 12-24, h 24-48)	Fr > 1 (h 12-24, h 24-48)
Correlations	classical	$L=U_n/f$	**-0.56, -0.56**	**-0.54, -0.51**	0.25, -0.10
		$L=Nh_m/f$	**0.52, 0.56**	**0.33, 0.37**	0.45, 0.15
		$L=Nh_d/f$	**0.66, 0.70**	**0.54, 0.58**	0.44, 0.35
	hybrid	$L=U_n/f$	**-0.74, -0.76**	**-0.85, -0.87**	**-0.66, -0.85**
		$L=Nh_m/f$	**0.59, 0.49**	**0.56, 0.51**	**-0.60, 0.73**
		$L=Nh_d/f$	**0.66, 0.63**	**0.64, 0.63**	0.08, 0.11
Mean bias errors (km)	classical	$L=U_n/f$	5, 1	-21, -26	90, 81
		$L=Nh_m/f$	64, 48	72, 53	37, 30
		$L=Nh_d/f$	14, -2	28, 8	-31, -31
	hybrid	$L=U_n/f$	-15, 1	-65, -46	57, 52
		$L=Nh_m/f$	33, 4	56, 44	1, -11
		$L=Nh_d/f$	-21, -38	15, -23	-52, -55

Table 5.1 Correlations (top) and mean errors (bottom) of barrier jet width determined from scale analysis or linear theory. The bold values represent correlations with p-values < 0.05, testing the hypothesis of no correlation against the alternative that there is a non-zero correlation.

Wind Speed Enhancement	**Jet type**	**Variable**	**All simulations** (h 12-24, h 24-48)	**Fr < 0.5** (h 12-24, h 24-48)	**Fr > 0.5** (h 12-24, h 24-48)
correlations	classical	$\Delta V=U_n$	0.00, 0.00	0.00, 0.00	0.00, 0.00
		$\Delta V=Nh_m$	**0.81, 0.81**	**0.57**, 0.37	**0.88, 0.87**
		BR99 approx	**0.85, 0.80**	0.35, 0.06	**0.79, 0.80**
		BR99 full	**0.80, 0.77**	0.34, 0.02	**0.73, 0.76**
	hybrid	$\Delta V=U_n$	0.00, 0.00	0.00, 0.00	0.00, 0.00
		$\Delta V=Nh_m$	**0.94, 0.85**	**0.89, 0.70**	**0.88, 0.93**
		BR99 approx	**0.94, 0.97**	**0.65, 0.72**	**0.92, 0.95**
		BR99 full	**0.94, 0.96**	**0.69, 0.78**	**0.91, 0.94**
Mean bias error (%)	classical	$\Delta V=U_n$	0, -8	-18, -21	42, 31
		$\Delta V=Nh_m$	79, 68	86, 91	7, -2
		BR99 approx	50, 30	66, 46	-10, -18
		BR99 full	63, 38	77, 53	-10, -17
	hybrid	$\Delta V=U_n$	-9, -5	-38, -33	31, 26
		$\Delta V=Nh_m$	80, 74	103, 96	40, 40
		BR99 approx	16, -2	45, 26	-23, -33
		BR99 full	21, 9	61, 42	-23, -32

Table 5.2 Correlations and mean % errors of wind speed enhancement estimated by scale analysis or linear theory compared to the measures idealized simulations. The bold values represent correlations with p-values < 0.05, testing the hypothesis of no correlation against the alternative that there is a non-zero correlation.

Figures

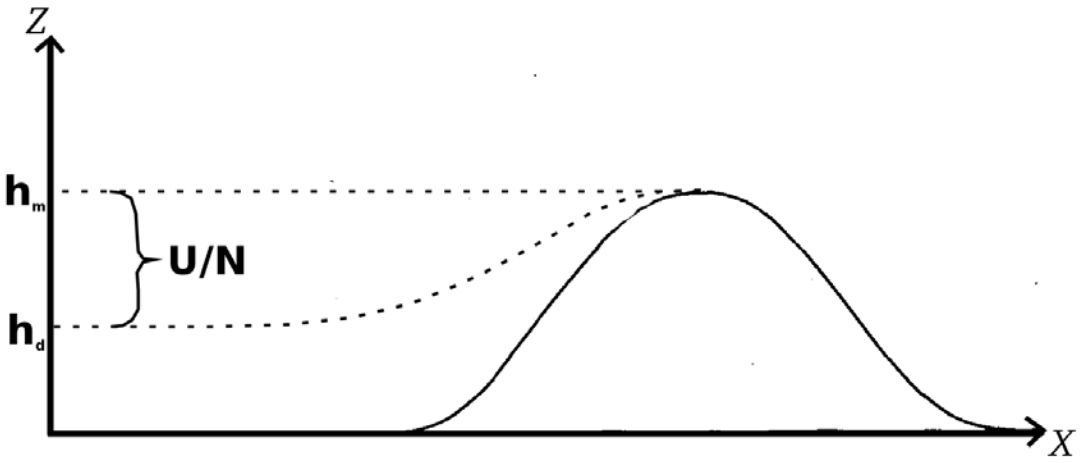

Figure 5.1 For blocked flow approaching a mountain of height h_m from the left, a dividing streamline at h_d separates the blocked flow (below) from the unblocked airflow (above), which passes over the mountain. The width of the unblocked layer is the gravity height (U_m/N).

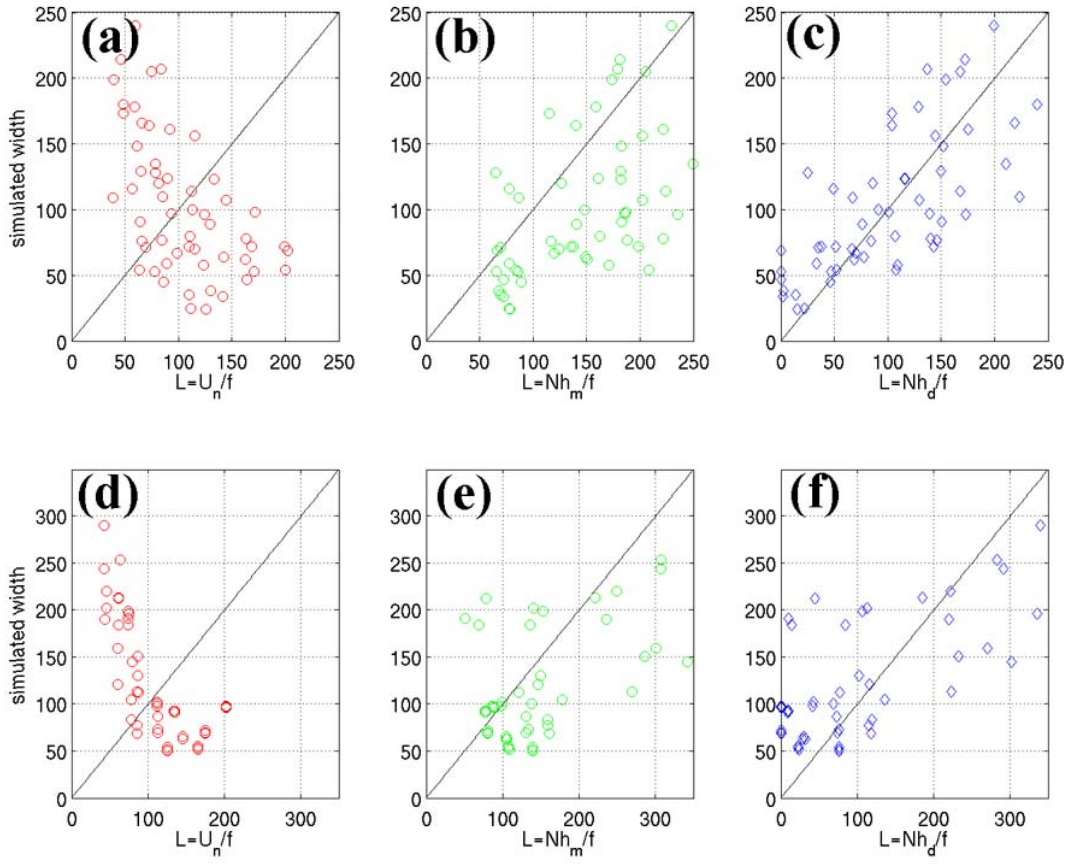

Figure 5.2 Comparison of the measured offshore extent of the coastal barrier jets and that estimated by (a) U_n/f (red), (b) Nh_m/f (green), and (c) Nh_d/f (blue) for the classical barrier jets (top row) and hybrid jets (bottom row).

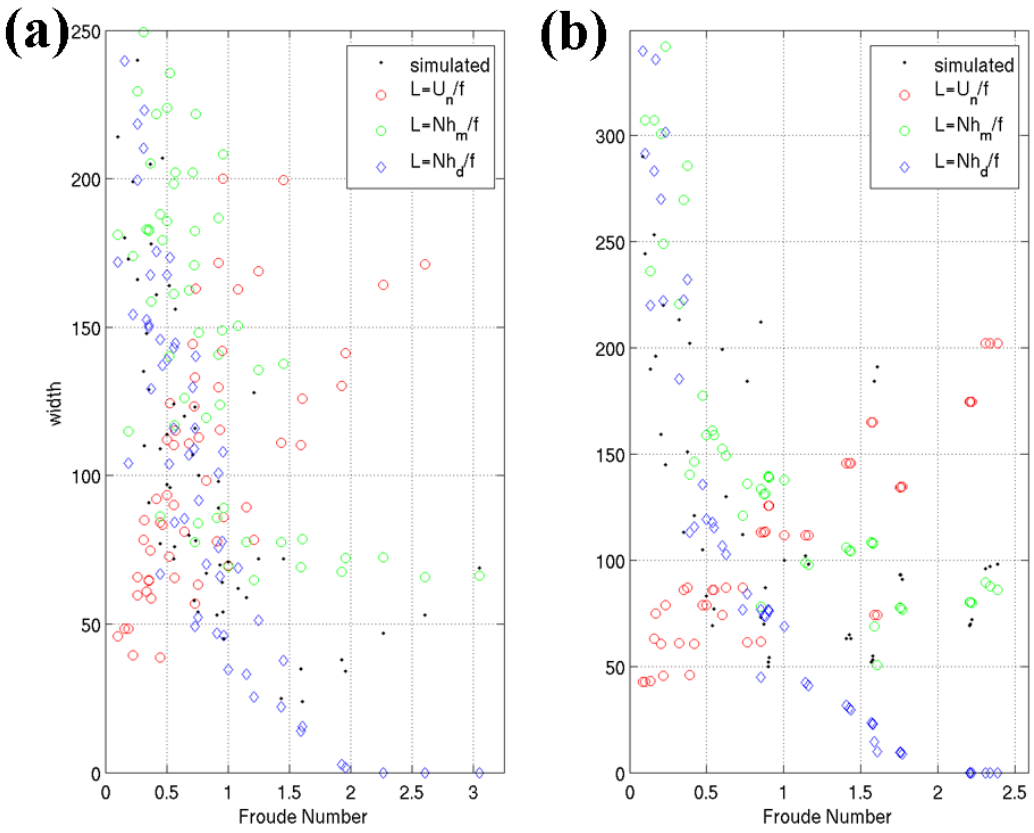

Figure 5.3 Simulated (black) and estimated widths by U_n/f, (red) Nh_m/f (green), and Nh_d/f (blue) as a function of Fr for the (a) classical jets and (b) hybrid jets.

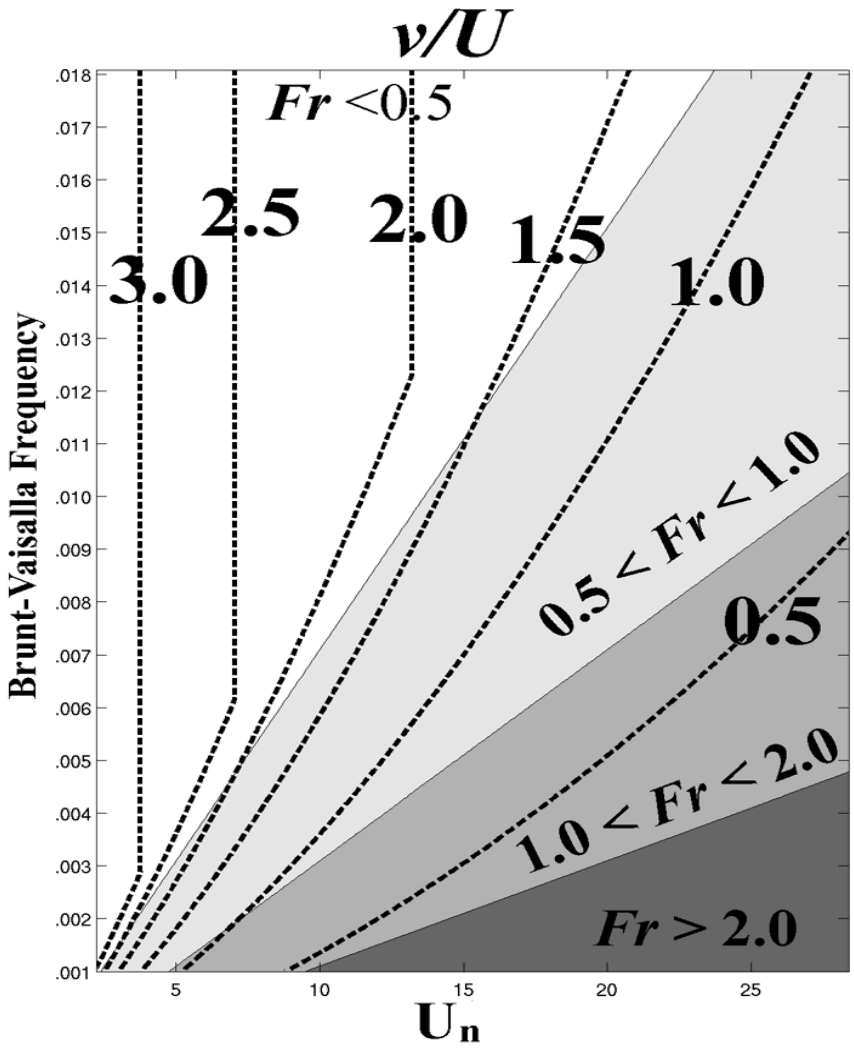

Figure 5.4 The wind speed enhancement (dashed) determined by the approximate form of BR99 (their eq. 20) as a function of Brunt-Väisälä frequency (s-1) and the barrier-normal wind speed (m s -1). The Froude number space is in gray shade and labeled in the plot.

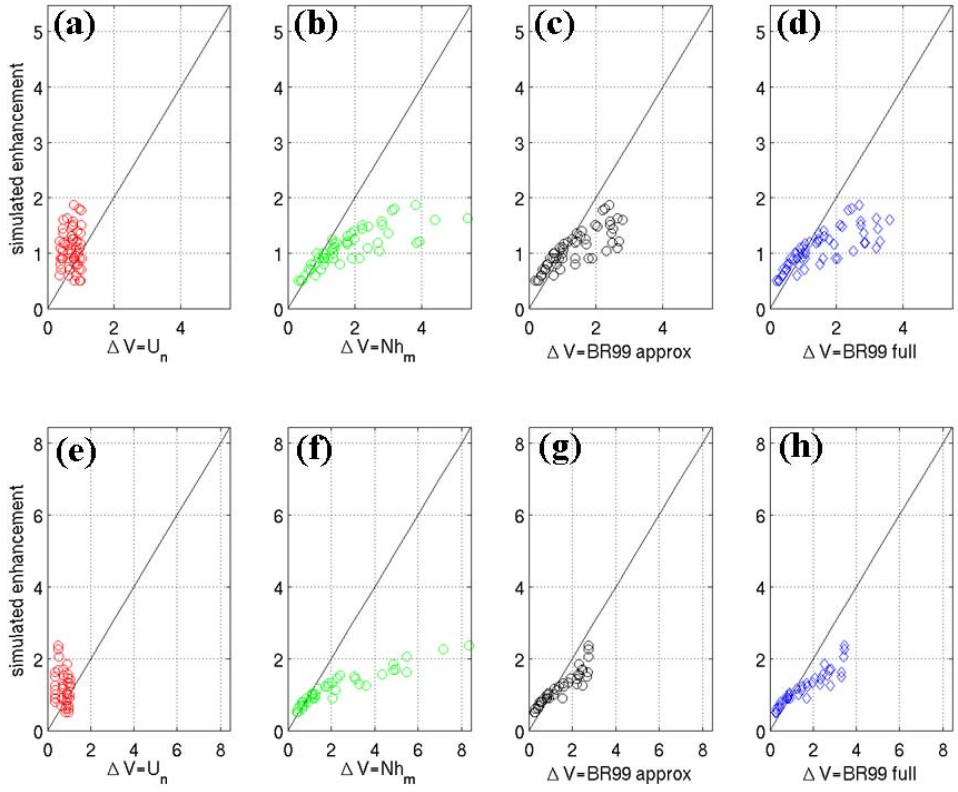

Figure 5.5 Comparison of the simulated wind speed enhancement of the classical barrier jets (top row) and hybrid jets (bottom row) with the estimates given by (a,e) U_n, (b,f) Nh_m, (c,g) BR99 approximate form, and (d,h) the full relationship.

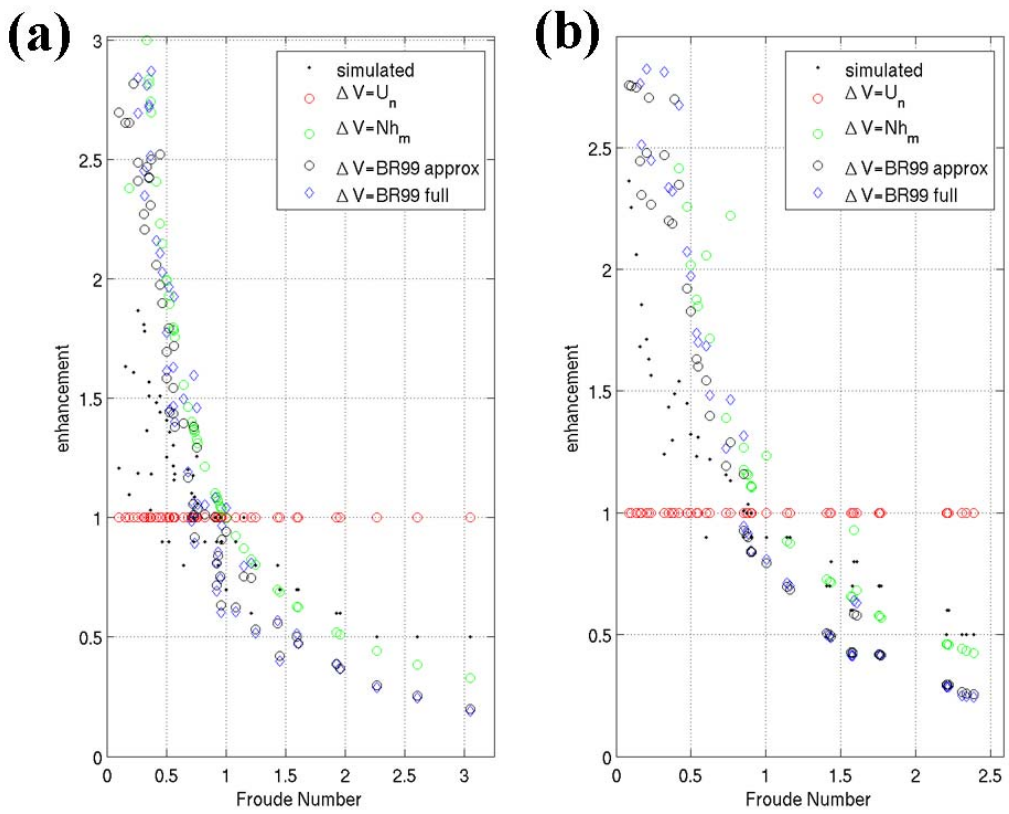

Figure 5.6 Simulated wind speed enhancement (v/U; black dots) and estimated wind speed enhancement by U_n, (red) Nh_m (green), approximate form of BR99 (black circles), and the full relationship (blue) for the (a) classical barrier jets and (b) hybrid barrier jets as a function of Fr.

Chapter VI:

Summary and Conclusions

6.1 Summary

This thesis presents a comprehensive investigation of coastal barrier jets along the steep orography of southeastern Alaska. A combination of field observations, case study simulations, and idealized simulations were used to examine the structure and intensity of both classical and hybrid barrier jets forced by a variety of ambient flows. The most important factors responsible in governing the development of the coastal barrier jets were identified and used to extend previous work on determining the offshore extent of the coastal barrier jets of Alaska.

6.2 New contributions to barrier jet research

Aircraft in situ measurements were collected during the Southeastern Alaskan Regional Jets experiment (SARJET; Winstead et al. 2006) to investigate the structure and physical processes of coastal barrier jets along the Fairweather Mountains near Juneau, Alaska. Two case studies from SARJET were completed in detail to compare the three-dimensional structural differences between a classical and hybrid barrier jet. This research represents the first detailed case studies of Alaskan barrier jets using a combination of field data and high resolution models. During IOP1, there was south-southeasterly flow preceding a landfalling trough, which became blocked by the coastal terrain and accelerated down the pressure gradient to produce a 5-10 m s^{-1} wind enhancement (maximum wind speeds ~30 m s^{-1}) in the alongshore direction near the Fairweathers. These features were similar to other "classical" barrier jet structures studied by Parrish (1982), Doyle (1997), and Yeh and Chen (2003), in which the windward pressure ridging and associated cold anomalies were produced from low-level upslope flow. In contrast, IOP7 featured greater surface pressure and colder low-level temperatures to the east (inland) of the study area than IOP1, which resulted in offshore-directed coastal gap flows below ~500 m ASL. This event was more similar to the barrier jet event near California's Petaluma Gap by Neiman et al. (2006), with pronounced gap

outflow from the adjacent mountain gap that merged with the ambient coastal jet to produce a "hybrid" barrier jet.

High-resolution simulations of both IOPs by the Penn State/NCAR MM5 down to 4-km grid spacing were performed to better understand the dynamical forcing. The MM5 was able to realistically predict the classic and hybrid jet structures observed by the aircraft. Momentum budget analysis by the model revealed the dynamical differences between the two IOPs. The gap outflow from Cross Sound during IOP7 was accelerated to the right (towards the coast) by downward mixing of onshore momentum, which produced more anticyclonic flow curvature than an inertial circle. Farther downstream (to the north), the momentum balance along the coast was more characteristic of a classical jet, with approximate geostrophy in the cross-barrier direction. The flow ~150 km upstream of the SARJET region in IOP1 was nearly geostrophic, while the upstream flow in IOP7 underwent a deceleration and forced lifting as it interacted with the gap outflow.

Model trajectories illustrated that IOP1 had onshore flow origins at low-levels, while the coastal winds during IOP7 had both gap and offshore origins. Low-level trajectories in IOP7 that originated offshore were deflected westward by the gap outflow rather than the coastal terrain. To test the impact of the gap flow on the hybrid jet, a simulation was performed with the Cross Sound gap filled (NOGAP). This produced a coastal jet with a similar maximum wind speed to the control run, but resulted in a reduced width of the coastal jet by about 40% and a shifting of the maximum winds towards the coast, which is similar to the classical jet in IOP1.

A new conceptual model of a southeast Alaskan hybrid jet was proposed, which summarized the three-dimensional structures using the IOP7 analysis as well as results from Winstead et al. (2006) and Loescher et al. (2006). For these events, the gap outflow rotates anticyclonically out of the coastal gap and merges with the ambient coastal jet adjacent to the steep coastal terrain. Unlike the classical jets (IOP1), there is a warm anomaly near the coast that resulted from the downslope flow off the southern end of the Fairweathers. A cold anomaly exists further offshore associated with the gap outflow. Above the shallow gap flow at mid-mountain level the flow is more representative of a classical barrier jet, with southerly flow deflecting and accelerating more parallel to the Fairweathers, and there is a weak cold anomaly against the barrier. Further downstream, the hybrid barrier jet structure becomes more similar to a terrain-parallel classical jet.

The generality of these SARJET results were tested by completing a set of three-dimensional idealized simulations of barrier jets along the Alaskan coast. In order to perform this task, a three-dimensional idealized initialization technique was developed, which is compatible with the MM5. This provided an efficient tool capable of generating a wide variety of initial conditions relevant for barrier jet development. This scheme was also extended to create three-dimensional idealized baroclinic waves for simulations of landfalling fronts in order to understand their interaction with barrier jets in future work. Both real and modified terrain was used to explore the influence of terrain geometry on the coastal jets and landfalling systems.

A total of 104 three-dimensional idealized simulations with the MM5 were completed down to 6-km grid spacing over the southeastern Alaskan coast. The model was initialized with varying wind speeds, wind directions, and static stabilities for a set of 56 classical barrier jet simulations, while an inland cold pool was initialized for 48 hybrid jet simulations. The diverse set of simulations produced a vast mixture of classical and

hybrid barrier jets, with large variations of width, height, and intensity, which compare reasonably to previous observational barrier jet studies (Schwerdtfeger 1975; Parish 1982; Marwitz 1982; Loescher et al. 2006; among others), as well as the SARJET IOPs of chapter 3.

The complete set of idealized simulations generated a distribution of jet widths and intensities, which compared reasonably well with the Synthetic Aperture Radar (SAR) climatology of Loescher et al. (2006) for coastal Alaska. As in the SAR analysis, there were comparable maximum wind speeds between the classical and hybrid jets and slightly wider jets for the hybrid runs. Our results suggest that the long (~250 km) tail in the frequency distribution of jet widths in Loescher et al. (2006) may be explained by events with ambient winds oriented nearly terrain-parallel (~160^{o}) and strong static stability ($N > 0.01$ s^{-1}).

When the low-level ambient flow was nearly coast-parallel with an inland cold pool, an offshore-directed gap outflow was initiated. This enhanced the offshore extent of the hybrid jets during periods of strong gap outflows, but had little effect after the inland cold pool was drained. The gap outflows also acted to shift the position of the jet maximum further away from the coast. In contrast, for onshore flows oriented more perpendicular to the coast (having a pressure gradient oriented more coast-parallel), the flow associated with the interior cold pool can not accelerate through the coastal gaps. Thus, the hybrid barrier jet structures during southwesterly ambient flows resembled the classical barrier simulations, which had no inland cold pool initialized.

The impact of the broad inland plateau was shown to rotate the upstream winds cyclonically to become more terrain-parallel 500-1000 km upstream of the coast. Simulations with the broad inland terrain removed resulted in less blocking and a weaker coastal barrier jet. The flow impinging on a wide barrier produces a time-dependent flow response, in which the mountain anticyclone begins to develop (hrs 0-12), but does not yet impact the flow well upstream of the coast. In this stage, the higher U_n creates a large pressure perturbation over the windward slopes and undergoes geostrophic adjustment within L_R of the barrier, resulting in a rapidly developing coastal barrier jet. After the large-scale circulation has developed (> 12 h), the far upstream flow is rotated cyclonically and develops a barrier-parallel component. Thus, a portion of the total geostrophic adjustment to the broad mountain already occurs by the time the flow is within L_R of the barrier, which develops a barrier-parallel component well upstream of the coastal region. Therefore, the large-scale mountain anticyclone acts to "precondition" the impinging flow for barrier jet development and the superimposed circulation of the mountain anticyclone on the accelerated coastal flow also acts to expand the region of enhanced barrier-parallel wind speeds. This reinforces the results obtained by the two-dimensional simulations of Braun et al. (1999a), which showed that barrier jets are stronger for flow over a plateau-like barrier, but our results expand on their results by showing that simulations with the same barrier-normal velocity, but different ambient wind direction, can slightly alter the barrier jet structures through changes in the large-scale response, which superimposing a terrain-parallel circulation onto the jet.

Our largest simulated barrier-parallel wind speed enhancements for the classical jets (~1.9) occurred for low *Fr*, consistent with other studies (Ólafsson and Bougeault 1996; Petersen et al. 2003), but we found a maximum at *Fr* ~0.3-0.4. Ambient flows with $Fr < 0.3$ are typically oriented more barrier-parallel, so there is less of an along-barrier

pressure gradient to accelerate the flow near the coast, since the sole contribution would come from the mesoscale perturbations as opposed to the large-scale pressure gradient. Low ambient wind speeds (10 –15 m s^{-1}) and southerly (170-180^o) wind directions (~30-45^o from coast-parallel) were also ingredients for the largest wind speed enhancements.

During periods of maximal gap outflow (hrs 6-18), the height of the jet maximums were typically lower than their counterparts in the classical simulations, since the jet maximum was located at the top of the shallow gap outflow. After the inland cold pool became drained, hybrid jet heights were comparable to the classical jet heights. The jet height was positively correlated with total wind speed, U_{total}, and negatively correlated with static stability, N, suggesting that the height of the jet maximum approximately scales as U_{total}/N. The total wind speed, U_{total}, governed the strength of the turbulent mixing in the PBL by increasing the wind shear, but this mixing was countered by increases in static stability. The turbulent mixing created an enhancement of the stability at the top of the PBL; thus regulating the height of the barrier jets. A larger U_n also produces a deeper flow perturbation, thus impacting the depth of the barrier jet.

In an attempt to improve our ability to quantify the properties of coastal barrier jets, an assessment of previous techniques was undertaken. The work of Overland and Bond (1995; OB95) and Braun et al. (1999a; BR99) was verified against a set of three-dimensional idealized barrier jet simulations spanning a wide range of Froude numbers. Modifications of the Rossby radius of deformations was proposed to more accurately describe the offshore extent of the coastal barrier jets.

To determine the offshore extent of the coastal barrier jets, it was found that the high Fr relationship of OB95 ($L = Nh_m/f$) performed better than the low Fr relationship ($L = U_n/f$) throughout the entire set of idealized simulations. The main reason for the poor performance of the low Fr relationship was shown to be the use of the gravity wave height ($h = U_n/N$), which is consistent with the results of Braun et al (1999a). The implementation of the dividing streamline concept of Sheppard's model for determining the proper scale height resulted in a modified form, $L = Nh_d/f = Nh_m/f(1 - Fr/2)$, which was shown to improve the correlations with the measured offshore extent. The modified form also helped to improve the predictive skill, especially for $0.5 < Fr < 1.0$, where OB95's high Fr relationship typically overestimated the offshore extent by ~50 km for both classical and hybrid barrier jets.

For the determination of maximum wind speeds, the high Fr relationship ($\Delta V = Nh_m$) of OB95 was found to better correlate with the measured values than the low Fr relationship ($\Delta V = U_n$) for the full range of Fr. However, the high Fr relationship overestimated the maximum wind speed enhancements for $Fr < 0.5$ by ~50-100%. The two-dimensional linear theory of BR99, which relates the wind speed enhancement to the non-dimensional mountain height and the inland plateau width, was well correlated with both classical jets (0.77−0.85) and hybrid jets (0.94−0.97) (Table 5.2). All relationships tested seem to struggle more with classical jets when $Fr < 0.5$, with correlations typically less than 0.50, but had much higher correlations (> 0.73) for $Fr > 0.5$. The relatively poor performance for low Fr regime was likely due to the inability of linear theory (and scale analysis) to address the nonlinear nature of strongly blocked flows.

6.3 Suggested future work

The material of this thesis can be extended in three directions: (1) the three-dimensional idealized simulations could be expanded to cover baroclinic basic states; (2) more complex physics can be added to include moist processes and surface fluxes; (3) exploring non-equilibrium solutions, such as the transient forcing associated with landfalling cyclones; or a combination of sorts. The first two options are logical intermediary steps worthy of research, since the inclusion of a baroclinic wave greatly increases the degrees of freedom.

The addition of baroclinic basic states should alter the jet structure significantly, since baroclinic environments have already been shown to have a large impact on the development of the large-scale mountain anticyclone. Bannon and Zhender (1989) have shown that forward shear (wind increasing with height) will weaken the cold-core mountain anticyclone, while backwards shear (wind decreasing with height) strengthens it. This is due to the warm- (cold-) air advection in the forward (backwards) shear case, which acts to offset (reinforce) the adiabatic cooling of air rising over the barrier. Therefore, the degree of upstream influence produced by the large-scale adjustment, which was shown to be an important influence on the barrier jet structure and intensity (chapter 4), may be significantly modified by a baroclinic environment. Based on the results of chapter 4, one may hypothesize that barrier jets should be weaker and thinner within the forward shear environment, due to the decrease in pressure ridge over the barrier. The relative decrease in barrier jet width and intensity with respect to magnitude of the baroclinicity should be addressed.

In the planetary boundary layer (PBL), Ekman turning of the surface winds within a baroclinic environment will result in temperature advections, which will further alter the stability profile. This effect could potentially result in a reduction in the static stability and further weaken the barrier jets. Idealized simulations with and without surface friction could help elucidate the importance of this effect.

The second avenue of future research should involve the exploration of moist physics and surface fluxes. Moist processes can complicate the barrier jet evolution, because the stability can be decrease with latent heat release, but this can also create stable layers due to melting of snow or by evaporative cooling. Some interesting questions that should be addressed are:

- What is the effect of stable layers on influencing the structure of the barrier jet?
- Is the maximum stability in the upstream profile (beneath the mountaintop) more relevant then the mean stability in determining the degree of blocking and barrier jet formation?
- How well can a mesoscale model or large eddy model predict the turbulent wind and temperature structures with the PBL of a barrier jet?

The effects of surface fluxes may also influence the low-level stability and impact the barrier jet structure. Surface fluxes were shown to vary between prefrontal and postfrontal conditions over the North Pacific (Bond and Fleagle 1988). They showed that the prefrontal boundary layers are nearly neutrally stratified and surface heat and moisture fluxes were both small and generally downward, while postfrontal cases had

stronger upward heat and moisture fluxes within the PBL. This suggests that barrier jets occurring in prefrontal environments may be less impacted by surface fluxes; however, the large postfrontal fluxes can result in cumulus convection, which may significantly alter the thermal profile, resulting in variations in jet structure along the coast. Future research may address whether the surface fluxes can account for the large degree of variation in barrier jet strength Loescher et al. (2006) observed in a small subset of their SAR climatology. The model surface fluxes need to be verified with field data as well for barrier jets.

The third avenue of research worth exploring is the interaction of barrier jets and landfalling fronts with the coastal orography. This avenue also allows the researcher to examine the structure and evolution of the barrier jet in a non-steady state framework. Results obtained from idealized simulations of baroclinic waves interacting with the coastal mountains of Alaska would be useful for comparing with the idealized simulations presented herein. Some important questions that could be addressed are:

- How does the structure and intensity of the barrier jet evolve relative to the steady state structure given similar ambient conditions?
- How does the vertical and horizontal shear of the baroclinic wave alter the barrier jet structures compared to those in the barotropic simulations?

Although a large quantity of mountain meteorology literature exists, more work is needed to progress our understanding of the multi-scale impact mountains have on our weather and climate. For example, the errors in numerical weather prediction models were shown to be generally larger in regions of mountainous terrain (Schultz et al. 2002), where complex flows create strong low-level winds (barrier jets and gap flows), orographic clouds, and precipitation. These features are challenging to simulate accurately due to unresolved processes (i.e. microphysics and turbulence) and inaccurate terrain and land-use representation. Better forecasts of these severe weather events will reduce costs and increase safety for the relatively populated regions along coastal mountains.

References

Bannon, P. R. and J. A. Zhender, 1989: Baroclinic flow over a mountain ridge. *J. Atmos. Sci.,* **46**, 703–714.

Barstad, I. and S. Grønås, 2005: Southwesterly flows over southern Norway - mesoscale sensitivity to large-scale wind direction and speed. *Tellus,* **57A,** 136-152.

Batchelor, G. K., 1967: *An Introduction to Fluid Dynamics.* Cambridge University Press, 615 pp.

Bell, G. D. and L. F. Bosart, 1988: Appalachian cold-air damming. *Mon. Wea. Rev.,* **116,** 137-161.

Bond, N. A. and R. G. Fleagle, 1988: Prefrontal and postfrontal boundary layer processes over the ocean*. *Mon. Wea. Rev.,* **116**, 1257–1273.

Braun, S. A., R. Rotunno, and J. B. Klemp, 1999a: Effects of coastal orography on landfalling cold fronts. Part I: Dry, inviscid dynamics. *J. Atmos. Sci.,* **56**, 517–533.

Braun, S. A., R. Rotunno, and J. B. Klemp, 1999b: Effects of coastal orography on landfalling cold fronts. Part II: Effects of surface friction. *J. Atmos. Sci.,* **56**, 3366–3384.

Buzzi, A. and S. Tibaldi, 1977: Inertial and frictional effects on rotating and stratified flow over topography. *Quart. J. Roy. Meteor. Soc.,* **103,** 135–150.

Chelton, D. B., M. H. Freilich, J. M. Sienkiewicz, and J. M. Von Ahn, 2006: On the use of QuikSCAT scatterometer measurements of surface winds for marine weather prediction, *Mon. Wea. Rev.,* **134**, 2055–2071.

Chen, S. S., and W. M. Frank, 1993: A numerical study of the genesis of extratropical convective mesovortices. Part I: Evolution and dynamics**.** *J. Atmos. Sci.,* **50**, 2401–2426.

Chen, W.-D. and R. B. Smith, 1987: Blocking and deflection of airflow by the Alps. *J. Atmos. Sci.,* **115,** 2578-2597.

Chuang, H-Y., and P. J. Sousounis, 2000: A technique for generating idealized initial and boundary conditions for the PSU/NCAR model MM5. *Mon. Wea. Rev.,***128,** 2875-2882.

_____, and P. J. Sousounis, 2003: The impact of the prevailing synoptic situation on the lake-aggregate effect**.** *Mon. Wea. Rev.,* **131**, 990–1010.

Colle, B. A., B. F. Smull, and M.-J. Yang, 2002: Numerical simulations of a landfalling cold front observed during COAST: rapid evolution and responsible mechanisms*. *Mon. Wea. Rev.,* **130**, 1945–1966.

Colle, B. A., K. A. Loescher, G. S. Young , and N. S. Winstead, 2006: Climatology of barrier jets along the Alaskan Coast. Part II: Large-scale and sounding composites. *Mon. Wea. Rev.,* **134,** 454-477.

Colle, B. A., J. B. Wolfe, W. J. Steenburgh, D. E. Kingsmill, J. A. W. Cox, and J. C. Shafer, 2005. High-resolution simulations and microphysical validation of an orographic precipitation event over the Wasatch Mountains during IPEX IOP3. **133**, 2947–2971.

Colle, B. A. and C. F. Mass, 1995: The structure and evolution of cold surges east of the Rocky Mountains. *Mon. Wea. Rev.,* **123,** 2577-2610.

Colle, B. A. and C. F. Mass, 2000: High-resolution observations and numerical simulations of easterly gap flow through the Strait of Juan de Fuca on 9-10 December 1995. *Mon. Wea. Rev.,* **128,** 2398-2422.

Cox, J. A. W., W. J. Steenburgh, D. E. Kingsmill, J. C. Shafer, B. A. Colle, O. Bousquet, B. F. Smull, and H Cai, 2005: The kinematic structure of a Wasatch mountain winter storm during IPEX IOP3. *Mon. Wea. Rev.,* **133**, 521–542

Cui, Z, M. Tjernström, and B. Grisogono, 1998: Idealized simulations of atmospheric coastal flow along the central coast of California. *J. Appl. Meteor,* **37,** 1332-1363.

Cushman-Roisin, B., 1994: *Introduction to Geophysical Fluid Dynamics.* Prentice Hall, 320 pp.

Davies, H. C., C. Schär, and H. Wernli, 1991: The palette of fronts and cyclones within a baroclinic wave development**.** *J. Atmos. Sci.*, **48**, 1666–1689.

Davis, C. A, 1997: The modification of baroclinic waves by the Rocky Mountains. *J. Atmos. Sci.*, **54**, 848–868.

_____, and M. T. Stoelinga, 1999: Interpretation of the effect of mountains on synoptic-scale baroclinic waves. *J. Atmos. Sci.*, **56**, 3303–3320.

Doyle, J. D., 1997: The influence of mesoscale orography on a coastal jet and rainband. *Mon. Wea. Rev.,* **125,** 1465-1488.

Doyle, J. D. and N. A. Bond, 2001: Research aircraft observations and numerical simulations of a warm front approaching Vancouver Island. *Mon. Wea. Rev.,* **129,** 978-998.

Dudhia, J., 1989: Numerical study of convection observed during the winter monsoon experiment using a mesoscale two-dimensional model. *J. Atmos. Sci.,* **46,** 3077-3107.

Durran, D. R. and J. B. Klemp, 1982: On the effects of moisture on the Brunt-Väisälä frequency. *J. Atmos. Sci.,* **39,** 2152-2158Fritsch, J. M., E. L. Magaziner, and C. F. Chappell, 1980: Analytical initialization for three-dimensional numerical models. *Jour. Appl. Met.,* **19,** 809-818.

Grell, G. A., J. Dudhia, and D. R. Stauffer, 1995: A description of the fifth-generation PSU/NCAR mesoscale model (MM5). NCAR Technical Note. No 398+STR.

Grell, G. A., 1993: Prognostic evaluation of assumptions used by cumulus parameterizations. *Mon. Wea. Rev.,* **121,** 764-787.

Gross, B. D., 1994: Frontal interaction with isolated orography**.** *J. Atmos. Sci.*, **51**, 1480–1496.

Haltiner, G. J., and R. T. Williams, 1980: *Numerical prediction and dynamic meteorology*. John Wiley & Sons, 477 pp.

Heckley, W. A. and B. J. Hoskins, 1982: Baroclinic waves and frontogenesis in a non-uniform potential vorticity semi-geostrophic model. *J. Atmos. Sci.*, **39**, 1999–2016.

Holton, J. R., 2004: *An Introduction to Dynamic Meteorology.* Academic Press, 535 pp.

Hoskins, B. J., and N. V. West, 1979: Baroclinic waves and frontogenesis. Part II: Uniform potential vorticity jet flows – cold and warm fronts. *J. Atmos. Sci.*, **36**, 1663–1680.

Klemp, J. B. and D. R. Durran, 1983: An upper boundary condition permitting internal gravity wave radiation in numerical mesoscale models. *J. Atmos. Sci.,* **111,** 430-444.

Kuettner, J. P., 1986: The aim and conduct of ALPEX. JCSU-WMO, GARP Publ. Ser. No. 27, 31-48.

Lackmann, G. M. and J. Overland, 1989: Atmospheric structure and momentum balance during a gap-wind event in Shelikof Strait, Alaska. *Mon. Wea. Rev.,* **116,** 1289-1301.

Li, J. and Y.-L. Chen, 1998: Barrier jets during TAMEX. *Mon. Wea. Rev.,* **126,** 959-971.

Li, S.-W., M. S. Peng, and R. T. Williams, 1996: A three-dimensional study of the influence of mountains on a front**.** *J. Atmos. Sci.*, **53**, 2757–2772.

Lin, Y.-L. and T.-A. Wang, 1996: Flow regimes and transient dynamics of two-dimensional flow over an isolated mountain ridge. *J. Atmos. Sci.*, **53**, 139–158.

Loescher, K. A., G. S. Young, B. A. Colle , and N. S. Winstead, 2006: Climatology of barrier jets along the Alaskan Coast. Part I: Spatial and temporal distributions. *Mon. Wea. Rev.,* **134,** 437-453.

Macklin, S. A., N. A. Bond , and J. P. Walker, 1990: Structure of a low-level jet over lower Cook Inlet, Alaska. *Mon. Wea. Rev.,* **118,** 2568-2578.

Malguzzi, P., A. Trevisan, and A. Speranza, 1987: The effects of finite height topography on nongeostrophic baroclinic instability: Implications to theories of lee cyclogenesis. *J. Atmos. Sci.*, **44**, 1475-1482.

Marwitz, J. D., 1983: The kinematics of orographic airflow during Sierra storms. *J. Atmos. Sci.,* **40,** 1218-1227.

Mass, C. F., S. Bussinger, M. Albright , and Z. A. Tucker, 1995: A windstorm in the lee of a gap in a coastal mountain barrier. *Mon. Wea. Rev.,* **123,** 315-331.

Mass, C. F. and G. K. Ferber, 1990: Surface pressure perturbations produced by an isolated mesoscale topographic barrier. Part I: General characteristics and dynamics. *Mon. Wea. Rev.,* **118,** 2579-2596.

Mass, C. F. and M. D. Albright, 1985: A Severe windstorm in the lee of the Cascade mountains of Washington State. *Mon. Wea. Rev.,* **113,** 1261–1281.

Mellor, G. L. and T. Yamada, 1974: A hierarchy of turbulence closure models for planetary boundary layers. *J. Atmos. Sci.,* **31,** 1791-1806.

Miles, J. W. and H. E. Huppert, 1969: Lee waves in stratified flow. Part IV: Perturbation approximations. *J. Fluid Mech.,* **35**, 497-525.

Montgomery, M. F., and B. F. Farrell, 1992: Polar low dynamics. *J. Atmos. Sci.*, **49**, 2484-2505.

Moore, G. W. K., and I. A. Renfrew, 2005: Tip jets and barrier winds: A QuikSCAT climatology of high wind speed events around Greenland. *J. Climate*. **18**, 3713-3715.

Moore, R. W. and M. T. Montgomery, 2005: Analysis of an idealized, three-dimensional diabatic rossby vortex: a coherent structure of the moist baroclinic atmosphere. *J. Atmos. Sci.,* **62**, 2703–2725.

Neiman, P. J., F. M. Ralph, A. B. White, D. D. Parrish, J. S. Holloway , and D. L. Bartels, 2006: A midwinter analysis of channeled flow through a prominent gap along northern California Coast during CALJET and PACJET. *Mon. Wea. Rev.,* **134,** 1815-1841.

Neiman, P. J., P. Ola G. Persson, F. M.Ralph, D. P. Jorgensen, A. B. White, and D. E. Kingsmill, 2004: Modification of fronts and precipitation by coastal blocking during an intense landfalling winter storm in southern California: Observations during CALJET. *Mon. Wea. Rev.,* **132,** 242-273.

Nuss, W. A., 1986: The influence of surface heat and moisture fluxes on explosive marine cyclogenesis. Ph.D. dissertation, University of Washington, 181 pp.

_____, and R. A. Anthes, 1987: A numerical investigation of low-level processes in rapid cyclogenesis. *Mon. Wea. Rev.*, **115,** 2728-2743.

Ólafsson, H. and Bougeault, P., 1996: Nonlinear flow past an elliptic mountain ridge. *J. Atmos. Sci.*, **53**, 2465–2489.

Orlanski, I., and B. D. Gross, 1994: Orographic modification of cyclone development**.** *J. Atmos. Sci.*, **51**, 589–612.

Overland, J. E. and N. A. Bond, 1995: Observations and scale analysis of coastal jets. *Mon. Wea. Rev.,* **42,** 271-282.

Overland, J. E. and N. A. Bond, 1993: The influence of coastal orography: The Yakutat storm. *Mon. Wea. Rev.,* **121,** 1388-1397.

Parish, T. R., 1982: Barrier winds along the Sierra Nevada Mountains. *J. Appl. Meteor,* **21,** 925-930.

Petersen, G. N., J. E. Kristjánsson, and H. Ólafsson (2003): The effect of upstream wind direction on atmospheric flow in the vicinity of a large mountain. *Quart. J. Roy. Meteor. Soc.,* **131,** 1113–1128.

Petterssen, S., and S. J. Smebye, 1971: On the development of extratropical cyclones. *Quart. J. Roy. Meteor. Soc.,* **97,** 457–482.

Pierrehumbert, R. T. and B. Wyman, 1985: Upstream effects of mesoscale mountains. *J. Atmos. Sci.,* **42,** 977-1003.

Queney, P., 1948: The problem of airflow over mountains: A summary of theoretical studies. .*Bull. Amer. Meteor. Soc.,* **42,** 16-26.

Richwien, B. A., 1980: The damming effect of the southern Appalachians. *Nat. Wea. Dig.,* **5**, 2-12

Sanders, F., and J. R. Gyakum, 1980: Synoptic-dynamic climatology of the "bomb"**.** *Mon. Wea. Rev.,* **108**, 1589–1606.

Schär, C., and H. Wernli, 1993: Structure and evolution of an isolated semi-geostrophic cyclone. *Quart. J.Roy. Metoer. Soc.*, **119,** 57-90.

Schultz, D. M., W. J. Steenburgh, R. J. Trapp, J. Horel, D. E. Kingsmill, L. B. Dunn, W. D. Rust, L. Cheng, A. Bansemer, J. Cox, J. Daugherty, D. P. Jorgensen, J. Meitín, L. Showell, B. F. Smull, K. Tarp, and M. Trainor, 2002: Understanding Utah winter storms: The intermountain precipitation experiment. **83**, 210–210.

Schumann, U., 1987: Influence of mesoscale orography on idealized cold fronts**.** *J. Atmos. Sci.*, **44**, 3423–3441.

Schwerdtfeger, W., 1974: Mountain barrier effect on the flow of stable air north of the Brooks Range. *Proc.24th Alaskan Science Conference* Fairbanks, AL, Geophysical Institute, University of Alaska Fairbanks*,* 204-208.

Schwerdtfeger, W., 1975: The effect of the Antarctic Peninsula on the temperature regime of the Wedell Sea. *Mon. Wea. Rev.,* **103,** 45-51.

Sheppard, P. A., 1956: Airflow over mountains. *Quart. J.Roy. Metoer. Soc.*, **82,** 528-529.

Simmons, A. J. and B. Hoskins, 1976: Baroclinic instability on the sphere: normal modes of the primitive and quasi-geostrophic equations. *J. Atmos. Sci.*, **33**, 1454-1477.

_____, and B. Hoskins, 1978: The life cycles of some nonlinear baroclinic waves. *J. Atmos. Sci.*, **35**, 414-432.

Skamarock, W. C., J. B. Klemp, J. Dudhia, D. O. Gill, D. M. Barker, W. Wang and J. G. Powers, 2005: A description of the advanced research WRF version 2. *NCAR Technical Note.*

Smith, R. B. and Grønås, S. 1993: Stagnation points and bifurcation in 3-D mountain air-flow. *Tellus A*. **45**, 28-43.

Smith, R. B. 1989a. Hydrostatic air-flow over mountains. *Adv. Geophys.* **31**, 1-41.

Smith, R. B, 1989b, Mountain induced stagnation points in hydrostatic flow. *Tellus*, **41**, 270-274.

Smith, R. B. 1982. Synoptic observations and theory of orographically disturbed wind and pressure. *J. Atmos. Sci.* **39**, 60-70.

Smith, R. B. 1980. Linear-theory of stratified hydrostatic flow past an isolated mountain. *Tellus* **32**, 348-364.

Smith, R. B., 1979a: The influence of mountains on the atamoshpere. *Advances in Geophysics,* **21**, Academic Press, 87-230.

Smith, R. B., 1979b: Some aspects of quasi-geostrophic flow over mountains. *J. Atmo. Sci.,* **36**, 2385-2393.

Smolarkiewicz, P. K. and R. Rotunno, 1989: Low Froude number flow past three-dimensional obstacles. Part 1: Baroclinically generated lee vortices. *J. Atmos. Sci.* **46**, 1154-1164.

Smolarkiewicz, P. K. and R. Rotunno, 1990: Low Froude number flow past three-dimensional obstacles. Part II: Upwind flow reversal zone. *J. Atmos. Sci.* **47**, 1498-1511.

Speranza, A, A. Buzzi, A. Trevisan, and P. Malguzzi, 1985: A theory of deep cyclogenesis in the lee of the Alps. Part I: Modifications of baroclinic instability by localized topography**.** *J. Atmos. Sci.*, **42**, 1521–1535.

Stauffer, D. R.. and N. L. Seaman, 1994: Multiscale Four-Dimensional Data Assimilation. *J. Appl. Meteor.,* **33,** 416-434.

Tan, Z-M., F. Zhang, R. Rotunno, and C. Snyder, 2004: Mesoscale Predictability of Moist Baroclinic Waves: Experiments with Parameterized Convection**.** *J. Atmos. Sci.,* **61**, 1794–1804.

Thorncroft, C. D., B. J. Hoskins, and M. E. McIntyre, 1993: Two paradigms of baroclinic-wave life-cycle behaviour. *Quart. J. Roy. Meteor. Soc.*, **119**, 17-56.

Tibaldi, S., A. Buzzi, and P. Malguzzi, 1980: Orographically induced cyclogenesis: analysis of numerical experiments**.** *Mon. Wea. Rev.*, **108**, 1302–1314.

Trombetti, F. and F. Tampieri, 1987: An application of the dividing-streamline concept to stable airflow over mesoscale mountains. *Mon. Wea. Rev.*, **115**, 1802–1806.

W.M.O, 1957: Meteorology—A three dimensional science. *WMO Bull.,* **6**, 134–138.

Wang, C-C, G. Tai-Jen Chen, Tzu-Chin Chen and K. Tsuboki, 2005: A numerical study on the effects of Taiwan topography on a convective line during the Mei-Yu season**.** *Mon. Wea. Rev*. **133**, 3217–3242.

Wernli, H., R. Fehlmann, and D. Lüthi, 1998: The effect of barotropic shear on upper-level induced cyclogenesis: semigeostrophic and primitive equation numerical simulations. *J. Atmos. Sci.*, **55**, 2080-2094.

Winstead, N. S., B. A. Colle, N. A. Bond, G. Young, J. B. Olson, K. Loescher, F. Monaldo, D. Thompson, and W. Pichel, 2006: Barrier jets: combining SAR remote sensing, field observations, and models to better understand coastal flows in the Gulf of Alaska. *Bull. Amer. Meteor. Soc.,* **87,** 787-800.

Xu, Q., 1990: A theoretical study of cold air damming with upslope cold air inflow. *J. Atmos. Sci.*, **53**, 312-326.

Xu, Q., 1996: A theoretical study of cold air damming. *J. Atmos. Sci.*, **47**, 2969-2985.

Yeh, H.-C. and Y.-L. Chen, 2003: Numerical simulations of the barrier jet over northwestern Taiwan during the Mei-Yu season. *Mon. Wea. Rev.,* **131,** 1396-1407.

Yu, C.-K. and B. F. Smull, 2000: Airborne observations of a landfalling cold front upstream of steep coastal orography. *Mon. Wea. Rev.,* **128,** 674-692.

Zängl, G., 2005: Formation of extreme cold-air pools in elevated sinkholes: An idealized numerical process study. *Mon. Wea. Rev.,* **133,** 925–941.

Zängl, G., 2003: The impact of upstream blocking, drainage flow, and the geostrophic pressure gradient on the persistence of cold-air pools. *Quart. J. Roy. Meteor. Soc.,* **129,** 117–137.

Zhang, D. and R. A. Anthes, 1982: A high-resolution model of the planetary boundary layer-Sensitivity tests and comparisons with SESAME-79 data. *J. Appl. Meteor.,* **21,** 1594-1609.